Genome-in-a-box: Building a Chromosome from the Bottom Up

Birnie, A.T.F.

DOI
10.4233/uuid:c9f643aa-c1a2-4028-bd82-2f2baf63c627

Publication date
2023

Document Version
Final published version

Citation (APA)
Birnie, A. T. F. (2023). *Genome-in-a-box: Building a Chromosome from the Bottom Up*. [Dissertation (TU Delft), Delft University of Technology]. https://doi.org/10.4233/uuid:c9f643aa-c1a2-4028-bd82-2f2baf63c627

Important note
To cite this publication, please use the final published version (if applicable).
Please check the document version above.

GENOME-IN-A-BOX

BUILDING A CHROMOSOME FROM THE BOTTOM UP

GENOME-IN-A-BOX

BUILDING A CHROMOSOME FROM THE BOTTOM UP

Dissertation

for the purpose of obtaining the degree of doctor

at Delft University of Technology,

by the authority of the Rector Magnificus prof.dr.ir. T.H.J.J. van der Hagen,

chair of the Board for Doctorates

to be defended publicly on

Friday 13 October 2023 at 15:00 o'clock

by

Anthony Thomas Frans BIRNIE

Bachelor of Science in Physics & Astronomy
Universiteit van Amsterdam, the Netherlands,

born in Amsterdam, the Netherlands

This dissertation has been approved by the promotor.

Composition of the doctoral committee:

Rector Magnificus,	chairperson
Prof. dr. C. Dekker	Delft University of Technology, promotor
Independent members:	
Prof. dr. N. H. Dekker	Delft University of Technology
Prof. dr. B. M. Mulder	AMOLF & Utrecht University
Prof. dr. W. T. S. Huck	Radboud University
Prof. dr. R. T. Dame	Leiden University
Prof. dr. G. J. L. Wuite	Vrije Universiteit Amsterdam
Dr. K. A. Ganzinger	AMOLF
Prof. dr. S. J. J. Brouns	Delft University of Technology, reserve member

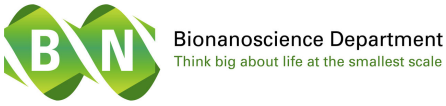

Printed by: Gildeprint

Front & Back: Anthony Birnie

Casimir PhD Series, Delft-Leiden 2023-27

ISBN/EAN: 978-90-8593-575-9

An electronic version of this dissertation is available at
`http://repository.tudelft.nl/`.

"The peculiar evil of silencing the expression of an opinion is, that it is robbing the human race; posterity as well as the existing generation; those who dissent from the opinion, still more than those who hold it. If the opinion is right, they are deprived of the opportunity of exchanging error for truth: if wrong, they lose, what is almost as great a benefit, the clearer perception and livelier impression of truth, produced by its collision with error."

John Stuart Mill

CONTENTS

SUMMARY

Chapter 1 gives a layman's introduction to DNA, the field of chromosome organization, and the scientific techniques used to study DNA. We discuss the structure of DNA, and why a cell needs its DNA to be neatly organized and what cellular components are involved in DNA organization. Then we explain how chromosome organization influences the processes of target search and transcription, which are crucial processes in living systems. To motivate our decision to develop a new method to study chromosome organization (called genome-in-a-box or GenBox), we first give an overview of current methods and their shortcomings. Lastly, we enumerate several scientific questions that could be addressed with the GenBox method and what the experimental requirements would be to implement the method in practice.

Chapter 2 provides a brief literature review of the chromosome organization field and a perspective on how GenBox as a new method expands the experimental toolbox available to researchers. Firstly, we give an overview of the chromosome building blocks, the DNA-structuring elements that influence the organization and dynamics of DNA inside cells. Examples of these chromosome building blocks are DNA-binding proteins, such as condensin which extrudes loops of DNA; crowding agents, such as the molecules in the nucleoplasm or cytoplasm which compact the DNA through volume exclusion and solvent related effects; and the cellular container, which confines the DNA thereby altering its dynamics and structure. Secondly, we make an inventory of the currently available methods to study chromosome organization in both living cells as well as *in vitro* in a test tube. Various techniques are discussed ranging from Chromosome Conformation Capture methods to quantify the contact frequencies of loci on the DNA, to single-molecule methods that can elucidate the forces, torques and binding kinetics of DNA-protein interactions. Finally, we propose GenBox as an additional *in vitro* method to study chromosome organization using large megabasepair DNA substrates, and in what way it would expand on the currently available methods.

Chapter 3 delves into the experimental realization of the proposal discussed in chapter 2. It provides an outline of the GenBox workflow in practice, and shows how we purify bacterial chromosomes from cells, remove DNA-binding proteins, and characterize the resulting DNA-objects. Starting from bacterial cells, two protocols are presented how to obtain the megabasepair DNA for GenBox experiments, namely the agarose plug protocol and the bulk protocol. In the former, the bacterial cells are lysed inside an agarose gel plug, while in the latter the cells are lysed directly into a solution. In both cases native DNA-binding proteins are removed using a protein-digesting enzyme. Then mass spectrometry and fluorescence imaging are performed on the resulting DNA objects to characterize the efficiency of the protein removal and to verify the size and integrity of

the megabasepair DNA. Lastly, three example experiments are shown that demonstrate the GenBox in practice, by for example adding DNA-compacting proteins (bacterial Fis) and a crowding agent (PEG) to the DNA.

In **Chapter 4** we explore how microfluidic structures can be used to manipulate the shape and size of droplets and double emulsions. Various biological processes (such as pattern formation) and macromolecular complexes (such as the cytoskeleton and the genome) are sensitive to the spatial confinement. We show how to change the shape and size of cell-sized droplets and double emulsions in order to study the influence of spatial confinement on cellular components contained within. We provide examples of the method using various cellular protein bundle networks (such as FtsZ, tubulin and collagen) encapsulated inside spherical and rod-shaped droplets. In the future, this toolbox may also be used to study confined megabasepair DNA in the context of a GenBox experiment.

Chapter 5 discusses experiments in which the protein complex condensin is added to isolated bacterial chromosomes as an example of a first application of the GenBox approach. The loop-extruding condensin compacts the megabasepair DNA in a concentration-dependent manner over the course of minutes, resulting in a heterogeneous object with dense DNA clusters. These experiments were performed with an earlier version of the protocols described in chapter 3 (without protein removal), meaning that the interpretation of the results was not unambiguous. Nevertheless, they do illustrate the type of experiments that can done with the GenBox approach.

SAMENVATTING

Hoofdstuk 1 introduceert op eenvoudige wijze het werkveld van DNA, chromosoomorgansisatie, en de experimentele technieken om DNA te bestuderen. We gaan dieper in op de structuur van DNA, en waarom het noodzakelijk is voor een cel om 'georganiseerd' DNA te hebben en welke celcomponenten dit voor elkaar krijgen. Dan leggen we uit hoe de DNA-structuur van invloed is op zoekprocessen van eiwitten (bijv. hoe een DNA-bindend eiwit zijn een bindingslocatie op het DNA kan vinden) en transcriptie, welke beiden van cruciaal belang voor een levend systeem. Om duidelijk te maken waarom we ervoor gekozen hebben om een nieuwe methode (genaamd "genome-in-box" oftewel, "genoom-in-een-doosje") te ontwikkelen waarmee we chromosoomorganisatie kunnen bestuderen, geven we eerst een overzicht van al bestaande methoden en hun beperkingen. Tenslotte bespreken we enkele wetenschappelijke vragen die met deze genoom-in-een-doosje (GenBox) methode beantwoord zouden kunnen worden, en welke vereisten er zijn om de methode in de praktijk te brengen.

Hoofdstuk 2 geeft een overzicht van relevante wetenschappelijk literatuur over het werkveld van chromosoomorganisatie en een vooruitblik hoe GenBox als een nieuwe methode de experimentele gereedschapskist uitbreidt voor wetenschappers. We beginnen met een uiteenzetting van de bouwstenen van het chromosoom, d.w.z. de cellulaire componenten die op verschillende manieren invloed hebben op de organisatie en dynamica van DNA in een cel. Er zijn legio voorbeelden van zulke bouwstenen, bijvoorbeeld DNA-bindende eiwitten zoals condensin dat lusjes van DNA kan maken. Of de zogenoemde 'verdringingsmoleculen', zoals moleculen in het cytoplasma of het nucleoplasma die DNA in een compactere vorm kunnen brengen door volume uitsluiting en andere effecten gerelateerd aan hun eigenschappen als oplosmiddel voor het DNA. En uiteraard ook het omhulsel van de cel, dat het DNA in een kleinere ruimte opsluit dan je zou verwachten op basis van de DNA-lengte, en dat daarmee de dynamica en structuur van het DNA verandert. Vervolgens inventariseren we welke methoden er op dit moment al beschikbaar zijn om DNA en chromosomen te bestuderen, zowel *in vivo* (in levende cellen) als *in vitro* (in een reageerbuisje). Verscheidene technieken komen aan bod, zoals de methode van Chromosoom Conformatie Vastlegging, waarmee bepaald wordt welke locaties op het DNA met elkaar fysiek in contact komen, tot en met methodes die op het niveau van een enkel molecuul kunnen meten wat de relevante krachten, koppels en bindingskinetica zijn voor de interactie tussen een eiwit en het DNA. Tenslotte stellen we GenBox voor als een *in vitro* methode om chromosoomorganisatie te bestuderen, gebruikmakend van megabasenparen-lange DNA-moleculen, en we geven aan in welk opzicht GenBox een waardevolle uitbreiding zal zijn van de al beschikbare technieken.

Hoofdstuk 3 beschrijft de experimentele verwezenlijking van het voorstel dat in hoofdstuk 2 is gedaan. Het verschaft een overzicht van alle stappen van het GenBox protocol in de praktijk, en laat zien hoe we bacteriële chromosomen purificeren uit cellen, de DNA-bindende eiwitten verwijderen en vervolgens de resulterende DNA-objecten karakteriseren. Uitgaande van bacteriële cellen presenteren we twee afzonderlijke protocollen om megabasenpaar-lang DNA voor GenBox experimenten te verkrijgen: het agarose gel protocol en het bulk protocol. In het eerstgenoemde protocol worden de cellen gelyseerd terwijl opgesloten zijn in een blokje agarose gel, daarentegen voor het bulk protocol gebeurt dat direct in een vloeibare oplossing. In beide gevallen worden de vanuit de cel aanwezige DNA-bindende eiwitten afgebroken met een eiwit-verterend enzym. Daarna gebruiken we massaspectrometrie en fluorescentiemicroscopie om de resulterende DNA-objecten te karakteriseren, en daarmee vast te stellen hoe effectief de eiwitverwijderingsstap was en of megabasenpaar-lange DNA nog intact is (dus of de grootte overeenkomt met wat we theoretisch zouden verwachten). Tot slot demonstreren we de GenBox methode in de praktijk door aan het geïsoleerde DNA verscheidene DNA-bindende eiwitten (bacterieel Fis) en verdringingmoleculen (PEG) toe te voegen, en dan te observeren hoe het DNA-object kleiner wordt.

Hoofdstuk 4 verkent de mogelijkheden om microfluïdica en microfabricage te gebruiken om de vorm en grootte van druppels en dubbele emulsies te manipuleren. Verschillende biologische processen (zoals patroonvorming) en macromoleculaire complexen (zoals het cytoskelet en het genoom) zijn gevoelig voor ruimtelijke opsluiting waar ze zich in bevinden. We laten zien hoe we de vorm van druppels en dubbele emulsies kunnen veranderen om de eigenschappen en conformatie van daarin opgesloten cellulaire componenten te beïnvloeden. We geven enkele voorbeelden van eiwitnetwerken zoals FtsZ, tubuline en collageen die andere ruimtelijke conformaties aannemen als ze in een cilindervormige druppel zitten, ten opzichte van een bolvormige druppel. In de toekomst kan deze gereedschapskist van microfluidica en microfabricage worden gebruikt om in een GenBox experiment een chromosoom in een druppel op te sluiten met dezelfde grootte en vorm van een echte cel.

Hoofdstuk 5 toont de resultaten van experimenten waarbij het DNA-lusjes-makende eiwitcomplex condensin wordt toegevoegd aan megabasenpaar-lang DNA, als een eerste uitgewerkte toepassing van een GenBox experiment. Condensin maakt het DNA compacter door lusjes DNA te vormen, en het doet dit op concentratieafhankelijke wijze binnen een tijdspanne van ongeveer 10 minuten. Dit proces resulteert in een compact DNA-object met een heterogene interne structuur waarbij sommige delen van het object dichter opeen zijn gepakt dan andere (DNA-clusters). Deze experimenten zijn uitgevoerd met een vroegere versie van de protocollen beschreven in hoofdstuk 3 (namelijk zonder verwijdering van de cellulaire eiwitten). Dit betekent dat de interpretatie van de resultaten nog niet definitief kan zijn, maar toch illustreert dit hoofdstuk de interessante experimenten die gedaan kunnen worden met de GenBox methode.

1

INTRODUCTION

For this thesis we set out to develop a new experimental method to study chromosome organization, which we call genome-in-a-box (GenBox). In this chapter, a question/answer-style non-technical introduction is given to the field of chromosome organization and what is already known about how cells organize their DNA. We briefly discuss current methods to study this topic, specifically cell-biology experiments and single-molecule *in vitro* experiments, and the limitations of these methods, thereby motivating our efforts to develop a different approach. Then we propose what scientific questions could be answered using GenBox. On a more practical side, we describe the experimental requirements for GenBox and possible avenues to achieve them. Finally, an overview of the thesis chapters is provided.

1

1.1. WHAT IS THE NEED FOR CHROMOSOME ORGANIZATION?

DNA is a polymeric molecule which resides in the cells of every living organism. Its structure is that of a double helix, with two polynucleotide strands wrapped around each other in a right-handed spiral. The monomers of the polymer chains are the nucleotides, and each contain a nucleobase (the 'letters' of the genetic code), a sugar (deoxyribose) and a phosphate group. The 'letters' (cytosine, C; and thymine, T; guanine, G; and adenine, A) on one of the polynucleotides chains are complementary to the those on the other polynucleotide chain. Complementarity means that hydrogen bridges are formed between the two chains according to the base pairing rules: A pairs with T; G pairs with C (figure 1.1a). The letters of the genetic code form 'sentences' or genes, which through the processes of transcription (reading out the gene into an mRNA molecule) and translation (converting the mRNA molecule into a protein) result in functional proteins, the workhorses of each cell.[1,2] There is a problem associated with DNA for which living organisms have found solutions over the course of evolution. This challenge is that DNA contains many genes (*e.g.*, ~20,000 protein-coding genes for the human genome[3]). This leads to two issues: first, the resulting DNA molecule is a very long polymer, and second, it would not be biologically useful if all the genes were active at the same time. Both of these issues are solved through chromosome organization. We first will expand on these two issues.

DNA is a molecule of a few millimeters in length in bacteria, but which can reach many meters in eukaryotes (for the total genome).[4] This length is the end-to-end distance of the molecule in a stretched form, and obviously, in real life the DNA molecule does not exist in such a stretched conformation. Polymer physics dictates that DNA will form a blob-like globular structure, if left unperturbed.[5] Nevertheless, even in this form, the resulting DNA object would be much larger than the cell that contains it. For example, if the 3 gigabasepair human genome were one long chromosome, it would form a globular object with a radius of 130 μm (assuming DNA behaves according to the worm-like chain polymer model[6,7]), while the nucleus of a human cell typically is only 10 μm large.[8] One should realize that there does not exist a stage in any cell's life cycle during which the genome is outside of the cell and needs to be compacted to fit back inside. Yet, the discrepancy between the size of the cell and the relaxed genome is certainly real. To solve this issue nature has "invented/evolved" chromosome organization to keep the large genomic polymer constrained enabling the cell to take on a physiologically manageable size.

The development of an organism, be it a bacterium or a complex multi-cellular organism, hinges on the timely expression of different sets of genes. Therefore, the regulation of gene expression is of utmost importance to the survival of each organism. This regulation consists of mechanisms that ensure that certain sets of genes are active, while others remain inactive, and to switch between these states, depending on, amongst others, environmental circumstances and the stage of development.[9]

As indicated before, cells use chromosome organization to solve both issues described above. The intriguing thing is that the first issue relates to the structure and physical

properties of the DNA molecule ('how will it fit in the cell') and the second relates to the function of the DNA molecule ('how is the genetic information read out in an organized manner'). It turns out that the structure and physical properties of the DNA are not only leading in solving of the first 'how will it fit in the cell?'-issue, but also relevant to the functional problem of gene regulation. Like for proteins, the structure and function of DNA are intimately intertwined.

1.2. HOW DO CELLS ACHIEVE CHROMOSOME ORGANIZATION?

Bacteria and eukaryotes have a variety of DNA-binding proteins which bend, wrap, twist, bridge, and loop the DNA, thereby altering both its spatial structure and physical properties.[10–15] In bacteria these proteins are distributed over the whole chromosome, with some proteins being restricted to certain regions of the chromosome. Eukaryotes wrap their DNA around histones forming nucleosomes of 10 nm in diameter in a beads-on-a-string structure, which is called chromatin. These nucleosomes can be modified not only to modulate the attractive and repulsive interactions between them, but also to dictate what genes can be activated or not.[16,17] Other elements of eukaryotic chromosome organization, such as loop extruding proteins condensin and cohesin, act on the chromatin.[14,15,18–20] Zooming out from the DNA and the proteins which attach to it directly, there is the cytoplasm and nucleoplasm which have a strong structural effect by compacting the DNA through crowding and solvent related effects.[21,22] Finally, there is the nuclear or cellular boundary which contains the DNA, and prevents it from exiting the cell and expanding to the natural size of the genome.[23,24]

1.3. HOW DOES CHROMOSOME ORGANIZATION INFLUENCE TRANSCRIPTION?

In order to transcribe a gene, an RNA polymerase must find and bind a promotor sequence, activate, and then initiate mRNA elongation. This sounds relatively easy, but each of these steps contains multiple regulated sub-steps. For example, the recruitment of a polymerase to the DNA is helped by transcription activators and inhibited by transcription repressors, which must find and bind to sequences near to the promotor. Similarly, once on the DNA, the polymerase needs to be activated through several phosphorylation steps and binding of co-factors. To even start this whole process, the DNA in eukaryotes needs to be made accessible, *i.e.*, chromatin needs to be locally remodeled (modification and displacement of nucleosomes) to expose relevant DNA sequences.[9] At every stage in the complex process described above, the common thread is that some protein complex must diffuse around, find, and bind, and finally unbind a particular sequence on the DNA (figure 1.1b). Furthermore, the binding and activation of the polymerase is not only under control of the promotor and nearby control sequences, but can also be influenced by transcription factors binding at sequences far away (even up to a million basepairs distance[25]) from the promotor at so-called enhancers. In a currently unknown manner, the signal of the factors binding at these far-away locations is

transmitted to the promotor, either through (transient) direct physical contact, *via* indirect contact through biomolecular condensates, or otherwise with a diffusion-mediated action-at-a-distance signal (figure 1.1c).[26–29] In two of four of these mechanisms, loci-loci interaction is not needed, meaning that it becomes more difficult to interpret the importance of contact maps with the averaged interaction probability between loci.

The two processes described in the previous paragraph (proteins finding their target on the DNA and genomic loci interacting) are related to the function of DNA. These processes are both regulated by the structure of the DNA polymer and the surrounding cytoplasm or nucleoplasm.[21,26,30,31] For example, the presence of loop factors could aid in the target search or the probability of far-away sequences coming into contact (figure 1.1c). Or otherwise, the local condensation of inactive DNA might speed up the target search process by reducing the search volume for the diffusing protein (figure 1.1b-*ii/iii*. Similarly, the viscoelastic properties of the nucleoplasm and the surrounding DNA mesh can promote or restrict the diffusion of proteins (figure 1.1b). Also, in a compacted DNA polymer entanglements might play a role, which would alter both factor diffusion and loci-loci contact probabilities. Therefore, regulation of the local fluidity of the DNA solution could be important.[32] For example, if the structure of the chromatin or DNA is such that it is very dynamic at a local scale, rather than static, this might increase the chance of a protein finding its binding sequence (figure 1.1d).

A recent preprint by Grosse-Holz *et al.*[33] provides a useful overview of the various experimental observables that together describe the structural and dynamic state of the DNA in a cell (figure 1.1e). These observables are: the mean-square displacement of the whole DNA coil or a long sub-chain within the viscoelastic solvent of the nucleoplasm/cytoplasm, and how this depends of the chain length; how the radius of the coil scales with chain length; what the mean square displacement is of a locus on the DNA; and how loci respond to external force perturbations. Any experimental system, either *in vivo* or *in vitro*, will need to measure these quantities in order to describe the chromosomal organization in a quantitative manner. Secondly, these "structural/organizational" observables need to be linked to functional outcomes, such as transcriptional activation or repression.

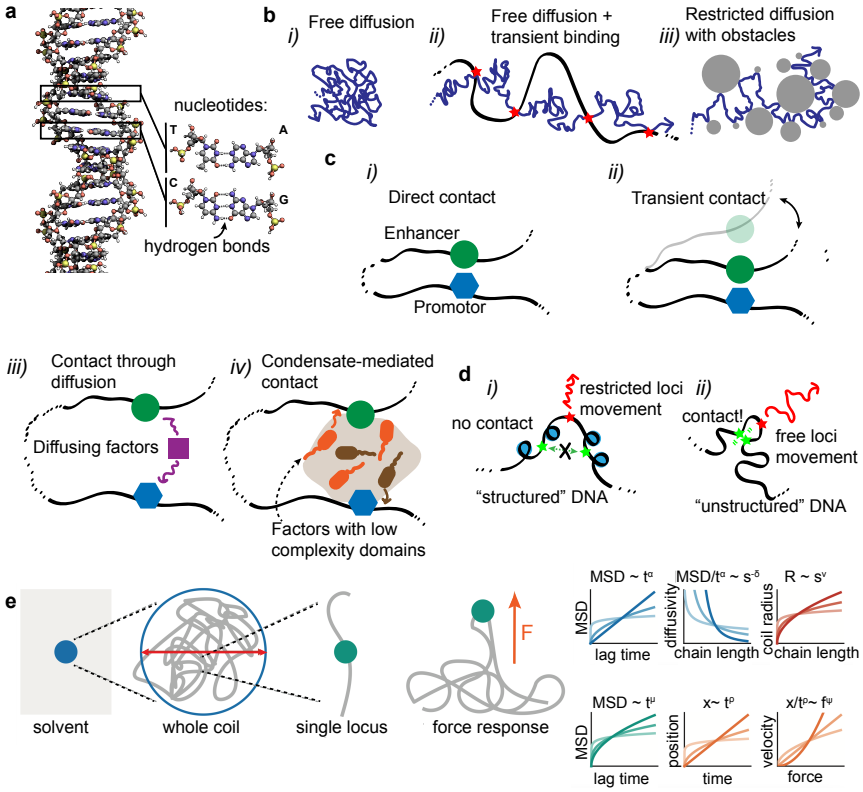

Figure 1.1: **Structure and physical properties of DNA influence its function.** **(a)** Model of the right-handed double helix of DNA, which is a polymer composed of nucleotide monomers, shown in the zoom on the right. Nucleotides Adenine (A) and Thymine (T) on the one hand, and Cytosine (C) and Guanine (G) on the other, form complementary basepairs connected by hydrogen bonds. Adapted from Ref [2]. **b** For the transcription of genes it is important that a transcription factor can find its target while diffusing through the heterogeneous cytoplasm/nucleoplasm surrounding by a web of DNA. ***(i)*** A track (blue) of a freely diffusing protein, which would occur in case there are no obstacles. ***(ii)*** A protein searches the space for a target, alternating transient binding events on the genome (red stars on black line) with diffusion in the medium (blue line). ***(iii)*** The cytoplasm/nucleoplasm contains many large objects (gray circles), one of which is the DNA, that restrict the diffusion of proteins (blue line) in their search for a target. Adapted from Ref [27]. **(c)** The structure and organization of DNA influence its local dynamics, which are relevant for the function of DNA. ***(i)*** DNA may contain some structuring proteins (blue circles) which alter the DNA structure in such a way that local fluctuations are damped (red line) and inter-locus contact is limited (green stars are far apart). ***(ii)*** If the DNA did not contain these proteins, it would have more freedom of movement at local scale (red line), leading to also more frequent inter-locus contacts (green stars are close). This process could influence the ability of a transcription factor to find its target on the DNA. **(d)** Transcription is not only influenced by control sequences near the promotor, but can also be regulated by enhancers, which can be placed at significant genomic distance. Several models exist how the enhancer transmits its signal to the promotor. Each of these models is influenced by the polymeric nature of DNA and the presence of structure-modifying elements. ***(i)*** Direct and prolonged physical contact between factors bound at the enhancer and the promotor. ***(ii)*** Transient physical contact to transfer factors between the enhancer and the promotor. ***(iii)*** Action at a distance: factors are modified at the enhancer and diffuse to the promotor to deliver their signal. ***(iv)*** It is possible that there is no direct contact between the enhancer and promotor, but that contact is mediated through a biomolecular condensate formed by transcription factors, other co-factors and stretches of DNA. Adapted from Ref [28] and [31]. **(e)** The various quantities and observables which together describe the organizational state of the DNA. From left to right: α relates to the viscoelasticity of the solvent (nucleoplasm/cytoplasm), and controls the mean square displacement (MSD) of the full DNA coil or a longer sub-chain, while δ determines how this MSD is dependent on chain length; ν relates to the physical size of the DNA (sub-)coil as function of the chain length; at the level of single loci, μ controls the MSD in a relaxed coil, whereas ρ and ψ determine how a locus changes it position and velocity as function of an externally applied force f. Different shades of the colored lines indicate the trend for different values of the parameter in question. Adapted from ref [33].

1

1.4. WHAT ARE CURRENT METHODS TO STUDY CHROMOSOME ORGANIZATION?

One can classify the various methods in two broad categories. The first category of methods studies DNA in its native environment, the living (or fixed) cell, whilst the second category observes the interactions between purified proteins and short strands of DNA with a variety of *in vitro* single-molecule techniques. For the cell-based methods, there are two approaches: first, various forms of imaging and microscopy, and second, techniques based on biochemistry and genomics/sequencing. In cells, one can observe chromosomes using microscopy, which in its simplest form gives information about the global distribution of the DNA (where is the DNA, how much of it is there, and how does this change through time). To gain information about DNA dynamics at a very local scale, it is possible to follow a spot label through time attached to a specific locus (figure 1.1d/e).[34] And to quantify interactions and binding events between single proteins and the DNA at a local level, single-molecule microscopy can be employed.[35] Lastly, to zoom in on the local structure of the DNA in high detail, super-resolution microscopy can be used on fixed cells.[36] The genomics-based techniques use DNA sequencing and biochemistry to find out what the interactions are for every locus on the DNA for a population of cells, although recent advances enable to do this also in single cells. Interactions in this case are defined as either close proximity or binding, and they can be between DNA loci (chromosome conformation capture techniques[37]) or between the DNA and a particular protein (ChiP-seq[38]). Similar techniques can also find out what loci on the DNA are accessible or not (ATAC-seq[39]).

The *in vitro* methods are mostly single-molecule techniques. Optical[40] and magnetic[41] tweezers are used to pull and rotate DNA while it interacts with DNA-binding proteins, thereby figuring out what forces, torques and energies are involved (figure 1.2a-*ii/iii*). Atomic force microscopy can be used to image the structure of a DNA-protein complex, but also to image with molecular detail the dynamics of that interaction.[42] Cryo-electron microscopy can visualize in detail the spatial interaction of DNA with a protein, for example what part of the protein is in contact with the DNA.[43] A variety of visualization assays use fluorescence microscopy of DNA molecules stretched on a surface to directly image the effect of a protein on the DNA (figure 1.2a-*i*).[44] Finally, some of these techniques can also be combined, for example, optical tweezers can be used together with fluorescence microscopy, to get information both on the structural effects as well as the forces involved in a DNA-protein interaction.[45]

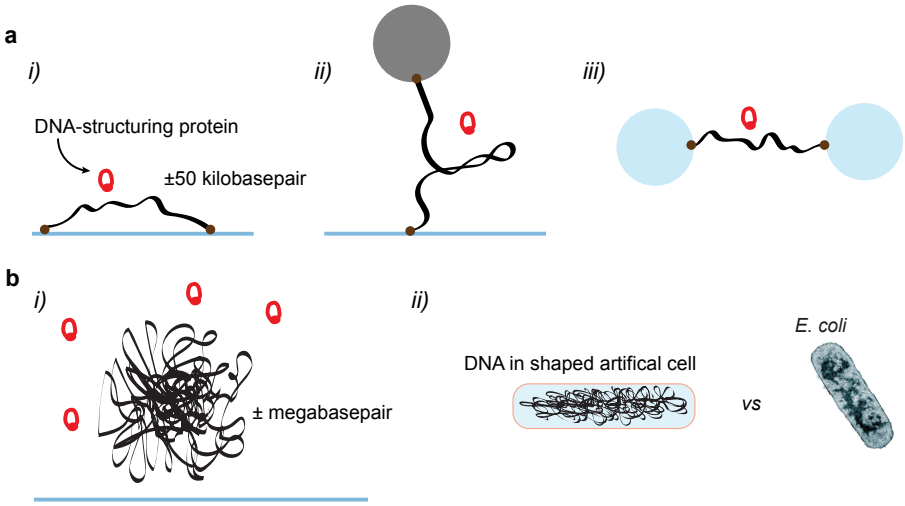

Figure 1.2: **Current in vitro methods to study chromosome organization compared to the proposed genome-in-a-box. (a)** A selection of *in vitro* single-molecule methods are shown. These methods use 'short' strands of max 50 kbp DNA to tease out local interactions between DNA and a purified protein (red). The DNA is constrained on a surface (blue line) or attached to a bead (blue and grey circles). ***(i)*** DNA visualization assays with stretched DNA attached to a surface; ***(ii)*** magnetic tweezers with the DNA attached between a bead and a surface; ***(iii)*** optical tweezers with the DNA attached between two optical beads held in place with lasers. **(b)** Genome-in-a-box proposes to use long DNA substrates in the megabasepair size range, which is free to explore its 3D conformational space, either when it is ***(i)*** unconfined, or ***(ii)*** inside a container, thereby mimicking the DNA densities found in cells, for example *E. coli*. In both situations, purified proteins may be added in a controlled manner to explore their effect on the large DNA substrate.

1

1.5. WHAT IS LACKING IN THE CURRENT METHODS THAT MOTIVATED US TO DEVELOP A NEW APPROACH?

In vitro single-molecule methods use short strands of DNA of up to ~50 kbp long (1 kbp = 1 kilobasepair = 1000 basepair) which are structurally and spatially constrained in a non-physiological manner (figure 1.2a). For Atomic Force Microscopy and cryo-electron microscopy the DNA is deposited on a surface, while optical tweezers suspend it between two beads. This is done to tease out the relevant interactions and forces at a local level. However, if one is interested in the collective effect of these proteins on the large-scale (chromosome-wide) structure and function, or if one wants to experiment with DNA at cell-level densities, one currently needs to do the experiment within a cell. Similarly, if one would like to explore DNA at cell-level densities, then the *in vitro* experiments usually do not suffice. Experiments in cells have different drawbacks, namely a lack of control and precision compared to *in vitro* experiments. This is where genome-in-a-box comes in. It is proposed as an *in vitro* method using fluorescence microscopy and a very large, genome-sized DNA substrate. This DNA is allowed to freely explore conformational space in 3D, while either in an unconfined state or otherwise confined inside a container of a physiologically relevant size and geometry. Additionally, it will be possible to add to the DNA purified proteins and other factors in a controlled manner.

1.6. WHAT SCIENTIFIC QUESTIONS CAN BE STUDIED USING GENOME-IN-A BOX?

There are several open questions to which Genbox could contribute, using its distinguishing features of long DNA substrates which are free to explore 3D conformational space (figure 1.2b-*i*). The *in vitro* study of transcription regulation through enhancers would be a good first candidate. To answer questions about how far-away enhancers can influence transcription initiation at a promotor, one would naturally need a long DNA substrate. Also, the fact that this DNA is not limited to a surface imitates the natural situation in the cell more closely. This makes it possible to figure out to what extent physical contact, an action at distance principle through diffusion, or indirect contact via biomolecular condensates is more likely to play a role in the function of enhancers.

GenBox would also be useful in the study of DNA at cell-level densities. There are several situations in living systems in which multiple DNA molecules occupy the same space (*e.g.*, during DNA replication in the nucleus[46] or in bacteria[24]). However, they do not seem to become entangled. It is unclear if this is due to some 'non-stick' proteins which might need to coat the DNA,[47] or if this is caused by an entropic effect predicted by polymer physics.[24] Additionally, it would be interesting to know how the local dynamics of DNA change when the DNA is confined to cell-level densities: do DNA loci more easily find each other, and how long does it take a protein to find its binding sequence? Both are relevant issues for a range of target search processes in the cell. To reach the high DNA densities needed for such experiments with short DNA molecules, two options are avail-

able: the confining space would either need to be exceedingly small, or, alternatively, the number of the short DNA molecules per container should be quite large. Furthermore, one would need to ascertain that multiple short DNA molecules at high number density behave similar to a single large DNA molecule. In any case, by using a single large substrate, the container would not need to be prohibitively small. This means that the long DNA substrates of GenBox in combination with some form of encapsulation would be a good system to start answering these questions (figure 1.2b-*ii*).

1.7. WHAT ARE THE REQUIRED EXPERIMENTAL ELEMENTS FOR GENOME-IN-A-BOX?

As mentioned above, GenBox is proposed as an *in vitro* technique using a long DNA substrate that would be able to explore its 3D conformation space freely, either in unconfined state or confined inside a container of physiological size/geometry. Let us get more specific about the requirements for GenBox and how we could achieve these.

Firstly, what would the length of the DNA need to be? The simple answer: longer than the 48.5 kbp lambda-phage DNA which is the current maximum size now in use. One could consider to use ligated concatenates of lambda-phage DNA,[48] but since the concatenation process is a chance process, it is difficult to obtain long concatenates of defined length in sufficiently large numbers. Also, the DNA should be long enough to be able to study DNA at cell-level densities without the encapsulating container needing to be impractically small. From an experimental point of view, it would be possible to encapsulate long DNA in a large droplet or liposome and then shrink it to a cell-size of 1 to 5 μm.[49] So, to reach cell-level density at those final droplet dimensions, we would need the DNA from an organism of the same size. For this thesis, we chose to use the 4.6 Mbp (megabasepair) DNA from *E. coli* bacteria. There are several possible methods to obtain this DNA. The basis of each of these methods is to degrade the cell wall of the bacteria, and then induce an osmotic shock, which literally make the bacteria explode, thereby exposing the contents of the cell to the environment. A question is in what environment one performs the cell lysis. Various options exist: it could be done on a microfluidic chip (figure 1.3a/c),[50,51] in an Eppendorf in solution (figure 3.2d),[52] or inside an agarose gel plug (figure 1.3b and figure 3.2d).[53,54] The final choice is dictated by compatibility with other downstream experimental steps.

In most *in vitro* experiments, DNA is tethered to either a surface or a bead. However, since we want to be able to observe the DNA dynamics of an untethered, free DNA object, it will be important to keep the DNA objects within the field of view. When the DNA is encapsulated in, for example, a droplet, this should not be much of an issue, because we can trap the droplet easily.[49] In other cases, microchambers can be used to laterally confine the DNA (figure S5.5). Without the lateral confinement, one would need to sufficiently reduce the amount of flow in the sample chamber to minimize the movement of the DNA objects through the field of view.

For controlled *in vitro* experiments, it is important to know the starting conditions of the experiment and to be able to perturb the system in an accurate manner. This means that we should know the number of basepairs of the object in view (*e.g.*, is the extracted *E. coli* DNA intact?), what natively bound *E. coli* proteins are still attached to the DNA, what is the topology of the DNA (linear or circular), and if we are dealing with a polymer free from supercoiling. In a typical experiment, one would add a purified protein to the sample and observe a change. In case the DNA is already encapsulated inside a container, such as a liposome, this might prove difficult. The protein would need to travel through a pore in the liposome membrane, or alternatively the protein activity would need to be triggered in some way, if it already was co-encapsulated with the DNA. So, an open-top observation chamber (figure 3.1) or microfabricated chambers attached to a main channel (figure 1.3c) would be preferable for such experiments, since purified proteins can be easily added.

Lastly, we would need a suitable readout, for which there are several options. In the first place, we would want to be able to 'see' the DNA using fluorescence microcopy, using some form of unspecific global DNA labeling. Typically, one would use a DNA intercalating dye for this, but it would also be possible to covalently attach fluorescent dyes to the DNA via modified nucleotides (figure 1.3d).[55] This latter method, although more difficult to achieve, would enable experiments of multiple chromosomes inside a container to, for example, study the process of possible entropic de-mixing. To follow the dynamics of the DNA at a local level and gain insight in the degrees of freedom at this scale, one could use a sequence specific spot label which could be experimentally achieved via CRISPR-dCas9,[56] ParB/S-system,[57] or a FROS array (figure 3.4a and figure S5.9).[58] For functional readout, one could use 'sticky' spot-labels to indicate if two loci have 'found' each other (figure 1.3e), FRET to signal that proteins have bound at a specific locus (figure 1.3f),[59] or an MS2-MCP reporter to signal that transcription has successfully started at a particular promotor.[60]

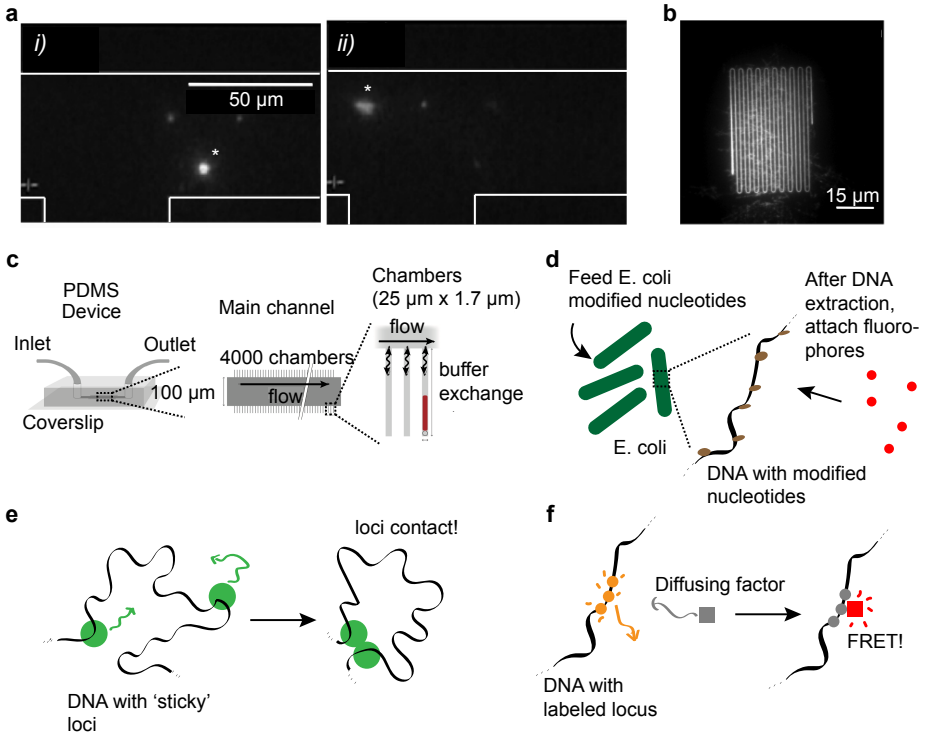

Figure 1.3: **Experimental approaches to genome-in-a-box experiments.** **(a)** Lysis of a spheroplast (bacterial cell without a cell-wall) inside a microfluidic channel: ***(i)*** A spheroplast (denoted with *, signal is from DNA) flows to the left through the horizontal channel. ***(ii)*** At the junction with a vertical channel containing lysis buffer, the spheroplasts receives an osmotic shock and bursts, exposing the DNA to the environment. Other side channels could contain buffers to remove proteins from the DNA. Adapted from Ref. [50]. **(b)** DNA signal from an *S. pombe* chromosome, purified inside an agarose plug and introduced into a long and narrow meandering microfluidic channel. The field-of-view contains the whole chromosome. Genome-in-a-box would be achieved by adding a chamber at the end of the narrow microfluidic channel and flowing the DNA into that area. Adapted from Ref. [54]. **(c)** Bacterial cells are introduced into a microfluidic device and trapped in narrow side-channels which branch off from a large main channel. Through the main channel, buffers are flown into the device, which convert the trapped bacteria to spheroplasts and lyse them, leading to extracted chromosomes in a narrow channel. Subsequently, buffers can be flown in for protein removal and addition of DNA-structuring elements. Adapted from Ref. [61]. **(d)** Strategy to covalently label DNA of isolated chromosomes, instead of using a DNA intercalating dye. Cells are fed modified nucleotides, to which (after chromosome extraction) fluorophores can be attached using click chemistry. **(e)** To estimate contact probability between two loci at a set distance, one could use 'sticky' spot labels. These are sequence-specific DNA-binding proteins with added low-complexity domains (LCD). The LCDs of one location would interact with those of the other location forming a single spot upon contact. **(f)** To estimate the target search time of a protein finding a specific locus on the DNA, as function of DNA polymer structure, one could use FRET. Binding of the protein to a labeled locus would change the FRET signal.

1

1.8. WHAT PARTS WILL BE PRESENTED IN THE THESIS?

Chapter 2 presents the GenBox concept in somewhat greater detail. **Chapter 3** discusses the GenBox workflow in practice, and shows how we purify bacterial chromosomes from cells, remove DNA-binding proteins, and characterize the resulting DNA-objects. **Chapter 4** shows how microfluidic structures can be used to manipulate the shape and sizes of droplets, double emulsions, and liposomes. These cell-sized containers could be used to study, for example, cytoskeletal proteins, and maybe in the future also chromosomes in confinement. **Chapter 5** presents an example of a first application of the GenBox approach where isolated chromosomes from bacteria were exposed to the loop-extruding protein condensin from yeast, resulting in a dynamic DNA compaction process.

REFERENCES

(1) Watson, J. D.; Crick, F. H. Molecular structure of nucleic acids: A structure for deoxyribose nucleic acid. *Nature* **1953**, *171*, 737–738.

(2) DNA - Wikipedia.

(3) Nurk, S.; Koren, S.; Rhie, A.; Rautiainen, M.; Bzikadze, A. V.; Mikheenko, A.; Vollger, M. R.; Altemose, N.; Uralsky, L.; Gershman, A.; Aganezov, S.; Hoyt, S. J.; Diekhans, M.; Logsdon, G. A.; Alonge, M., et al. The complete sequence of a human genome. *Science* **2022**, *376*, 44–53.

(4) Sessions, S. K., Genome Size In *Brenner's Encyclopedia of Genetics: Second Edition*, 2nd ed.; Elsevier: 2013, pp 301–305.

(5) De Gennes, P. G., *Scaling Concepts in Polymer Physics*; Cornell University Press: 1979.

(6) Peters, J. P.; Maher, L. J. DNA curvature and flexibility in vitro and in vivo. *Quarterly Reviews of Biophysics* **2010**, *43*, 23–63.

(7) Rittman, M.; Gilroy, E.; Koohy, H.; Rodger, A.; Richards, A. Is DNA a worm-like chain in Couette flow?: In search of persistence length, a critical review. *Science Progress* **2009**, *92*, 163–204.

(8) Sun, H. B.; Shen, J.; Yokota, H. Size-dependent positioning of human chromosomes in interphase nuclei. *Biophysical Journal* **2000**, *79*, 184–190.

(9) Cramer, P. Organization and regulation of gene transcription. *Nature* **2019**, *573*, 45–54.

(10) Dame, R. T.; Rashid, F.-Z. M.; Grainger, D. C. Chromosome organization in bacteria: mechanistic insights into genome structure and function. *Nature Reviews Genetics* **2020**, *21*, 227–242.

(11) Luger, K.; Mäder, A. W.; Richmond, R. K.; Sargent, D. F.; Richmond, T. J. Crystal structure of the nucleosome core particle at 2.8 Å resolution. *Nature* **1997**, *389*, 251–260.

(12) Dillon, S. C.; Dorman, C. J. Bacterial nucleoid-associated proteins, nucleoid structure and gene expression. *Nature Reviews Microbiology* **2010**, *8*, 185–95.

(13) Corless, S.; Gilbert, N. Investigating DNA supercoiling in eukaryotic genomes. *Briefings in Functional Genomics* **2017**, *16*, 379–389.

(14) Ganji, M.; Shaltiel, I. A.; Bisht, S.; Kim, E.; Kalichava, A.; Haering, C. H.; Dekker, C. Real-time imaging of DNA loop extrusion by condensin. *Science (New York, N.Y.)* **2018**, *360*, 102–105.

(15) Davidson, I. F.; Bauer, B.; Goetz, D.; Tang, W.; Wutz, G.; Peters, J.-M. M. DNA loop extrusion by human cohesin. *Science (New York, N.Y.)* **2019**, *366*, 1338–1345.

(16) Bannister, A. J.; Kouzarides, T. Regulation of chromatin by histone modifications. *Cell Research* **2011**, *21*, 381–395.

(17) Strom, A. R.; Emelyanov, A. V.; Mir, M.; Fyodorov, D. V.; Darzacq, X.; Karpen, G. H. Phase separation drives heterochromatin domain formation. *Nature* **2017**, *547*, 241–245.

(18) Golfier, S.; Quail, T.; Kimura, H.; Brugués, J. Cohesin and condensin extrude DNA loops in a cell-cycle dependent manner. *eLife* **2020**, *9*, e53885.

(19) Kim, Y.; Shi, Z.; Zhang, H.; Finkelstein, I. J.; Yu, H. Human cohesin compacts DNA by loop extrusion. *Science (New York, N.Y.)* **2019**, *366*, 1345–1349.

(20) Kong, M.; Cutts, E. E.; Pan, D.; Beuron, F.; Kaliyappan, T.; Xue, C.; Morris, E. P.; Musacchio, A.; Vannini, A.; Greene, E. C. Human Condensin I and II Drive Extensive ATP-Dependent Compaction of Nucleosome-Bound DNA. *Molecular Cell* **2020**, *79*, 99–114.

(21) Erdel, F.; Baum, M.; Rippe, K. The viscoelastic properties of chromatin and the nucleoplasm revealed by scale-dependent protein mobility. *Journal of Physics: Condensed Matter* **2015**, *27*, 064115.

(22) Xiang, Y.; Surovtsev, I. V.; Chang, Y.; Govers, S. K.; Parry, B. R.; Liu, J.; Jacobs-Wagner, C. Interconnecting solvent quality, transcription, and chromosome folding in Escherichia coli. *Cell* **2021**, *184*, 3626–3642.

(23) Wu, F.; Swain, P.; Kuijpers, L.; Zheng, X.; Felter, K.; Guurink, M.; Solari, J.; Jun, S.; Shimizu, T. S.; Chaudhuri, D.; Mulder, B.; Dekker, C. Cell Boundary Confinement Sets the Size and Position of the E. coli Chromosome. *Current Biology* **2019**, *29*, 2131–2144.

(24) Jun, S.; Mulder, B. Entropy-driven spatial organization of highly confined polymers: Lessons for the bacterial chromosome. *Proceedings of the National Academy of Sciences* **2006**, *103*, 12388–12393.

(25) Lettice, L. A.; Heaney, S. J.; Purdie, L. A.; Li, L.; de Beer, P.; Oostra, B. A.; Goode, D.; Elgar, G.; Hill, R. E.; de Graaff, E. A long-range Shh enhancer regulates expression in the developing limb and fin and is associated with preaxial polydactyly. *Human Molecular Genetics* **2003**, *12*, 1725–1735.

(26) Dekker, J.; Mirny, L. The 3D Genome as Moderator of Chromosomal Communication. *Cell* **2016**, *164*, 1110–1121.

(27) Woringer, M.; Darzacq, X. Protein motion in the nucleus: from anomalous diffusion to weak interactions. *Biochemical Society Transactions* **2018**, *46*, 945–956.

(28) Karr, J. P.; Ferrie, J. J.; Tjian, R.; Darzacq, X. The transcription factor activity gradient (TAG) model: contemplating a contact-independent mechanism for enhancer–promoter communication. *Genes & Development* **2022**, *36*, 7–16.

(29) Shrinivas, K.; Sabari, B. R.; Coffey, E. L.; Klein, I. A.; Boija, A.; Zamudio, A. V.; Schuijers, J.; Hannett, N. M.; Sharp, P. A.; Young, R. A.; Chakraborty, A. K. Enhancer Features that Drive Formation of Transcriptional Condensates. *Molecular Cell* **2019**, *75*, 549–561.

(30) Parry, B. R.; Surovtsev, I. V.; Cabeen, M. T.; O'Hern, C. S.; Dufresne, E. R.; Jacobs-Wagner, C. The Bacterial Cytoplasm Has Glass-like Properties and Is Fluidized by Metabolic Activity. *Cell* **2014**, *156*, 183–194.

(31) Liu, Z.; Tjian, R. Visualizing transcription factor dynamics in living cells. *Journal of Cell Biology* **2018**, *217*, 1181–1191.

(32) Fosado, Y. A. G.; Howard, J.; Weir, S.; Noy, A.; Leake, M. C.; Michieletto, D. Fluidification of Entanglements by a DNA Bending Protein. *Physical review letters* **2023**, *130*, 058203.

(33) Grosse-Holz, S.; Coulon, A.; Mirny, L. Scale-free models of chromosome structure, dynamics, and mechanics. *bioRxiv* **2023**, DOI: https://doi.org/10.1101/2023.04.14.536939.

(34) Wang, X.; Reyes-Lamothe, R.; Sheratt, D. J. Visualizing genetic loci and molecular machines in living bacteria. *Biochemical Society Transactions* **2008**, *36*, 749–753.

(35) Chong, S.; Dugast-Darzacq, C.; Liu, Z.; Dong, P.; Dailey, G. M.; Cattoglio, C.; Heckert, A.; Banala, S.; Lavis, L.; Darzacq, X.; Tjian, R. Imaging dynamic and selective low-complexity domain interactions that control gene transcription. *Science* **2018**, *361*, eaar2555.

(36) Ricci, M. A.; Manzo, C.; García-Parajo, M. F.; Lakadamyali, M.; Cosma, M. P. Chromatin fibers are formed by heterogeneous groups of nucleosomes in vivo. *Cell* **2015**, *160*, 1145–58.

(37) Schmitt, A. D.; Hu, M.; Ren, B. Genome-wide mapping and analysis of chromosome architecture. *Nature Reviews Molecular Cell Biology* **2016**, *17*, 743–755.

(38) Klein, D. C.; Hainer, S. J. Genomic methods in profiling DNA accessibility and factor localization. *Chromosome Research* **2020**, *28*, 69–85.

(39) Klemm, S. L.; Shipony, Z.; Greenleaf, W. J. Chromatin accessibility and the regulatory epigenome. *Nature Reviews Genetics* **2019**, *20*, 207–220.

(40) Ritchie, D. B.; Woodside, M. T. Probing the structural dynamics of proteins and nucleic acids with optical tweezers. *Current Opinion in Structural Biology* **2015**, *34*, 43–51.

(41) Kriegel, F.; Ermann, N.; Lipfert, J. Probing the mechanical properties, conformational changes, and interactions of nucleic acids with magnetic tweezers. *Journal of Structural Biology* **2017**, *197*, 26–36.

(42) Dufrêne, Y. F.; Ando, T.; Garcia, R.; Alsteens, D.; Martinez-Martin, D.; Engel, A.; Gerber, C.; Müller, D. J. Imaging modes of atomic force microscopy for application in molecular and cell biology. *Nature Nanotechnology* **2017**, *12*, 295–307.

(43) Wilson, M. D.; Costa, A. Cryo-electron microscopy of chromatin biology. *Acta Crystallographica Section D Structural Biology* **2017**, *73*, 541–548.

(44) Kaur, G.; Lewis, J.; van Oijen, A. Shining a Spotlight on DNA: Single-Molecule Methods to Visualise DNA. *Molecules* **2019**, *24*, 491.

(45) Hashemi Shabestari, M.; Meijering, A.; Roos, W.; Wuite, G.; Peterman, E. Recent Advances in Biological Single-Molecule Applications of Optical Tweezers and Fluorescence Microscopy. *Methods in Enzymology* **2017**, *582*, 85–119.

(46) Branco, M. R.; Pombo, A. Intermingling of Chromosome Territories in Interphase Suggests Role in Translocations and Transcription-Dependent Associations. *PLoS Biology* **2006**, *4*, e138.

(47) Cuylen, S.; Blaukopf, C.; Politi, A. Z.; Muller-Reichert, T.; Neumann, B.; Poser, I.; Ellenberg, J.; Hyman, A. A.; Gerlich, D. W. Ki-67 acts as a biological surfactant to disperse mitotic chromosomes. *Nature* **2016**, *535*, 308–312.

(48) Smith, D. E.; Perkins, T. T.; Chu, S. Dynamical Scaling of DNA Diffusion Coefficients. *Macromolecules* **1996**, *29*, 1372–1373.

(49) Fanalista, F.; Birnie, A.; Maan, R.; Burla, F.; Charles, K.; Pawlik, G.; Deshpande, S.; Koenderink, G. H.; Dogterom, M.; Dekker, C. Shape and Size Control of Artificial Cells for Bottom-Up Biology. *ACS Nano* **2019**, *13*, 5439–5450.

(50) Prinz, C.; Tegenfeldt, J. O.; Austin, R. H.; Cox, E. C.; Sturm, J. C. Bacterial chromosome extraction and isolation. *Lab on a Chip* **2002**, *2*, 207–212.

(51) Pelletier, J.; Halvorsen, K.; Ha, B.-Y.; Paparcone, R.; Sandler, S. J.; Woldringh, C. L.; Wong, W. P.; Jun, S. Physical manipulation of the Escherichia coli chromosome reveals its soft nature. *Proceedings of the National Academy of Sciences* **2012**, *109*, E2649–E2656.

(52) Wegner, A. S.; Alexeeva, S.; Odijk, T.; Woldringh, C. L. Characterization of Escherichia coli nucleoids released by osmotic shock. *Journal of Structural Biology* **2012**, *178*, 260–269.

(53) Lartigue, C.; Glass, J. I.; Alperovich, N.; Pieper, R.; Parmar, P. P.; Hutchison, C. A.; Smith, H. O.; Venter, J. C. Genome transplantation in bacteria: Changing one species to another. *Science (New York, N.Y.)* **2007**, *317*, 632–638.

(54) Freitag, C.; Noble, C.; Fritzsche, J.; Persson, F.; Reiter-Schad, M.; Nilsson, A. N.; Granéli, A.; Ambjörnsson, T.; Mir, K. U.; Tegenfeldt, J. O. Visualizing the entire DNA from a chromosome in a single frame. *Biomicrofluidics* **2015**, *9*, 044114.

(55) Spahn, C. K.; Glaesmann, M.; Grimm, J. B.; Ayala, A. X.; Lavis, L. D.; Heilemann, M. A toolbox for multiplexed super-resolution imaging of the E. coli nucleoid and membrane using novel PAINT labels. *Scientific reports* **2018**, *8*, 14768.

(56) Deng, W.; Shi, X.; Tjian, R.; Lionnet, T.; Singer, R. H. CASFISH: CRISPR/Cas9-mediated in situ labeling of genomic loci in fixed cells. *Proceedings of the National Academy of Sciences* **2015**, *112*, 11870–11875.

(57) Germier, T.; Audibert, S.; Kocanova, S.; Lane, D.; Bystricky, K. Real-time imaging of specific genomic loci in eukaryotic cells using the ANCHOR DNA labelling system. *Methods* **2018**, *142*, 16–23.

(58) Gordon, G.; Sitnikov, D.; Webb, C. D.; Teleman, A.; Straight, A.; Losick, R.; Murray, A. W.; Wright, A. Chromosome and Low Copy Plasmid Segregation in E. coli: Visual Evidence for Distinct Mechanisms. *Cell* **1997**, *90*, 1113–1121.

(59) Sustarsic, M.; Kapanidis, A. N. Taking the ruler to the jungle: single-molecule FRET for understanding biomolecular structure and dynamics in live cells. *Current Opinion in Structural Biology* **2015**, *34*, 52–59.

(60) Weng, X.; Xiao, J. Spatial organization of transcription in bacterial cells. *Trends in genetics : TIG* **2014**, *30*, 287–97.

(61) Pelletier, J.; Jun, S. Isolation and Characterization of Bacterial Nucleoids in Microfluidic Devices. *Methods in Molecular Biology* **2017**, *1624*, 311–322.

2

GENOME-IN-A-BOX: BUILDING A CHROMOSOME FROM THE BOTTOM UP

Chromosome structure and dynamics are essential for life, as the way that our genomes are spatially organized within cells is crucial for gene expression, differentiation, and genome transfer to daughter cells. There is a wide variety of methods available to study chromosomes, ranging from live-cell studies to single-molecule biophysics, which we briefly review. While these technologies have yielded a wealth of data, such studies still leave a significant gap between top-down experiments on live cells and bottom-up *in vitro* single-molecule studies of DNA-protein interactions. Here, we introduce "genome-in-a-box" (GenBox) as an alternative *in vitro* approach to build and study chromosomes, which bridges this gap. The concept is to assemble a chromosome from the bottom up by taking deproteinated genome-sized DNA isolated from live cells and subsequently add purified DNA-organizing elements, followed by encapsulation in cell-sized containers using microfluidics. Grounded in the rationale of synthetic cell research, the approach would enable to experimentally study emergent effects at the global genome level that arise from the collective action of local DNA-structuring elements. We review the various DNA-structuring elements present in nature, from nucleoid-associated proteins and SMC complexes to phase separation and macromolecular crowders. Finally, we discuss how GenBox can contribute to several open questions on chromosome structure and dynamics.

This chapter has been published: Anthony Birnie and Cees Dekker, *Genome-in-a-Box: Building a Chromosome from the Bottom Up*, ACS Nano, 15, 1, 111–124 (2021).

2.1. INTRODUCTION

Ever since Watson and Crick discovered that the innate double-helix structure of DNA was key to its hereditary function,[1] a major question has been how the physical structure of the genome underlies its biological function. Historically, the study of chromosomes started at the phenomenological level already in the 19th century, when Flemming reported on the changing shape of chromosomes across the phases of the cell cycle from interphase to mitosis.[2] Significant progress was made in the second half of the 20th century when the molecular biology revolution opened access to studying the many nanoscopic elements that underlie chromosomal structure – a development that has continued until the present day. The past decade, in particular, rapidly expanded our knowledge on how the genetic material is physically organized within the cells of the various kingdoms of life, yielding a string of notable discoveries on the interplay between function, structure, and dynamics of chromosomes. Breakthroughs were, for example, the structural mapping of the genomes using chromosome conformation capture (Hi-C and related) techniques,[3,4] the capability of structural maintenance of chromosomes (SMC) protein complexes to extrude loops of DNA as demonstrated using single-molecule fluorescence assays,[5–9] how the properties of the cytoplasm, nucleoplasm and confinement influence the dynamics and structure of chromosomes across species,[10–19] or the discovery of the importance of phase separation in various aspects of chromosome organization,[20–25] from transcriptional condensates[26–33] to heterochromatin formation.[34–36] From this brief list, it is already apparent that chromosome organization spans a multitude of scales from single molecules to full chromosomes.

Eukaryotes and prokaryotes organize their genomes differently, storing a large 10^7 - 10^{11} basepair (bp) eukaryotic genome[37] in multiple chromosomes inside a nucleus (Figure 2.1a) *versus* packaging a smaller 10^5 - 10^7 bp prokaryotic genome[37] in one chromosome, also called the nucleoid, that is freely floating within the cell cytosol (Figure 2.1b). Yet, the basic genetic material, the double-helix DNA polymer, is the same, and it is becoming clear that there are many homologies indicating similar building principles across the various kingdoms of life. Indeed, in this review, we will stress the similarities between the organization of eukaryotic and prokaryotic organisms.

At the most basic level (Figure 2.1), nanometer-sized proteins such as histones[38] or bacterial nucleoid-associated proteins[39,40] bind the DNA, where they locally modulate the structure and mechanical properties of the DNA, thereby establishing a "beads-on-a-string" conformation. These chromatin fibers are further organized in loop-like structures that are formed either through the action of protein complexes[5–9,41,42] or *via* supercoiling[43–45] by twisting the DNA about its axis. Larger-scale levels of organization are characterized by the amount of interactions or contact frequencies that DNA loci have with each other. At the scale of ~300 nm or 10^5 - 10^6 bp, topologically associated domains (TADs) have been identified in eukaryotes,[3,46] while their counterparts in bacteria are called chromosome interaction domains (CIDs),[47] which are at the scale of 10^4 - 10^5 bp. Beyond the level of TADs/CIDs, bacteria have macrodomains,[48,49] while in eukaryotes alternating chromosomal regions (compartmental domains) are segregated into two types of compartments that feature either relatively high or low gene-

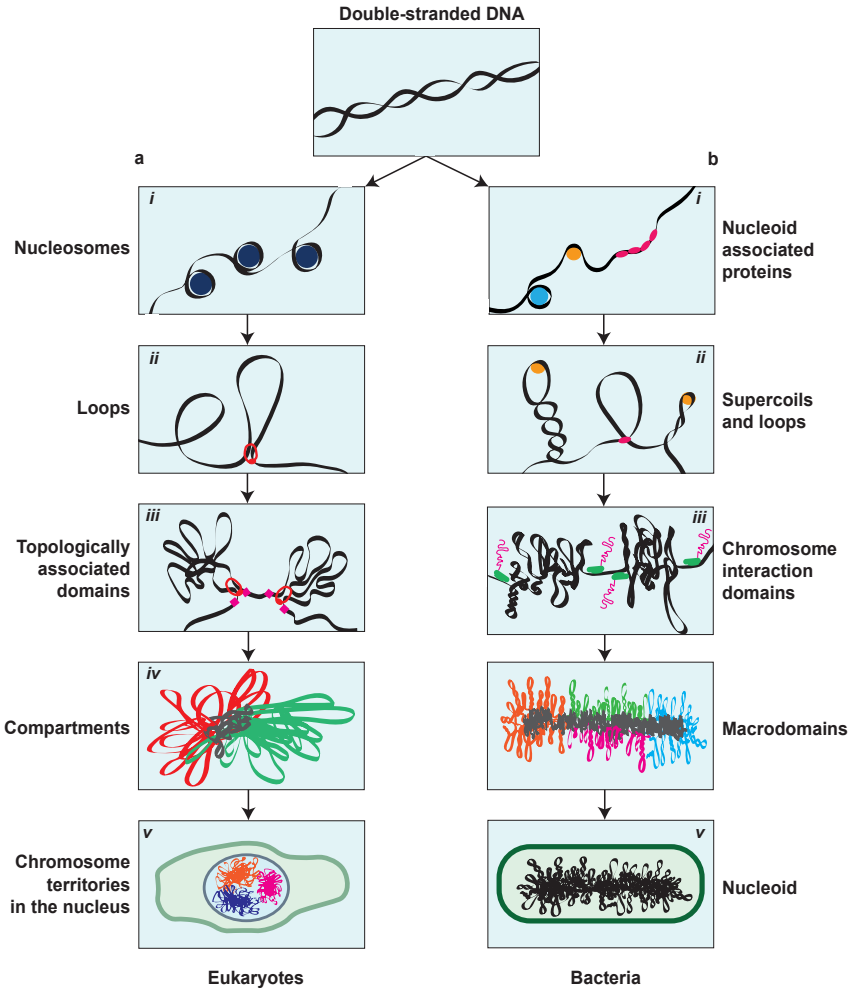

Figure 2.1: **The hierarchical chromosome organization in eukaryotes and bacteria.** Double-stranded DNA is the basic component of all chromosomes in both **(a)** eukaryotes and **(b)** prokaryotes. **(a, *i*)** DNA in eukaryotes is wrapped around histones into nucleosomes, forming a beads-on-a-string structure. **(a, *ii*)** Loops are formed through passive bridging or active loop extrusion. **(a, *iii*)** TADs are large-scale structures that have increased contact frequency among their DNA loci. **(a, *iv*)** Epigenetic markers define if parts of the genome are either transcriptionally active (euchromatin) or repressed (heterochromatin), which are spatially organized in A- and B-compartments, respectively. **(a, *v*)** Within the eukaryotic nucleus, chromosomes each occupy their own 'territory' that is segregated from the other chromosomes. **(b, *i*)** In bacteria, the local structure of the DNA is modulated by NAPs. **(b, *ii*)** Most DNA in bacteria is negatively supercoiled, forming plectonemes. Additionally, bridging proteins and SMCs form loop-like structures. **(b, *iii*)** Actively transcribed long genes form boundaries for plectonemes, demarcating CIDs. **(b,*iv*)** On a larger scale, the circular bacterial genome is organized in macrodomains. **(b, *v*)** The bacterial chromosome, called the nucleoid, is embedded in the cytosol and confined by the cell boundary.

expression levels, and which are collectively called A-compartments (euchromatin) and B-compartments (heterochromatin), respectively.[3,50] Finally, in the nucleus, individual chromosomes do not mix but each occupy distinct locations called chromosome territories, albeit with a limited and transcription-dependent overlap between them.[51–53] The cell cycle, and in particular cell division, is associated with major rearrangements of the chromosomal structure. During interphase in eukaryotes, chromosomes are geared toward accessibility and gene expression, whereas in mitosis the structure is strongly compacted into a bottlebrush structure for faithful transmission of the genetic material to daughter cells.[54] Bacteria, by contrast, do not possess such distinct mitotic and interphase chromosome structures. Nevertheless, they also regulate the spatial segregation of replicated chromosomes before cell division.[45] Despite this broad spectrum of different phenomenological aspects in the organization of genomes, it increasingly appears possible to explain major characteristics of chromosome organization by a limited number of overarching physical principles,[23,25] such as polymer physics, DNA looping, and phase separation.

In this review, we first make a concise survey of various experimental techniques to study chromosome organization and the type of information that these techniques yield about DNA-organizing elements and their local mechanisms. Then we describe an alternative experimental approach, coined 'genome-in-a-box' (GenBox), which is an *in vitro* method for studying genome-sized DNA to which purified DNA-organizing elements can be added. Subsequently, we provide an overview of how various such 'chromosome building blocks' contribute to chromosomal organization. Finally, we elaborate in what manner GenBox can contribute to several relevant scientific questions in the field.

2.2. COMPLEMENTARY APPROACHES TO STUDY CHROMOSOME ORGANIZATION

A wide range of methods is available for studying chromosome organization. Broadly speaking, one can use *in vivo* studies in either live or fixed cells or *in vitro* single-molecule biophysical methods. These approaches provide complementary information about chromosome organization and the various DNA-organizing elements.

Methods that explore chromosomes in cells fall into two broad categories: fluorescence-based imaging and methods involving sequencing and immunoprecipitation. Fluorescence-based methods[55,56] require a fluorescent reporter for visualization. These reporters can be nonspecifically targeted to the DNA on a global level (*e.g.*, a DNA dye) or locally in a sequence-specific manner via hybridization of a fluorescent oligonucleotide to a complementary sequence (*e.g.*, Oligo-PAINT FISH-probes[57,58]) or via the binding of a fluorescently labeled protein to its specific DNA-binding site. Examples of the latter include CRISPR-dCas9[59,60] that binds to a site defined by the guide RNA, operators binding to arrays of repressor sites (FROS arrays),[61,62] or ParB proteins binding and oligomerizing near parS sites.[63,64] Using these labeling techniques and (super-resolution) microscopy, structural and dynamic data can be collected across

a wide range of time and length scales.[12,46,65]

Methods based on sequencing and immunoprecipitation make it possible to figure out three types of information for each locus on a chromosome: (i) the average proximity of a particular DNA locus to other loci, resulting in a contact-frequency map[66,67] (*e.g.*, Hi-C and related techniques); (ii) what proteins are bound or not bound to a specific locus, revealing a map of either protein-DNA interactions[68] (*e.g.*, ChIP-seq or DamID) or DNA-accessibility[69] (*e.g.*, MNAse-seq or ATAC-seq); and (iii) a combination of these two, in order to, for example, show what proteins mediate a particular long-range interaction[70,71] (*e.g.*, Hi-ChIP or ChIA-PET). The aforementioned methods generally result in population-averaged data, making it difficult to determine how the presence or absence of a feature on a interaction map might correspond to the situation inside a single cell.[72,73] To counter this, single-cell or single-molecule alternatives have been developed, such as single-cell Hi-C[74] for loci contact mapping, single-molecule ATAC-seq (SMAC-seq[75]) for DNA-accessibility mapping, or single-cell DamID[76] to map protein-DNA interactions. Furthermore, these methods can be combined with transcriptome profiling, in order to get insight in the relationship between local genome structure and gene expression,[77,78] for example, scDAM&T-seq[79] combines single-cell DamID with mRNA sequencing.

A diverse array of single-molecule biophysics techniques can be used to study DNA and its binding proteins. In DNA-curtains and other visualization assays,[80,81] long DNA molecules (up to 50 kbp) are attached to a surface in a flow cell, which allows time-resolved fluorescence imaging of the stretched DNA and the action of single proteins thereupon. Atomic force microscopy (AFM)[82,83] provides a label-free scanning probe technique, resulting in a topographic map of the (typically dried) sample at nanometer resolution. Additionally, AFM can be used for dynamics since it is able to image at video rates in liquid, which enables to observe, at the single-molecule level, conformational changes of a protein while it interacts with DNA. Transmission electron microscopy (TEM) uses electrons to image a fixed sample with superb angstrom-level resolution, but it needs a vacuum environment and the imaging contrast depends on the use of staining agents and sample thickness. Cryo-electron microscopy[84–87] is best suited for biological samples, as the biomolecule of interest is embedded inside a thin layer of amorphous ice, yielding three-dimensional structures at subnanometer resolution. Optical FRET assays use the principle of Förster energy resonance transfer,[88–90] in which energy is transferred between two fluorophores, depending on the distance between the molecules. Upon site-specific fluorescent labeling, FRET can be used to measure time-resolved nanometer-scale conformational changes of the protein and the DNA. In magnetic tweezers,[91] a DNA molecule is attached between a surface and a bead, of which the position and rotation can be manipulated by a magnet. This allows to get information about the force (at subpiconewton resolution) or torque that DNA-structuring proteins exert on the DNA. Optical tweezers[92,93] use a focused laser beam to trap one or more beads, to which biomolecules such as DNA are attached. Manipulation of the beads enables force spectroscopy on single molecules, as well as complicated topological perturbations, for example to enable the construction of complex protein bridges between two DNA molecules. Notably, it is possible to combine optical tweezers with FRET, con-

focal fluorescence microscopy, and super-resolution microscopy, making it possible to observe conformational changes, binding kinetics, and localization of fluorescently labeled proteins to DNA as function of applied force.

Chromosomes have also been studied extensively *in silico*.[94–98] Modeling a chromosome and the effects of DNA-structuring proteins starts with modeling DNA itself, for which there is a range of parameters that can be tweaked: the total polymer length, the persistence length, attractive or repulsive interactions between DNA monomers on either a global scale or locally between specific monomers, the composition and quality of the solvent and surrounding medium, the level of supercoiling dictated by the amount of twist and writhe, the topology of the DNA (linear, circular, knotted), and the confinement volume and geometry. Due to the relative ease of scanning these parameters individually or in various combinations, computer simulations have been a very fertile ground for studying DNA organization. An intriguing early example was the finding that two genome-sized polymers spontaneously demix and spatially segregate inside a cylindrical confinement, related to the entropy of (de)mixing of chromosomes[19] (Figure 2.2a). More recently, by using simple principles of multivalent interactions and bridging by DNA-binding proteins, simulations of phase separation showed clusters relevant for chromosome structure[99] (Figure 2.2b). Furthermore, models have been built for eukaryotic chromosomes, showing, for example, that loop-extruding elements acting on DNA can spontaneously disentangle newly replicated DNA into structures that closely resemble mitotic chromosomes[4,100] (Figure 2.2c). Loop-extrusion polymer-simulation models can also recapitulate the TAD structures found in interphase chromosomes.[101,102]

These approaches each have their advantages and drawbacks. The main strength of *in vivo* live-cell studies is, obviously, that they inherently examine chromosomes within the natural context of the genomic polymer, the living cell. Their major downside is the vast complexity of the inner environment of cells with their multitude of simultaneously interacting biomolecular components. This makes it challenging to provide clear cause-effect relations. *In vitro* biophysics experiments, on the other hand, provide detailed and mechanistic information at the single-molecule level with clear cause-effect relations about specific DNA-protein interactions. However, these experiments are generally performed on short DNA fragments that interact with only one or a few purified proteins near a surface, and as such they are quite detached from the natural cellular environment. Indeed, the strength of the single-molecule approach is at the same time its weakness, as it does not allow to probe the bigger picture of the combined effect of these DNA-structuring elements on the genome as a whole. *In silico* experiments are able to study full genomes (by coarse-graining the polymer to a relevant length-scale) with single-parameter control. However, one-to-one corresponding experimental verification of such *in silico* results is often lacking.

2.3. BUILDING A SYNTHETIC CELL FROM THE BOTTOM UP

In recent years, synthetic biology has gained traction as a third experimental avenue for studying living systems.[103] Synthetic cell research deals with the construction of new bi-

ological molecules and systems in order to redesign those found in nature, and it does so in one of two approaches. In a top-down approach, synthetic circuits are added to cells, or nonessential elements of living cells are stripped away in an attempt to establish a minimally functional cell. In a bottom-up approach, on the other hand, one tries to compose minimal sets of components that can perform rudimentary functions of living cells. In particular, the aim is to first build modules to establish functional cellular subsystems in isolation, before combining them at a later stage into a synthetic cell. Examples of such cellular modules could be circuits for a machinery for cell division,[104,105] transcription-translation for genetic information transfer,[106] pattern formation for spatial control,[107] and cell-cell communication.[108] This approach to synthetic cell research can be called "bottom-up biology", since its goal is to establish biological function from the bottom up, that is, to construct the essential characteristics of living cells out of a set of well-understood but lifeless components. Notably, various projects have been started across the world that aim at building a synthetic cell.[109–112]

Although also an *in vitro* methodology, the bottom-up biology approach significantly exceeds the single-molecule biophysics methodology in multiple ways. First, it literally is scaling up by orders of magnitude, from single proteins to elaborate but controlled protein mixtures and from local molecular-level interactions to collective behavior and their emergent effects. Second, bottom-up synthetic-cell research specifically aims to study the functional subsystems within mimics of the cellular container, for which there is a wide range of possible scaffolds[113] (*e.g.* liposomes, droplets, polymersomes, or microfabricated chambers) and microfluidic technologies[104,114] to manipulate them.

Can the bottom-up approach beneficially be applied to study whole chromosomes? In the 1970s, bacterial chromosomes were isolated from cells and prepared for electron microscopy imaging, showing DNA supercoiled loop structures (Figure 2.2d).[116] About two decades ago, Woldringh *et al.* provided a relatively simple method to isolate bacterial chromosomes from cells for optical microscopy (Figure 2.2e).[121] Jun *et al.* used this method to study such nucleoids inside microfluidic channels, providing insights into the effects of confinement and macromolecular crowding on DNA organization (Figure 2.2f).[118] Genome transplantation, as developed by Glass *et al.*,[122] made it possible to isolate a chromosome from a cell, remove the DNA-binding proteins, and insert this bare genome into a host cell that had its genome removed. This "rebooted cell" was then able to grow and multiply.[122] This approach has been expanded by using a synthetic minimized genome for the purpose of finding a functional minimal version of the original genome (Figure 2.2g).[119] While most of the early efforts involved taking chromosomes out of living cells, and simply observing them, Hirano *et al.* attempted to mimic the construction of mitotic chromosomes *in vitro* when they combined frog sperm chromatin with six purified protein complexes, leading to structures that, at face value, appeared strikingly similar to mitotic chromatids (Figure 2.2h).[120] This approach was an extension of experiments involving reconstituted chromatin in *Xenopus leavis* egg extract,[123,124] which also included examples of the use of microfluidics to encapsulate the egg extract together with reconstituted chromatin to explore the influence of confinement on the size of the mitotic spindle.[125,126]

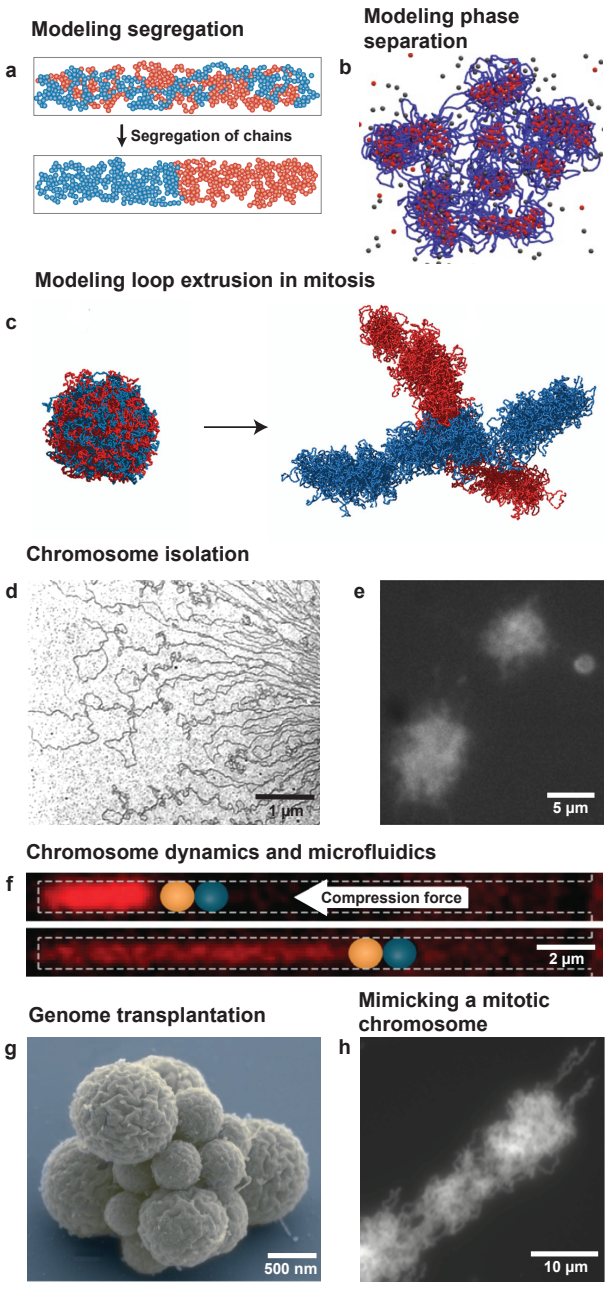

Figure 2.2: **Examples of previous in silico and in vitro research on genome-sized DNA.** *(For caption see next page)*

Figure 2.2 *(continued from previous page)*: **Examples of previous in silico and in vitro research on genome-sized DNA. (a)** Confinement can induce the entropic demixing of two long polymers. Counterintuitively, the segregated state has a higher entropy than the mixed state. Adapted with permission from ref [115]. Copyright 2010 Springer Nature. **(b)** DNA-binding proteins that bridge DNA can lead to phase separation into clusters. Adapted with permission from ref [96]. Copyright 2020 Springer Nature. **(c)** SMC loop extruders can segregate a replicated random polymer into an object resembling a mitotic chromosome. Adapted with permission from ref [100]. Copyright 2016 Goloborodko *et al.* **(d)** Electron microscopy image of an *E. coli* chromosome, showing supercoiled plectonemes. Adapted with permission from ref [116]. Copyright 1976 Springer Nature. **(e)** Fluorescence image of isolated *E. coli* chromosomes in solution. Adapted with permission from ref [117]. Copyright 2012 Elsevier. **(f)** An *E. coli* chromosome is compacted by a piston formed by an optical tweezer bead (blue) inside a micron-sized channel. Adapted with permission from ref [118]. Copyright 2012 National Academy of Sciences. **(g)** A synthetic genome can be transplanted into a host cell, which leads to the creation of a synthetic cell *JCVI-syn3.0*, shown here. Adapted with permission from ref [119]. Copyright 2016 The American Association for the Advancement of Science. **(h)** Frog-sperm chromatin can be combined with six purified protein complexes to yield structures similar to mitotic chromosomes. Adapted with permission from ref [120]. Copyright 2015 Springer Nature.

2.4. A GENOME-IN-A-BOX

Here, we would like to argue that the time is ripe to embark on an effort to build chromosomes from the bottom up, that is, to establish, *in vitro*, the full complexity of prokaryotic or eukaryotic chromosomes from basic elements through a systematic hierarchical assembly. We coin this approach 'genome-in-a-box' (GenBox). This name derives inspiration from the "particle-in-a-box" models that famously provided basic insights in quantum mechanics, as we hope that GenBox may similarly help to unravel key properties of chromosomal organization. This approach is grounded in the fields of bottom-up biology and synthetic-cell research, and extends upon previous research on genome-sized DNA, as described above.

In GenBox (Figure 2.3), we envision to first isolate chromosomes from cells and strip them of all DNA-binding proteins, resulting in a genome-sized deproteinated DNA substrate, similar to the sample-preparation steps in genome transplantation.[122] Subsequently, one can add purified DNA-structuring elements (mostly protein complexes), which can be seen as 'chromosome building blocks', with the aim to study their specific effect on the structure and dynamics of the genome-sized DNA. There is a wide range of such building blocks known, for example, SMC protein complexes, topoisomerases, RNA polymerases, crowders, *etc.*, which are reviewed below. Finally, microfluidics and liposome technologies can be used to define a cell/nucleus-sized confinement – the 'box' part of the GenBox. Using this scheme, it will be possible to perform *in vitro* studies of chromosomes in a regime of previously unexplored DNA sizes with great control of the mutual interactions between the various actors. Additionally, it will allow to study chromosome organization *in vitro* at all its hierarchical levels, with examples ranging from simple DNA-binding proteins inducing various levels of compaction to the influence of loop formation at a global scale and to the interaction between multiple chromosomes in the same confining container as a mimic of chromosome territories. In the spirit of Richard Feynman's famous saying, "What I cannot create, I do not understand", GenBox uses the concept of 'building leads to understanding' in order to study chromosome

organization.

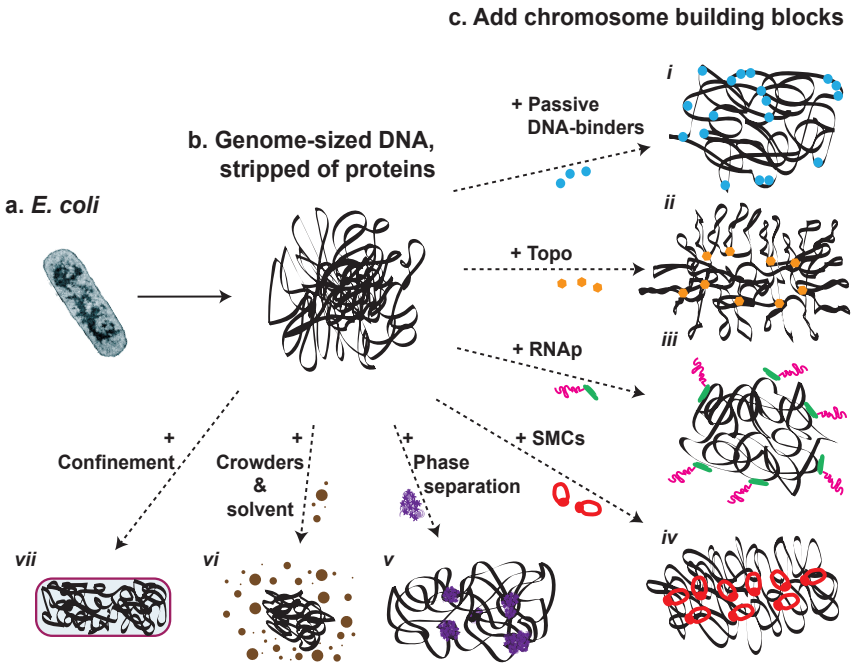

Figure 2.3: **GenBox: recreate genome structure by mixing genome-sized DNA and chromosome building blocks. (a)** Chromosomes can be extracted from live cells, for example the circular bacterial chromosome from *E. coli*. **(b)** Stripping chromosomes of its DNA-binding proteins results in genome-sized DNA molecules that act as a substrate for subsequent experiments. **(c)** Next, DNA-structuring elements are added, one at a time. Various categories of such chromosome building blocks are indicated: ***(i)*** Passive DNA-binding proteins. ***(ii)*** Topoisomerases (Topo) involved in supercoiling and decatenation control. ***(iii)*** RNA polymerase (RNAp) responsible for transcription. ***(iv)*** SMC proteins that underlie the looping structure of chromosomes. ***(v)*** Phase separation that is implicated in transcriptional condensates and the formation of compartments. ***(vi)*** Crowders and solvent molecules that modulate compaction of a polymer through entropic depletion forces and solvent-polymer interactions, respectively. ***(vii)*** Confinement provided by the cellular or nuclear boundary in cells, which can be mimicked by artificial cell-sized containers.

A key feature in this approach is the use of genome-sized DNA as a substrate. Notably, 'genome-sized' is not a very accurate descriptor since genomes from different species vary over 6 orders of magnitude in size, from 0.6 megabasepair (*Mycoplasma genitalium*[127]) to 150 gigabasepair (*Pieris japonica*[128]). The relevant point, however, is that emergent effects can be expected to come into play in the large-scale DNA organization once the substrate size approaches the ~megabasepair range, where, for example, TADs and compartmentalization occur.[3,46,50] The source (organism) of the DNA can in principle be freely chosen, as many major features of chromosomal structures occur widely across the domains of life. There are examples, however, where it is desirable to include species-specific sequences on the DNA substrate, because a particular DNA-structuring element needs that sequence to function. For example, CTCF sites (and associated pro-

teins) are crucial in human interphase chromosome organization due to their interaction with cohesin SMCs,[3] but these CTCF sites are absent in nonmetazoan eukaryotes and bacteria.

As indicated above, an extensive toolbox of techniques is available to study chromosome structure and dynamics. The most obvious read-out in GenBox experiments would, in first instance, be time-resolved fluorescence imaging that provides dynamic structural information. Global information about the density distribution of the DNA in space and time can be monitored with DNA dyes, and local dynamics of specific spots along the genome can be quantified using sequence-specific fluorescent labels. Fortunately, *in vitro* experiments allow for much relaxed constraints regarding phototoxicity and choices of fluorophores, in contrast to live-cell imaging. Probing the functional relevance of the GenBox chromosomes will be a next step. As, for example, DNA-binding proteins can lead to structures of varying degrees of compaction, gene accessibility and expression may be influenced. The ability of transcription machinery to transcribe a set of genes can be monitored, for example, by quantitative PCR (qPCR). In parallel to imaging and functional qPCR assays, chromosome conformation capture experiments on these GenBox chromosomes can provide high-resolution information on how a particular chromosome building block affects the contact frequencies among loci.

2.5. AN OVERVIEW OF CHROMOSOME BUILDING BLOCKS

One underlying assumption in this approach is that, to first approximation, chromosome organization can be decomposed into the action of various chromosome building blocks that each have their distinct effect (Figure 2.4). Below we provide a brief overview of some major chromosome building blocks, which gives a glimpse of the diversity of components involved in chromosome organization.

A starting point is to realize that DNA is a very long macromolecule and hence polymer physics dictates important aspects of its behavior. Bare DNA has a persistence length of 50 nm and can be described by a worm-like chain model.[129,130] For genome-sized DNA, this leads to a random polymer coil structure with a sizeable radius of gyration, from 3.6 μm for a 4.6 megabasepair circular *Escherichia coli* bacterial genome to 130 μm for the 3 gigabasepair linear human genome (if it were all to be connected in one linear DNA polymer). Such a random coil is a large and rather open structure of low DNA density that *a priori* clearly would not fit within the typically available space, which is the set by the ~1 μm cell size for *E. coli*[131] (volume of ~0.5 μm^3) and by the ~10 μm nucleus size for human cells[132] (volume of ~525 μm^3). Hence, the DNA needs to be condensed, thereby increasing the DNA density by 2-4 orders of magnitude. A range of passively acting DNA-binding proteins is available for a first level of condensation (Figure 2.4a). In eukaryotes, the major binding protein is the nucleosome, which consists of 146 base pairs of DNA wrapped around a histone octamer in 1.7 turns.[38] These nucleosomes package DNA into a beads-on-a-string structure, thus compacting DNA by shortening the total polymer length, changing the level of supercoiling,[145] and altering flexibility of the DNA fiber.[146] Nucleosome-like structures have also been identified in archaea, albeit with different

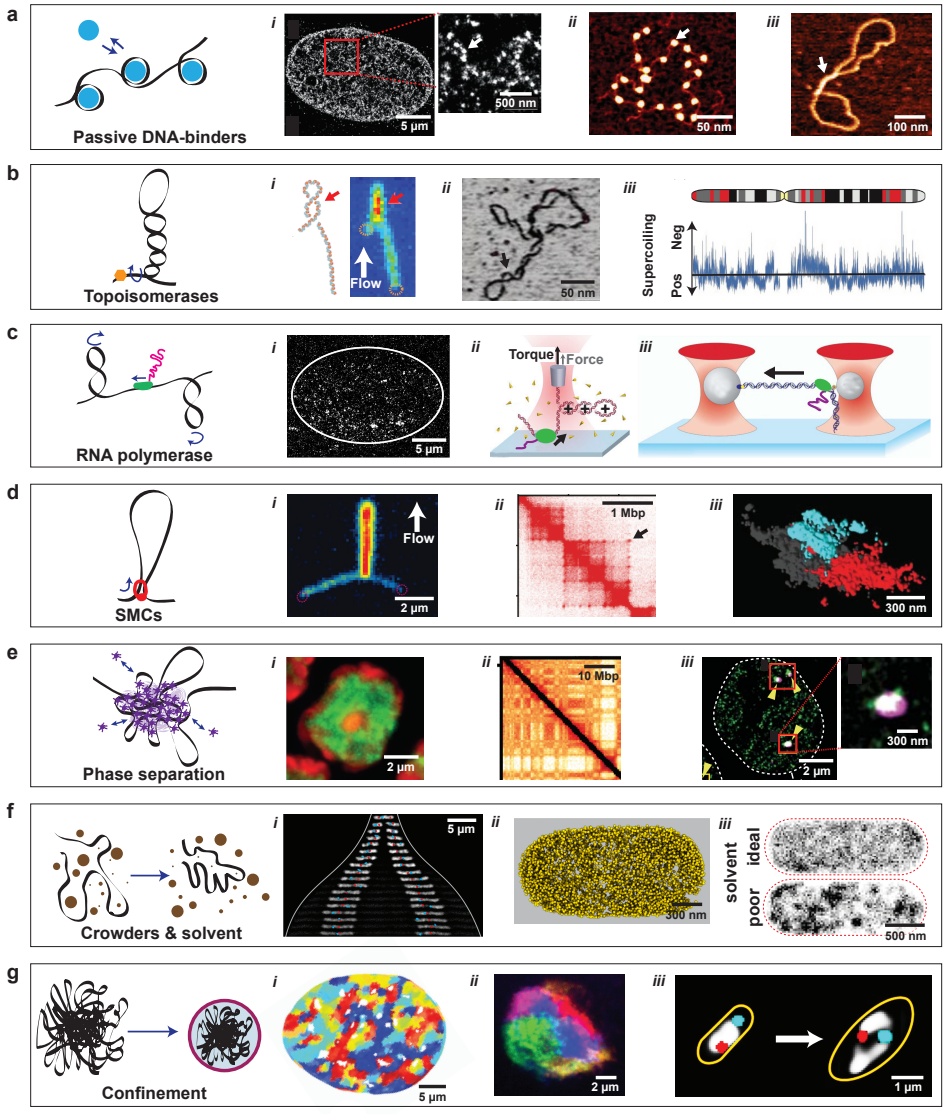

Figure 2.4: **Examples of previous in silico and in vitro research on genome-sized DNA.** *(For caption see next page)*

properties as compared to eukaryotes, such as oligomerization.[147] In bacteria, DNA-binding proteins known as nucleoid-associated proteins (NAPs) similarly condense the chromosome.[39,40] Upon binding the DNA either nonspecifically or at sequence-specific target sites, these NAPs wrap (IHF, Dps), bend (Fis, HU), or bridge (H-NS) the DNA. Aside

Figure 2.4 *(continued from previous page)*: **Chromosome building blocks: the elements that constitute chromosome organization.**
(a) Local DNA-binding proteins bend, wrap, or bridge DNA. ***(i)*** Super-resolution image of a eukaryotic nucleus with fluorescently labeled histones. Red box is zoomed in on the right: arrow points to a nucleosome nanodomain ('nucleosome clutch') composed of a small number of nucleosomes. Adapted with permission from ref [133]. Copyright 2015 Elsevier. ***(ii)*** AFM image of DNA with nucleosomes (arrow). Adapted with permission from ref [134]. Copyright 2009 Springer Nature. ***(iii)*** AFM image of DNA with an H-NS bridge (arrow). Adapted with permission from ref [135]. Copyright 2017 The American Society for Biochemistry and Molecular Biology, Inc.
(b) Topoisomerases control DNA supercoiling by inducing or relaxing supercoils in the DNA. ***(i)*** Optical image and schematic of a plectonemic supercoil on a flow-stretched 20 kbp DNA molecule. Red arrow indicates the plectoneme. Adapted with permission from ref [136]. Copyright 2016 American Chemical Society. ***(ii)*** AFM image of a supercoiled plasmid. Adapted with permission from ref [137]. Copyright 2018 Springer Nature. ***(iii)*** Supercoiling density varies between negative and positive along a eukaryotic chromosome. Adapted with permission from ref [138]. Copyright 2013 Springer Nature.
(c) RNA polymerase (RNAp) transcribes genes in DNA. ***(i)*** Super-resolution image of labeled RNAp in a nucleus (white line). The RNAp is found to be nonhomogeneously distributed in small clusters. Adapted with permission from ref [139]. Copyright 2013 The American Association for the Advancement of Science. ***(ii)*** Optical tweezers with a quartz cylinder can probe both the force and torque exerted by an RNAp (green) acting on a short DNA molecule. Adapted with permission from ref [140]. Copyright 2019 National Academy of Sciences. ***(iii)*** Optical tweezers can probe the stepping of RNAp (green) along DNA. Adapted with permission from ref [141]. Copyright 2006 Royal Society of Chemistry.
(d) SMC complexes extrude loops of DNA and are involved in the formation of TADs. ***(i)*** Fluorescence image of a flow-stretched DNA molecule, in which an SMC condensin has extruded a loop. Adapted with permission from ref [5]. Copyright 2018 The American Association for the Advancement of Science. ***(ii)*** A section of a Hi-C contact map, showing TADs (squares) and loops (dots, see arrow). Adapted with permission from ref [142]. Copyright 2017 Elsevier. ***(iii)*** Super-resolution image of two TAD-like domains (red and cyan) labeled by multiple rounds of FISH Oligopaint. Adapted with permission from ref [46]. Copyright 2018 The American Association for the Advancement of Science.
(e) Phase separation in chromosomes can occur through multivalent interactions between DNA-binding proteins. ***(i)*** Heterochromatin (red) and euchromatin (green) segregate within the nucleus through phase separation. Adapted with permission from ref [34]. Copyright 2019 Springer Nature. ***(ii)*** A section of a Hi-C map showing a checkerboard pattern indicating that alternating regions of a chromosome interact over large distances through the formation of A and B compartments. Adapted with permission from ref [34]. Copyright 2019 Springer Nature. ***(iii)*** Super-resolution image of a transcriptional condensate (red boxes) of mediator-coactivator (magenta) and RNAp (green) inside the nucleus (white outline). Adapted with permission from ref [30]. Copyright 2018 The American Association for the Advancement of Science.
(f) Macromolecular crowders and the solvent quality of the cytosol or nucleoplasm can modulate the compaction of DNA. ***(i)*** Crowding influences the expansion and position of two chromosomes (white) within an *E. coli* cell that expands in size from top to bottom (cell outer edge shown as white line). Adapted with permission from ref [14]. Copyright 2019 Elsevier. ***(ii)*** Distribution of ribosomes (that act as crowders) in *E. coli* from cryo-electron tomograms. Adapted with permission from ref [10]. Copyright 2020 Xiang *et al.* ***(iii)*** Computer simulation that shows that DNA in a poor solvent (bottom) forms heterogeneous structures, while DNA in an ideal solvent (top) is homogeneously distributed throughout the cell (dashed red line). Adapted with permission from ref [10]. Copyright 2020 Xiang *et al.*
(g) Confinement is provided by the cell wall in bacteria and by the nuclear envelope in eukaryotes. ***(i)*** Possibly due to confinement-induced glassy dynamics, micrometer-sized regions move coherently within the nucleus on a timescale of seconds. Adapted with permission from ref [143]. Copyright 2018 Oxford University Press. ***(ii)*** Chromosomes territories inside the nuclear confinement. Adapted with permission from ref [144]. Copyright 2019 eLife Sciences Publications, Ltd. ***(iii)*** Relaxation of the cell-wall confinement (orange line) of *E. coli* leads to an opening up of the circular bacterial chromosome (white). Adapted with permission from ref [13]. Copyright 2019 Springer Nature.

from the structural role, NAPs also influence gene expression. NAPs such as MatP are

implied in the organization and demarcation of the Terminus macrodomain in *E. coli*, which is flanked by left/right macrodomains that connect to a macrodomain at the origin of replication.[148] The mechanism behind the formation of these macrodomains still remains largely unclear. In eukaryotes[149] and bacteria,[150] post-translational modifications (such as phosphorylation, methylation, and acetylation) of histone tails or NAPs play an important regulatory role by modulating their influence on gene expression and chromosome-structural properties. These modifications work at various levels, as they, for example, change the mutual interactions between DNA-binding proteins which may cause the formation of A/B compartments through phase separation.

Supercoiling[43–45] is relevant in both eukaryotes and bacteria (Figure 2.4b,c). Bacterial genomes exhibit on average negative supercoiling, that is, their DNA is under-twisted compared to the regular right-handed double-helix. In all organisms, the local supercoiling is continuously altered by transcribing RNA polymerases that move along the DNA, introducing positive supercoils ahead of them and negative supercoils in their wake.[151] In bacteria, transcription processes at highly expressed long genes can lead to both diffusion barriers for supercoils as well as extended decompacted regions that may cause segmentation of the bacterial chromosome into chromosome interaction domains (CIDs).[47,152] Control of the supercoiling state happens in two ways. First, passive control of supercoiling is provided by NAPs, such as HU[153] and Fis[154] which bind at supercoiled plectonemes, thereby stabilizing them. Second, active control of the torsional state of DNA is provided by a variety of topoisomerases[155,156] that introduce or relax supercoiling within the DNA. Topoisomerases also play a role in decatenation, thus controlling the topology of the DNA polymer, which is relevant at all stages of the cell cycle, but especially for faithful chromosome segregation in both bacteria and eukaryotes.

A central organizational motif of chromosome structures is DNA looping (Figure 2.4d). Loops can form if proteins passively bridge two distant points along the DNA.[41,42] Alternatively, loops can be produced in an energy-driven process by structural maintenance of chromosomes (SMC) complexes. A wide range of methods (Hi-C,[4,101,102] biochemical assays,[157–159] and single-molecule experiments[160,161]) have provided evidence for loop extrusion by SMCs. Direct imaging of the loop extrusion process by a single SMC complex, such as cohesin and condensin, was provided in single-molecule optical visualization assays.[5–9] SMCs are motor proteins that bind DNA and then start reeling in the DNA strand, thereby forming a loop. They are fast but weak motors, translocating DNA at rates up to 2000 bp/s but stalling their motor action at forces of less than a piconewton.[5–9] The precise molecular mechanism behind SMC loop extrusion is still unknown, although parts of the molecular puzzle are being solved by structural studies with cryo-EM[162–165] and dynamical studies with high-speed AFM.[166,167] In interphase, cohesin-mediated loops are associated with TADs that often link promoters and enhancers and also correlate with gene activation,[3] although the latter is under dispute.[168] It is still incompletely understood how the boundaries of TADs are defined in many organisms, and how TADs correspond to actual physical structures in single cells.[72,73] Metazoan TAD boundaries are often signaled by DNA sites that are bound by CTCF proteins that act as a stop or pause sign for loop extrusion by cohesin.[3,142] In preparation of eukaryotic cell division, loop formation by condensin ensures that newly replicated chromosomes are

compacted, disentangled, and segregated from each other.[54,169] Lastly, in *E. coli*, Hi-C maps show that the SMC complex MukBEF promotes long-range DNA contacts,[49] and live-cell imaging reported that MukBEF occupies a thin axial core within the nucleoid, consistent with a bottle-brush chromosome structure.[170]

More recently, it has become clear that phase separation likely plays an important role in organizing chromosomes, for example, in the formation of chromosomal compartments and transcriptional hubs, which provide a fast-tunable and selectively accessible environment for gene expression (Figure 2.4e). Phase separation is often mediated by multiple weak interactions between intrinsically disordered or low-complexity protein domains.[171] Attractive interactions between heterochromatin nucleosomes, mediated by histone tails[20] or histone-binding proteins[35,36] as well as the interaction between heterochromatin and the nuclear boundary or lamina, have been reported to underlie the formation of chromosomal compartments and their organization relative to the nuclear lamina.[34,172] The HP1α histone-binding protein, for example, forms liquid droplets *in vitro* when it is phosphorylated at the N-terminal extension,[35] though it did not do so in live mouse cells,[173] underlining the need for careful experiments when phase separation is involved.[174,175] This process of microphase separation, which segregates the heterochromatin (B-compartmental domains) from the euchromatin (A-compartmental domains), is further modulated by active mixing caused by SMC loop extrusion.[24] Zooming in within the A-compartmental domains, transcribed euchromatin may segregate from dormant euchromatin through the formation of active microemulsions with RNA transcripts.[26] Chromosomal compartments linked to gene expression levels have also been observed in *Sulfolobus* archaea, where they correlate with the energy-driven action of an SMC-like protein called coalescin.[176] Furthermore, transcriptional hubs in eukaryotes display properties of liquid condensates, where multiple components have been implicated with the phase separation, namely transcription factors,[27,28] coactivators,[30,31] the enhancer sequence,[29] and RNA polymerase.[27,28,30,33] Lastly, phase separation is also significant for bacterial chromosomes,[177,178] for example, in transcriptional hubs surrounding the nucleoid in *E. coli*,[32] and in ParB protein clusters in *B. subtilis*.[179] ParB loads the bacterial SMCs onto the DNA, whereupon the SMCs actively proceed along the DNA wrapping the two chromosome arms together.[180]

Finally, chromosomes are spatially confined within the nucleus (eukaryotes) or cell boundary (bacteria and archaea) and are suspended inside the crowded nucleoplasm or cytosol, respectively (Figure 2.4f,g). The size and shape of the confinement can strongly impact the chromosome structure. For example, while a spherical container allows mixing of chromosomes, deformation into a cylindrical or disc-like shape may lead to spontaneous de-mixing and segregation.[19] Yet, chromosomes occupy distinct chromosome territories within the roughly spherical nucleus, indicating additional mechanisms. It has been suggested that chromosomes get kinetically trapped into such territories at the start of interphase after the decondensation of mitotic chromosomes.[18] Combined with confinement by the cell wall, crowding by macromolecular complexes in the *E. coli* cytoplasm compacts and positions chromosomes, leading also to a strongly varying ratio between nucleoid size and cell size across bacterial species.[13,14,17] Furthermore, the cytoplasm in bacteria is a poor solvent for DNA, causing the spontaneous compaction and

formation of domain-like structures.[10] Lastly, the DNA polymer itself as well as the surrounding cytoplasm were found to exhibit confinement-induced glassy dynamics, both in bacteria[11] and in human cells.[12,15,16]

2.6. OUTLOOK

We reviewed research on chromosome structure and introduced the 'genome-in-a-box' (GenBox) as an alternative *in vitro* approach to build and study chromosomes. GenBox bridges the traditional methodologies of live-cell experiments and *in vitro* single-molecule studies by using a genome-sized DNA substrate and subsequent addition of DNA-organizing elements. As a method which is based on the principle of 'to build is to understand', it will allow to study how local interactions between chromosome building blocks and DNA lead to emergent genome-wide organizing effects. For example, while we know in quite some detail how single SMCs extrude loops of DNA,[5–9] it remains unclear how these molecular motors collectively act to form a structured interphase or mitotic chromosome. A GenBox approach enables such studies, while also generally addressing the distinct effects of NAPs, topoisomerases, polymerases, crowding agents, *etc.* In order to build up further hierarchical levels of complexity, combinations of chromosome building blocks can be probed, since many of these building blocks mutually interact, as detailed in the overview above. In this light, it will be interesting to explore whether it is possible to re-create chromosome-mimicking structures from a minimal set of multiple DNA-structuring elements. For example, a chromosome-mimic together with macromolecular crowders can be placed inside a liposome, which is subsequently shaped with microfabricated structures,[104,114] similar to *in vivo* experiments with shape-manipulated *E. coli* cells.[13,14] Furthermore, we expect a lively interplay with polymer physics modeling, as the GenBox approach is closely related to the typical setup for *in silico* modeling.

While GenBox will allow a wide array of interesting experiments on genome-sized DNA substrates, no experimental method is without its challenges. For example, this approach does not lend itself well to the discovery of so far unknown building blocks. Hence, like in any *in vitro* experiment, an attempt to re-create chromosomes with a minimal set of building blocks may fail if a component is missing, indicating the need for a close feedback loop with live-cell experiments. In order to gain access to such a missing component, it may be possible to combine GenBox experiments with cell extracts, that is, combining genome-sized DNA and purified chromosome building blocks with the complexity of the cytoplasm or nucleoplasm of natural cells. Clearly, many technical hurdles will need to be overcome to realize GenBox, for example, to prevent the shearing of the very large and fragile DNA molecules. Quantitation may also pose a challenge as copy numbers of DNA-binding proteins in a cell may not directly translate to *in vitro* concentrations, since crowding conditions may differ and protein concentrations in cells vary across time as they are under the control of the cell-cycle. In order to study the effects of developmental trajectories and cellular cycles, for example, the transition from interphase to mitotic chromosomes or *vice versa*, one would need to engineer the ability

to temporally control the concentrations of chromosome building blocks. Fortunately, this should be feasible by using microfluidics, in a similar manner to the experiments of Jun *et al.*, who observed compaction and de-compaction of isolated chromosomes inside microchannels when crowding agents were added and removed.[118]

In closing, we like to point out that GenBox is one of multiple avenues that are inspired by research aimed at assembling a synthetic cell. This bottom-up biology approach distinguishes itself from the usual *in vitro* single-molecule experiments, by acknowledging the importance of size, complexity, and collectivity in biological organization and processes. By acting as an intermediary between the current approaches of live-cell experiments and single-molecule techniques, we foresee that GenBox may offer a fruitful avenue to study chromosomes *in vitro* in a bottom up-manner, yielding valuable insights on chromosome structure and dynamics.

VOCABULARY

Bottom-up biology, bottom-up biology research aims to engineer and study life from the bottom up, from molecules to cells to tissues; **synthetic cell**, synthetic biology research deals with the construction of new biological molecules and systems in order to redesign those found in nature. An ultimate aim in this field is the synthetic cell: to construct an artificial cell-like object that exhibits characteristics of natural cells; **chromosome organization**, the structure of a genome in both the spatial and temporal sense, as it is organized in living systems; **polymer physics**, the physical study of polymers that shows how the global configuration of polymers (e.g., biopolymers such as DNA) is guided by local physical properties such as the stiffness, interactions between different monomers and interactions of the polymer with the surrounding medium; **chromosome building blocks**, DNA-organizing elements, such as DNA-binding proteins or components of the surrounding medium, which interact with and give structure to the genome through a variety of local mechanisms such as bending, bridging, wrapping, looping, crowding, and phase separation.

REFERENCES

(1) Watson, J. D.; Crick, F. H. Molecular structure of nucleic acids: A structure for deoxyribose nucleic acid. *Nature* **1953**, *171*, 737–738.

(2) Flemming, W., *Zellsubstanz, Kern und Zelltheilung*; Verlag von F.C.W. Vogel: Leipzig, 1882.

(3) Rao, S. S.; Huntley, M. H.; Durand, N. C.; Stamenova, E. K.; Bochkov, I. D.; Robinson, J. T.; Sanborn, A. L.; Machol, I.; Omer, A. D.; Lander, E. S.; Aiden, E. L. A 3D Map of the Human Genome at Kilobase Resolution Reveals Principles of Chromatin Looping. *Cell* **2014**, *159*, 1665–1680.

(4) Gibcus, J. H.; Samejima, K.; Goloborodko, A.; Samejima, I.; Naumova, N.; Nuebler, J.; Kanemaki, M. T.; Xie, L.; Paulson, J. R.; Earnshaw, W. C.; Mirny, L. A.; Dekker, J. A pathway for mitotic chromosome formation. *Science* **2018**, *359*, eaao6135.

(5) Ganji, M.; Shaltiel, I. A.; Bisht, S.; Kim, E.; Kalichava, A.; Haering, C. H.; Dekker, C. Real-time imaging of DNA loop extrusion by condensin. *Science (New York, N.Y.)* **2018**, *360*, 102–105.

(6) Davidson, I. F.; Bauer, B.; Goetz, D.; Tang, W.; Wutz, G.; Peters, J.-M. M. DNA loop extrusion by human cohesin. *Science (New York, N.Y.)* **2019**, *366*, 1338–1345.

(7) Kim, Y.; Shi, Z.; Zhang, H.; Finkelstein, I. J.; Yu, H. Human cohesin compacts DNA by loop extrusion. *Science (New York, N.Y.)* **2019**, *366*, 1345–1349.

(8) Kong, M.; Cutts, E. E.; Pan, D.; Beuron, F.; Kaliyappan, T.; Xue, C.; Morris, E. P.; Musacchio, A.; Vannini, A.; Greene, E. C. Human Condensin I and II Drive Extensive ATP-Dependent Compaction of Nucleosome-Bound DNA. *Molecular Cell* **2020**, *79*, 99–114.

(9) Golfier, S.; Quail, T.; Kimura, H.; Brugués, J. Cohesin and condensin extrude DNA loops in a cell-cycle dependent manner. *eLife* **2020**, *9*, e53885.

(10) Xiang, Y.; Surovtsev, I. V.; Chang, Y.; Govers, S. K.; Parry, B. R.; Liu, J.; Jacobs-Wagner, C. Interconnecting solvent quality, transcription, and chromosome folding in Escherichia coli. *Cell* **2021**, *184*, 3626–3642.

(11) Parry, B. R.; Surovtsev, I. V.; Cabeen, M. T.; O'Hern, C. S.; Dufresne, E. R.; Jacobs-Wagner, C. The Bacterial Cytoplasm Has Glass-like Properties and Is Fluidized by Metabolic Activity. *Cell* **2014**, *156*, 183–194.

(12) Zidovska, A.; Weitz, D. A.; Mitchison, T. J. Micron-scale coherence in interphase chromatin dynamics. *Proceedings of the National Academy of Sciences* **2013**, *110*, 15555–15560.

(13) Wu, F.; Japaridze, A.; Zheng, X.; Wiktor, J.; Kerssemakers, J. W. J.; Dekker, C. Direct imaging of the circular chromosome in a live bacterium. *Nature Communications* **2019**, *10*, 2194.

(14) Wu, F.; Swain, P.; Kuijpers, L.; Zheng, X.; Felter, K.; Guurink, M.; Solari, J.; Jun, S.; Shimizu, T. S.; Chaudhuri, D.; Mulder, B.; Dekker, C. Cell Boundary Confinement Sets the Size and Position of the E. coli Chromosome. *Current Biology* **2019**, *29*, 2131–2144.

(15) Kang, H.; Yoon, Y.-G.; Thirumalai, D.; Hyeon, C. Confinement-Induced Glassy Dynamics in a Model for Chromosome Organization. *Physical Review Letters* **2015**, *115*, 198102.

(16) Erdel, F.; Baum, M.; Rippe, K. The viscoelastic properties of chromatin and the nucleoplasm revealed by scale-dependent protein mobility. *Journal of Physics: Condensed Matter* **2015**, *27*, 064115.

(17) Gray, W. T.; Govers, S. K.; Xiang, Y.; Parry, B. R.; Campos, M.; Kim, S.; Jacobs-Wagner, C. Nucleoid Size Scaling and Intracellular Organization of Translation across Bacteria. *Cell* **2019**, *177*, 1632–1648.

(18) Rosa, A.; Everaers, R. Structure and dynamics of interphase chromosomes. *PLoS Computational Biology* **2008**, *4*, e1000153.

(19) Jun, S.; Mulder, B. Entropy-driven spatial organization of highly confined polymers: Lessons for the bacterial chromosome. *Proceedings of the National Academy of Sciences* **2006**, *103*, 12388–12393.

(20) Gibson, B. A.; Doolittle, L. K.; Schneider, M. W.; Jensen, L. E.; Gamarra, N.; Henry, L.; Gerlich, D. W.; Redding, S.; Rosen, M. K. Organization of Chromatin by Intrinsic and Regulated Phase Separation. *Cell* **2019**, *179*, 470–484.

(21) Erdel, F.; Rippe, K. Formation of Chromatin Subcompartments by Phase Separation. *Biophysical Journal* **2018**, *114*, 2262–2270.

(22) Hildebrand, E. M.; Dekker, J. Mechanisms and Functions of Chromosome Compartmentalization. *Trends in Biochemical Sciences* **2020**, *45*, 385–396.

(23) Mirny, L. A.; Imakaev, M.; Abdennur, N. Two major mechanisms of chromosome organization. *Current Opinion in Cell Biology* **2019**, *58*, 142–152.

(24) Nuebler, J.; Fudenberg, G.; Imakaev, M.; Abdennur, N.; Mirny, L. A. Chromatin organization by an interplay of loop extrusion and compartmental segregation. *Proceedings of the National Academy of Sciences* **2018**, *115*, E6697–E6706.

(25) Rowley, M. J.; Corces, V. G. Organizational principles of 3D genome architecture. *Nature Reviews Genetics* **2018**, *19*, 789–800.

(26) Hilbert, L.; Sato, Y.; Kuznetsova, K.; Bianucci, T.; Kimura, H.; Jülicher, F.; Honigmann, A.; Zaburdaev, V.; Vastenhouw, N. L. Transcription organizes euchromatin via microphase separation. *Nature Communications* **2021**, *12*, 1–12.

(27) Chong, S.; Dugast-Darzacq, C.; Liu, Z.; Dong, P.; Dailey, G. M.; Cattoglio, C.; Heckert, A.; Banala, S.; Lavis, L.; Darzacq, X.; Tjian, R. Imaging dynamic and selective low-complexity domain interactions that control gene transcription. *Science* **2018**, *361*, eaar2555.

(28) Wei, M.-T.; Chang, Y.-C.; Shimobayashi, S. F.; Shin, Y.; Strom, A. R.; Brangwynne, C. P. Nucleated transcriptional condensates amplify gene expression. *Nature Cell Biology* **2020**, *22*, 1187–1196.

(29) Shrinivas, K.; Sabari, B. R.; Coffey, E. L.; Klein, I. A.; Boija, A.; Zamudio, A. V.; Schuijers, J.; Hannett, N. M.; Sharp, P. A.; Young, R. A.; Chakraborty, A. K. Enhancer Features that Drive Formation of Transcriptional Condensates. *Molecular Cell* **2019**, *75*, 549–561.

(30) Cho, W. K.; Spille, J. H.; Hecht, M.; Lee, C.; Li, C.; Grube, V.; Cisse, I. I. Mediator and RNA polymerase II clusters associate in transcription-dependent condensates. *Science* **2018**, *361*, 412–415.

(31) Sabari, B. R.; Dall'Agnese, A.; Boija, A.; Klein, I. A.; Coffey, E. L.; Shrinivas, K.; Abraham, B. J.; Hannett, N. M.; Zamudio, A. V.; Manteiga, J. C.; Li, C. H.; Guo, Y. E.; Day, D. S.; Schuijers, J.; Vasile, E., et al. Coactivator condensation at super-enhancers links phase separation and gene control. *Science* **2018**, *361*, eaar3958.

(32) Ladouceur, A.-M.; Parmar, B. S.; Biedzinski, S.; Wall, J.; Tope, S. G.; Cohn, D.; Kim, A.; Soubry, N.; Reyes-Lamothe, R.; Weber, S. C. Clusters of bacterial RNA polymerase are biomolecular condensates that assemble through liquid–liquid phase separation. *Proceedings of the National Academy of Sciences* **2020**, *117*, 18540–18549.

(33) Boehning, M.; Dugast-Darzacq, C.; Rankovic, M.; Hansen, A. S.; Yu, T.; Marie-Nelly, H.; McSwiggen, D. T.; Kokic, G.; Dailey, G. M.; Cramer, P.; Darzacq, X.; Zweckstetter, M. RNA polymerase II clustering through carboxy-terminal domain phase separation. *Nature Structural & Molecular Biology* **2018**, *25*, 833–840.

(34) Falk, M.; Feodorova, Y.; Naumova, N.; Imakaev, M.; Lajoie, B. R.; Leonhardt, H.; Joffe, B.; Dekker, J.; Fudenberg, G.; Solovei, I.; Mirny, L. A. Heterochromatin drives compartmentalization of inverted and conventional nuclei. *Nature* **2019**, *570*, 395–399.

(35) Larson, A. G.; Elnatan, D.; Keenen, M. M.; Trnka, M. J.; Johnston, B.; Burlingame, A. L.; Agard, D. A.; Redding, S.; Narlikar, G. J.; Johnston, J. B.; Burlingame, A. L.; Agard, D. A.; Redding, S.; Narlikar, G. J. Liquid droplet formation by HP1α suggests a role for phase separation in heterochromatin. *Nature* **2017**, *547*, 236–240.

(36) Strom, A. R.; Emelyanov, A. V.; Mir, M.; Fyodorov, D. V.; Darzacq, X.; Karpen, G. H. Phase separation drives heterochromatin domain formation. *Nature* **2017**, *547*, 241–245.

(37) Sessions, S. K., Genome Size In *Brenner's Encyclopedia of Genetics: Second Edition*, 2nd ed.; Elsevier: 2013, pp 301–305.

(38) Luger, K.; Mäder, A. W.; Richmond, R. K.; Sargent, D. F.; Richmond, T. J. Crystal structure of the nucleosome core particle at 2.8 Å resolution. *Nature* **1997**, *389*, 251–260.

(39) Dame, R. T.; Rashid, F.-Z. M.; Grainger, D. C. Chromosome organization in bacteria: mechanistic insights into genome structure and function. *Nature Reviews Genetics* **2020**, *21*, 227–242.

(40) Dillon, S. C.; Dorman, C. J. Bacterial nucleoid-associated proteins, nucleoid structure and gene expression. *Nature Reviews Microbiology* **2010**, *8*, 185–95.

(41) Dupaigne, P.; Tonthat, N. K.; Espéli, O.; Whitfill, T.; Boccard, F.; Schumacher, M. A. Molecular Basis for a Protein-Mediated DNA-Bridging Mechanism that Functions in Condensation of the E. coli Chromosome. *Molecular Cell* **2012**, *48*, 560–571.

(42) Dame, R. T.; Wyman, C.; Goosen, N. H-NS mediated compaction of DNA visualised by atomic force microscopy. *Nucleic Acids Research* **2000**, *28*, 3504–3510.

(43) Corless, S.; Gilbert, N. Investigating DNA supercoiling in eukaryotic genomes. *Briefings in Functional Genomics* **2017**, *16*, 379–389.

(44) Koster, D. A.; Crut, A.; Shuman, S.; Bjornsti, M. A.; Dekker, N. H. Cellular strategies for regulating DNA supercoiling: A single-molecule perspective. *Cell* **2010**, *142*, 519–530.

(45) Badrinarayanan, A.; Le, T. B.; Laub, M. T. Bacterial Chromosome Organization and Segregation. *Annual Review of Cell and Developmental Biology* **2015**, *31*, 171–199.

(46) Bintu, B.; Mateo, L. J.; Su, J.-H.; Sinnott-Armstrong, N. A.; Parker, M.; Kinrot, S.; Yamaya, K.; Boettiger, A. N.; Zhuang, X. Super-resolution chromatin tracing reveals domains and cooperative interactions in single cells. *Science (New York, N.Y.)* **2018**, *362*, eaau1783.

(47) Le, T. B. K.; Imakaev, M. V.; Mirny, L. a.; Laub, M. T. High-resolution mapping of the spatial organization of a bacterial chromosome. *Science* **2013**, *342*, 731–734.

(48) Valens, M.; Penaud, S.; Rossignol, M.; Cornet, F.; Boccard, F. Macrodomain organization of the Escherichia coli chromosome. *The EMBO journal* **2004**, *23*, 4330–4341.

(49) Lioy, V. S.; Cournac, A.; Marbouty, M.; Duigou, S.; Mozziconacci, J.; Espéli, O.; Boccard, F.; Koszul, R. Multiscale Structuring of the E. coli Chromosome by Nucleoid-Associated and Condensin Proteins. *Cell* **2018**, *172*, 771–783.

(50) Van Steensel, B.; Furlong, E. E. The role of transcription in shaping the spatial organization of the genome. *Nature Reviews Molecular Cell Biology* **2019**, *20*, 327–337.

(51) Shah, S.; Takei, Y.; Zhou, W.; Lubeck, E.; Yun, J.; Eng, C.-H. L.; Koulena, N.; Cronin, C.; Karp, C.; Liaw, E. J.; Amin, M.; Cai, L. Dynamics and Spatial Genomics of the Nascent Transcriptome by Intron seqFISH. *Cell* **2018**, *174*, 363–376.

(52) Stevens, T. J.; Lando, D.; Basu, S.; Atkinson, l. P.; Cao, Y.; Lee, S. F.; Leeb, M.; Wohlfahrt, K. J.; Boucher, W.; O'Shaughnessy-Kirwan, A.; Cramard, J.; Faure, A. J.; Ralser, M.; Blanco, E.; Morey, L., et al. 3D structures of individual mammalian genomes studied by single-cell Hi-C. *Nature* **2017**, *544*, 59–64.

(53) Branco, M. R.; Pombo, A. Intermingling of Chromosome Territories in Interphase Suggests Role in Translocations and Transcription-Dependent Associations. *PLoS Biology* **2006**, *4*, e138.

(54) Batty, P.; Gerlich, D. W. Mitotic Chromosome Mechanics: How Cells Segregate Their Genome. *Trends in Cell Biology* **2019**, *29*, 717–726.

(55) Lakadamyali, M.; Cosma, M. P. Advanced microscopy methods for visualizing chromatin structure. *FEBS Letters* **2015**, *589*, 3023–3030.

(56) Bystricky, K. Chromosome dynamics and folding in eukaryotes: Insights from live cell microscopy. *FEBS Letters* **2015**, *589*, 3014–3022.

(57) Jungmann, R.; Avendaño, M. S.; Woehrstein, J. B.; Dai, M.; Shih, W. M.; Yin, P. Multiplexed 3D cellular super-resolution imaging with DNA-PAINT and Exchange-PAINT. *Nature Methods* **2014**, *11*, 313–318.

(58) Beliveau, B. J.; Joyce, E. F.; Apostolopoulos, N.; Yilmaz, F.; Fonseka, C. Y.; McCole, R. B.; Chang, Y.; Li, J. B.; Senaratne, T. N.; Williams, B. R.; Rouillard, J.-M.; Wu, C.-t. Versatile design and synthesis platform for visualizing genomes with Oligopaint FISH probes. *Proceedings of the National Academy of Sciences* **2012**, *109*, 21301–21306.

(59) Deng, W.; Shi, X.; Tjian, R.; Lionnet, T.; Singer, R. H. CASFISH: CRISPR/Cas9-mediated in situ labeling of genomic loci in fixed cells. *Proceedings of the National Academy of Sciences* **2015**, *112*, 11870–11875.

(60) Chen, B.; Gilbert, L. A.; Cimini, B. A.; Schnitzbauer, J.; Zhang, W.; Li, G.-W.; Park, J.; Blackburn, E. H.; Weissman, J. S.; Qi, L. S.; Huang, B. Dynamic Imaging of Genomic Loci in Living Human Cells by an Optimized CRISPR/Cas System. *Cell* **2013**, *155*, 1479–1491.

(61) Lau, I. F.; Filipe, S. R.; Søballe, B.; Økstad, O.-A.; Barre, F.-X.; Sherratt, D. J. Spatial and temporal organization of replicating Escherichia coli chromosomes. *Molecular microbiology* **2003**, *49*, 731–43.

(62) Gordon, G.; Sitnikov, D.; Webb, C. D.; Teleman, A.; Straight, A.; Losick, R.; Murray, A. W.; Wright, A. Chromosome and Low Copy Plasmid Segregation in E. coli: Visual Evidence for Distinct Mechanisms. *Cell* **1997**, *90*, 1113–1121.

(63) Germier, T.; Audibert, S.; Kocanova, S.; Lane, D.; Bystricky, K. Real-time imaging of specific genomic loci in eukaryotic cells using the ANCHOR DNA labelling system. *Methods* **2018**, *142*, 16–23.

(64) Li, Y.; Sergueev, K.; Austin, S. The segregation of the Escherichia coli origin and terminus of replication. *Molecular Microbiology* **2002**, *46*, 985–996.

(65) Cardozo Gizzi, A. M.; Cattoni, D. I.; Fiche, J. B.; Espinola, S. M.; Gurgo, J.; Messina, O.; Houbron, C.; Ogiyama, Y.; Papadopoulos, G. L.; Cavalli, G.; Lagha, M.; Nollmann, M. Microscopy-Based Chromosome Conformation Capture Enables Simultaneous Visualization of Genome Organization and Transcription in Intact Organisms. *Molecular Cell* **2019**, *74*, 212–222.

(66) Schmitt, A. D.; Hu, M.; Ren, B. Genome-wide mapping and analysis of chromosome architecture. *Nature Reviews Molecular Cell Biology* **2016**, *17*, 743–755.

(67) Denker, A.; de Laat, W. The second decade of 3C technologies: detailed insights into nuclear organization. *Genes & development* **2016**, *30*, 1357–1382.

(68) Klein, D. C.; Hainer, S. J. Genomic methods in profiling DNA accessibility and factor localization. *Chromosome Research* **2020**, *28*, 69–85.

(69) Klemm, S. L.; Shipony, Z.; Greenleaf, W. J. Chromatin accessibility and the regulatory epigenome. *Nature Reviews Genetics* **2019**, *20*, 207–220.

(70) Kempfer, R.; Pombo, A. Methods for mapping 3D chromosome architecture. *Nature Reviews Genetics* **2020**, *21*, 207–226.

(71) Jiang, S.; Mortazavi, A. Integrating ChIP-seq with other functional genomics data. *Briefings in Functional Genomics* **2018**, *17*, 104–115.

(72) Beagan, J. A.; Phillips-Cremins, J. E. On the existence and functionality of topologically associating domains. *Nature Genetics* **2020**, *52*, 8–16.

(73) Cardozo Gizzi, A. M.; Cattoni, D. I. TADs or no TADS: Lessons From Single-cell Imaging of Chromosome Architecture. *Journal of Molecular Biology* **2020**, *432*, 682–693.

(74) Nagano, T.; Lubling, Y.; Stevens, T. J.; Schoenfelder, S.; Yaffe, E.; Dean, W.; Laue, E. D.; Tanay, A.; Fraser, P. Single-cell Hi-C reveals cell-to-cell variability in chromosome structure. *Nature* **2013**, *502*, 59–64.

(75) Shipony, Z.; Marinov, G. K.; Swaffer, M. P.; Sinnott-Armstrong, N. A.; Skotheim, J. M.; Kundaje, A.; Greenleaf, W. J. Long-range single-molecule mapping of chromatin accessibility in eukaryotes. *Nature Methods* **2020**, *17*, 319–327.

(76) Kind, J.; Pagie, L.; de Vries, S. S.; Nahidiazar, L.; Dey, S. S. S.; Bienko, M.; Zhan, Y.; Lajoie, B.; de Graaf, C. A.; Amendola, M.; Fudenberg, G.; Imakaev, M.; Mirny, L. A. A.; Jalink, K.; Dekker, J., et al. Genome-wide maps of nuclear lamina interactions in single human cells. *Cell* **2015**, *163*, 134–147.

(77) Rhie, S. K.; Perez, A. A.; Lay, F. D.; Schreiner, S.; Shi, J.; Polin, J.; Farnham, P. J. A high-resolution 3D epigenomic map reveals insights into the creation of the prostate cancer transcriptome. *Nature Communications* **2019**, *10*, 4154.

(78) Höllbacher, B.; Balázs, K.; Heinig, M.; Uhlenhaut, N. H. Seq-ing answers: Current data integration approaches to uncover mechanisms of transcriptional regulation. *Computational and Structural Biotechnology Journal* **2020**, *18*, 1330–1341.

(79) Rooijers, K.; Markodimitraki, C. M.; Rang, F. J.; de Vries, S. S.; Chialastri, A.; de Luca, K. L.; Mooijman, D.; Dey, S. S.; Kind, J. Simultaneous quantification of protein–DNA contacts and transcriptomes in single cells. *Nature Biotechnology* **2019**, *37*, 766–772.

(80) Kaur, G.; Lewis, J.; van Oijen, A. Shining a Spotlight on DNA: Single-Molecule Methods to Visualise DNA. *Molecules* **2019**, *24*, 491.

(81) Zhao, Y.; Jiang, Y.; Qi, Z. Visualizing biological reaction intermediates with DNA curtains. *Journal of Physics D: Applied Physics* **2017**, *50*, 153001.

(82) Dufrêne, Y. F.; Ando, T.; Garcia, R.; Alsteens, D.; Martinez-Martin, D.; Engel, A.; Gerber, C.; Müller, D. J. Imaging modes of atomic force microscopy for application in molecular and cell biology. *Nature Nanotechnology* **2017**, *12*, 295–307.

(83) Katan, A. J.; Dekker, C. High-Speed AFM Reveals the Dynamics of Single Biomolecules at the Nanometer Scale. *Cell* **2011**, *147*, 979–982.

(84) Wilson, M. D.; Costa, A. Cryo-electron microscopy of chromatin biology. *Acta Crystallographica Section D Structural Biology* **2017**, *73*, 541–548.

(85) Orlov, I.; Myasnikov, A. G.; Andronov, L.; Natchiar, S. K.; Khatter, H.; Beinsteiner, B.; Ménétret, J.-F.; Hazemann, I.; Mohideen, K.; Tazibt, K.; Tabaroni, R.; Kratzat, H.; Djabeur, N.; Bruxelles, T.; Raivoniaina, F., et al. The integrative role of cryo electron microscopy in molecular and cellular structural biology. *Biology of the Cell* **2017**, *109*, 81–93.

(86) Murata, K.; Wolf, M. Cryo-electron microscopy for structural analysis of dynamic biological macromolecules. *Biochimica et Biophysica Acta (BBA) - General Subjects* **2018**, *1862*, 324–334.

(87) Ou, H. D.; Phan, S.; Deerinck, T. J.; Thor, A.; Ellisman, M. H.; O'Shea, C. C. ChromEMT: Visualizing 3D chromatin structure and compaction in interphase and mitotic cells. *Science* **2017**, *357*, eaag0025.

(88) Lerner, E.; Cordes, T.; Ingargiola, A.; Alhadid, Y.; Chung, S.; Michalet, X.; Weiss, S. Toward dynamic structural biology: Two decades of single-molecule Förster resonance energy transfer. *Science* **2018**, *359*, eaan1133.

(89) Sustarsic, M.; Kapanidis, A. N. Taking the ruler to the jungle: single-molecule FRET for understanding biomolecular structure and dynamics in live cells. *Current Opinion in Structural Biology* **2015**, *34*, 52–59.

(90) Schuler, B.; Soranno, A.; Hofmann, H.; Nettels, D. Single-Molecule FRET Spectroscopy and the Polymer Physics of Unfolded and Intrinsically Disordered Proteins. *Annual Review of Biophysics* **2016**, *45*, 207–231.

(91) Kriegel, F.; Ermann, N.; Lipfert, J. Probing the mechanical properties, conformational changes, and interactions of nucleic acids with magnetic tweezers. *Journal of Structural Biology* **2017**, *197*, 26–36.

(92) Ritchie, D. B.; Woodside, M. T. Probing the structural dynamics of proteins and nucleic acids with optical tweezers. *Current Opinion in Structural Biology* **2015**, *34*, 43–51.

(93) Hashemi Shabestari, M.; Meijering, A.; Roos, W.; Wuite, G.; Peterman, E. Recent Advances in Biological Single-Molecule Applications of Optical Tweezers and Fluorescence Microscopy. *Methods in Enzymology* **2017**, *582*, 85–119.

(94) Fudenberg, G.; Mirny, L. A. Higher-order chromatin structure: bridging physics and biology. *Current Opinion in Genetics & Development* **2012**, *22*, 115–124.

(95) Imakaev, M. V.; Fudenberg, G.; Mirny, L. A. Modeling chromosomes: Beyond pretty pictures. *FEBS Letters* **2015**, *589*, 3031–3036.

(96) Brackey, C. A.; Marenduzzo, D.; Gilbert, N. Mechanistic modeling of chromatin folding to understand function. *Nature Methods* **2020**, *17*, 767–775.

(97) Barbieri, M.; Scialdone, A.; Gamba, A.; Pombo, A.; Nicodemi, M. Polymer physics, scaling and heterogeneity in the spatial organisation of chromosomes in the cell nucleus. *Soft Matter* **2013**, *9*, 8631.

(98) Bianco, S.; Chiariello, A. M.; Conte, M.; Esposito, A.; Fiorillo, L.; Musella, F.; Nicodemi, M. Computational approaches from polymer physics to investigate chromatin folding. *Current Opinion in Cell Biology* **2020**, *64*, 10–17.

(99) Michieletto, D.; Colì, D.; Marenduzzo, D.; Orlandini, E. Nonequilibrium Theory of Epigenomic Microphase Separation in the Cell Nucleus. *Physical Review Letters* **2019**, *123*, 228101.

(100) Goloborodko, A.; Imakaev, M. V.; Marko, J. F.; Mirny, L. Compaction and segregation of sister chromatids via active loop extrusion. *eLife* **2016**, *5*, e14864.

(101) Sanborn, A. L.; Rao, S. S. P.; Huang, S.-C.; Durand, N. C.; Huntley, M. H.; Jewett, A. I.; Bochkov, I. D.; Chinnappan, D.; Cutkosky, A.; Li, J.; Geeting, K. P.; Gnirke, A.; Melnikov, A.; McKenna, D.; Stamenova, E. K., et al. Chromatin extrusion explains key features of loop and domain formation in wild-type and engineered genomes. *Proceedings of the National Academy of Sciences* **2015**, *112*, E6456–E6465.

(102) Fudenberg, G.; Imakaev, M.; Lu, C.; Goloborodko, A.; Abdennur, N.; Mirny, L. A. Formation of Chromosomal Domains by Loop Extrusion. *Cell Reports* **2016**, *15*, 2038–2049.

(103) Schwille, P. Jump-starting life? Fundamental aspects of synthetic biology. *The Journal of Cell Biology* **2015**, *210*, 687–690.

(104) Ganzinger, K. A.; Merino-Salomón, A.; García-Soriano, D. A.; Butterfield, A. N.; Litschel, T.; Siedler, F.; Schwille, P. FtsZ Reorganization Facilitates Deformation of Giant Vesicles in Microfluidic Traps. *Angewandte Chemie International Edition* **2020**, *59*, 21372–21376.

(105) Litschel, T.; Kelley, C. F.; Holz, D.; Adeli Koudehi, M.; Vogel, S. K.; Burbaum, L.; Mizuno, N.; Vavylonis, D.; Schwille, P. Reconstitution of contractile actomyosin rings in vesicles. *Nature Communications* **2021**, *12*, 2254.

(106) Van Nies, P.; Westerlaken, I.; Blanken, D.; Salas, M.; Mencía, M.; Danelon, C. Self-replication of DNA by its encoded proteins in liposome-based synthetic cells. *Nature Communications* **2018**, *9*, 1583.

(107) Litschel, T.; Ramm, B.; Maas, R.; Heymann, M.; Schwille, P. Beating Vesicles: Encapsulated Protein Oscillations Cause Dynamic Membrane Deformations. *Angewandte Chemie International Edition* **2018**, *57*, 16286–16290.

(108) Joesaar, A.; Yang, S.; Bögels, B.; van der Linden, A.; Pieters, P.; Kumar, B. V. V. S. P.; Dalchau, N.; Phillips, A.; Mann, S.; de Greef, T. F. A. DNA-based communication in populations of synthetic protocells. *Nature Nanotechnology* **2019**, *14*, 369–378.

(109) BaSyC. *http://www.basyc.nl*.

(110) Build-a-cell. *https://www.buildacell.org*.

(111) MaxSynBio. *https://www.maxsynbio.mpg.de*.

(112) Synthetic Cell EU. *http://www.syntheticcell.eu*.

(113) Spoelstra, W. K.; Deshpande, S.; Dekker, C. Tailoring the appearance: what will synthetic cells look like? *Current Opinion in Biotechnology* **2018**, *51*, 47–56.

(114) Fanalista, F.; Birnie, A.; Maan, R.; Burla, F.; Charles, K.; Pawlik, G.; Deshpande, S.; Koenderink, G. H.; Dogterom, M.; Dekker, C. Shape and Size Control of Artificial Cells for Bottom-Up Biology. *ACS Nano* **2019**, *13*, 5439–5450.

(115) Jun, S., Polymer Physics for Understanding Bacterial Chromosomes In *Bacterial Chromatin*, Dame, R. T., Dorman, C. J., Eds.; Springer Netherlands: Dordrecht, 2010, pp 97–116.

(116) Kavenoff, R.; Bowen, B. C. Electron microscopy of membrane-free folded chromosomes from Escherichia coli. *Chromosoma* **1976**, *59*, 89–101.

(117) Wegner, A. S.; Alexeeva, S.; Odijk, T.; Woldringh, C. L. Characterization of Escherichia coli nucleoids released by osmotic shock. *Journal of Structural Biology* **2012**, *178*, 260–269.

(118) Pelletier, J.; Halvorsen, K.; Ha, B.-Y.; Paparcone, R.; Sandler, S. J.; Woldringh, C. L.; Wong, W. P.; Jun, S. Physical manipulation of the Escherichia coli chromosome reveals its soft nature. *Proceedings of the National Academy of Sciences* **2012**, *109*, E2649–E2656.

(119) Hutchison, C. A.; Chuang, R.-Y.; Noskov, V. N.; Assad-Garcia, N.; Deerinck, T. J.; Ellisman, M. H.; Gill, J.; Kannan, K.; Karas, B. J.; Ma, L.; Pelletier, J. F.; Qi, Z.-Q.; Richter, R. A.; Strychalski, E. A.; Sun, L., et al. Design and synthesis of a minimal bacterial genome. *Science* **2016**, *351*, aad6253–aad6253.

(120) Shintomi, K.; Takahashi, T. S.; Hirano, T. Reconstitution of mitotic chromatids with a minimum set of purified factors. *Nature Cell Biology* **2015**, *17*, 1014–1023.

(121) Cunha, S.; Woldringh, C. L.; Odijk, T. Polymer-Mediated Compaction and Internal Dynamics of Isolated Escherichia Coli Nucleoids. *Journal of Structural Biology* **2001**, *136*, 53–66.

(122) Lartigue, C.; Glass, J. I.; Alperovich, N.; Pieper, R.; Parmar, P. P.; Hutchison, C. A.; Smith, H. O.; Venter, J. C. Genome transplantation in bacteria: Changing one species to another. *Science (New York, N.Y.)* **2007**, *317*, 632–638.

(123) Shintomi, K.; Inoue, F.; Watanabe, H.; Ohsumi, K.; Ohsugi, M.; Hirano, T. Mitotic chromosome assembly despite nucleosome depletion in Xenopus egg extracts. *Science* **2017**, *356*, 1284–1287.

(124) Kinoshita, K.; Kobayashi, T. J.; Hirano, T. Balancing acts of two HEAT subunits of condensin I support dynamic assembly of chromosome axes. *Developmental Cell* **2015**, *33*, 94–106.

(125) Hazel, J.; Krutkramelis, K.; Mooney, P.; Tomschik, M.; Gerow, K.; Oakey, J.; Gatlin, J. C. Changes in Cytoplasmic Volume Are Sufficient to Drive Spindle Scaling. *Science* **2013**, *342*, 853–856.

(126) Good, M. C.; Vahey, M. D.; Skandarajah, A.; Fletcher, D. A.; Heald, R. Cytoplasmic volume modulates spindle size during embryogenesis. *Science* **2013**, *342*, 856–860.

(127) Cole, S. T.; Saint-Girons, I., Bacterial Genomes-All Shapes and Sizes In *Organization of the Prokaryotic Genome*; ASM Press: Washington, DC, USA, 2014, pp 35–62.

(128) Pellicer, J.; Fay, M. F.; Leitch, I. J. The largest eukaryotic genome of them all? *Botanical Journal of the Linnean Society* **2010**, *164*, 10–15.

(129) Rittman, M.; Gilroy, E.; Koohy, H.; Rodger, A.; Richards, A. Is DNA a worm-like chain in Couette flow?: In search of persistence length, a critical review. *Science Progress* **2009**, *92*, 163–204.

(130) Peters, J. P.; Maher, L. J. DNA curvature and flexibility in vitro and in vivo. *Quarterly Reviews of Biophysics* **2010**, *43*, 23–63.

(131) Kubitschek, H. E.; Friske, J. A. Determination of bacterial cell volume with the Coulter Counter. *Journal of bacteriology* **1986**, *168*, 1466–1467.

(132) Sun, H. B.; Shen, J.; Yokota, H. Size-dependent positioning of human chromosomes in interphase nuclei. *Biophysical Journal* **2000**, *79*, 184–190.

(133) Ricci, M. A.; Manzo, C.; García-Parajo, M. F.; Lakadamyali, M.; Cosma, M. P. Chromatin fibers are formed by heterogeneous groups of nucleosomes in vivo. *Cell* **2015**, *160*, 1145–58.

(134) Kruithof, M.; Chien, F.-T.; Routh, A.; Logie, C.; Rhodes, D.; van Noort, J. Single-molecule force spectroscopy reveals a highly compliant helical folding for the 30-nm chromatin fiber. *Nature Structural & Molecular Biology* **2009**, *16*, 534–540.

(135) Japaridze, A.; Renevey, S.; Sobetzko, P.; Stoliar, L.; Nasser, W.; Dietler, G.; Muskhelishvili, G. Spatial organization of DNA sequences directs the assembly of bacterial chromatin by a nucleoid-associated protein. *The Journal of biological chemistry* **2017**, *292*, 7607–7618.

(136) Ganji, M.; Kim, S. H.; van der Torre, J.; Abbondanzieri, E.; Dekker, C. Intercalation-Based Single-Molecule Fluorescence Assay To Study DNA Supercoil Dynamics. *Nano Letters* **2016**, *16*, 4699–4707.

(137) Bettotti, P.; Visone, V.; Lunelli, L.; Perugino, G.; Ciaramella, M.; Valenti, A. Structure and Properties of DNA Molecules Over The Full Range of Biologically Relevant Supercoiling States. *Scientific Reports* **2018**, *8*, 6163.

(138) Naughton, C.; Avlonitis, N.; Corless, S.; Prendergast, J. G.; Mati, I. K.; Eijk, P. P.; Cockroft, S. L.; Bradley, M.; Ylstra, B.; Gilbert, N. Transcription forms and remodels supercoiling domains unfolding large-scale chromatin structures. *Nature Structural and Molecular Biology* **2013**, *20*, 387–395.

(139) Cisse, I. I.; Izeddin, I.; Causse, S. Z.; Boudarene, L.; Senecal, A.; Muresan, L.; Dugast-Darzacq, C.; Hajj, B.; Dahan, M.; Darzacq, X. Real-Time Dynamics of RNA Polymerase II Clustering in Live Human Cells. *Science* **2013**, *341*, 664–667.

(140) Ma, J.; Tan, C.; Gao, X.; Fulbright, R. M.; Roberts, J. W.; Wang, M. D. Transcription factor regulation of RNA polymerase's torque generation capacity. *Proceedings of the National Academy of Sciences* **2019**, *116*, 2583–2588.

(141) Kimura, Y.; Bianco, P. R. Single molecule studies of DNA binding proteins using optical tweezers. *The Analyst* **2006**, *131*, 868.

(142) Haarhuis, J. H.; van der Weide, R. H.; Blomen, V. A.; Yáñez-Cuna, J. O.; Amendola, M.; van Ruiten, M. S.; Krijger, P. H.; Teunissen, H.; Medema, R. H.; van Steensel, B.; Brummelkamp, T. R.; de Wit, E.; Rowland, B. D. The Cohesin Release Factor WAPL Restricts Chromatin Loop Extension. *Cell* **2017**, *169*, 693–707.

(143) Shaban, H. A.; Barth, R.; Bystricky, K. Formation of correlated chromatin domains at nanoscale dynamic resolution during transcription. *Nucleic Acids Research* **2018**, *46*, e77.

(144) Fields, B. D.; Nguyen, S. C.; Nir, G.; Kennedy, S. A multiplexed DNA FISH strategy for assessing genome architecture in Caenorhabditis elegans. *eLife* **2019**, *8*, e42823.

(145) Richmond, T. J.; Davey, C. A. The structure of DNA in the nucleosome core. *Nature* **2003**, *423*, 145–150.

(146) Kaczmarczyk, A.; Meng, H.; Ordu, O.; Noort, J. v.; Dekker, N. H. Chromatin fibers stabilize nucleosomes under torsional stress. *Nature Communications* **2020**, *11*, 126.

(147) Mattiroli, F.; Bhattacharyya, S.; Dyer, P. N.; White, A. E.; Sandman, K.; Burkhart, B. W.; Byrne, K. R.; Lee, T.; Ahn, N. G.; Santangelo, T. J.; Reeve, J. N.; Luger, K. Structure of histone-based chromatin in Archaea. *Science* **2017**, *357*, 609–612.

(148) Mercier, R.; Petit, M.-A.; Schbath, S.; Robin, S.; El Karoui, M.; Boccard, F.; Espéli, O. The MatP/matS Site-Specific System Organizes the Terminus Region of the E. coli Chromosome into a Macrodomain. *Cell* **2008**, *135*, 475–485.

(149) Bannister, A. J.; Kouzarides, T. Regulation of chromatin by histone modifications. *Cell Research* **2011**, *21*, 381–395.

(150) Dilweg, I. W.; Dame, R. T. Post-translational modification of nucleoid-associated proteins: an extra layer of functional modulation in bacteria? *Biochemical Society Transactions* **2018**, *46*, 1381–1392.

(151) Wang, M. D.; Schnitzer, M. J.; Yin, H.; Landick, R.; Gelles, J.; Block, S. M. Force and Velocity Measured for Single Molecules of RNA Polymerase. *Science* **1998**, *282*, 902–907.

(152) Le, T. B.; Laub, M. T. Transcription rate and transcript length drive formation of chromosomal interaction domain boundaries. *The EMBO Journal* **2016**, *35*, 1582–1595.

(153) Lal, A.; Dhar, A.; Trostel, A.; Kouzine, F.; Seshasayee, A. S. N.; Adhya, S. Genome scale patterns of supercoiling in a bacterial chromosome. *Nature communications* **2016**, *7*, 11055.

(154) Schneider, R.; Lurz, R.; Lüder, G.; Tolksdorf, C.; Travers, A.; Muskhelishvili, G. An architectural role of the Escherichia coli chromatin protein FIS in organising DNA. *Nucleic Acids Research* **2001**, *29*, 5107–5114.

(155) Pommier, Y.; Sun, Y.; Huang, S.-y. N.; Nitiss, J. L. Roles of eukaryotic topoisomerases in transcription, replication and genomic stability. *Nature Reviews Molecular Cell Biology* **2016**, *17*, 703–721.

(156) Champoux, J. J. DNA Topoisomerases: Structure, Function, and Mechanism. *Annual Review of Biochemistry* **2001**, *70*, 369–413.

(157) Piazza, I.; Rutkowska, A.; Ori, A.; Walczak, M.; Metz, J.; Pelechano, V.; Beck, M.; Haering, C. H. Association of condensin with chromosomes depends on DNA binding by its HEAT-repeat subunits. *Nature Structural and Molecular Biology* **2014**, *21*, 560–568.

(158) Cuylen, S.; Metz, J.; Haering, C. H. Condensin structures chromosomal DNA through topological links. *Nature Structural and Molecular Biology* **2011**, *18*, 894–901.

(159) Kimura, K.; Hirano, T. ATP-dependent positive supercoiling of DNA by 13S condensin: a biochemical implication for chromosome condensation. *Cell* **1997**, *90*, 625–634.

(160) Keenholtz, R. A.; Dhanaraman, T.; Palou, R.; Yu, J.; D'Amours, D.; Marko, J. F. Oligomerization and ATP stimulate condensin-mediated DNA compaction. *Scientific Reports* **2017**, *7*, 14279.

(161) Eeftens, J. M.; Bisht, S.; Kerssemakers, J.; Kschonsak, M.; Haering, C. H.; Dekker, C. Real-time detection of condensin-driven DNA compaction reveals a multistep binding mechanism. *The EMBO Journal* **2017**, *36*, 3448–3457.

(162) Kschonsak, M.; Merkel, F.; Bisht, S.; Metz, J.; Rybin, V.; Hassler, M.; Haering, C. H. Structural Basis for a Safety-Belt Mechanism That Anchors Condensin to Chromosomes. *Cell* **2017**, *171*, 588–600.

(163) Shi, Z.; Gao, H.; Bai, X.-C.; Yu, H. Cryo-EM structure of the human cohesin-NIPBL-DNA complex. *Science (New York, N.Y.)* **2020**, *368*, 1454–1459.

(164) Bürmann, F.; Lee, B.-G. G.; Than, T.; Sinn, L.; O'Reilly, F. J.; Yatskevich, S.; Rappsilber, J.; Hu, B.; Nasmyth, K.; Löwe, J. A folded conformation of MukBEF and cohesin. *Nature Structural and Molecular Biology* **2019**, *26*, 227–236.

(165) Diebold-Durand, M.-L.; Lee, H.; Ruiz, L. B.; Oh, B.-H.; Correspondence, S. G. Structure of Full-Length SMC and Rearrangements Required for Chromosome Organization. *Molecular Cell* **2017**, *67*, 334–347.

(166) Eeftens, J. M.; Katan, A. J.; Kschonsak, M.; Hassler, M.; de Wilde, L.; Dief, E. M.; Haering, C. H.; Dekker, C. Condensin Smc2-Smc4 Dimers Are Flexible and Dynamic. *Cell Reports* **2016**, *14*, 1813–1818.

(167) Ryu, J.-K.; Katan, A. J.; van der Sluis, E. O.; Wisse, T.; de Groot, R.; Haering, C. H.; Dekker, C. The condensin holocomplex cycles dynamically between open and collapsed states. *Nature Structural & Molecular Biology* **2020**, *27*, 1134–1141.

(168) Rao, S. S.; Huang, S.-C.; Glenn St Hilaire, B.; Engreitz, J. M.; Perez, E. M.; Kieffer-Kwon, K.-R.; Sanborn, A. L.; Johnstone, S. E.; Bascom, G. D.; Bochkov, I. D.; Huang, X.; Shamim, M. S.; Shin, J.; Turner, D.; Ye, Z., et al. Cohesin Loss Eliminates All Loop Domains. *Cell* **2017**, *171*, 305–320.

(169) Cuylen, S.; Blaukopf, C.; Politi, A. Z.; Muller-Reichert, T.; Neumann, B.; Poser, I.; Ellenberg, J.; Hyman, A. A.; Gerlich, D. W. Ki-67 acts as a biological surfactant to disperse mitotic chromosomes. *Nature* **2016**, *535*, 308–312.

(170) Mäkelä, J.; Sherratt, D. J. Organization of the Escherichia coli Chromosome by a MukBEF Axial Core. *Molecular Cell* **2020**, *78*, 250–260.

(171) Hyman, A. A.; Weber, C. A.; Jülicher, F. Liquid-Liquid Phase Separation in Biology. *Annual Review of Cell and Developmental Biology* **2014**, *30*, 39–58.

(172) Van Steensel, B.; Belmont, A. S. Lamina-Associated Domains: Links with Chromosome Architecture, Heterochromatin, and Gene Repression. *Cell* **2017**, *169*, 780–791.

(173) Erdel, F.; Rademacher, A.; Vlijm, R.; Tünnermann, J.; Frank, L.; Weinmann, R.; Schweigert, E.; Yserentant, K.; Hummert, J.; Bauer, C.; Schumacher, S.; Al Alwash, A.; Normand, C.; Herten, D.-P.; Engelhardt, J., et al. Mouse Heterochromatin Adopts Digital Compaction States without Showing Hallmarks of HP1-Driven Liquid-Liquid Phase Separation. *Molecular Cell* **2020**, *78*, 236–249.

(174) McSwiggen, D. T.; Mir, M.; Darzacq, X.; Tjian, R. Evaluating phase separation in live cells: diagnosis, caveats, and functional consequences. *Genes & development* **2019**, *33*, 1619–1634.

(175) Alberti, S.; Gladfelter, A.; Mittag, T. Considerations and Challenges in Studying Liquid-Liquid Phase Separation and Biomolecular Condensates. *Cell* **2019**, *176*, 419–434.

(176) Takemata, N.; Samson, R. Y.; Bell, S. D. Physical and Functional Compartmentalization of Archaeal Chromosomes. *Cell* **2019**, *179*, 165–179.

(177) Azaldegui, C. A.; Vecchiarelli, A. G.; Biteen, J. S. The Emergence of Phase Separation as an Organizing Principle in Bacteria. *Biophysical Journal* **2020**, *20*, 239012.

(178) Choi, J.-M.; Holehouse, A. S.; Pappu, R. V. Physical Principles Underlying the Complex Biology of Intracellular Phase Transitions. *Annual Review of Biophysics* **2020**, *49*, 107–133.

(179) Guilhas, B.; Walter, J.-C.; Rech, J.; David, G.; Walliser, N. O.; Palmeri, J.; Mathieu-Demaziere, C.; Parmeggiani, A.; Bouet, J.-Y.; Le Gall, A.; Nollmann, M. ATP-Driven Separation of Liquid Phase Condensates in Bacteria. *Molecular Cell* **2020**, *79*, 293–303.

(180) Wang, X.; Hughes, A. C.; Brandão, H. B.; Walker, B.; Lierz, C.; Cochran, J. C.; Oakley, M. G.; Kruse, A. C.; Rudner, D. Z. In Vivo Evidence for ATPase-Dependent DNA Translocation by the Bacillus subtilis SMC Condensin Complex. *Molecular Cell* **2018**, *71*, 841–847.

3

EXTRACTING AND CHARACTERIZING PROTEIN-FREE MEGABASEPAIR DNA FOR *in vitro* EXPERIMENTS

Chromosome structure and function is studied using various cell-based methods as well as with a range of *in vitro* single-molecule techniques on short DNA substrates. Here we present a method to obtain megabasepair length deproteinated DNA for *in vitro* studies. We isolated chromosomes from bacterial cells and enzymatically digested the native proteins. Mass spectrometry indicated that 97-100% of DNA-binding proteins are removed from the sample. Fluorescence-microscopy analysis showed an increase in the radius of gyration of the DNA polymers, while the DNA length remained megabasepair sized. In proof-of-concept experiments using these deproteinated long DNA molecules, we observed DNA compaction upon adding the DNA-binding protein Fis or PEG crowding agents and showed that it is possible to track the motion of a fluorescently labelled DNA locus. These results indicate the practical feasibility of a 'genome-in-a-box' approach to study chromosome organization from the bottom up.

This chapter has been published: Martin Holub*, Anthony Birnie*, Aleksandre Japaridze, Jaco van der Torre, Maxime den Ridder, Carol de Ram, Martin Pabst, Cees Dekker, *Extracting and characterizing protein-free megabasepair DNA for in vitro experiments*, Cell Reports Methods 2, 100366 (2022). *Equal contribution

3.1. INTRODUCTION

Over the past decade, bottom-up synthetic cell research or 'bottom-up biology' has gained traction as a method to study components of living systems. The ultimate aim of such efforts is to build a synthetic cell by assembling biological functionalities from the bottom up. This involves the reconstitution of the various parts of living cells from a set of well-characterized but lifeless molecules such as DNA and proteins.[1] While the end goal of building a functional synthetic cell is yet far off, the bottom-up approach has already successfully been applied to constitute and study minimal cellular systems, for example, intracellular pattern formation,[2] cell division,[3] the cytoskeleton,[4] and cellular communication.[5]

For studying chromosome organization in the eukaryotic nucleus or in bacterial cells, numerous studies have been made on live or fixed cells through imaging,[6,7] chromosome conformation capture techniques,[8,9] *etc.*, while *in vitro* protein-DNA interactions are often characterized at the single-molecule level using techniques such as Atomic Force Microscopy,[10–12] magnetic[13,14] and optical tweezers,[15,16] and DNA visualization assays.[17–21] While these complementary approaches have yielded great insights, they leave a significant gap since typical single-molecule methods address the kilobasepair (kbp) scale while actual genomes consist of 10^5 – 10^{11} bp long DNA. It would therefore be useful to study DNA in the megabasepair size range with bottom-up *in vitro* methods, including the emergent collective behavior associated with this length scale. We propose that such experiments, which we coin a 'genome-in-a-box' (GenBox) approach,[22] may provide valuable insights into chromosome organization, somewhat analogous to the 'particle-in-a-box' experiments in physics which proved a useful abstraction to understand basic phenomena in quantum mechanics. However, such a GenBox method has so far been lacking. Expanding from the kbp to the Mbp scale poses technical challenges, both in the handling of long DNA that is prone to shearing,[23–25] and in the availability of long DNA, as common *in vitro* experiments[26–28] are done on viral DNA (such as the 48.5 kbp lambda-phage DNA) which however is limited in length. Several previous studies have proposed methods to extract chromosomes from cells, and some have even used protein-removal steps to obtain deproteinated DNA.[29–34] However, most of these studies lacked an imaging-based characterization of the resulting DNA objects, regarding their size, level of deproteination, and suitability for *in vitro* imaging-based experiments.

Here, we present a methodology for the extraction of chromosomal DNA from *E. coli* bacteria and the subsequent removal of native proteins, resulting in deproteinated DNA of megabasepair size which can be used for *in vitro* bottom-up experiments to study chromosome organization (Figure 3.1). We describe the extraction and purification protocol, characterize the DNA objects obtained, and present some first proof-of-principle experiments.

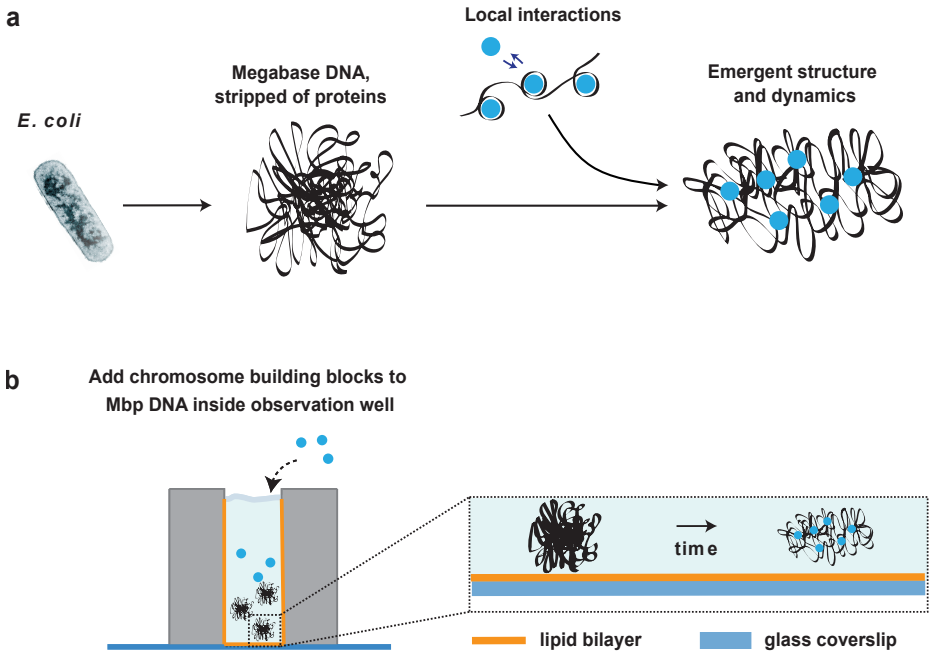

Figure 3.1: **Methodology of extracting, purifying, and studying a bacterial chromosome.** **(a)** In a Genome-in-a-box (GenBox) approach, one isolates chromosomes from bacterial cells, removes the natively bound proteins, to subsequently add DNA-structuring elements and thus study the resulting emergent DNA structure. **(b)** Typical setup where a deproteinated megabasepair-long DNA is suspended in solution in an observation well attached to a glass coverslip. The surface of the observation well is coated with a lipid bilayer to prevent DNA adhesion to the surface. DNA-binding elements are added and the resulting DNA structure is observed using fluorescence microscopy.

3.2. RESULTS

The workflow to obtain and characterize deproteinated megabasepair DNA consisted of several experimental steps, which are discussed in the following sections. First, we ensured and verified that the *E. coli* bacteria contained a single 4.6 Mbp chromosome by cell-cycle arrest. Then chromosomes were extracted from the cells in one of two routes, either directly in solution or *via* embedding them in an agarose gel plug. Lastly, the isolated chromosomes were deproteinated using a protease enzyme. Mass spectrometry was used to confirm the level of deproteination, followed by microscopy imaging and quantitative analysis of the total fluorescence intensity per object and the radius of gyration (R_g). This was done in order to verify if the chromosomes remained intact throughout the protocol, as well as to assess the effect of deproteination of the size of the DNA objects. Finally, as a proof of concept, three examples of possible experiments are shown.

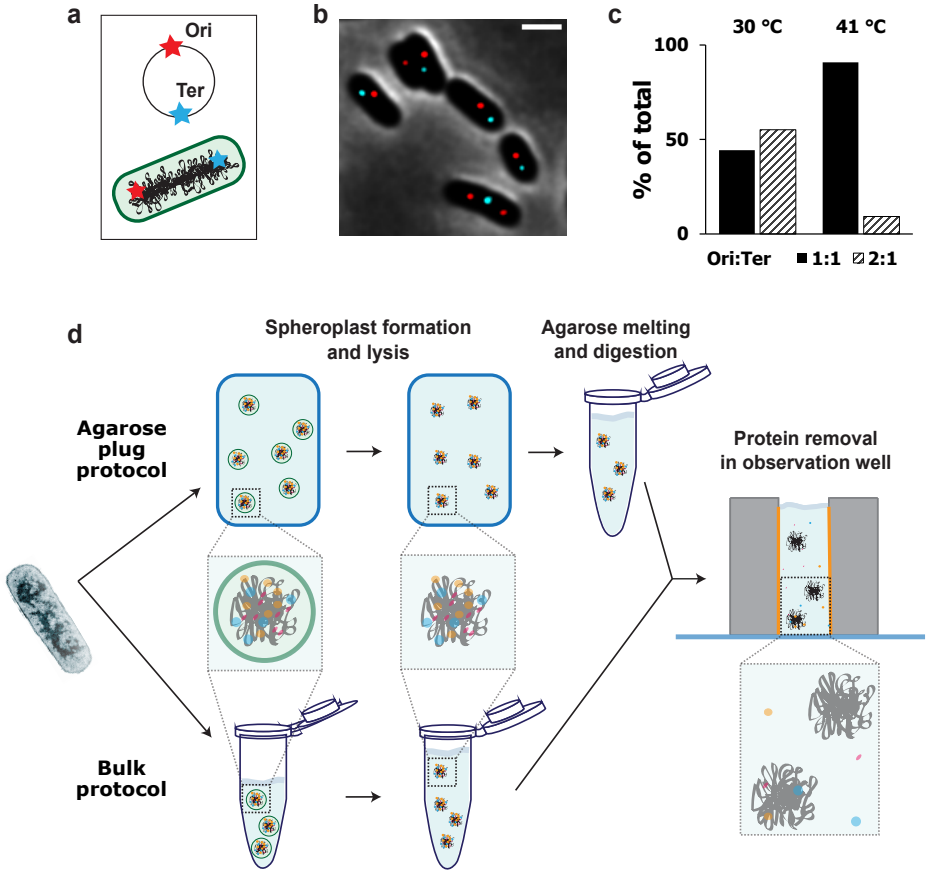

Figure 3.2: **Workflow of the protocol.** **(a)** The *E. coli* chromosome is circular and contains FROS arrays near the Origin of replication (Ori) and Terminus of replication (Ter). **(b)** Deconvolved image of *E. coli* cells with the Ori and Ter location labeled in red and cyan, respectively. Scale bar 2 μm. **(c)** Origin to Terminus of replication (Ori:Ter) ratio in control and temperature-treated *E. coli* cells (N = 185 and 178, respectively). **(d)** Agarose plug and bulk protocol to prepare deproteinated megabasepair DNA. Starting from *E. coli* cells, the cell wall is digested and the resulting spheroplasts are either embedded and lysed inside an agarose plug or directly lysed in a solution. After lysis in the agarose plugs, the agarose matrix is digested. At this stage, the chromosomes in both protocols are suspended in a solution and transferred to an observation well for protein removal and study of the deproteinated chromosomes.

3.2.1. EXTRACTING A SINGLE CHROMOSOME FROM *E. coli*

We prepared *E. coli* cells that contain only a single chromosome. In the exponential growth phase of bacteria, chromosomes are permanently replicating and typically exhibiting multiple replication forks on the DNA. For the purpose of controlled *in vitro* experiments this is undesirable for two reasons: first, halfway replicated DNA and multiple replication forks make the exact amount of DNA per cell unknown, and second,

DNA near replication forks is prone to damage and breaking.[35] As our aim is to extract DNA of a well-defined size, it is needed to obtain conditions that yield a known number of chromosomes per cell, ideally only a single chromosome per cell.

For this purpose, we used minimal media to avoid the occurrence of nested replication forks[36] as well as a temperature-sensitive *E. coli* strain where replication initiation was arrested by culturing the cells at an elevated temperature.[37,38] We grew cells for 2 hours (*i.e.*, for a time period longer than the doubling time in minimal media) at 41 °C and subsequently determined the number of chromosomes per cell by fluorescence imaging. The *E. coli* cells were engineered to contain Fluorescent Repressor Activator System (FROS) arrays near the Origin (Ori) and Terminus (Ter) locations (Figure 3.2a). At the start of the DNA replication process, the Ori is duplicated upon which the remainder of the chromosome follows, while the Ter is only duplicated at the end. This means that cells with a partly replicated chromosome will contain two Ori spots and a single Ter spot, whereas cells containing a single chromosome will only show one Ori and Ter. By counting the Ori and Ter fluorescence spots per cell, we confirmed that 90% of cells contained a single chromosome (Figure 3.2b and 3.2c, Ori:Ter ratio 1:1), while 10% of cells were still in the process of DNA replication (Ori:Ter ratio 2:1). If one were to extract the DNA from these cells, one would therefore expect a size distribution in which 90% of the objects are 4.6 Mbp, whereas the remaining 10% would contain DNA at an amount of between 4.6 and 9.2 Mbp, depending on how far genome replication in the cell had proceeded at the time of DNA extraction. In control experiment with growth at 30 °C instead of replication arrest, 55% of cells were in a state of active DNA replication whereas 45% contained a single chromosome (Figure 3.2c).

In order to extract the chromosomes from *E. coli* cells, the peptidoglycan cell wall was degraded using lysozyme enzyme, resulting in spheroplasts which are wall-less rounded *E. coli* cells that merely are contained in their plasma membranes. To release the cellular contents including the DNA, the spheroplasts were submerged in a low-osmolarity buffer, which forces water to enter the spheroplasts, thereby rupturing them. This so-called lysis by osmotic shock was achieved on spheroplasts that were prepared with one of two methods (Figure 3.2d): *i)* direct lysis of the cytosolic content of the spheroplasts into solution, based on a protocol developed in the Woldringh lab[30,39] (hereafter called 'bulk protocol'), or *ii)* embedding of spheroplasts inside agarose gel plugs where they were subsequently lysed, following a protocol from the Glass lab[32] (hereafter called 'agarose plug protocol'). Embedding of the spheroplasts inside the agarose plug resulted in intact spheroplasts that did not get lysed prematurely (figure S3.1). Bulk isolation yielded DNA that could be used on the same day, while the agarose-plug protocol produced samples that could be stored for a period of up to weeks after isolation. Depending on the application, the agarose plug protocol may also present advantages regarding the handing of the DNA material, such as a reduced shearing in transferring between experimental steps.

3.2.2. VIRTUALLY ALL PROTEINS CAN BE REMOVED FROM EXTRACTED CHROMOSOMES

DNA in cells is compacted by confinement, crowding, and binding of DNA-associated proteins. After cell lysis, the boundary conditions of confinement and crowding no longer apply, but DNA-binding proteins can in principle remain attached to the DNA. To digest such DNA-binding proteins in the sample, we incubated the bulk and plug protocol samples with a thermolabile Proteinase K enzyme, which is a broad range serine protease that cleaves peptide bonds at the carboxylic sides at a variety of positions (*i.e.*, after aliphatic, aromatic, and hydrophobic amino acids). We observed increased DNA fragmentation after digesting and melting agarose plugs that had undergone proteinase treatment. Contrary to previous work,[32] we therefore opted for treating the agarose sample in liquid, instead of in the gel state. While the bulk protocol sample already was liquid, agarose plugs had to be first digested using beta-agarase enzyme that breaks down the polymers forming the agarose gel. After the 15 min deproteination treatment and subsequent enzyme heat-inactivation (to prevent protein digestion in downstream experiments), we quantified the resulting degree of protein removal by mass spectrometry (MS).

	Bulk Protocol	**Agarose Protocol**
DNA-binding proteins (%)	0	3.9 ± 1.4
Non-DNA-binding proteins (%)	1.9 ± 0.3	7.0 ± 2.5

Table 3.1: **Overall protein removal efficiency as measured by mass spectrometry.** Overall percentage of proteins remaining after the protein removal treatment for bulk protocol and agarose protocols.

Two categories of proteins were distinguished in the MS experiments, namely DNA-binding proteins and non-DNA-binding proteins. Obviously, the removal of the DNA-binding proteins is most critical for obtaining deproteinated DNA for GenBox experiments. To aid the quantification, we compiled a list of the 38 most abundant DNA-binding proteins as well as DNA-binding protein sub-units (Table S3.1), based on the protein's description in the UniProt database as DNA-binding or DNA processing. For the bulk protocol (Table 3.1 and 3.2), we found that all DNA-binding proteins were removed (100%, at the MS resolution). For the agarose plug protocol (Table 3.1 and 3.3), the vast majority of the DNA-binding proteins, 97%, was removed. These percentages refer to protein abundances relative to control samples that underwent exactly the same treatment steps, but to which no Proteinase K was added. For the agarose plug protocol (Table 3.3), the major remaining DNA-binding proteins were IHF-A (14.8% remaining) and various RNA polymerase sub-units (rpoA/B/C, up to 4.5% remaining). The non-DNA-binding proteins were removed to the degree of 98.1% and 93.0% for the bulk and agarose plug protocol, respectively. More specifically, several ribosomal proteins were still present at large percentages (>40%) in the agarose plug sample.

Protein	Function	Percentage (%) remaining
Non-DNA-binding:		
thrS	Threonine–tRNA ligase	56 ± 22
trxA	Thioredoxin 1	7.0 ± 2.5

Table 3.2: **Protein removal efficiency in bulk protocol as measured by mass spectrometry.** Individual remaining proteins in the bulk protocol. Only those non-DNA-binding proteins with more than 40% remaining are included in the table. Errors are standard deviation from the mean obtained from three independent experiments per condition ('before' and 'after'). See also Table S3.1.

Protein	Function	Percentage (%) remaining
DNA-binding:		
ihfA	Integration host factor subunit alpha	15 ± 11
rpoC	RNA polymerase subunit beta'	4.5 ± 1.5
rpoA	RNA polymerase subunit alpha	4.2 ± 3.2
rpoB	RNA polymerase subunit beta	0.9 ± 0.4
Non-DNA-binding:		
dppB	Dipeptide transport system permease protein	>100
rpmG	50S ribosomal protein L33	>100
lhgD	L-2-hydroxyglutarate dehy-drogenase	>100
frsA	Esterase FrsA	>100
rpmB	50S ribosomal protein L28	80 ± 61
cydA	Cytochrome bd-I ubiquinol oxidase subunit 1	60 ± 15
uraA	Uracil permease	50 ± 50
mlaB	Intermembrane phospholipid transport system binding protein	50 ± 46
rplU	50S ribosomal protein L21	50 ± 27
rplJ	50S ribosomal protein L10	45 ± 8
yraR	Putative NAD(P)-binding protein	43 ± 42
cyoB	Cytochrome bo(3) ubiquinol oxidase subunit 1	43 ± 15

Table 3.3: **Protein removal efficiency in agarose plug protocol as measured by mass spectrometry.** Individual remaining proteins in the agarose plug protocol. All remaining DNA-binding protein are included. while for non-DNA-binding proteins only those with more than 40% remaining are included in the table. The agarose plug protocol contained a few lower abundant proteins (dppB, rpmG, IhgD, frsA) for which higher relative abundancies were estimated (denoted with >100%) due to low level of protein removal. Errors are standard deviation from the mean obtained from three independent experiments per condition ('before' and 'after'). See also Table S3.1.

3.2.3. EXTRACTED CHROMOSOMES REMAIN OF MEGABASEPAIR LENGTH AND EXPAND IN SIZE AFTER PROTEIN REMOVAL

We imaged DNA resulting from the bulk and agarose plug protocols before and after protein removal by fluorescence imaging on a spinning disc confocal microscope using the DNA-intercalating dye Sytox-Orange (Figure 3.3c/d and Figure S3.2). From a first visual inspection we observed that, before protein removal, the DNA objects contain a dense/bright core with a lower density 'cloud' surrounding it (Figure 3.3c-purple, Figure 3.3d-orange/purple, and Figure S3.2a/c/d). After protein removal, the objects seemed to be larger and more spread out (Figure 3.3c/d-green, and Figure S3.2b/e). In order to make more quantitative statements, we developed a semi-automated analysis script in Python (see STAR Methods for a detailed description), with which we identified individual DNA objects in the images, segmented them from the background, and quantified their radius of gyration R_g (a measure of the spatial extent of a polymer) as well as the sum of the fluorescence intensity.

In our image analysis, the positions of DNA-objects were automatically determined from three-dimensional *z*-stacks followed by a manual curation step (Figure 3.3a-object detection). Objects were then segmented in cube-shaped crops centered at each object's center of mass. The DNA objects were further segmented from background within these cubes based on a globally (within the cube) determined threshold,[40] yielding a 3-dimensional foreground mask containing only the DNA object, and a minimal amount of background (Figure 3.3a-segmentation and Figure S3.3b). Masks determined on the individual crops were registered within the full field-of-view volume resulting in a labeled image. Individual masks were additionally checked in a curation step and manually adjusted if upon visual inspection they did not contain single objects or did not mask objects in their entirety. Sum intensity was calculated as the total sum of all pixel intensities within a foreground mask and the radius of gyration was calculated by squaring the sum of all foreground pixels' intensity-weighted distances from the object's center of mass (Figure 3.3b).[41]

In order to monitor the integrity of the extracted chromosomes at various steps of the protocol, we measured the total per-object fluorescence intensity, *i.e.*, the sum of the intensities across all layers of the *z*-stack. While the sum intensity of a DNA object is expected to be set by the number of DNA basepairs, the measured distributions appeared to be fairly broad. In order to best compare the distributions before and after protein removal, we scaled the sum intensity values of each distribution with the mean value. We assume that the points in the 'before'-distributions (before protein removal) in Figure 3.3e and 3.3g represented those of intact chromosomes. This appears to be is a reasonable assumption since we observed similarly broad distributions of the sum intensity for lambda (λ)-DNA molecules (Figure S3.5).

To estimate the fraction of chromosomes that got fragmented in the process, we counted

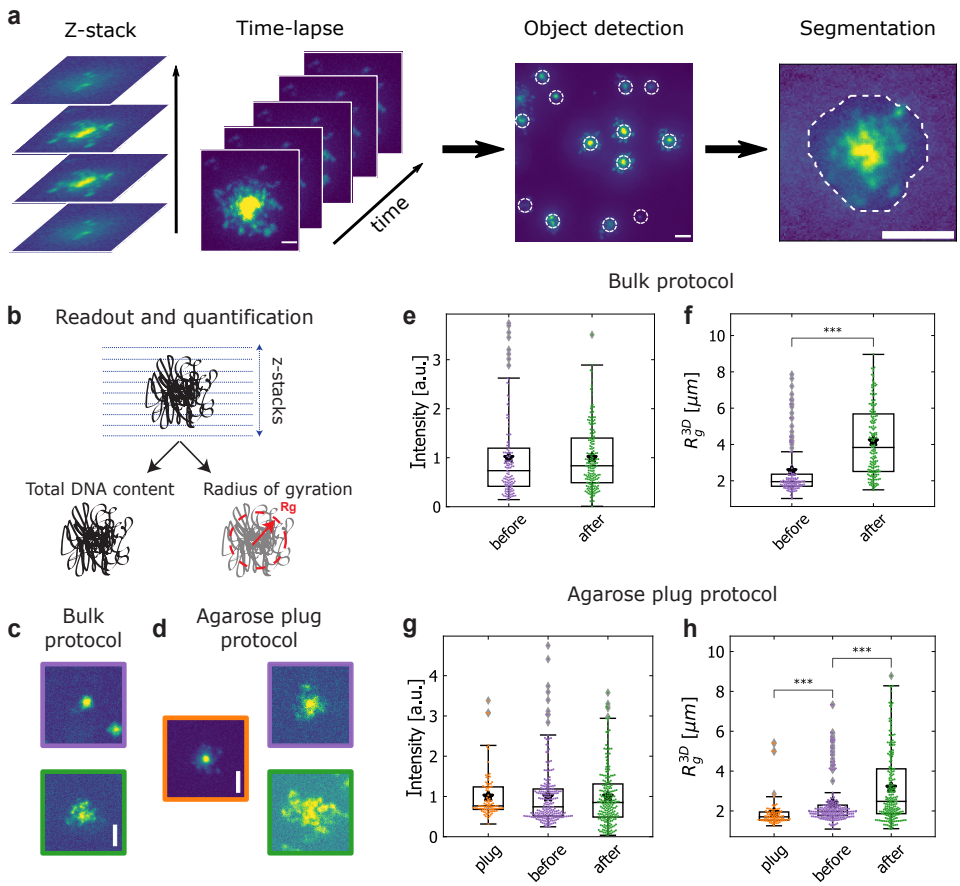

Figure 3.3: **Characterization of isolated chromosomes before and after protein removal.** **(a)** Image analysis workflow for a GenBox experiment. In each image, objects are detected and segmented from the background. **(b)** Within the segmentation boundary of each DNA object, the R_g and the total fluorescence intensity are calculated. **(c)** Images of typical DNA objects before (violet) and after (green) protein removal. **(d)** Images of typical DNA objects in each condition of the agarose protocol: in plug (orange), before (violet) and after (green) protein removal. **(e)** Total fluorescence intensity per DNA object before and after protein removal for the bulk protocol. **(f)** R_g distribution before and after protein removal for the bulk protocol ($p = 2.5e^{-15}$). **(g)** Total fluorescence intensity per DNA object before (in the plug and after plug melting) and after protein removal for the agarose plug protocol. **(h)** R_g distribution in the plug (orange), before protein removal but plug melting (purple) and after protein removal (green) for the agarose plug protocol ($p = 2.6e^{-5}$, $p = 5.8e^{-8}$ with independent two-sample t-test). Boxplots show the median and 25^{th}-75^{th} percentiles, thick star denotes mean. Scale bars are 5 μm. Intensity values in each distribution in panel e and g are scaled to the mean of the respective sum intensity distribution. Sample sizes in panels e and f are N=125 and 181 for before and after. Sample sizes in panels g and h are N=90, 223, 222 for plug, before, and after, respectively.

the objects in the distributions after protein removal that had a lower sum intensity value than a threshold of 1.5 times below the 25^{th} percentile of the data. For the bulk protocol, this fraction was 4 of 181 objects, while for the agarose plug protocol it was 24 of

222 objects. In other words, only a low percentage of fragmented objects of 2% and 11% was estimated for bulk and agarose plug protocol, respectively. Another indication that our observed DNA objects remain well contained in the megabasepair size range comes from comparing their sum intensities with those of λ-DNA molecules (Table S3.2). We found that the mean of the 'after' sum intensity distribution is a factor 50 (bulk protocol) or 64 (agarose plug protocol) larger than the mean of the sum intensity distribution of the 48.5 kbp long lambda-DNA molecules. Assuming that the sum intensity scales linearly with the number of basepairs, which was demonstrated previously for the dye used here in flow cytometry experiments,[42] this indicates that the DNA objects after protein removal have an average length of 2.4 Mbp (bulk protocol) and 3.1 Mbp (agarose plug protocol). However, these numbers are lower limits and the molecules are likely larger, because, following the same calculation, even the in-plug 4.6 Mbp chromosomes, which clearly are not fragmented, would be estimated to be 3.5 Mbp long.

The effect of deproteination of the extracted chromosomes is also evident from an expansion in the size of the DNA objects, which can be characterized by measuring its radius of gyration. The mean R_g in the bulk protocol increased from 2.55 ± 0.14 μm to 4.24 ± 0.14 μm (mean ± S.E.M) before and after protein removal respectively (Fig. 3.3f, Fig. S3.4a), and from 2.38 ± 0.08 μm to 3.18 ± 0.12 μm for the agarose plug protocol (Figure 3.3h and S3.4b). These results indicate that the removal of the proteins had a clear effect on the mean R_g, namely a 35% to 65% increase of the size for the agarose plug and bulk protocols (p-values 5.8e^{-8} and 2.5e^{-15}), respectively. The measured radii of gyration exhibited a rather broad distribution (Figure 3.3f/h). Notably, the measured R_g values are extracted from momentarily measured snapshot images of the DNA objects, which yielded a broader distribution than the single value for the theoretical radius of gyration of a polymer which is a steady-state property.[43]

3.2.4. FIRST PROOF-OF-PRINCIPLE GENBOX EXPERIMENTS

In order to demonstrate the potential of the GenBox approach, some first example experiments were performed. First, purified protein LacI was added to chromosomes that were deproteinated with the agarose plug protocol. These fluorescently labelled proteins bind sequence-specifically to FROS arrays that were inserted near the Ori position of the chromosomes. This yielded a well-visible fluorescent spot on the isolated chromosome (Figure 3.4a-*ii*). Using a custom tracking script, the spot's locations were tracked and the mean square displacement (MSD) was computed (Figure 3.4a-*iii*). In line with the literature of local motion of chromosomal loci,[45,46] the data for this example indicate that the DNA locus moved in a sub-diffusive manner, as the MSD curve tended to plateau towards longer lag times.

For a second example, the DNA-binding protein Fis was added to deproteinated chromosomes. Figure 3.4b-*ii* shows an example of a typical DNA object before and after addition of 550 nM Fis. A significant compaction of the DNA upon Fis addition is clear. The distributions of R_g can be used to quantify the level of DNA compaction at increasing levels of added Fis (Figure 3.4b-*iii*). As the Fis levels increased from 0 nM to 550

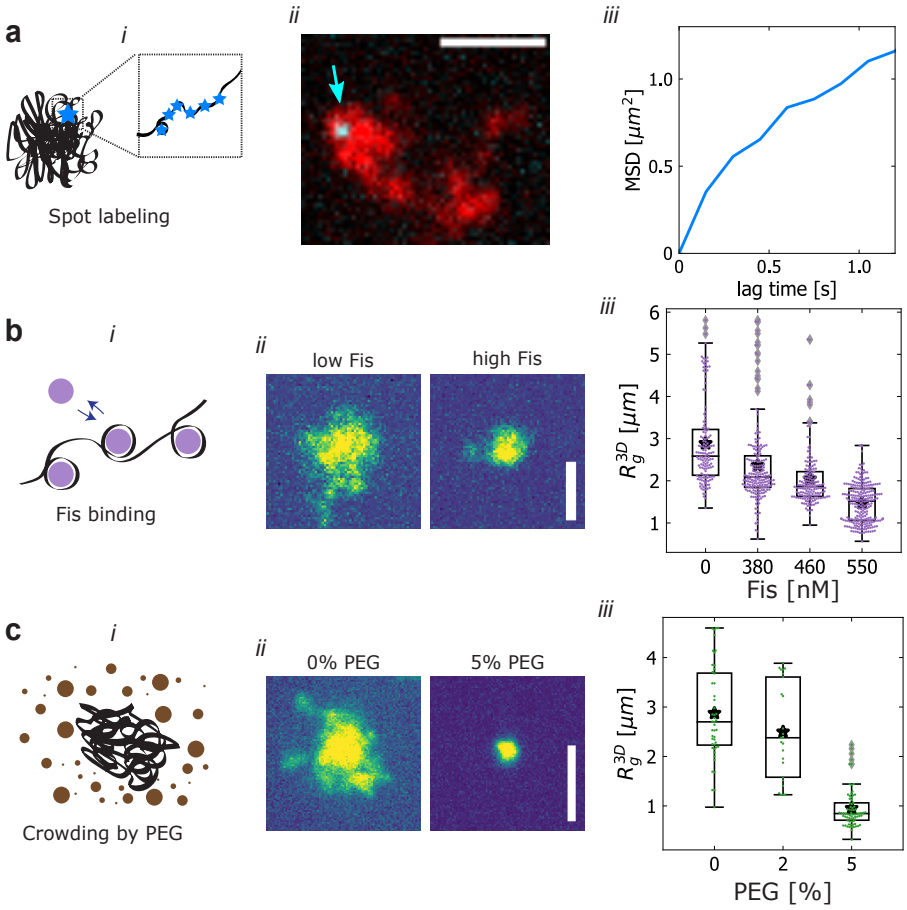

Figure 3.4: **Proof-of-concept GenBox experiments.** **(a)** Example of a fluorescent spot located near the Ori (cyan). Location on the isolated chromosome (red) is tracked, yielding the MSD *vs.* time (right).[44] **(b)** Fis protein is added at increasing concentrations of 380 nM and 550 nM, and the resulting compaction is observed in the shifting and narrowing distribution of R_g (right). **(c)** PEG crowding agent is added at increasing concentrations of 2% and 5% and the resulting compaction is observed from the shifting and narrowing distribution of R_g. Boxplots show the median and 25$^{\text{th}}$-75$^{\text{th}}$ percentiles, star denotes mean. Sample sizes are N=141, 201 and 242 in panel b and N=48, 25, 74 in panel c. All scale bars are 5 μm.

nM, the average R_g decreased gradually from 2.89 ± 0.08 μm to 1.47 ± 0.03 μm (mean ± S.E.M.), while the standard deviation of the distribution also decreased significantly from 1.00 μm to 0.45 μm. From recent single-molecule Atomic Force Microscopy (AFM) experiments[47] it was observed that Fis induces a strong global compaction of ~30% and also reduced the persistence length by ~20% (at a 1:40 protein:bp ratio). This compacting action was achieved by stabilization of loops and DNA crossovers. Our observation of a strong global DNA compaction of megabasepair DNA at a comparable protein:bp

ratio (1:10) are consistent with these AFM experiments.

For a final example, the crowding agent PEG was added at increasing concentrations to deproteinated chromosomes. A pronounced compaction was observed, when adding 5% PEG (Figure 3.4c-*ii*), consistent with previous reports.[48,49] The increase of PEG from 0% to 2% resulted in the mean R_g decreasing slightly from 2.87 ± 0.14 μm to 2.5 ± 0.2 μm, while the standard deviation remained steady at around 0.95 μm. However, at 5% PEG the mean and standard deviation of the R_g distribution dropped to 0.95 ± 0.05 μm and 0.39 μm, respectively (Figure 3.4c-*iii*).

3.3. DISCUSSION

In this paper, we present a methodology to prepare megabasepair deproteinated DNA, characterized the resulting DNA objects, and we provide first proof-of principle experiments to illustrate the utility of the method. The work expands on previous *in vitro* studies of large DNA molecules.[29,32–34,50,51] For example, Wegner *et al.*[30,49] and Cunha *et al.*[39,52] studied bacterial chromosomes directly after isolation from cells in an aqueous solution, while Pelletier *et al.*[48] used microfluidic devices to perform cell lysis on-chip in cell-sized channels for studying the compaction of DNA with crowding agents. A limitation of these interesting first studies was that the megabasepair DNA substrates still contained an unknown number of natively bound proteins. Our GenBox protocol builds upon these previous experiments by explicitly removing the proteins and characterizing the remaining protein content with mass spectrometry and quantitative fluorescence imaging.

We presented two variants to prepare the deproteinated DNA sample, namely the bulk protocol and the agarose plug protocol. From a practical point of view, the agarose plug protocol has some advantages compared to the bulk protocol. First, samples can be made in advance and stored until needed for further processing. Secondly, unlike the bulk protocol sample, the agarose plugs are compatible with protocols that necessitate washing steps. One the other hand, the main advantage of the bulk protocol is the lower number of experimental steps. Our mass spectrometry data (Table 3.1) showed that the deproteinated chromosomes of the bulk protocol contained fewer remaining DNA-binding proteins than those resulting from the agarose plug sample (0% vs 3%). Additionally, the bulk protocol results in a lower amount of fragmentation compared to the agarose plug protocol (as 98% vs. 89% of DNA objects classified as intact after protein removal). Since long DNA is easily sheared, it is important to limit the number of pipetting steps of DNA in solution. For both the bulk and agarose plug protocol, there is one major pipetting step involving the long DNA, namely the transfer to the observation well before the protein removal treatment. Conducting the chromosome extraction and protein removal inside a microfluidic chip could possibly eliminate this single pipetting step to further increase the number of intact DNA objects.

Modelling would be welcome to describe the observed radius of gyration of the deproteinated chromosomes. Polymer models connect the DNA contour length to a radius

of gyration R_g of the polymer blob that it forms in solution, but a broad spectrum of model variants that have been reported in literature yielded widely ranging values for R_g. Indeed, how the theoretical R_g scales with polymer length depends on multiple external parameters.[43] These include, but are not limited to experimental parameters such as the fluorescent dyes,[53] buffer salts[54,55] and divalent cations,[56–59] which set the solvent conditions and the resulting self-avoidance/attraction of the polymer, as well branches in the form of supercoils, the DNA topology of linear *vs.* circular polymers, *etc.* Variation of these factors can yield very different predicted values for R_g ranging from 1 to 6 μm for 4.6 Mbp DNA, as illustrated in Table S3.3. The values of R_g that we observed in our experiments fall within this range. Notably, bacterial chromosomes may be natively supercoiled.[60] While the removal of supercoil-stabilizing proteins as well as potential local nicks in the DNA will likely reduce the level of supercoiling significantly, some degree of supercoiling may remain in the DNA objects that result from the protocol.

We hope that the results presented in this paper open a way to start GenBox experiments that may subsequently provide a valuable bottom-up approach to the field of chromosome organization. Promising avenues may include encapsulation of megabasepair DNA inside droplets or liposomes to study the effects of spatial confinement, addition of loop extruding proteins such as cohesin or condensin to elucidate the effect of loop formation on the structure of large DNA substrates, and experiments with phase-separating DNA-binding proteins to observe the effects of polymer-mediated phase separation at long length scales.

3.4. LIMITATIONS OF STUDY

While we established and characterized two related strategies to isolate megabasepair deproteinated DNA, the approach inevitably also has limitations. First, while we reduced the number of pipetting steps in the protocols to a single one, this final slow pipetting step may still lead to unwanted DNA damage due to mechanical shearing. Indeed, the isolated megabasepair DNA blobs may contain single- and double- stranded DNA breaks, which also may result in an unknown residual level of supercoiling. Second, due to liquid motion, it proved challenging to track the objects through time in the 3D time-resolved imaging of isolated DNA objects in bulk volume. We were therefore unable to link initial state to a state at some later time during the experiment on object-per-object basis. This disadvantage may be solved by using microfabricated chambers.

Regarding the presence of residual ribosomal subunits after deproteination (Table 3.3), we can make the following comment. Although previous studies with chromosomes isolated by osmotic shock (in absence of protein removal) did not observe any difference in chromosome conformations in the presence or absence of RNase,[30] we opted to perform the RNAse treatment, for which we doubled the supplier's treatment time and used a 100-fold higher amount than the lowest recommended concentration. We suspect that any remaining ribosomal proteins may aggregate and become non-specifically trapped in the agarose matrix, later eluting with fragments of digested agarose.

One might consider the addition of DNase in the protocol for MS sample preparation, in order to ensure that tightly bound proteins would also reach the mass spectrometer. We did not adopt this approach for multiple reasons. Firstly, every enzymatic step reduces the sensitivity of the mass spectrometry quantification by the introduction of additional protein species. Secondly, DNase I treatment has been reported to introduce bias in protein-abundance patterns, and is therefore advised against.[61] Finally, under the used conditions (buffers, incubation time, dilution of crowding) it is unlikely that a protein species would remain bound to DNA so strongly that virtually none of the molecules would dissociate into solution.

3.5. METHODS

3.5.1. RESOURCE AVAILABILITY

DATA AND CODE AVAILABILITY

• Data reported in this paper will be shared by the lead contact upon reasonable request. • The Python code used throughout the analysis has been deposited on Zenodo (DOI: 10.5281/zenodo.6677094). • Any additional information required to reanalyze the data reported in this paper is available from the lead contact upon request.

3.5.2. METHODS DETAILS

PREPARATION OF SPHEROPLASTS AND IMAGING OF CELLS AND ORI/TER RATIO

E. coli bacterial cells (HupA-mYPet frt, Ori1::lacOx240 frt, ter3::tetOx240 gmR, ΔgalK::tetR-mCerulean frt, ΔleuB::lacI-mCherry frt, DnaC::mdoB::kanR frt)[62] were incubated from glycerol stock in M9 minimal media (1x M9 minimal salts, 0.01% v/v protein hydrolysate amicase, 0.8% glycerol, 0.1 mM $CaCl_2$, 2 mM $MgSO_4$) supplemented with 50 μg/mL Kanamycin antibiotic (K1876, Sigma-Aldrich) in a shaking incubator at 30 °C and 300 rpm and allowed to reach OD_{600} of 0.1 to 0.15. The cells were then grown for 2 to 2.5 hours at 41 °C shaking at 900 rpm in order to arrest replication initiation.

In order to determine the Ori/Ter ratio, 1.25 μL cells were deposited on a cover slip (15707592, Thermo Fischer) and covered with an agarose pad. The cells were imaged with a Nikon Ti2-E microscope with a 100X CFI Plan Apo Lambda Oil objective with an NA of 1.45 and SpectraX LED (Lumencor) illumination system using phase contrast, cyan (CFP filter cube $\lambda_{ex}/\lambda_{bs}/\lambda_{em}$ = 426–446/455/460–500 nm), yellow (triple bandpass filter λ_{em} = 465/25–545/30–630/60 nm) and red (the same triple bandpass filter). Spots corresponding to Ori and Ter were identified on the red and cyan channels and counted either manually or with an automated routine, producing the same results.

Next, appropriate volume of cell culture was spun down at 10000 g for 2.5 min, in order to obtain a pellet at OD_{eq} = 1 (approx. 8 x 10^8 cells). The pellet was resuspended in

475 μL cold (4 °C) sucrose buffer (0.58 M sucrose, 10 mM Sodium Phosphate pH 7.2, 10 mM NaCl, 100 mM NaCl). 25 μL lysozyme (L6876 Sigma-Aldrich, 1 mg/mL in ultrapure water) was immediately added and gently mixed into the cell/sucrose buffer suspension, followed by either *i)* 15 min incubation at room temperature (bulk protocol) or *ii)* a 10 min incubation at room temperature and a 5 min incubation at 42 °C in a heat block (agarose plug protocol). The lysozyme digests the cell wall, resulting in spheroplasts.

PREPARATION OF ISOLATED CHROMOSOMES (BULK PROTOCOL)

Spheroplasts were prepared as described above. Cell lysis and nucleoid release was achieved by pipetting 10 μL of spheroplasts into 1 mL of lysis buffer (20 mM Tris-HCl pH 8) with a cut pipette tip, after which the tube was once gently inverted for mixing. Immediately thereafter, buffer composition was adjusted to match the one of agarose plug protocol (50 mM Tris-HCl pH 8, 50 mM NaCl, 1 mM EDTA pH 8.0 and 5% glycerol). After this stage, we continued to the preparation of the observation well.

PREPARATION OF ISOLATED CHROMOSOMES (AGAROSE PLUG PROTOCOL)

500 μL warmed (42 °C) spheroplast/sucrose buffer suspension was added to 500 μL warm (42 °C) agarose solution (low melting point agarose, V2831 Promega, 2% w/v in sucrose buffer) using a cut pipette tip. In the following steps, the Eppendorf tubes were kept at 42 °C to prevent gelation of the agarose solution. The spheroplast/agarose mixture was gently mixed using a cut pipette tip, and casted in volumes of 100 μL into a plug mold (Bio-Rad laboratories, Veenendaal, The Netherlands). In order to produce a larger number of agarose plugs, it proved most optimal to perform the protocol with multiple Eppendorf tubes in parallel, rather than increasing the number of cells and volumes of sucrose buffer and agarose solution used per Eppendorf tube. To solidify the agarose plugs, the plug mold was stored at 4 °C for 1 h.

The solidified agarose plugs containing spheroplasts were removed from the plug mold and added to 25 mL per plug lysis buffer (10 mM Sodium Phosphate pH 7.2, 10 mM EDTA pH 8.0, 100 μg/mL RNase-A), thereby lysing the cells and thus merely trapping the nucleoids from the spheroplasts in the agarose gel matrix. The plugs were incubated tumbling in the lysis buffer for 1 h. Subsequently, the plugs were removed from the lysis buffer and each plug was stored in 2 mL TE wash buffer (20 mM Tris-HCl pH 8, 50 mM EDTA pH 8.0) at 4 °C until further use.

In order to transfer agarose plugs from one container to another, a sheet of aluminum foil was put over the top of a glass beaker. Using a 200 μL pipette tip holes were punched into the aluminum foil and the foil was gently pressed down into a concave shape to prevent liquid spilling over the edge. The container containing the plugs was emptied through the strainer into the beaker, leaving the agarose plugs behind on the strainer. Using flat-headed tweezers the agarose plugs were transferred to the new container. To prevent cross-contamination, the tweezers were washed after each handing step with 70% ethanol and dried using a pressurized air gun.

For releasing the purified chromosomes from the agarose plugs for experiments, agarose plugs were incubated for 1 hour in buffer A (50 mM Tris-HC pH 8, 50 mM NaCl, 1 mM EDTA pH 8.0, 5% glycerol) and then transferred to 150 μL of buffer A preheated to 71 °C. The plug was then melted at 71 °C for 15 minutes before equilibrating at 42 °C. The agarose was digested by 1 hour incubation at 42 °C with 2 units of beta-agarase (M0392, New England Biolabs). After this stage, we continued to the preparation of the observation well.

IMAGING OF SPHEROPLASTS AND CHROMOSOMES INSIDE THE AGAROSE PLUG

A plug containing spheroplasts was deposited on a KOH-cleaned cover slip. Spheroplasts were imaged with a Nikon Ti2-E microscope with a 100X CFI Plan Apo Lambda Oil objective with an NA of 1.45 and SpectraX LED (Lumencor) illumination system using the channels phase contrast, cyan (CFP filter cube $\lambda_{ex}/\lambda_{bs}/\lambda_{em}$ = 426–446/455/460–500 nm), yellow (triple bandpass filter λ_{em} = 465/25–545/30–630/60 nm) and red (the same triple bandpass filter). The imaging protocol was composed of a single time-point, using a 2 μm z-stack with 200 nm *z*-slices.

For imaging chromosomes after lysing the spheroplasts, a nucleoid-containing plug was incubated in 2 mL buffer A (50 mM Tris-HC pH 8, 50 mM NaCl, 1 mM EDTA pH 8.0, 5% glycerol) at 4 °C for 1 h. The plug was transferred to 2 mL imaging buffer (50 mM Tris-HC pH 8, 50 mM NaCl, 1 mM EDTA pH 8.0, 5% glycerol, 3.5 mM $MgCl_2$, 1 mM DTT, 500 nM Sytox Orange) and incubated for 15 min. Then the plug was deposited on a KOH-cleaned cover slip and 30 μL imaging buffer was added onto the plug to prevent drying. The plug was imaged using an Andor Spinning Disk Confocal microscope with a 100X oil immersion objective, 20% 561 laser, filters, 250x gain, and 10 ms exposure. The imaging protocol resulted in 30 μm *z*-stacks with 250 nm *z*-slices and was repeated at 15 distinct *xy* positions.

TREATMENT WITH PROTEINASE K FOR PROTEIN REMOVAL

Thermolabile Proteinase K (P8111S, New England Biolabs) was added to isolated chromosomes (0.01 unit per 1 μL of nucleoid suspension) in buffer containing 2.5 mM $MgCl_2$ and 50 mM NaCl. The samples were then incubated for 15 minutes at 37 °C for treatment and for 10 minutes at 56 °C for Proteinase K inactivation. The samples were equilibrated to RT for at least 30 minutes before imaging or and further experiments.

MASS SPECTROMETRY

Bulk and agarose plug samples were treated with Proteinase K as described above. Each sample contained nucleoids from an amount of cells corresponding to OD 5.0 (ca. $5x10^9$ cells in 100 μL). With two different DNA isolation approaches (bulk and agarose plug) and two conditions (control and Proteinase K), four triplicate samples were analyzed (twelve samples in total) by mass spectrometry. The control sample underwent exactly the same steps as the treated sample, but equal volume of 50 % glycerol (corresponding

to Proteinase K storage buffer concentration) was used instead of Proteinase K enzyme. 200 mM ammonium bicarbonate buffer (ABC) was prepared by dissolving ammonium bicarbonate powder (A6141, Sigma-Aldrich) in LC-MS grade quality water. 10 mM DTT (43815, Sigma-Aldrich) and iodoacetamide (IAA) (I1149, Sigma-Aldrich) solutions were made fresh by dissolving stock powders in 200 mM ABC. Next, 25 μL of 200 mM ABC buffer was added to each sample to adjust pH, immediately followed by addition of 30 μL of 10 mM DTT and 1 hour incubation at 37 °C and 300 rpm. Next, 30 µL of 20 mM IAA was added and samples were incubated in dark at room temperature for 30 min. Finally, 10 μL of 0.1 mg/mL trypsin (V5111, Promega) was added and samples were incubated overnight at 37 °C and 300 rpm.

On the following day, samples were purified by solid phase extraction (SPE). SPE cartridges (Oasis HLB 96-well μElution plate, Waters, Milford, USA) were washed with 700 μL of 100% methanol and equilibrated with 2x500 μL LC-MS grade water. Next, 200 μL of each sample was loaded to separate SPE cartridge wells and wells were washed sequentially with 700 μL 0.1% formic acid, 500 μL of 200 mM ABC buffer and 700 μL of 5% methanol. Samples were then eluted with 200 μL 2% formic acid in 80% methanol and 200 μL 80% 10 mM ABC in methanol. Finally, each sample was collected to separate low-binding 1.5 μL tubes and speedvac dried for 1-2 hours at 55 °C. Samples were stored frozen at -20 °C until further analysis. Desalted peptides were reconstituted in 15 μL of 3% acetonitrile/0.01% trifluoroacetic acid prior to MS-analysis.

Per sample, 3 μL of protein digest was analysed using a one-dimensional shotgun proteomics approach.[63,64] Briefly, samples were analysed using a nano-liquid-chromatography system consisting of an EASY nano LC 1200, equipped with an Acclaim PepMap RSLC RP C18 separation column (50 μm x 150 mm, 2 μm, Cat. No. 164568), and a QE plus Orbitrap mass spectrometer (Thermo Fisher Scientific, Germany). The flow rate was maintained at 350 nL·min^{-1} over a linear gradient from 5% to 25% solvent B over 90 min, then from 25% to 55% over 60 min, followed by back equilibration to starting conditions. Data were acquired from 5 to 175 min. Solvent A was water containing 0.1% FA, and solvent B consisted of 80% ACN in water and 0.1% FA. The Orbitrap was operated in data-dependent acquisition (DDA) mode acquiring peptide signals from 385–1250 m/z at 70,000 resolution in full MS mode with a maximum ion injection time (IT) of 75 ms and an automatic gain control (AGC) target of 3E6. The top 10 precursors were selected for MS/MS analysis and subjected to fragmentation using higher-energy collisional dissociation (HCD). MS/MS scans were acquired at 17,500 resolution with AGC target of 2E5 and IT of 100 ms, 1.0 m/z isolation width and normalized collision energy (NCE) of 28.

PREPARATION OF OBSERVATION WELLS

Cover slips (15707592, Thermo Fischer) were loaded onto a teflon slide holder. The coverslips were sonicated in a bath sonicator in a beaker containing ultrapure water for 5 min, followed by sonication in acetone for 20 min, a rinse with ultrapure water, sonication in KOH (1 M) for 15 min, a rinse with ultrapure water, and finally sonication in methanol for 15 min. Cleaned cover slips were stored in methanol at 4 °C.

To assemble the observation well, a PDMS block with a 4 mm punched (504651 World Precision Instruments) through hole was bonded on a cleaned coverslip. PDMS block was obtained from PDMS slab of ± 5 mm thickness which was casted from mixture of 10:1 = PDMS:curing agent (Sylgard 184 Dow Corning GmbH) and allowed to cure for 4 hours at 80 °C. The bonding was done immediately after exposing both surfaces, glass and PDMS, to oxygen plasma (2 minutes at 20 W) and the bond was allowed to cure for 10 minutes at 80 °C.

Immediately after the bonding, the inner surface of the observation well was treated to create a lipid bilayer to prevent sticking of DNA and proteins. To do so, DOPC liposomes were used. DOPC and PE-CF lipids from chloroform stocks (both Avanti Polar Lipids, Inc.) were combined in 999:1 mol-ratio DOPC:PE-CF in a glass vial for final lipid concentration of 4 mg/mL. Chloroform was evaporated by slowly turning the vial in a gentle nitrogen steam for 15 minutes or until dry. The vial was then placed in a desiccator for 1 hour to further dry its contents. The lipids were then resuspended in SUV buffer (25 mM Tris-HCl pH 7.5, 150 mM KCl, 5 mM $MgCl_2$) and vortexed until solution appears opaque and homogeneous to the eye. Any large lipid aggregates were broken up by 7 to 10 freeze-thaw cycles of repeated immersion into liquid nitrogen and water at 70-90 °C. The lipid suspension was loaded in a glass syringe (250 μL, Hamilton) and extruded through 30 nm polycarbonate membrane (610002, Avanti Polar Lipids, Inc.) fixed in mini-extruder (610020, Avanti Polar Lipids, Inc.) at 40 °C. Lipids were stored at -20 °C for up to several months. SUV suspension (99.9 mol% DOPC, 0.1 mol% PE:CF - both Avanti Polar Lipids, Inc.) was sonicated for 10 minutes at RT and pipetted into the well to cover the area to be treated. After 1 minute of incubation, the solution was diluted by adding 3x fold excess off SUV buffer (25 mM Tris-HCl pH 7.5, 150 mM KCl, 5 mM $MgCl_2$). Subsequently, the solution in the well was exchange at least 5-times, without de-wetting the surface of the glass, for imaging buffer (50 mM Tris-HC pH 8, 50 mM NaCl, 1 mM EDTA pH 8.0, 5% glycerol, 3.75 mM $MgCl_2$, 1.5 mM DTT, 750 nM Sytox Orange). As final step, a sample with nucleoids from either the bulk or plug protocol was added to the imaging buffer in ratio 1:2 (nucleoids to imaging buffer), after which the well was ready for imaging.

EXPERIMENTS WITH SPOT LABELING, FIS, AND PEG

For the experiments of figure 3.4, the protocol for imaging digested plugs was followed, but with some modifications for the imaging. Plugs with ProtK protein removal treatment were used. The imaging protocol was as follows: *i)* a 30 μm *z*-stack was taken with 250 nm *z*-slices, and this was repeated at 5 *xy* positions; *ii)* a 30 μm *z*-stack was taken with 1 μm *z*-slices at 5 *xy* positions, repeated 10 times; *iii)* the protein of interest was added to the observation well at a final concentration of 1.25 nM (LacI), 380 or 550 nM (Fis), 2 or 5% (PEG-8000, Sigma Aldrich); *iv)* a 30 μm *z*-stack was taken with 1 μm *z*-slices at 5 *xy* positions, repeated 50 times. Once the compaction process reached a steady state, the imaging step *i)* was repeated.

Fis protein was a kind gift of William Nasser, and was purified as described previously.[47] 8xHis-tagged LacI-SNAP fusions in pBAD plasmids were ordered from GenScript. BL21(DE3)-competent *E.coli* cells (New England Biolabs) were transformed with the

plasmids and plated with Ampicillin (Amp). Overnight colonies were inoculated in LB with Amp and incubated overnight at 37 °C and 150 rpm. Cells were diluted 1:100 into fresh media with Amp and grown at 37 °C at 150 rpm until OD_{600} of 0.5 - 0.6 after which 2 g/L arabinose was added to induce expression for 3-4 hours. Next, cells were harvested by centrifugation and resuspended in buffer A (50 mM Tris-HCl pH 7.5, 200 mM NaCl, 5% w/v glycerol). Lysis was performed with French Press and supernatant was recovered after centrifugation. His-tagged proteins were bound to beads in talon resin and column was then in turns washed with 50 mL of buffer A1 (buffer A + 10 mM imidazole), buffer A2 (buffer A + 0.01% Tween-20), and buffer A3 (buffer A + 0.5 M NaCl). Next, the sample was eluted with 15 mL buffer B (buffer A + 3C protease + 1 mM β-Mercaptoethanol) and diluted 10x in buffer C (50 mM Tris-HCl pH 8.0). Anion exchange chromatography was done with Mono Q-ion exchange column (Cytiva) equilibrated with buffer C and sample was eluted to buffer D (50 mM Tris-HCl pH 8.0 with 1 M NaCl). Next, size exclusion chromatography was done on Superdex S200 (Cytiva) column equilibrated with buffer A, collected and fractions were run on gel to check for purity. Finally, purified proteins were labelled with SNAP-Surface Alexa Fluor 647 tag (New England Biolabs) following manufacturer's instructions.

3.5.3. QUANTIFICATION AND STATISTICAL ANALYSIS

IMAGE PROCESSING AND ANALYSIS

We developed a custom analysis pipeline for quantifying DNA objects in fluorescent images obtained from GenBox experiments, written entirely in Python. The analysis proceeds in three main steps: *i)* identification of individual DNA objects, *ii)* segmentation of these objects from background, *iii)* quantification of relevant observables (*e.g.*, a calculation of the radius of gyration).

Positions of individual objects were determined automatically from three-dimensional stacks using *skimage* function *peak_local_max*.[65] Maxima were required to be at least twice as bright as globally determined threshold[40] (see next paragraph for description). If objects' maxima were closer than 30 pixels from each other, or from any image boundary, the objects were discarded from further analysis. Next, all locations were visually inspected with *napari*'s viewer[66] using Image and Points layers. Typically, none or few changes had to be made (*e.g.*, if one object was identified as two or vice-versa).

Objects were segmented from the background in crops corresponding to 25x25x25 μm^3 centered at each object's center of mass. First, the raw data in any crop was binarized based on a globally determined threshold.[40] Pixels' intensity values were sorted increasingly, and two lines were fitted to such curve *a)* a line fitted to the first half of the pixels in the image (estimate of background), and *b)* a line fitted to all pixels brighter than half of the maximum intensity (estimate of foreground). The intensity threshold value was then determined from the point on the sorted intensity curve which was closest to intersection of the two lines (figure S3.3a). Images before and after background subtraction were inspected and confirmed that the approach was able to discriminate background

and foreground well (figure S3.3b). The crops were then traversed plane-by-plane in *z*-direction, discarding small regions, dilating remaining region(s) and filling holes. The mask contours were smoothed in each plane with a Savitzky-Golay filter with a window size of quarter the contour length of the mask. Finally, only the most central 3D contiguous binary object was retained as foreground mask for each object.

Masks determined on individual crops were subsequently registered within full FOV volume (typically about 100x100x100 μm^3) producing a labeled image. If shared pixels resulted at masks overlap, these pixels were assigned to the mask which center of mass was the closest. Subsequently, the masks were inspected with *napari*'s viewer using Image and Label layers and manually adjusted if upon visual inspection they did not contain single objects or did not mask those in their entirety.

The quantification of the objects' properties was done within the volume of the foreground mask applied onto the raw data after subtracting globally determined threshold (as described earlier) from each crop. Sum intensity was calculated as the total sum of all pixel intensities within a foreground mask and the radius of gyration was calculated by squaring the sum of all foreground pixels' intensity-weighted distances from the object's center of mass. The resulting measurements were saved as structured JSON files, one per each FOV, and aggregated based on condition to produce R_g and intensity plots. The MSD in spot-labeling experiment was calculated using the *xy*-coordinates of fluorescent spots obtained with the ImageJ TrackMate plugin.[67,68]

MASS SPECTROMETRY ANALYSIS

Mass spectrometry data were analysed against the proteome database from *Escherichia coli* (UniProt, strain K12, Tax ID: 83333, November 2021, https://www.uniprot.org/), including Proteinase K from *Parengyodontium album* (UniProt ID: P06873) and Beta-agarase I from *Pseudoalteromonas atlantica* (UniProt ID: Q59078),[69] using PEAKS Studio X+ (Bioinformatics Solutions Inc., Waterloo, Canada),[70] allowing for 20 ppm parent ion and 0.02 m/z fragment ion mass error, 3 missed cleavages, carbamidomethylation as fixed and methionine oxidation and N/Q deamidation as variable modifications. Peptide spectrum matches were filtered for 1% false discovery rates (FDR) and identifications with ≥ 1 unique peptide matches. For the case that a protein in the sample was identified by only a single peptide in only one out of three runs, the protein identification was only considered if the same peptide sequence was also identified in unpurified control (within a retention time window of ± 2 min).

For determination of relative amounts of protein remaining after Proteinase K treatment, protein abundances were expressed as 'spectral counts' normalized by their molecular weight (*i.e.*, $\frac{\text{spectral counts}}{\text{molecular weight}}$x1000). Using the normalized spectral counts per protein in the three replicate experiments per condition ('before' and 'after'), the mean was calculated for each protein individually and for the aggregated DNA-binding and non-DNA-binding categories. Uncertainties were expressed as standard deviations from the means due to inter-sample variation. Relative amounts (for individual proteins and the aggregated categories) were defined as the ratio of the 'after' over the 'before' means, with

uncertainties calculated by propagating the errors through this ratio.

3.6. SUPPLEMENTARY INFORMATION

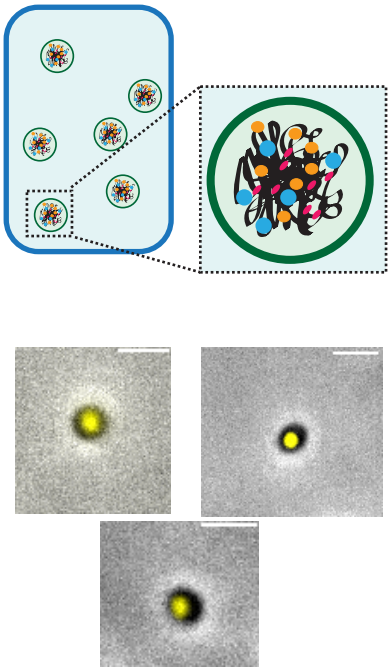

Figure S3.1: **Spheroplasts in plug. Related to figure 3.2.** Schematic (top) and microscopy images (bottom) of spheroplasts embedded inside an agarose plug. The yellow signal comes from fluorescently labeled HU-protein and thus serves as a DNA marker. The greyscale signal is phase contrast. Scale bars are 2 μm.

Protein	Function
rpoC	DNA-directed RNA polymerase subunit beta'
rpoB	DNA-directed RNA polymerase subunit beta
rpoA	DNA-directed RNA polymerase subunit alpha
gyrA	DNA gyrase subunit A
topA	DNA topoisomerase 1
gyrB	DNA gyrase subunit B
stpA	DNA-binding protein StpA
hupA	DNA-binding protein HU-alpha
dps	DNA protection during starvation protein
ybiB	Uncharacterized protein
Fis	DNA-binding protein Fis
cbpA	Curved DNA-binding protein
rpoZ	DNA-directed RNA polymerase subunit omega

Continued on next page

Table S3.1 – *Continued from previous page*

Protein	**Function**
polA	DNA polymerase I
hupB	DNA-binding protein HU-beta
ihfA	Integration host factor subunit alpha
ihfB	Integration host factor subunit beta
helD	DNA helicase IV
kdgR	Transcriptional regulator
uvrD	DNA helicase II
oxyR	Hydrogen peroxide-inducible genes activator
parE	DNA topoisomerase 4 subunit B
rpoS	RNA polymerase sigma factor
rpoD	RNA polymerase sigma factor
crl	Sigma factor-binding protein
yejK	Nucleoid-associated protein
ybaB	Nucleoid-associated protein
dnaE	DNA polymerase III subunit alpha
dnaA	Chromosomal replication initiator protein
ebfC	Nucleoid-associated protein
slmA	Nucleoid occlusion factor
crfC	Clamp-binding protein CrfC
mukB	Chromosome partition protein
mukF	Chromosome partition protein
matP	Macrodomain Ter protein
topo3	DNA topoisomerase
parC	DNA topoisomerase 4 subunit A
mukE	Chromosome partition protein

Table S3.1: **List of DNA-binding proteins used for mass spectrometry analysis. Related to Table 3.2 and Table 3.3.** Proteins' description is taken UniProt (UniProt, strain K12, Tax ID: 83333, November 2021) database. Shortlist contains proteins identified as DNA-binding or DNA processing.

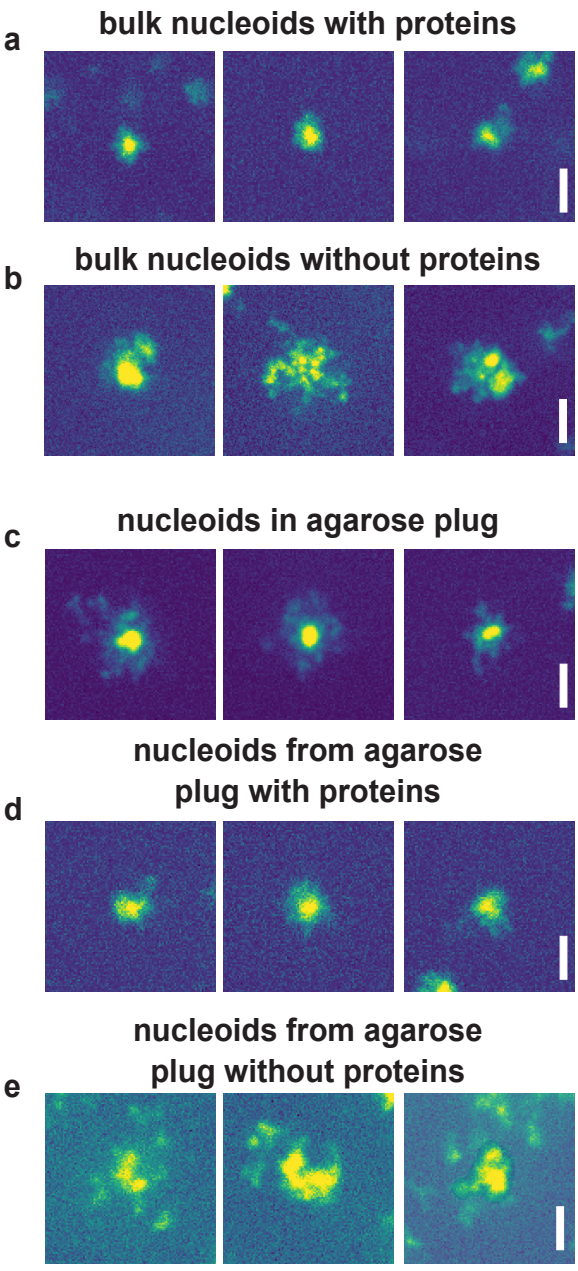

Figure S3.2: **Examples of DNA-objects. Related to figure 3.2.** Fluorescence images of DNA objects in various conditions: **(a)** Bulk protocol chromosomes before protein removal. **(b)** Bulk protocol chromosomes after protein removal. **(c)** Agarose plug protocol chromosomes inside the agarose plug before protein removal. **(d)** Agarose plug protocol chromosome in solution before protein removal. **(e)** Agarose plug protocol chromosomes in solution after protein removal. Scale bars are 5 μm.

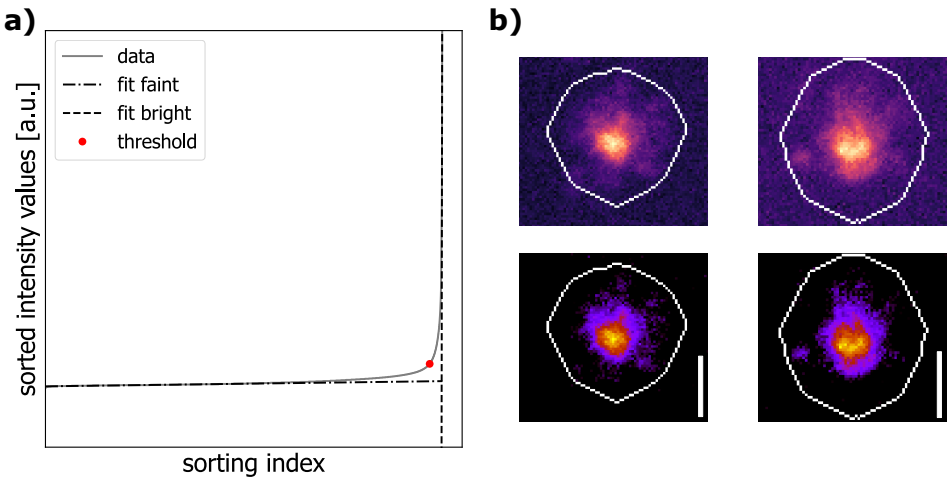

Figure S3.3: **Visualization of thresholding procedure. Related to figure 3.3.** **(a)** Pixel intensity values were sorted by increasing intensity, and two lines were fitted to this curve: a line fitted to the first half of the pixels in the image (which is the estimate of background, dash-dot), and a line fitted to all pixels brighter than half of the maximum intensity (estimate of foreground, dash). The intensity threshold value was then determined from the point on the sorted intensity curve (red dot) which was closest to intersection of the two lines. **(b)** Images before (top) and after (bottom) background subtraction. Inspection confirmed that the approach was able to discriminate background and foreground well. White line is contour of the mask. Scale bars are 5 μm.

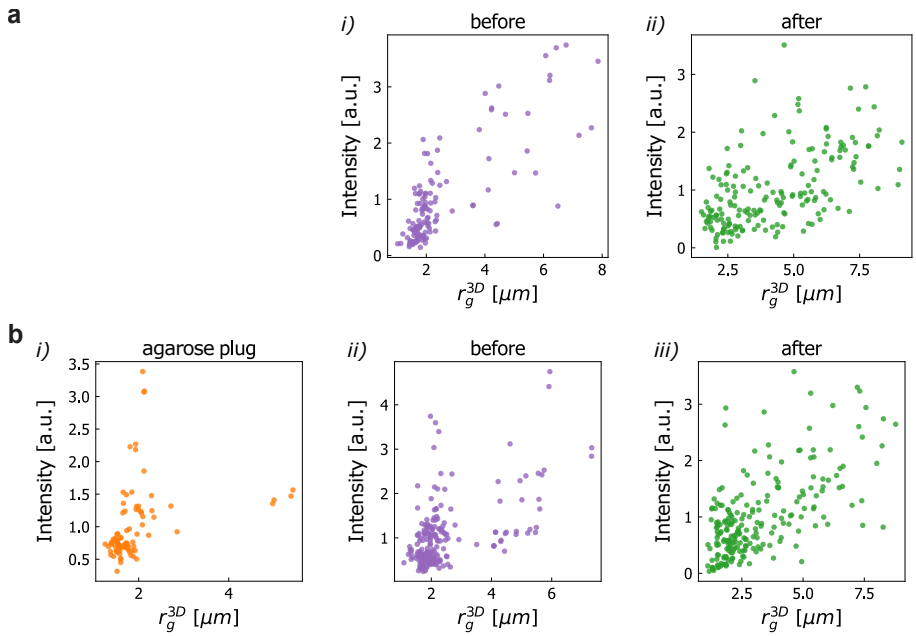

Figure S3.4: **Radius of gyration versus sum intensity distributions. Related to figure 3.3.** Scatter plots of the radius of gyration and sum intensity of observed DNA objects in various conditions: **(a)** *i)* Bulk protocol chromosomes before protein removal. *ii)* Bulk protocol chromosomes after protein removal. **(b)** *i)* Agarose plug protocol chromosomes inside the agarose plug before protein removal. *ii)* Plug protocol chromosome in solution before protein removal. *iii)* Agarose plug protocol chromosomes in solution after protein removal. Intensity values in each scatter plot are scaled to the mean of the applicable sum intensity distribution. Sample sizes are N=125 and 181 in panel a; and N=90, 223, 222 in panel b.

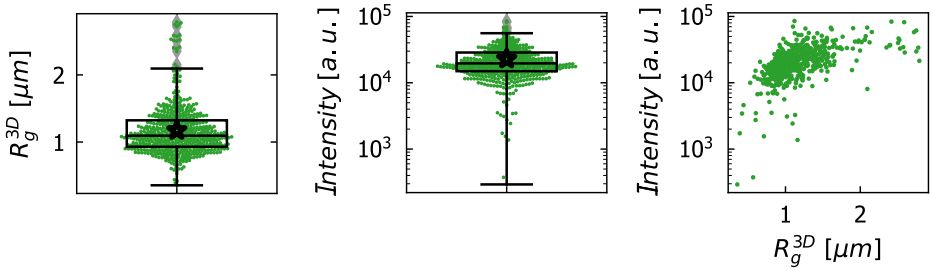

Figure S3.5: **Characterization of lambda-DNA molecules. Related to figure 3.3.** (left) R_g distribution for lambda DNA molecules. (center) Total fluorescence intensity per identified λ-DNA molecule. (right) R_g *vs.* total fluorescence intensity per DNA object distribution. Boxplots show the median and 25^{th}-75^{th} percentiles, star denotes mean, N=534.

Sample	**Condition**	**Intensity (a.u.)**	**Relative intensity**	**(theoretical) number of kbp**
bulk	after	1133034	49.5	2403
plug	after	1466184	64.1	3109
plug	in plug	1658675	72.5	3518
lambda		22870	1	48.5

Table S3.2: **Total and relative total intensities of DNA molecules. Related to Figure 3.3.** Mean sum intensity per molecule is reported. Bulk and plug condition values of intensity are compared relative to lambda-DNA molecules, and from this an expected number of base pairs is calculated.

	Topology	**Solvent**	N = 1 Mbp, L_p = 25 nm	N = 1 Mbp, L_p = 50 nm	N = 4.6 Mbp, L_p = 25 nm	N = 4.6 Mbp, L_p = 50 nm
Ideal chain[71]	L	n.a.	1.7	2.4	3.6	5.1
	R	n.a.	1.2	1.7	2.6	3.6
Worm-like chain[71]	L	n.a.	1.7	2.4	3.6	5.1
	R	n.a.	0.8	1.2	1.8	2.6
Self-avoiding polymer with solvent interaction (Flory theory)[71]	R	good	2.6	3.4	6.3	8.4
	R	ideal	1.2	1.7	2.6	3.6
	R	poor	0.35	0.54	0.6	0.9
Self-avoiding polymer with solvent interaction (Flory theory)[71]	L	good	3.7	4.9	9.0	12.0
	L	ideal	1.7	2.4	3.6	5.1
	L	poor	0.5	0.76	0.8	1.3
Non-crosslinked supercoiled polymer[39,72]	L/C	n.a.	1.35	0.83	1.5	2.5

Continued on next page

Table S3.3 – *Continued from previous page*

Table S3.3: **Gyration radii (μm) for various length DNA and various persistence length values. Related to Figure 3.3.** The persistence length of bare DNA is commonly 50 nm. However buffer conditions (*e.g.*, high concentrations of mono- and di-valent ions, as well as varying concentrations of intercalating dyes) can substantially decrease it. At conditions used in this study we do not expect persistence lengths lower than 25 nm.[73–75] Topology: L - linear, R - ring. Solvent: good - ν = 0.588, ideal - ν = 0.5, poor - ν = 0.36.

REFERENCES

(1) Schwille, P. Jump-starting life? Fundamental aspects of synthetic biology. *The Journal of Cell Biology* **2015**, *210*, 687–690.

(2) Litschel, T.; Ramm, B.; Maas, R.; Heymann, M.; Schwille, P. Beating Vesicles: Encapsulated Protein Oscillations Cause Dynamic Membrane Deformations. *Angewandte Chemie International Edition* **2018**, *57*, 16286–16290.

(3) Ganzinger, K. A.; Merino-Salomón, A.; García-Soriano, D. A.; Butterfield, A. N.; Litschel, T.; Siedler, F.; Schwille, P. FtsZ Reorganization Facilitates Deformation of Giant Vesicles in Microfluidic Traps. *Angewandte Chemie International Edition* **2020**, *59*, 21372–21376.

(4) Litschel, T.; Kelley, C. F.; Holz, D.; Adeli Koudehi, M.; Vogel, S. K.; Burbaum, L.; Mizuno, N.; Vavylonis, D.; Schwille, P. Reconstitution of contractile actomyosin rings in vesicles. *Nature Communications* **2021**, *12*, 2254.

(5) Joesaar, A.; Yang, S.; Bögels, B.; van der Linden, A.; Pieters, P.; Kumar, B. V. V. S. P.; Dalchau, N.; Phillips, A.; Mann, S.; de Greef, T. F. A. DNA-based communication in populations of synthetic protocells. *Nature Nanotechnology* **2019**, *14*, 369–378.

(6) Bintu, B.; Mateo, L. J.; Su, J.-H.; Sinnott-Armstrong, N. A.; Parker, M.; Kinrot, S.; Yamaya, K.; Boettiger, A. N.; Zhuang, X. Super-resolution chromatin tracing reveals domains and cooperative interactions in single cells. *Science (New York, N.Y.)* **2018**, *362*, eaau1783.

(7) Ricci, M. A.; Manzo, C.; García-Parajo, M. F.; Lakadamyali, M.; Cosma, M. P. Chromatin fibers are formed by heterogeneous groups of nucleosomes in vivo. *Cell* **2015**, *160*, 1145–58.

(8) Falk, M.; Feodorova, Y.; Naumova, N.; Imakaev, M.; Lajoie, B. R.; Leonhardt, H.; Joffe, B.; Dekker, J.; Fudenberg, G.; Solovei, I.; Mirny, L. A. Heterochromatin drives compartmentalization of inverted and conventional nuclei. *Nature* **2019**, *570*, 395–399.

(9) Brandão, H. B.; Ren, Z.; Karaboja, X.; Mirny, L. A.; Wang, X. DNA-loop-extruding SMC complexes can traverse one another in vivo. *Nature Structural & Molecular Biology 2021 28:8* **2021**, *28*, 642–651.

(10) Liang, Y.; van der Valk, R. A.; Dame, R. T.; Roos, W. H.; Wuite, G. J. L. Probing the mechanical stability of bridged DNA-H-NS protein complexes by single-molecule AFM pulling. *Scientific Reports* **2017**, *7*, 15275.

(11) Dame, R. T.; Wyman, C.; Goosen, N. H-NS mediated compaction of DNA visualised by atomic force microscopy. *Nucleic Acids Research* **2000**, *28*, 3504–3510.

(12) Japaridze, A.; Muskhelishvili, G.; Benedetti, F.; Gavriilidou, A. F. M.; Zenobi, R.; De Los Rios, P.; Longo, G.; Dietler, G. Hyperplectonemes: A Higher Order Compact and Dynamic DNA Self-Organization. *Nano Letters* **2017**, *17*, 1938–1948.

(13) Kaczmarczyk, A.; Meng, H.; Ordu, O.; Noort, J. v.; Dekker, N. H. Chromatin fibers stabilize nucleosomes under torsional stress. *Nature Communications* **2020**, *11*, 126.

(14) Sun, M.; Nishino, T.; Marko, J. F. The SMC1-SMC3 cohesin heterodimer structures DNA through supercoiling-dependent loop formation. *Nucleic Acids Research* **2013**, *41*, 6149–6160.

(15) Renger, R.; Morin, J. A.; Lemaitre, R.; Ruer-Gruss, M.; Jülicher, F.; Hermann, A.; Grill, S. W. Co-condensation of proteins with single- and double-stranded DNA. *Proceedings of the National Academy of Sciences of the United States of America* **2022**, *119*, DOI: 10.1073/pnas.2107871119.

(16) Lin, S. N.; Dame, R. T.; Wuite, G. J. Direct visualization of the effect of DNA structure and ionic conditions on HU–DNA interactions. *Scientific Reports 2021 11:1* **2021**, *11*, 1–10.

(17) Davidson, I. F.; Bauer, B.; Goetz, D.; Tang, W.; Wutz, G.; Peters, J.-M. M. DNA loop extrusion by human cohesin. *Science (New York, N.Y.)* **2019**, *366*, 1338–1345.

(18) Golfier, S.; Quail, T.; Kimura, H.; Brugués, J. Cohesin and condensin extrude DNA loops in a cell-cycle dependent manner. *eLife* **2020**, *9*, e53885.

(19) Ganji, M.; Shaltiel, I. A.; Bisht, S.; Kim, E.; Kalichava, A.; Haering, C. H.; Dekker, C. Real-time imaging of DNA loop extrusion by condensin. *Science (New York, N.Y.)* **2018**, *360*, 102–105.

(20) Kim, Y.; Shi, Z.; Zhang, H.; Finkelstein, I. J.; Yu, H. Human cohesin compacts DNA by loop extrusion. *Science (New York, N.Y.)* **2019**, *366*, 1345–1349.

(21) Greene, E. C.; Wind, S.; Fazio, T.; Gorman, J.; Visnapuu, M.-L., DNA Curtains for High-Throughput Single-Molecule Optical Imaging In *Methods in Enzymology*; Elsevier Inc.: 2010; Chapter 14, pp 293–315.

(22) Birnie, A.; Dekker, C. Genome-in-a-Box: Building a Chromosome from the Bottom Up. *ACS Nano* **2021**, *15*, 111–124.

(23) Yoo, H.-B.; Lim, H.-M.; Yang, I.; Kim, S.-K.; Park, S.-R. Flow cytometric investigation on degradation of macro-DNA by common laboratory manipulations. *Journal of Biophysical Chemistry* **2011**, *02*, 102–111.

(24) Adam, R. E.; Zimm, B. H. Shear degradation of DNA. *Nucleic Acids Research* **1977**, *4*, 1513–1538.

(25) Vanapalli, S. A.; Ceccio, S. L.; Solomon, M. J. Universal scaling for polymer chain scission in turbulence. *Proceedings of the National Academy of Sciences of the United States of America* **2006**, *103*, 16660–16665.

(26) Kaur, G.; Lewis, J.; van Oijen, A. Shining a Spotlight on DNA: Single-Molecule Methods to Visualise DNA. *Molecules* **2019**, *24*, 491.

(27) Dufrêne, Y. F.; Ando, T.; Garcia, R.; Alsteens, D.; Martinez-Martin, D.; Engel, A.; Gerber, C.; Müller, D. J. Imaging modes of atomic force microscopy for application in molecular and cell biology. *Nature Nanotechnology* **2017**, *12*, 295–307.

(28) Kriegel, F.; Ermann, N.; Lipfert, J. Probing the mechanical properties, conformational changes, and interactions of nucleic acids with magnetic tweezers. *Journal of Structural Biology* **2017**, *197*, 26–36.

(29) Shintomi, K.; Takahashi, T. S.; Hirano, T. Reconstitution of mitotic chromatids with a minimum set of purified factors. *Nature Cell Biology* **2015**, *17*, 1014–1023.

(30) Wegner, A. S.; Alexeeva, S.; Odijk, T.; Woldringh, C. L. Characterization of Escherichia coli nucleoids released by osmotic shock. *Journal of Structural Biology* **2012**, *178*, 260–269.

(31) Pelletier, J.; Jun, S. Isolation and Characterization of Bacterial Nucleoids in Microfluidic Devices. *Methods in Molecular Biology* **2017**, *1624*, 311–322.

(32) Lartigue, C.; Glass, J. I.; Alperovich, N.; Pieper, R.; Parmar, P. P.; Hutchison, C. A.; Smith, H. O.; Venter, J. C. Genome transplantation in bacteria: Changing one species to another. *Science (New York, N.Y.)* **2007**, *317*, 632–638.

(33) Zhang, M.; Zhang, Y.; Scheuring, C. F.; Wu, C. C.; Dong, J. J.; Zhang, H. B. Preparation of megabase-sized DNA from a variety of organisms using the nuclei method for advanced genomics research. *Nature Protocols 2012 7:3* **2012**, *7*, 467–478.

(34) Łopacińska-Jørgensen, J. M.; Pedersen, J. N.; Bak, M.; Mehrjouy, M. M.; Sørensen, K. T.; Østergaard, P. F.; Bilenberg, B.; Kristensen, A.; Taboryski, R. J.; Flyvbjerg, H.; Marie, R.; Tommerup, N.; Silahtaroglu, A. Enrichment of megabase-sized DNA molecules for single-molecule optical mapping and next-generation sequencing. *Scientific Reports* **2017**, *7*, 1–10.

(35) Merrikh, H.; Zhang, Y.; Grossman, A. D.; Wang, J. D. Replication–transcription conflicts in bacteria. *Nature Reviews Microbiology 2012 10:7* **2012**, *10*, 449–458.

(36) Bird, R. E.; Louarn, J.; Martuscelli, J.; Caro, L. Origin and sequence of chromosome replication in Escherichia coli. *Journal of Molecular Biology* **1972**, *70*, 549–566.

(37) Saifi, B.; Ferat, J. L. Replication Fork Reactivation in a dnaC2 Mutant at Non-Permissive Temperature in Escherichia coli. *PLOS ONE* **2012**, *7*, e33613.

(38) Japaridze, A.; Gogou, C.; Kerssemakers, J. W.; Nguyen, H. M.; Dekker, C. Direct observation of independently moving replisomes in Escherichia coli. *Nature Communications 2020 11:1* **2020**, *11*, 1–10.

(39) Cunha, S.; Woldringh, C. L.; Odijk, T. Polymer-Mediated Compaction and Internal Dynamics of Isolated Escherichia Coli Nucleoids. *Journal of Structural Biology* **2001**, *136*, 53–66.

(40) Vtyurina, N. What makes long DNA short? Modulation of DNA structure by Dps protein: cooperating & reorganizing, Ph.D. Thesis, Delft University of Technology, 2016, p 184.

(41) Strychalski, E. A.; Geist, J.; Gaitan, M.; Locascio, L. E.; Stavis, S. M. Quantitative measurements of the size scaling of linear and circular DNA in nanofluidic slitlike confinement. *Macromolecules* **2012**, *45*, 1602–1611.

(42) Yan, X.; Habbersett, R. C.; Yoshida, T. M.; Nolan, J. P.; Jett, J. H.; Marrone, B. L. Probing the kinetics of SYTOX Orange stain binding to double-stranded DNA with implications for DNA analysis. *Analytical Chemistry* **2005**, *77*, 3554–3562.

(43) De Gennes, P. G., *Scaling Concepts in Polymer Physics*; Cornell University Press: 1979.

(44) Vink, J. N.; Brouns, S. J.; Hohlbein, J. Extracting Transition Rates in Particle Tracking Using Analytical Diffusion Distribution Analysis. *Biophysical Journal* **2020**, *119*, 1970–1983.

(45) Weber, S. C.; Spakowitz, A. J.; Theriot, J. A. Bacterial Chromosomal Loci Move Subdiffusively through a Viscoelastic Cytoplasm. *Physical Review Letters* **2010**, *104*, 238102.

(46) Javer, A.; Kuwada, N. J.; Long, Z.; Benza, V. G.; Dorfman, K. D.; Wiggins, P. A.; Cicuta, P.; Lagomarsino, M. C. Persistent super-diffusive motion of Escherichia coli chromosomal loci. *Nature Communications* **2014**, *5*, 3854.

(47) Japaridze, A.; Yang, W.; Dekker, C.; Nasser, W.; Muskhelishvili, G. DNA sequence-directed cooperation between nucleoid-associated proteins. *iScience* **2021**, *24*, 102408.

(48) Pelletier, J.; Halvorsen, K.; Ha, B.-Y.; Paparcone, R.; Sandler, S. J.; Woldringh, C. L.; Wong, W. P.; Jun, S. Physical manipulation of the Escherichia coli chromosome reveals its soft nature. *Proceedings of the National Academy of Sciences* **2012**, *109*, E2649–E2656.

(49) Wegner, A. S.; Wintraecken, K.; Spurio, R.; Woldringh, C. L.; de Vries, R.; Odijk, T. Compaction of isolated Escherichia coli nucleoids: Polymer and H-NS protein synergetics. *Journal of Structural Biology* **2016**, *194*, 129–137.

(50) Shintomi, K.; Inoue, F.; Watanabe, H.; Ohsumi, K.; Ohsugi, M.; Hirano, T. Mitotic chromosome assembly despite nucleosome depletion in Xenopus egg extracts. *Science* **2017**, *356*, 1284–1287.

(51) Shintomi, K. Making Mitotic Chromosomes in a Test Tube. *Epigenomes* **2022**, *6*, 20.

(52) Cunha, S.; Woldringh, C. L.; Odijk, T. Restricted diffusion of DNA segments within the isolated Escherichia coli nucleoid. *Journal of structural biology* **2005**, *150*, 226–32.

(53) Japaridze, A.; Benke, A.; Renevey, S.; Benadiba, C.; Dietler, G. Influence of DNA binding dyes on bare DNA structure studied with atomic force microscopy. *Macromolecules* **2015**, *48*, 1860–1865.

(54) Cruz-León, S.; Vanderlinden, W.; Müller, P.; Forster, T.; Staudt, G.; Lin, Y.-Y.; Lipfert, J.; Schwierz, N. Twisting DNA by salt. *Nucleic Acids Research* **2022**, *50*, 5726–5738.

(55) Schlick, T.; Li, B.; Olson, W. K. The influence of salt on the structure and energetics of supercoiled DNA. *Biophysical Journal* **1994**, *67*, 2146–2166.

(56) Thomas, G. J.; Benevides, J. M.; Duguid, J.; Bloomfield, V. A. Roles of Cations in the Structure, Stability and Condensation of DNA. *Fifth International Conference on the Spectroscopy of Biological Molecules* **1993**, 39–45.

(57) Srivastava, A.; Timsina, R.; Heo, S.; Dewage, S. W.; Kirmizialtin, S.; Qiu, X. Structure-guided DNA–DNA attraction mediated by divalent cations. *Nucleic Acids Research* **2020**, *48*, 7018–7026.

(58) Bloomfield, V. A. DNA Condensation by Multivalent Cations. *Biopolymers* **1998**, *44*, 269–282.

(59) Hagerman, P. J. FLEXIBILITY OF DNA. *Ann. Rev. Biophys. Biophys. Chem* **1988**, *17*, 265–86.

(60) Kavenoff, R.; Bowen, B. C. Electron microscopy of membrane-free folded chromosomes from Escherichia coli. *Chromosoma* **1976**, *59*, 89–101.

(61) Acosta-Martin, A. E.; Chwastyniak, M.; Beseme, O.; Drobecq, H.; Amouyel, P.; Pinet, F. Impact of incomplete DNase I treatment on human macrophage proteome analysis. *Proteomics - Clinical Applications* **2009**, *3*, 1236–1246.

(62) Wu, F.; Japaridze, A.; Zheng, X.; Wiktor, J.; Kerssemakers, J. W. J.; Dekker, C. Direct imaging of the circular chromosome in a live bacterium. *Nature Communications* **2019**, *10*, 2194.

(63) Köcher, T.; Pichler, P.; Swart, R.; Mechtler, K. Analysis of protein mixtures from whole-cell extracts by single-run nanoLC-MS/MS using ultralong gradients. *Nature Protocols 2012 7:5* **2012**, *7*, 882–890.

(64) Den Ridder, M.; Knibbe, E.; van den Brandeler, W.; Daran-Lapujade, P.; Pabst, M. A systematic evaluation of yeast sample preparation protocols for spectral identifications, proteome coverage and post-isolation modifications. *Journal of Proteomics* **2022**, *261*, 104576.

(65) Van Der Walt, S.; Schönberger, J. L.; Nunez-Iglesias, J.; Boulogne, F.; Warner, J. D.; Yager, N.; Gouillart, E.; Yu, T. Scikit-image: Image processing in python. *PeerJ* **2014**, *2014*, e453.

(66) Sofroniew, N.; Lambert, T.; Evans, K.; Nunez-Iglesias, J.; Bokota, G.; Winston, P.; Peña-Castellanos, G.; Yamauchi, K.; Bussonnier, M.; Doncila Pop, D.; Can Solak, A.; Liu, Z.; Wadhwa, P.; Burt, A.; Buckley, G., et al. napari: a multi-dimensional image viewer for Python. **2022**, DOI: 10.5281/ZENODO.6598542.

(67) Schindelin, J.; Arganda-Carreras, I.; Frise, E.; Kaynig, V.; Longair, M.; Pietzsch, T.; Preibisch, S.; Rueden, C.; Saalfeld, S.; Schmid, B.; Tinevez, J. Y.; White, D. J.; Hartenstein, V.; Eliceiri, K.; Tomancak, P., et al. Fiji: an open-source platform for biological-image analysis. *Nature Methods 2012 9:7* **2012**, *9*, 676–682.

(68) Tinevez, J. Y.; Perry, N.; Schindelin, J.; Hoopes, G. M.; Reynolds, G. D.; Laplantine, E.; Bednarek, S. Y.; Shorte, S. L.; Eliceiri, K. W. TrackMate: An open and extensible platform for single-particle tracking. *Methods* **2017**, *115*, 80–90.

(69) Bateman, A.; Martin, M. J.; O'Donovan, C.; Magrane, M.; Alpi, E.; Antunes, R.; Bely, B.; Bingley, M.; Bonilla, C.; Britto, R.; Bursteinas, B.; Bye-AJee, H.; Cowley, A.; Da Silva, A.; De Giorgi, M., et al. UniProt: the universal protein knowledgebase. *Nucleic Acids Research* **2017**, *45*, D158–D169.

(70) Ma, B.; Zhang, K.; Hendrie, C.; Liang, C.; Li, M.; Doherty-Kirby, A.; Lajoie, G. PEAKS: powerful software for peptide de novo sequencing by tandem mass spectrometry. *Rapid Communications in Mass Spectrometry* **2003**, *17*, 2337–2342.

(71) Michael Rubinstein; Ralph H. Colby, *Polymer physics*; Oxford University Press: 2016.

(72) Zimm, B. H.; Stockmayer, W. H. The dimensions of chain molecules containing branches and rings. *The Journal of Chemical Physics* **1949**, *17*, 1301–1314.

(73) Davidson, I. F.; Barth, R.; Zaczek, M.; van der Torre, J.; Tang, W.; Nagasaka, K.; Janissen, R.; Kerssemakers, J.; Wutz, G.; Dekker, C.; Peters, J.-M. CTCF is a DNA-tension-dependent barrier to cohesin-mediated loop extrusion. *Nature 2023 616:7958* **2023**, *616*, 822–827.

(74) Brunet, A.; Tardin, C.; Salomé, L.; Rousseau, P.; Destainville, N.; Manghi, M. Dependence of DNA Persistence Length on Ionic Strength of Solutions with Monovalent and Divalent Salts: A Joint Theory-Experiment Study. *Macromolecules* **2015**, *48*, 3641–3652.

(75) Newton, M. D.; Fairbanks, S. D.; Thomas, J. A.; Rueda, D. S. A Minimal Load-and-Lock RuII Luminescent DNA Probe. *Angewandte Chemie International Edition* **2021**, *60*, 20952–20959.

4

SHAPE AND SIZE CONTROL OF ARTIFICIAL CELLS FOR BOTTOM-UP BIOLOGY

Bottom-up biology is an expanding research field that aims to understand the mechanisms underlying biological processes *via in vitro* assembly of their essential components in synthetic cells. As encapsulation and controlled manipulation of these elements is a crucial step in the recreation of such cell-like objects, microfluidics is increasingly used for the production of minimal artificial containers such as single-emulsion droplets, double-emulsion droplets, and liposomes. Despite the importance of cell morphology on cellular dynamics, current synthetic-cell studies mainly use spherical containers, and methods to actively shape manipulate these have been lacking. In this paper, we describe a microfluidic platform to deform the shape of artificial cells into a variety of shapes (rods and discs) with adjustable cell-like dimensions below 5 μm, thereby mimicking realistic cell morphologies. To illustrate the potential of our method, we reconstitute three biologically relevant protein systems (FtsZ, microtubules, collagen) inside rod-shaped containers and study the arrangement of the protein networks inside these synthetic containers with physiologically relevant morphologies resembling those found in living cells.

This chapter has been published: F. Fanalista*, A. Birnie*, R. Maan, F. Burla, K. Charles, G. Pawlik, S. Deshpande, G. H. Koenderink, M. Dogterom, and C. Dekker, *Shape and Size Control of Artificial Cells for Bottom-Up Biology*, ACS Nano 13, 5439 (2019). *Equal contribution

4.1. INTRODUCTION

Throughout evolution, cells have radiated into a dazzling variety of morphologies, where prokaryotes are found in the shape of, for example, rods, spheres, and spirals,[1] archaea can exhibit even triangular or flattened square shapes,[2] and eukaryotic cells range from orderly shaped plant cells[3] to the extensively branched dendritic cells of the immune system.[4] This wide morphological diversity raises questions on the underlying reasons and the interplay between morphology and the myriad of internal cellular processes. The shape and size of a cell are the product of internal molecular processes that drive cellular growth and division and are also guided by external environmental factors such as the surrounding cells or simply the amount of available space. The cellular container shell itself is maintained by cytoskeleton and membrane machineries[5–9] that are present in all kingdoms of life.

Unicellular organisms may benefit from specific shapes for a selective advantage,[10,11] while for multicellular organisms, the cellular morphology is closely linked to cell-cell interactions and the extracellular matrix (ECM).[12,13] Similarly, cells in colonies of unicellular organisms such as biofilms display a morphological variation depending on their function at a particular position and time within the colony lifecycle.[14,15] To accommodate such variations in morphology, the processes inside a cell should be robust against variations of the cellular shape. For example, to ensure faithful division, pattern-formation processes should successfully guide the cellular division machinery to the right location, irrespective of the precise shape and size of the cellular boundary.[16,17] The mechanisms through which such processes remain robust in varying environments and boundary conditions are a topic of active research.[18] Confinement and shape not only influence cellular processes but also have an effect on extracellular structures such as the ECM, the fibrous network located in the space between eukaryotic cells in tissues and prokaryotic cells in biofilms.[19,20] The large morphological variety of cells also poses interesting questions from the perspective of polymer physics. Cells contain many polymers, such as cytoskeletal components and the genomic material. The spatial distribution and dynamics of polymers are in general sensitive to the spatial confinement,[21–26] and as a result, biopolymers such as actin networks[27] and the genome[28–30] will reorganize upon morphological perturbation of the cellular container.

Confronted with the imposing complexity and connectivity of cellular processes, researchers are aiming to reconstitute essential cellular systems with a minimal set of components inside controlled confinements.[31,32] The nature of the artificial containers used in these endeavors is quite diverse, ranging from liposomes, single-emulsion droplets (water-in-oil droplets, from now on called droplets), to double-emulsion droplets (water-in-oil-in-water droplets, henceforth called double emulsions) and even solid-state microchambers.[33,34] With such bottom-up approaches, cytoskeletal components (*e.g.*, actin,[35] tubulin,[36] MreB,[37], FtsZ[38]), cytokinesis and segregation machinery (*e.g.*, actin-myosin rings,[39] mitotic spindles[40]), cell-free expression systems (*e.g.*, cell extracts,[41] PURE system[42]), pattern formation systems (*e.g.*, the Min system[43]), and genomes[44] can be encapsulated inside such artificial containers (Figure 4.1, top).

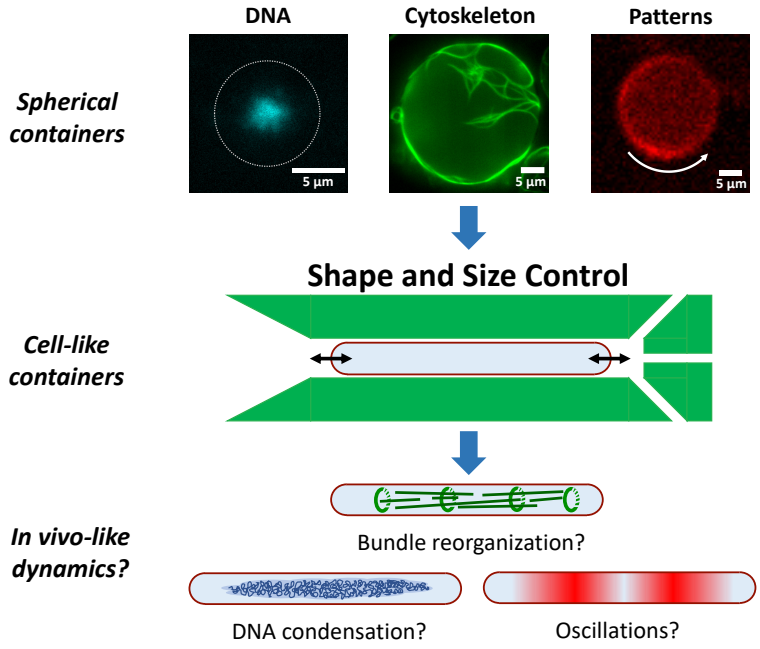

Figure 4.1: **Shape and size control of synthetic cells to explore the influence of confinement and geometry on cellular processes.** Most current approaches to bottom-up biology encapsulate purified cellular components inside large, spherical containers. For example, on the top row, three prokaryotic key systems, which in some form are present in all kingdoms of life, are reconstituted in spherical droplets: DNA (*E. coli* nucleoid, blue), cytoskeletal components (FtsZ, green), and pattern formation systems (Min proteins, red). However, these key systems are, like most processes and structures inside a cell, sensitive to the confinement size and the geometry. Using a microfluidic approach (middle), we manipulate the shape and size of the initially spherical synthetic cells. In this manner, we are able to experimentally access a set of parameters which were hitherto unexplored in the field of bottom-up biology. The method offers the possibility of observing more *in vivo*-like dynamics for various cellular systems encapsulated inside synthetic cells (bottom).

The shape of the artificial containers is an often-overlooked parameter in mimicking cells. Indeed, thus far, the majority of synthetic cell studies used simple spherical containers with a diameter of 10-50 μm.[33] However, most living cells are nonspherical, and while this size range is fitting for eukaryotic cells, it applies much less so for the more abundant bacterial and archaeal cells. In the past two decades, research in bottom-up biology has also been performed in microfabricated chambers that allow for a range of shapes,[45–47] but those are obviously nondeformable, preventing the observation of dynamics as a function of changing confinement size. Furthermore, the open-top geometry ("a chamber without a roof") that was used in some cases[45] decreases the ratio between the bulk volume of the protein reservoir and the surface with which these proteins interact, introducing ambiguities in the local protein concentrations that are important for pattern-formation processes.[18] There have been some reports on the manipulation of spherical vesicles, but these efforts mainly concentrated on the immobilization of droplets through mechanical trapping[48–51] and some elaborated manipulation

with dielectrophoresis.[52] While Boukellal *et al.* introduced a method to trap droplets in tubular-shaped confinements,[53] these containers were so large (upward of 100 μm) that they were not well applicable for synthetic cell research. Furthermore, methods to split containers on-chip by running them against T- or Y-shaped junctions have been developed both for droplets[54] and liposomes,[55] offering a tool to obtain containers with half the original volumes. Some osmosis-based size control of spherical droplets and double emulsions was demonstrated recently as well,[41,44] but again, the involved size ranges were not well suited for reconstituting bacterial systems in artificial cells.

Here, we introduce a general microfluidic platform to control the shape and size of various deformable containers, from droplets to liposomes, at cell-like scales in the sub-5 μm range (Figure 4.1, middle). Using this system, we are able to access the same shape and size parameter space as is present in the cells from which the reconstituted components are isolated. Specifically, we are able to shape various artificial cell containers into confinements with dimensions down to almost 1 μm. Furthermore, we demonstrate the ability to precisely and reversibly control the size of these containers. The method offers experimental avenues to unravel the interconnection between cellular processes and the confinement geometry. We provide examples for three biologically relevant protein systems (FtsZ, microtubules, collagen) inside rod-shaped containers. We anticipate that this platform will contribute to closing the gap between the dynamics in artificial cells and the *in vivo* dynamics of real cells (Figure 4.1, bottom).

4.2. RESULTS AND DISCUSSION

To obtain an efficient system for shaping artificial cells on-chip and impose user-defined dimensions to a variety of initially spherical containers, we designed and fabricated a simple but effective microfluidic chip with an array of local micropatterned structures ("traps"). We first tested the functionality of the design using water-in-oil droplets. Technical details of the experimental procedure, from the droplet production to the device design and operation, are described in Figure S4.1. Figure 4.2a shows an example of the shape manipulation process of a droplet that is transformed into a tubular geometry: A spherical droplet gets caught at the trap entrance and subsequently is reshaped into a cylindrical shape. Because of the presence of fluorescent lipids into the oil phase, the trap profile and the droplet are clearly distinguishable as dark regions. Fluid flow through the trap, necessary to catch the droplets, was ensured by including three exit holes that are visible at the end of the structure. The entrance of the traps has a conical funnel shape that narrows down to the predefined trap width, so that a minimal fluid pressure has to be applied to squeeze the droplets inside. Upon entering the trap, the droplet gets deformed and remains fixed in the desired shape. With an array of these traps, it is possible to stably observe tens of such rod-shaped droplets in a single field-of-view (Figure S4.2a). Aided by the precision provided by cleanroom-based fabrication techniques, we tested the versatility of our trap design over a wide range of confinements and aspect ratios. To mimic small organisms such as *Escherichia coli*, we mainly focused our efforts on obtaining small containers with diameters below 5 μm, thereby

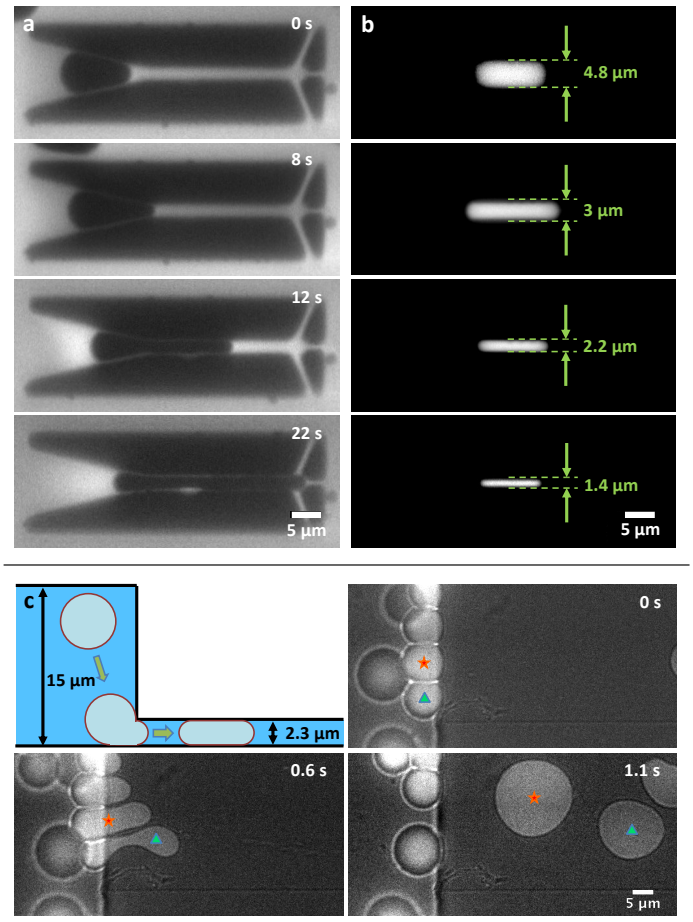

Figure 4.2: **Shape control of water-in-oil droplets *via* microfluidic structures. (a)** Droplet loading into a tubular trap: the droplet is captured at the entrance of the trap and progressively squeezed into the confinement, assuming the imposed geometry. RhodPE lipids are dissolved in the oil phase to enhance the contrast between the oil phase, the aqueous phase, and the profile of the trap. **(b)** The tubular trap design offers the possibility to deform droplets into rod-shaped geometries of different dimensions. To visualize the droplets, Alexa647 fluorescent dye is encapsulated in the aqueous phase. **(c)** A multiheight microfluidic device is used for the deformation of spherical droplets into thin disc-shaped containers or "pancakes". As they pass from a 15 μm to a 2 μm high channel, the spherical droplets get consequently squeezed into a disc shape. The figure shows the deformation process of two droplets, marked with a red star and green triangle. The images combine both bright-field and fluorescent signals from the Alexa647 fluorescent dye encapsulated inside the droplets.

recreating the rod-shaped morphology that many bacteria possess.[1] By varying both the width of the traps and the overall height of the device, we obtained rod-shaped droplets of arbitrary lengths and widths ranging from 4.8 μm down to 1.4 μm (Figure 4.2b and Figure S4.2b). We determined the trapping efficiency of these designs as the ratio of the number of traps that stably contained a tubular droplet over the total number of

traps present in the device: For the design with the largest trap width (4.8 μm, Figure 4.2b), we found that 98% of the traps (N = 103/105) contained a rod-shaped droplet. Designs with narrower traps have a higher hydrodynamic resistance[56] and hence require higher fluid pressures and, as a result, are less straightforward to operate. For the design with the narrowest traps achieved in this work (1.4 μm, Figure 4.2b), we found that 33% (N = 19/57) of the traps contained a rod-shaped droplet. We also explored the potential of our microfluidics-based approach to deform spherical droplets into flat circular discs ("pancakes"). To do so, we employed multiheight microfluidic devices. Figure 4.2c shows an example where spherical droplets first travel undeformed within a large channel of 15 μm height. When they encounter narrower channels of 2 μm height, they are forced into the confining channels by the fluid pressure and consequently are deformed into pancake-like containers that mimic the morphology of, for example, certain disc-shaped archaea.[2] In addition, the disc-shaped droplets can be immobilized and stored for analysis in an array of microfluidic traps, as shown in Figure S4.1c.

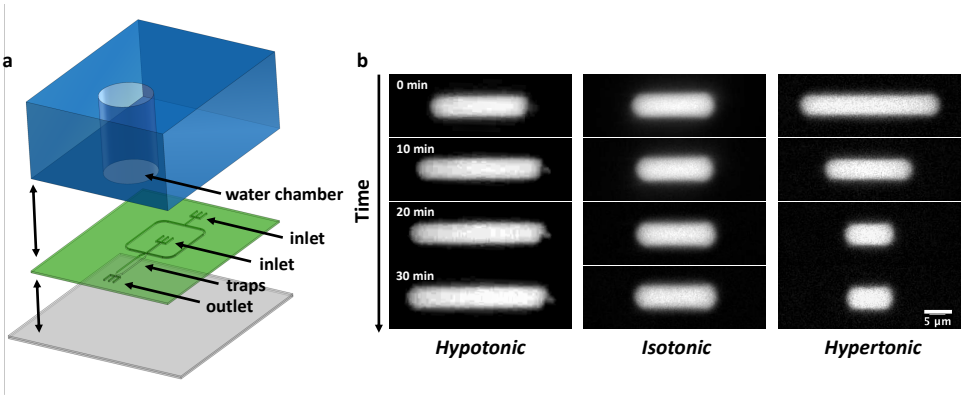

Figure 4.3: **Size control of water-in-oil droplets *via* a multilayer microfluidic device. (a)** Schematic of the three different layers composing the device. The bottom layer (gray) consists of a PMDS-covered glass coverslip, followed by a second layer (green) of a thin PDMS membrane imprinted with the microfluidic channels and traps design. The design includes two inlet channels, the first one for the droplets and a second one for oil, which cross each other in a large T-junction. After this junction, a single large channel leads to the array of traps to capture and manipulate the droplets. The third layer (blue) is a thicker piece of PDMS containing a water chamber, placed above the array of traps. **(b)** Water-in-oil droplets contain Alexa647 for visualization and 200 mM KCl. Depending on the relative salt concentration between the water chamber and the droplets, different behaviors are observed over time: in hypotonic conditions (100 mM KCl in water chamber), the droplets expand (left); in isotonic conditions (200 mM KCl in the water chamber), the droplet size remains qualitatively stable (center); and in hypertonic conditions (300 mM KCl in the water chamber), the droplets shrink consistently relative to their original volume (right).

Another fascinating aspect of living systems is the capacity of cellular processes to adapt and re-arrange over time as the cell changes during its growth and life cycle. To enable the investigation of such phenomena *in vitro*, isolated cellular components should be reconstituted into artificial containers with a size that can be controllably changed over time. Using a system inspired by the work of Shim *et al.*,[57] we managed to vary the size of the droplets captured in the traps. Specifically, we assembled a multilayer polydimethylsiloxane (PDMS) device consisting of three parts, see Figure 4.3a: a thick rectangular

piece of PDMS containing a hole ("water chamber") sitting on top of a thin layer imprinted with microfluidic traps, which in its turn is sealed off at the bottom by a PDMS-covered glass coverslip. By taking advantage of the fact that PDMS is permeable to water, it is possible to induce osmosis between the droplets and the water chamber through the thin PDMS membrane that separates them. Consequently, when the aqueous solution of the droplets has a salt concentration lower or higher compared to the one in the water chamber, water is able to flow across the PDMS membrane to restore isotonicity, leading to, respectively, shrinking or expanding droplets. When forced into a tubular shape, the droplets consequently re-adjusted their volume by shortening or elongating along their main axis inside the traps (Figure 4.3b, left and right). Immediately after the trapping, for the first 20 min, the length of the droplets changed quickly to reduce the osmolarity difference with the water chamber. As the osmotic balance between the droplets and the water chamber is approached, the size of the droplets tended to stabilize. By contrast, in isotonic conditions, the volume of the droplets remained approximately constant (Figure 4.3b, middle).

Beyond droplets, we explored size and shape manipulation of containers that are physiologically closer to living cells, namely, double emulsions and liposomes. We used our microfluidic octanol-assisted liposome assembly (OLA) platform to produce double emulsions on-chip (Figure 4.4a). By dissolving the lipids in oleic acid, the double emulsions undergo a process of partial dewetting,[58,59] by which the excess solvent and lipids accumulate in a side pocket. The volume of double emulsions can be varied using an applied osmotic pressure difference due to new buffer fluid that is administered through side channels (Figure 4.4a). Upon inducing such volume changes, excess material in the side-pocket may act as a reservoir to concurrently re-adjust the surface area (Figure 4.4b). In other words, as the water flows through the membrane to restore osmotic balance, the surface automatically re-adjusts its area to fit the new volume, using the side pocket as a source or sink for membrane lipids.

To check this hypothesis, we produced and immobilized oleic acid double emulsions in an array of traps (Figure 4.4c). Next, an aqueous solution was flushed *via* a feeding channel to create an osmotic imbalance between the inner and outer aqueous environment of the double emulsions. In hypertonic conditions, the osmosis process led to a fast reduction of the double emulsion volume (Figure 4.4d, top), which shrank from an average diameter value d = 12.3 ± 0.1 μm down to d = 7.5 ± 0.1 μm (N = 45). Simultaneously, the membrane surface area re-adjusted to the new volume, with a consequent visible growth of the side pockets. When the original osmotic conditions were restored, the same double emulsions underwent the inverse process (Figure 4.4d, bottom): the volume expanded back close to the original size (d = 11.1 ± 0.2 μm), with an associated membrane area increase at the cost of the side pocket, showing that the process is largely reversible. Looking at the variation of the double emulsion diameters over time compared to their original size (Figure 4.4e), the shrinkage and the expansion processes appeared symmetric. The size variation was initially slow and then was followed by a phase of faster size change. As the osmolarity difference between the outer and the inner aqueous phases was re-equilibrated, the size variation slowed down again. The degree by which the double emulsions shrank or expanded under, respectively, hypertonic or

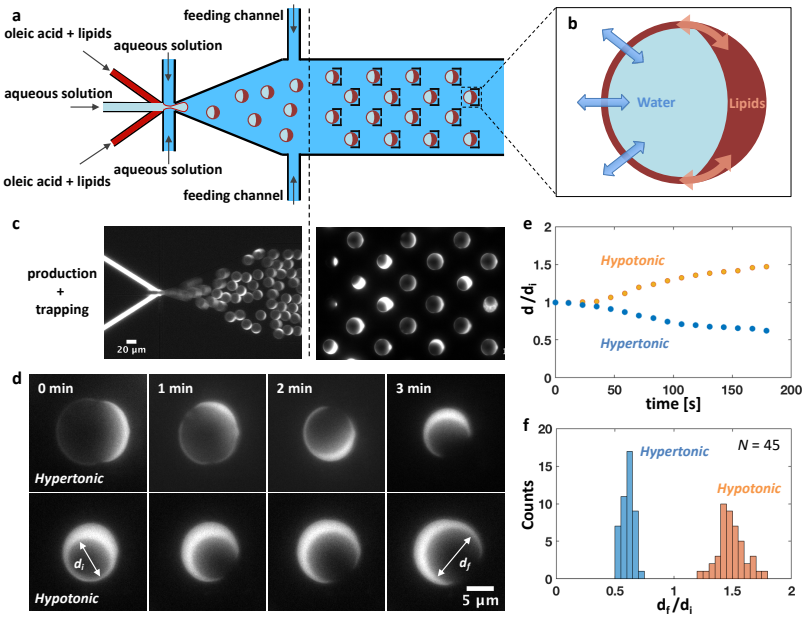

Figure 4.4: **Size control of oleic acid double emulsions on-chip.** **(a)** Design of the microfluidic device: six channels containing an inner aqueous phase, a lipid phase, and an outer aqueous phase cross in a junction where double emulsions are produced. The inner aqueous solution blows a bubble into two streams of DOPC lipids dissolved in oleic acid. The resulting lipid film is pinched-off by the outer aqueous stream, and a double emulsion is formed. An array of traps downstream from the production junction immobilizes the double emulsions, and two additional feeding channels allow further adjustment of the outer aqueous solution forming the environment of the trapped double emulsions. **(b)** Schematic representation of an oleic acid double emulsion: by inducing an osmotic pressure difference, water is able to flow through the membrane to re-establish osmotic equilibrium. At the same time, the side pocket formed by the excess of lipids and solvent can serve as a reservoir for the surface to expand or shrink as required by the volume change. **(c)** Fluorescent image showing the production process and the trapping of oleic acid double emulsions on-chip. RhodPE fluorescent lipids allow the visualization of the lipid phase. **(d)** By inducing an osmotic pressure difference, it is possible to vary the size of double emulsions. Both inner aqueous and outer aqueous solutions initially contain 25 mM sucrose. After a solution containing 200 mM sucrose is flushed through the feeding channel, to re-establish osmotic equilibrium, the double emulsions consequently shrink (top). Afterward, the same batch of double emulsions is re-exposed to the original outer aqueous solution (bottom), so their volume re-expanded. **(e)** Size variation of double emulsions (N = 10) over time: in hypotonic or hypertonic conditions, the diameter of the double emulsions, respectively, increased or decreased over time. **(f)** Histogram showing the ratio of the double emulsion (N = 45) diameters measured at the end (d_f) and at the beginning (d_i) of both processes. In a hypertonic condition, the double emulsions shrink by an average factor of $d_f/d_i = 0.61 \pm 0.01$. When back in hypotonic conditions, we measured a factor $d_f/d_i = 1.49 \pm 0.02$.

hypotonic conditions was quantified by measuring the diameter of each double emulsion after and before each size manipulation. The ratio between these diameters was obtained, and two distinct peaks are observed (Figure 4.4f). This indicates that specific osmolarity differences lead to specific volume re-adjustments and that the size manipulation is a well-controlled process. These data show that the size of the double emulsions can be tuned through the surrounding osmotic conditions in a reversible manner, pro-

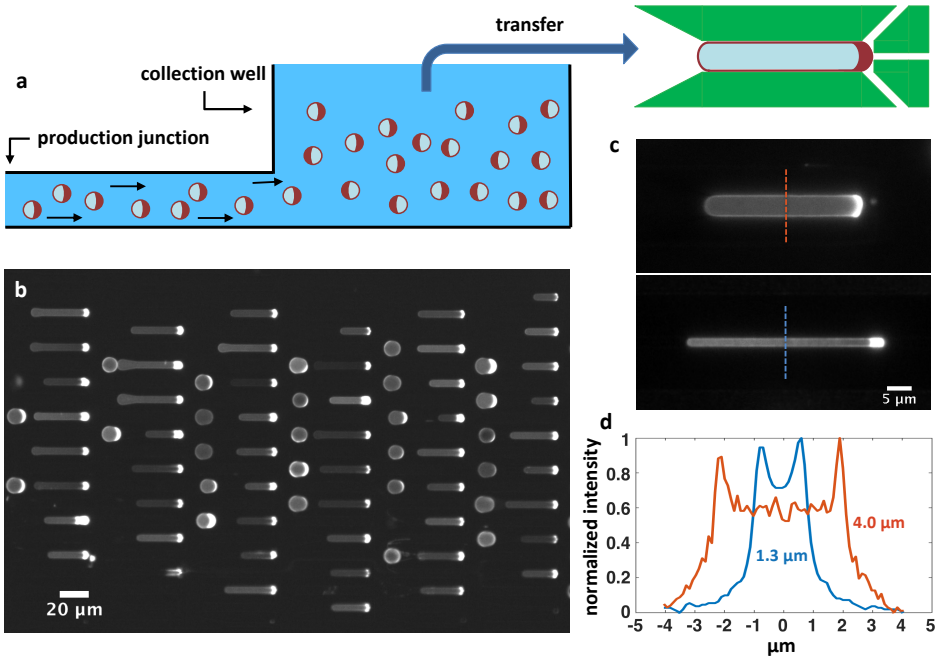

Figure 4.5: **Shape manipulation of oleic acid double emulsions on-chip.** **(a)** Schematic cross section of the collection well: at the end of the microfluidic circuit, after the production junction, a 4 mm diameter hole is punched. The double emulsions contain 5 mM dextran to make them denser than the environment and consequently sink to the bottom of the well. After sufficient production, double emulsions are pipetted from the well and introduced into a device containing the microfluidic traps. **(b)** Fluorescent image showing an array of double emulsions captured in tubular traps. Thanks to their side pocket, which serves as a membrane reservoir, double emulsions are easily reshaped, so that almost all traps in the device (N = 105) contained a double emulsion. Fluorescent signal comes from RhodPE lipids in the lipid phase. **(c)** Zoom-in of single double emulsions in tubular traps of different dimensions: 5 μm diameter (top) and 2 μm diameter (bottom). **(d)** Fluorescent profiles measured at the midcell cross section of tubular double emulsions. The peaks indicate the location of the membrane and provide a measure of the width of the double emulsion.

viding artificial scaffolds for reconstituting cellular systems into containers of adaptable size.

Encouraged by the ease of the size manipulation of double emulsions, we verified that it is possible to deform them into rod shapes resembling bacterial cells. To do so, we punched a hole at the end of the microfluidic circuit ("collection well", Figure 4.5a) and collected double emulsions from the well to transfer them into the device containing the tubular traps. The insertion of double emulsions into the traps is found to be significantly aided by the presence of the side-pocket, since the membrane can dynamically adapt to the new geometry by using material from the side-pocket reservoir to accommodate the changing surface-to-volume ratio. Figure 4.4c–d shows two examples where we deformed double emulsions into tubular geometries with widths of 4 and 1.3 μm. For the former design, we found that a trapping yield of nearly 100% (Figure 4.5b) is easily

achievable, meaning that essentially all the traps (N = 105 per device) contained a double emulsion after a few minutes. As with droplets, filling smaller traps appeared more difficult as double emulsions occasionally broke as a result of the higher pressure required for the entrapping due to the higher hydrodynamic resistance.[56] Given that the deformation of double emulsions worked for the traps with dimensions as small as 1.3 μm, we assumed that it would also be successful for the larger sizes explored with droplets (Figure 4.2b). Next to double emulsions, we also explored the deformation of liposomes from spherical into other shapes. Since liposomes only tolerate a small areal strain (5%) before rupture,[60] we induced an external osmotic pressure to create a reduced volume and thus excess surface area,[61] which made the liposomes "floppy" and predisposed to accommodate the increase in surface-to-volume ratio upon shape change. When transferred inside the trap device, we observed a fraction of liposomes that successfully deformed into the traps, alongside with liposomes showing various defects (Figure S4.3a). Possibly, the induced floppiness made the liposomes prone to damage during the transfer process into the trap device, resulting in the observed heterogeneous population. Still, we managed to obtain liposomes comparable in size and shape to *E. coli* cells (Figure S4.3b), which is a helpful step toward the proper recreation of artificial minimal cells.

To illustrate how our platform can be useful for applications in the synthetic cell field, we encapsulated a variety of fiber-network forming proteins inside nonspherical containers. For these experiments, we chose droplets, due to the ease of their production process. Specifically, we studied three important proteins from diverse biological systems and environments: FtsZ, a key protein necessary for division in almost all bacteria;[62] its eukaryotic homologue tubulin, which is a key element of the cytoskeleton in eukaryotic cells; and collagen,[63] the most abundant protein in extracellular matrix structures.

First, to reconstitute FtsZ bundles on a lipid membrane, a soluble version of ZipA, a protein responsible for anchoring FtsZ to the membrane in Gammaproteobacteria (like *E. coli*),[64] was added to the inner aqueous phase. This soluble version of ZipA, provided with a His-Tag, offers to FtsZ-filaments a way to properly dock to a membrane composed by a mixture of DOPC and DGS-NTA lipids. When such a system was reconstituted in liposomes, FtsZ formed long filamentous bundles on the surface (Figure S4.4), which arranged in a single ring-like structure as the dimensions of the liposomes approached the sub-5 μm range. To verify whether such a system could also be reconstituted into droplets for subsequent shape-manipulation with our microfluidic platform, we assembled a lipid monolayer at the water-oil interface of droplets by adding the necessary lipids to the oil phase. Similar to what was observed in liposomes, both in spherical (Figure 4.6a, top) and in rod-shaped droplets (Figure 4.6a, middle), FtsZ formed long filamentous bundles localized at the droplet surface. The clear presence of bundles on the surface, compared to the lumen, indicates the successful attachment of FtsZ to the lipid monolayer at the interface.

Next, we tested whether it is possible to grow microtubules inside the rod-shaped droplets. Tubulin seeds bound to nonhydrolyzable guanosine triphosphate (GMPCPP) were co-encapsulated in the inner aqueous solution, together with tubulin dimers and guanosine triphosphate (GTP) (Figure 4.6b, middle). As GTP hydrolysis is required for

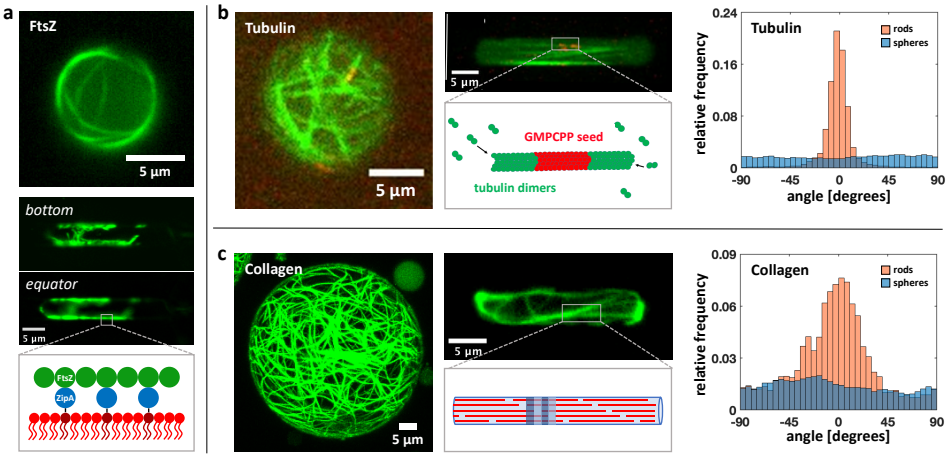

Figure 4.6: **Impact of container geometry on the organization of various protein bundle networks encapsulated inside rod-shaped droplets. (a)** FtsZ filamentous bundles in spherical (top) and rod-shaped (middle) water-in-oil droplets. The FtsZ superstructures visible on the bottom plane of the rod-shaped droplet (middle) adhere to the surface of the droplet, as is also seen on the equatorial plane. A lipid monolayer containing DGS-NTA lipids (dark red) and DOPC (red) is assembled at the water–oil interface. By replacing its transmembrane tail with a His-tag, which can bind to the Ni-tag on the headgroup of DGS-NTA lipids, ZipA functions as a membrane anchor for the FtsZ filaments (bottom). FtsZ is labeled with Alexa488. **(b)** Microtubules grown in spherical (left) and rod-shaped droplets (middle). As shown both qualitatively in the images and quantitatively by the analysis of the fiber orientations (right), the microtubules inside spherical droplets (N = 10) grow without any strong preferential orientation, whereas in the rod-shaped droplets (N = 10), the network appears to follow the symmetry axis of the droplet. For the reconstitution of microtubules, GMPCPP stabilized seeds (labeled with rhodamine tubulin) serve as templates for the growth of microtubules through the addition of tubulin dimers in solution (bottom). Fluorescent HiLyte 488 tubulin was used to label the microtubules. **(c)** Collagen fibril reconstituted inside spherical- (left) and rod-shaped droplets (middle). Similar to what is observed for microtubules, the analysis of the fiber orientation (right) shows that the collagen network in spherical droplets (N = 4) remains weakly organized, but inside the rod-shaped droplets (N = 4), it re-arranges to align with the symmetry axis of the droplet. As sketched (middle-bottom), a collagen fibril is formed by the staggering of collagen triple-helix monomers (red) driven by noncovalent interactions, which give rise to a characteristic periodic pattern (blue and light-blue).

the disassembly of microtubules, the tubulin seeds act as a stable template from which the microtubules can grow. Since the seeds and the tubulin dimers were labeled with different dyes, it was possible to observe long microtubules (green) that were grown from the seeds (red) and spanned the length of the rod-shaped droplet following the prevalent axis of symmetry (Figure 4.6b, right), contrasting to the situation in spherical droplets (Figure 4.6a, left), where the microtubules grew without an obvious preferential orientation. This observation is confirmed by a quantitative analysis of the microtubule orientations: In the spherical droplets, microtubules did not show any strong preferential orientation, while in rod-shaped droplets, the measured angles distinctly peaked around 0°, that is, the microtubules were aligned along the droplet main axis (Figure 4.6b, right).

Finally, we applied our method to an *in vitro* assay for collagen type 1, which is an important component of the extracellular matrix. Figure 4.6c shows that it is possible to

successfully reconstitute collagen type 1 fibers inside rod-shaped droplets. Similar to the microtubules, a quantitative analysis of the fiber orientations (Figure 4.6c, right) showed that the collagen fibers oriented themselves along the symmetry axis of the cylindrical container, which again is markedly different to what is observed in spherical droplets.

4.3. CONCLUSIONS

In this paper, we presented a method that enables the control of the shape and the size of a range of cell-like containers, a useful research tool within the synthetic cell field. In fact, as is schematically illustrated in Figure 4.7, our system provides access to a much broader range of morphologies than is currently possible in the synthetic cell field. By pushing the boundaries of both volume and aspect ratio by 1-2 orders of magnitude as compared to previous methods, we bridged the gap between the dimensions of natural cells and artificial containers inside which the isolated cellular components are reconstituted.

We showed that droplets, double emulsions, and liposomes can be deformed into a variety of shapes, from tubes of different diameters and lengths, to pancake-shape discs with a high aspect ratio between their height and diameter. Second, through the principle of osmosis, we were able to regulate the volume of such artificial cells. And finally, as a proof-of-concept of the range of possibilities that our approach offers, we encapsulated three different filamentous protein networks inside droplets with a tubular shape. The resulting organization of the protein networks in the tubular containers was markedly different from the situation in spherical droplets, underlining the importance of the container shape and size.

Reconstitution of protein bundles such as microtubules and extracellular matrix collagen inside shaped droplets enables us to study how fibrous networks adapt their conformation depending on the geometry of the confinement. Microtubule orientation is an important feature in eukaryotic cells to establish cell polarity: By elongating from the nucleus toward cell extremities, microtubules drive several polarizing factors toward opposite cell poles. Differently from what is observed in spherical droplets, microtubules encapsulated into rod-shaped droplets appeared aligned along the main symmetry axis of the confinement. The shape and dimensions of the confinement, together with the microtubule alignment, are features that well resemble the conditions found in model eukaryotic cells, such as fission yeast.[65] The possibility to control the orientation of cytoskeletal components inside artificial containers thus offers the possibility to reconstitute microtubule-driven polarization in minimal artificial cells. Similar phenomena are observed for the extracellular matrix. *In vivo*, the ECM is secreted and assembled in the narrow spaces between cells, and collagen matrix fibers therefore adapt their arrangement depending on the imposed geometrical constraints. Our microfluidic platform provides microscopic confinements with dimensions spanning a broad range of aspect ratios, resembling those found in some tissues.[66] As *in vivo*, our results indicate that the geometry of the confinement directly influences the collagen matrix configuration. Similar to what is observed in many tissues, *e.g.*, the cornea or the tendon,[67,68] we can in-

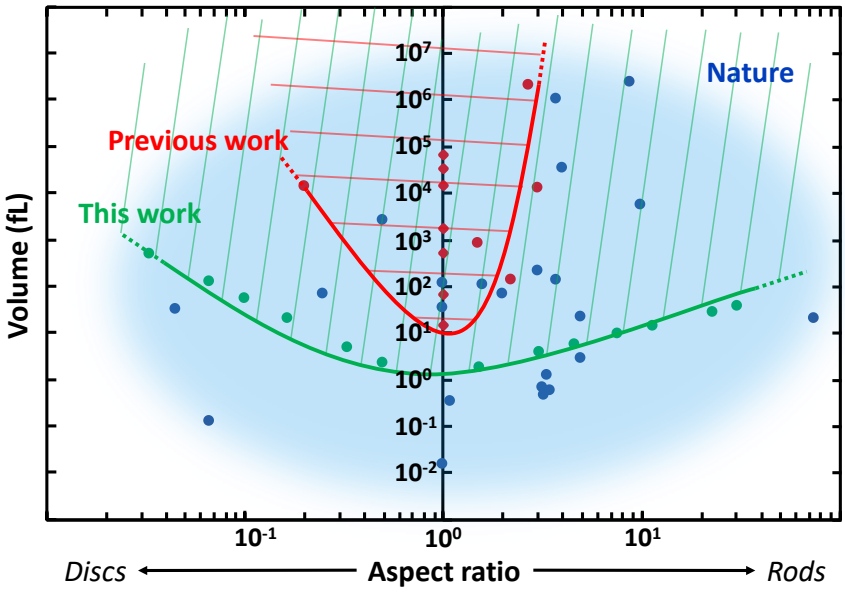

Figure 4.7: **Phase diagram comparing the shape and size of various cells found in nature with the deformable artificial containers used in previous research work and those presented in this paper.** Assuming roughly spheroid-like containers and cells, the morphological space is defined by the aspect ratio of the smallest and the largest axis of the containers (x-axis), and the volume (y-axis). The space is divided between rods (right), spheres (y-axis), and discs (left). In blue, an approximate cloud encircles the morphologies adopted by a selected number of living organisms (blue dots, see Table S4.1). The red dots represent container geometries reported previously in the field (see Table S4.1), with the red line showing the lower morphological boundaries achieved so far. Similarly, the green line delineates the new lower boundaries achieved within this work. Compared to previous research, we expanded the boundaries of volume and aspect ratio by one to two orders of magnitude. This advance enables us to cover a broader range of shapes and sizes and it bridges the gap between artificial and natural cells.

duce the collagen fibers to align along a prevalent symmetry axis. Being able to recreate the orientation of the collagen fibers in the extracellular matrix is of fundamental importance, since the network architecture determines the tissue response to mechanical deformations. Thus, we anticipate that the possibility provided by our method to control the collagen network arrangement *via* the morphology of the container will allow to more closely mimic the architecture and mechanical response of living tissues.

Moreover, since our platform uses deformable containers, it provides the opportunity to observe how protein networks and other biopolymers re-arrange dynamically in response to evolving boundaries and gradual changes in crowding and salt concentrations. The reversibility of the volume change of double emulsions (Figure 4.4) makes it possible to study whether changes in the protein network configuration are reversible or display some form of hysteresis. Given the range of sizes that can be enforced upon vesicles, our approach also allows to study the influence of the confinement surface curvature on the alignment and positioning of membrane-bound proteins, which is key for many

proteins involved in membrane remodeling.

We believe that our approach to shape and size control can be broadly applied. The ability to tune the container volume will, for example, aid the study of how the crowding environment impacts the dynamics of various cellular processes. The approach also allows to explore the relation between membrane curvature and the spatial arrangement of lipids domains and membrane proteins.[69] Finally, similar to recent *in vivo* studies of shape-sculpted bacteria,[16,17,29,30,70] the platform offers the chance to investigate pattern formation and chromosome dynamics as a function of confinement geometry.

4.4. METHODS

MICROFABRICATION

Microfluidic devices were fabricated in a cleanroom with the following protocol. A layer of hexamethyldisilazane (HMDS, BASF SE) was deposited on a 4-in. silicon wafer by spin-coating at 1000 rpm for 1 min. The wafer was baked at 200 °C for 2 min. Subsequently, a layer of NEB22a negative e-beam resist (Sumitomo Chemical) was spin-coated at 1000 rpm for 1 min and baked at 110 °C for 3 min. Correct adhesion of the NEB22a onto the silicon surface is ensured by the first HMDS layer. The designs were written on the coated wafer using electron beam lithography (EBPG-5000+, Raith GmbH, dose: 16 μC cm^{-2}, acceleration voltage: 100 kV, aperture: 400 μm). Post-exposure baking of wafer was performed at 105 °C for 3 min. The patterns were then developed by submerging the wafer in MF322 (Dow Chemical Company) for 1 min, then in diluted MF322 (distilled water:MF322 = 1:10) for 30 s, and finally rinsing in distilled water for 30 s. Bosch process deep reactive-ion etching was used to dry etch the structures into the silicon wafer, with an inductive coupled plasma reactive-ion etcher (Adixen AMS 100 I-speeder). During the process, the pressure was kept at about 0.04 mbar, the temperature of the wafer was kept at 10 °C, while the plasma temperature was 200 °C. The sample holder was held at 200 mm from the plasma source. The etching step involved 200 sccm SF6 for 7 s with the ICP power set to 2000 W without a bias on the wafer itself. The passivation step was done with 80 sccm C4F8 for 3 s with the ICP power set to 2000 W and the bias power on the wafer alternate with a low frequency: 80 W, for 10 ms, and 0 W for 90 ms. Total etching time depended on the desired final height of the device (etching depths for the wafers containing tubular traps used in each figure are listed in Table S4.2). Finally, the excess of resist was removed from the wafer by exposure to oxygen plasma for 10 min. In the case of multiheight devices (Figure 4.2b), the parts of the device with bigger height were patterned on the wafer after the small channels through optical lithography, being careful to properly align the two structures. To do so, silicon wafer was spin-coated with a SU-8 2000 negative resist (Microchem), then soft baked for 3 min at 95 °C, exposed with 140 mJ cm^{-2} dose, and then baked at 4 min 95 °C. Development of the structured followed as described. Silanization of the wafer was done with (tridecafluoro-1,1,2,2-tetrahydrooctyl) trichlorosilane (ABCR GmbH & Co.) overnight in a vacuum desiccator to enhance hydrophobicity of the surface and facilitate subsequent peeling-off of the PDMS.

SOFT LITHOGRAPHY

Single-layer PDMS devices were cured and assembled following the procedure previously described.[71] Multilayer devices for control of water-in-oil droplets size were produced by the assembly of three different layers obtained from three different wafers. A thin layer of PDMS was spin-coated on the device-wafer using a spin-coater (POLOS) at 200 rpm for 5 s and 300 rpm for 20 s (acceleration 100 rpm/s). The second wafer (silanized and without any patterned structures) was used to prepare glass coverslips with a thin PDMS coating. This was achieved by firmly pressing down the coverslips on the wafer through the uncured PDMS, so that a thin PDMS layer was formed beneath them. The third wafer (silanized and without any patterned structures) was used to produce a ~5 mm-thick PDMS slab. All of the wafers were baked for 4 h at 80 °C. The coverslips and the PDMS slab were removed from the plain wafers. The slab was cut into separate pieces (approximately 1 cm × 2 cm), and a 4 mm hole was punched in each of them to create a water chamber using a rapid core punch (World Precision Instruments, 4 mm diameter). Both the PDMS-covered device-wafer and the water chambers were cleaned with isopropanol, blow-dried with nitrogen, and then activated by exposing them to oxygen plasma (Plasmatic System, Inc.) for about 10 s. Each water chamber was then bonded to the device-wafer, taking care that the water chamber was aligned with the part of the device containing the microfluidic traps. The device-wafer with bonded water chambers was then baked for 20 min at 80 °C. Subsequently, the thin PDMS layer with bonded water chambers on top was peeled off from the device-wafer. The devices were cut to size with scissors, and inlet and exit holes were punched into the devices using a rapid core punch (World Precision Instruments, 0.75 mm diameter). Both PDMS coverslips and devices were cleaned with isopropanol and bonded by the oxygen plasma procedure described above. After bonding, devices were left overnight at 80 °C to enhance the device hydrophobicity. For the experiment shown in Figure 4.6a, the channels walls were treated by flushing RainX for 2 min immediately after bonding, in order to further enhance surface hydrophobicity. The solutions were introduced into the devices *via* tubing (Tygon Microbore Tubing, 0.2 mm inner diameter) fitted with home-built metal connectors using pressure-driven microfluidic pumps (Fluigent, controlled by Fluigent MAESFLO software).

IMAGE ACQUISITION AND PROCESSING

Wide-field microscopy measurements were performed using an Olympus IX-81 inverted microscope combined with epifluorescence illumination and appropriate filter sets. Images were acquired and recorded using an Olympus 60× PlanApo (NA 1.45, oil) objective and a Zyla 4.2 PLUS CMOS camera (Andor Technology). The microscope was operated through Micromanager software (version 1.4.14). Confocal microscopy of fluorescent collagen fibers was performed using an inverted Olympus IX81 combined with an Andor Revolution illumination system and a Yokogawa CSU X1 detection system. Images were acquired with a 60× UPlanFLN (NA 1.25, oil) objective and recorded with an EM-CCD Andor iXon X3 DU897 camera. Confocal microscopy of tubulin was performed at 30 °C using Nikon Ti-E microscope (Nikon, Japan) equipped with a Nikon plan Apo 100× 1.45

NA oil immersion objective and an Evolve 512 EMCCD camera (Roper Scientific, Germany). Images of collagen in spherical droplets were captured with an inverted Eclipse Ti Nikon microscope in combination with a Nikon 100× objective (NA 1.49, oil). The resulting images (Figures 1 and 6c) were obtained by a z-stack projection over a depth of 20 μm (0.2 μm step size). Images were analyzed and background appropriately subtracted using Fiji (ImageJ).

LIPID SOLUTIONS

All lipids were purchased from Avanti Polar lipids, Inc. in chloroform solutions. For water-in-oil droplets, lipids were mixed according to the required ratios and dried in a glass tube by desiccating for at least 1 h. The resulting dried film was then resuspended in mineral oil (light oil bioXtra, Sigma-Aldrich) at the desired concentration and sonicated for 30 min at room temperature. For production of double emulsion and liposomes, lipids were mixed in the desired ratios, dried for at least 1 h, and then resuspended in chloroform or ethanol at a concentration of 100 mg mL^{-1}.

DOUBLE EMULSIONS

Three solutions were used to produce double emulsions on-chip: a lipid-containing solution, an inner aqueous solution, and an outer aqueous solution. The lipid-containing solution was composed of 2 mg mL^{-1} lipids (99.9 mol % DOPC + 0.1 mol % Liss Rhod PE) dissolved in oleic acid. In all of the experiments involving double emulsions, both inner and outer aqueous and the feeding channel solutions contained 5% v/v pluronic surfactant (poloxamer 188, Sigma-Aldrich) and 15% v/v glycerol. For the experiments shown in Figure 4.4, the inner aqueous and outer aqueous contained an additional 25 mM sucrose and 5 mM $MgCl_2$. The solution flushed through the feeding channel to induce an osmotic pressure difference contained an additional 200 mM sucrose. To make the double emulsion denser than the surrounding solution and thereby facilitate their extraction from the device (Figure 4.5), an additional 5 mM dextran was added to the inner aqueous solution and osmotically balanced by 5 mM of glucose in the outer aqueous solution.

LIPOSOMES

Liposomes were produced using OLA, an on-chip microfluidic method that results in unilamellar liposomes.[71] All liposomes in Figure S4.3 were made with the lipid-carrying organic phase containing 2 mg mL^{-1} lipids (99.9 mol % DOPC + 0.1 mol % Liss Rhod PE) dissolved in 1-octanol. The inner aqueous phase consisted of 15% v/v glycerol (Figure S4.3a–b), 5 μM Alexa-647 (Figure S4.3a), 5 mM PEG-8000 (Figure S4.3a), 100 mM sucrose (Figure S4.3b), and 5 μM 72-bases long ssDNA (Figure S4.3b); the outer aqueous phase was a solution of 5% v/v pluronic surfactant poloxamer 188 (Figure S4.3a–b), 15% v/v glycerol (Figure S4.3a–b), 5 mM PEG-8000 (Figure S4.3a), 100 mM sucrose (Figure S4.3b); the collection well contained 20 μL (added upon the liposomes reaching the collection well) of 15% v/v glycerol (Figure S4.3a–b), 5 mM PEG-8000 (Figure S4.3a), and 100

mM glucose (Figure S4.3b). After sufficient production (thousands of liposomes in the collection well), liposomes were carefully harvested from the collection well by pipetting out 15 μL of the solution. The liposomes were then pumped into the microfluidic device containing the trap design. For Figure S4.2a, before being pumped into the device containing the traps, the liposomes were mixed with another solution in order to bring the outside environment to a concentration of 8 mM PEG-8000 and 15% v/v glycerol and to induce an osmotic pressure difference.

WATER-IN-OIL DROPLETS

Water-in-oil droplets were produced with two different protocols: droplets in Figure 4.1a containing nucleoids, and droplets in Figures 2a and 6b were produced on-chip *via* a standard cross-junction method, where the aqueous stream gets pinched into droplets by the continuous oil stream. The droplets produced were then trapped downstream from the junction on the same device. All of the droplets showed in the other figures were produced by pipetting up and down a few microliters (2-5 μL) of aqueous solutions into 100 μL of oil solution. The shear forces provided by the pipetting broke the droplets into smaller ones. In Figure 4.2a, to enhance the contrast with the microfluidic traps, fluorescent lipids were added to the oil solution (0.1 mol % Liss Rhod PE) together with 1% v/v SPAN 80 surfactant. For the experiments shown in Figures 2 and 3, the oil solution contained 5% v/v SPAN 80 surfactant. The inner aqueous solution of the droplets shown in Figures 2 and 3 contained 5 μM Alexa 647 fluorescent dye. Additionally, droplets shown in Figure 4.3 contained 200 mM KCl, while the water chamber contained 100, 200, and 300 mM KCl water solution to, respectively, create hypotonic, isotonic, and hypertonic environments for the droplets.

MIN PROTEINS IN DROPLETS

Min protein oscillations in spherical droplets (Figure 4.1a) were observed in water-in-oil droplets containing the following inner aqueous: 0.8 μM MinD, 0.2 μM MinD-Cy3, 0.8 μM MinE, 0.2 μM MinE-Cy5, 5 mM ATP, 4 mM phosphoenolpyruvate, 0.01 mg mL^{-1} of pyruvate kinase, 25 mM Tris-HCl (pH 7.5), 150 mM KCL, and 5 mM MgCl^2. Min proteins were isolated and labeled as described previously. For these experiments, 2 mg mL^{-1} of lipids (66.6 mol % DOPC + 33.3 mol % DOPG + 0.1 mol % Liss Rhod PE) were dissolved in mineral oil as described above.

FTSZ IN DROPLETS

The inner aqueous solution for experiments involving FtsZ in water-in-oil droplets contained 12 μM FtsZ, 6 μM ZipA, 2 mM guanosine triphosphate (GTP), 180 mM KCl, 25 mM Tris-HCl (pH 7.4), 5 mM $MgCl_2$, and 15% v/v glycerol. The oil phase contained 25 mg mL^{-1} of lipids (89.9 mol % DOPC+10 mol % DGS-NTA(Ni) + 0.1 mol % Liss Rhod-PE) for spherical droplets (Figure 4.1), while the same composition at a lower concentration (1 mg mL^{-1}) was used for tubular droplets (Figure 4.6a). Proteins were isolated and labeled as described previously.[72]

NUCLEOIDS IN DROPLETS

The nucleoid isolation protocol is based on Cunha *et al.*[73] The BN2179 strain containing Ori1/Ter3 labels and HUmYpet (AB1157, *Ori1::lacOx240-hygR, Ter3::tetOx240-accC1* Δ*galK::tetR-mCerulean frt,* Δ*leuB::lacI-mCherry frt*) was used for the experiments.[30] Cells were grown in LB medium for 65 h. One mL of culture was spun down at 10000*g* for 2.5 min and resuspended in 475 μL of ice cold sucrose buffer, containing 0.58 M sucrose, 10 mM NaPi buffer (pH 7.0-7.4, Na^2HPO^4/NaH^2PO^4), 10 mM EDTA, and 100 mM NaCl. Immediately after this cold shock, 25 μL of lysozyme solution (1 mg mL^{-1} in ultrapure water) was added, and the cell suspension was briefly vortexed and incubated at room temperature for 15 min, resulting in spheroplasts. To lyse the spheroplasts and obtain isolated nucleoids, 20 μL of the spheroplast suspension was slowly added, using a cut pipet tip, to 1 mL of a solution containing 10 mM NaPi (pH 7.4) and 100 ng mL^{-1} DAPI, after which the Eppendorf was inverted once. This nucleoid suspension was used as the aqueous phase for microfluidically produced water-in-oil droplets of 10 μm diameter. The oil phase was HFE-7500 (Novec Engineering Fluids) with 0.1% v/v Picosurf-1 surfactant (Dolomite Microfluidics). The droplets were immobilized for observation using an array of traps that was placed downstream of the production junction.

TUBULIN IN DROPLETS

The aqueous solution contained MRB80 buffer (80 mM PIPES, 4 mM $MgCl_2$, 1 mM EGTA, pH 6.8) with 39 μM unlabeled tubulin, 1 μM labeled tubulin (HiLyte 488), 3 mM GTP, 50 mM KCl, 4 mM DTT, 2 mg mL^{-1} of bovine serum albumin, 1 mg mL^{-1} of glucose oxidase, 0.5 mg mL^{-1} of catalase, and 50 mM glucose. The oil phase contained 1 mg mL^{-1} of lipids (90% DOPS + 10% PEG2000-PE) in mineral oil with 2% v/v SPAN 80. To nucleate microtubules in droplets, short microtubules (labeled with 12% Hilyte 561 tubulin) of an approximate length of 1 μM were added, stabilized with guanylyl-(α,β)-methylene-diphosphonate (GMPCPP), into the aqueous solution.

COLLAGEN IN DROPLETS

To obtain collagen networks in spherical confinement, telopeptide collagen (TeloCol, CellSystems, supplied at 3.1 mg mL^{-1} in 0.01 M HCl) was brought to a neutral pH with the addition of NaOH (Sigma Aldrich) in phosphate buffered saline (PBS, Sigma Aldrich), to obtain a final collagen concentration of 1 mg mL^{-1} for the spherical droplets and 2 mg mL^{-1} for the droplets in the tubular confinement. The collagen-binding protein CNA35 fluorescently labelled with EGFP (a kind gift from Maarten Merkx, AddGene) was added to collagen in a molar ratio 20 : 1 to allow for collagen network visualization. The oil phase contained 2% v/v SPAN 80 surfactant in mineral oil (Sigma Aldrich). The collagen was allowed to polymerize for at least 90 minutes at room temperature before visualization. For imaging the spherical droplets, the water-in-oil solution was placed between two coverslips (Menzel™Microscope Coverslips 24 mm x 60 mm, #1, Thermo Scientific) separated by a silicone chamber (Grace Bio-Labs CultureWell™chambered coverglass, Sigma Aldrich).

DATA ANALYSIS

The width of the droplets in Figure 4.2 were obtained from the fluorescent profiles measured at the middle of the tubular droplet across its width (see Figure S4.2b) of ten individual droplets per type of trap. For each droplet, the width was obtained from the FWHM (full width at half maximum) of its profile and these values were then averaged to obtain, for each type of trap, a measure of the width. Errors were omitted since the standard error-of-the-mean value (<100 nm) was smaller than the optical resolution of our microscope. The size change of the double emulsions in Figure 4.4 was measured every 12 frames (12 seconds) in the 3-minute time lapse, for both the shrinking process (hypertonic condition) and the expansion process (hypotonic condition). Using Fiji (ImageJ), a circle was manually fitted to the outer contour of the double emulsion, excluding the side-pocket. The errors quoted in Figure 4.4 are the standard error-of-the-mean.

In Figure 4.6, the values of tubulin and collagen bundle orientations were obtained using Fiji (OrientationJ plugin) after background was appropriately subtracted. In Figure 4.7 we calculated the aspect ratio and volumes of the artificial cell containers and natural cells, of which the smallest and largest dimensions are listed in Table S4.1 as obtained from literature (for dots denoted as 'Previous Work' and 'Nature') or as measured in our experiments (for dots labeled as 'This Work'). We approximated the cell shapes as spheroids characterized by longest and shortest semi-axes a and c. Discs correspond to oblate spheroids with $c < a$, while rods are equivalent to prolate spheroids with $c > a$. The aspect ratio in Figure 4.7 is defined as c/a. The volume of a spheroid is calculated as $V = (4\pi/3)\, a^2 c$.

4.5. SUPPLEMENTARY INFORMATION

Category	Type	Largest dimension (μm)	Smallest dimension (μm)	Reference
Previous work	Spheres	3	3	[38, 43]
		5	5	[38, 43]
		10	10	[38, 43]
		15	15	[38, 43]
		30	30	[38, 43]
		40	40	[38, 43]
		50	50	[38, 43]
	Discs	50	10	[38]
	Rods	11	5	[74]
		15	10	[74]
		60	20	[38]
		300	110	[53]
This work	Discs	2	1	
		3	1	
		6	1	
		10	1	
		15	1	
		30	1	
	Rods	3	1.4	
		4	1.4	
		5	1.4	
		10	1.4	
		15	1.3	
		30	1.3	
		40	1.3	
		50	1.3	
Nature	*Escherichia coli*	2.05	0.63	[75]
		2.35	0.67	[75]
		2.34	0.73	[75]
		2.94	0.87	[75]
	Saccharomyces cerevisiae	3	3	[76]
		6	6	[76]
	Schizosaccharomyces pombe	7	3	[74]
		14	3	[74]
	Bacillus subtilis	5	1	[77]

Continued on next page

Table S4.1 – *Continued from previous page*

Category	Type	Largest dimension (μm)	Smallest dimension (μm)	Reference
		10	2	[77]
	S. aureus	0.9	0.82	[78]
	HeLa cells	20	10	[79]
	Red blood cell	8	2	[80]
	Cardiomyocyte	100	10	[81]
		100	25	[81]
	Haloquadratum walsbyi	1.5	0.1	[82]
		11	0.5	[82]
	Onion epidermis	300	80	[83]
	Filamentous *E.coli*	60	0.80	[84]
	Filamentous *Epulopiscium*	600	80	[7]
	Mycoplasma (average size)	0.3	0.3	[85]

Table S4.1: **Dimensions of deformable artificial cell containers and natural cells displayed in Figure 4.7.** The dimensions of the artificial cell containers are taken from 'Previous Work' (spheres, discs and rods) and 'This Work' (discs and rods), whereas the 'Nature' section includes a representative selection of sizes and aspect ratios covered by natural cells used to sketch the blue area in Figure 4.7. For 'Previous Work', we selected spherical containers employed so far in the synthetic cell field. In addition, we included examples of previous attempts at deforming spherical containers into discs and rods. For 'This Work', we selected the largest aspect ratios that we experimentally achieved for this paper. These points then form the lower boundary of the green area in Figure 4.7.

Figure	Etch depth (μm)
2.2b, i (top); 2.3b; 2.6b; 2.8a	5.2
2.2b, iii	3.0
2.2b, iv (bottom); 2.9b	2.5
2.5c ii (bottom)	1.9
2.6a; 2.6c; 2.5b; 2.5c, i (top); 2.9a	5.3

Table S4.2: **The etch depths of the wafers containing tubular traps used in the various figures.** The measurements were done at three different points on the wafer using a profilometer. The quoted value is the mean of these measurements.

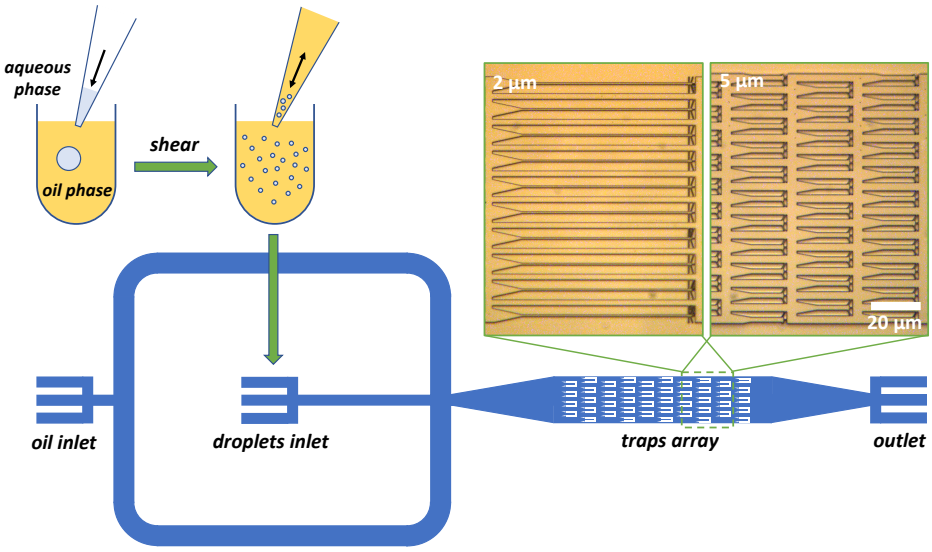

Figure S4.1: **Schematic of the experimental procedure and device operation to obtain rod-shape droplets.** A few microliters (2-5 μL) of an aqueous solution are pipetted into 100 μL of oil solution. Shear forces induced by repeatedly pipetting the solution up and down break the large droplets into smaller ones.[43] Droplet coalescence is prevented by surfactant molecules dissolved in the oil, which stabilize the water-oil interface of the droplets. The oil solution containing the droplets and a second oil solution without droplets are inserted *via* a pressure-driven pump into the device through two different inlets, as indicated. Past a junction where these two fluid streams meet, the droplets enter into a chamber containing an array of microfluidic traps. Once a satisfying number of droplets is caught at the entrance of the traps, the pressure of the outer oil stream is increased. In this way, the droplets get pushed inside the traps and thus deformed into the desired shape. The droplets that do not get caught by a trap are pushed towards the outlet and removed from the chamber. The pressure required to insert the droplets into the device is lower than the one required to insert the droplets inside the traps, and both pressures strongly depend on the dimensions of the device. As representative examples, two trap designs with dimensions on the opposite sides of the size range explored in this work are visible in the bright-field microscopy images in the top right part of the figure. In the case of traps with a 5 μm x 5 μm square cross-section (right), we experience that a minimum overpressure of ~0.1 bar is required to insert droplets into the device, which has to be increased to roughly ~0.2 bar to squeeze the droplets into the traps. For traps with a 2 μm x 2 μm cross-section, the minimal overpressures required to insert droplets into the device and then into the traps are respectively around ~0.5 bar and ~0.8 bar. The droplets remained stably trapped as long as the pressure is kept constant. Otherwise, it is possible to release the droplets by lowering the pressure, as they slide back towards the entrance of the trap to minimize deformation. Alternatively, by increasing the pressure up to >1 bar, the droplets would eventually escape through the small exit holes of the traps. The detailed design of the traps varies depending on the final desired shape to be imposed on the artificial containers. Given that smaller structures require higher pressures, the walls of narrower traps are wider, in order to ensure that the trap walls remain bonded to the top PDMS membrane during the experiments. At the end of each trap, exit holes provide fluid flow through the structure. Generally speaking, the width of the exit hole equals half of the trap width. Also, to further facilitate the flow through the smaller traps, the number of lateral exit holes is increased. Finally, as the artificial containers preserve their original volume during deformation, the traps with smaller cross-sections are designed with an increased length. As the fluidic chamber containing the traps has the same dimension for all designs, the chamber contains a different number of traps depending on the trap dimensions: 57 for the 2 μm design and 105 for the 5 μm design. In principle the chamber can be designed as large as preferred, for example to accommodate a higher number of traps, as these devices are scalable, due the lithography-based method of fabrication.

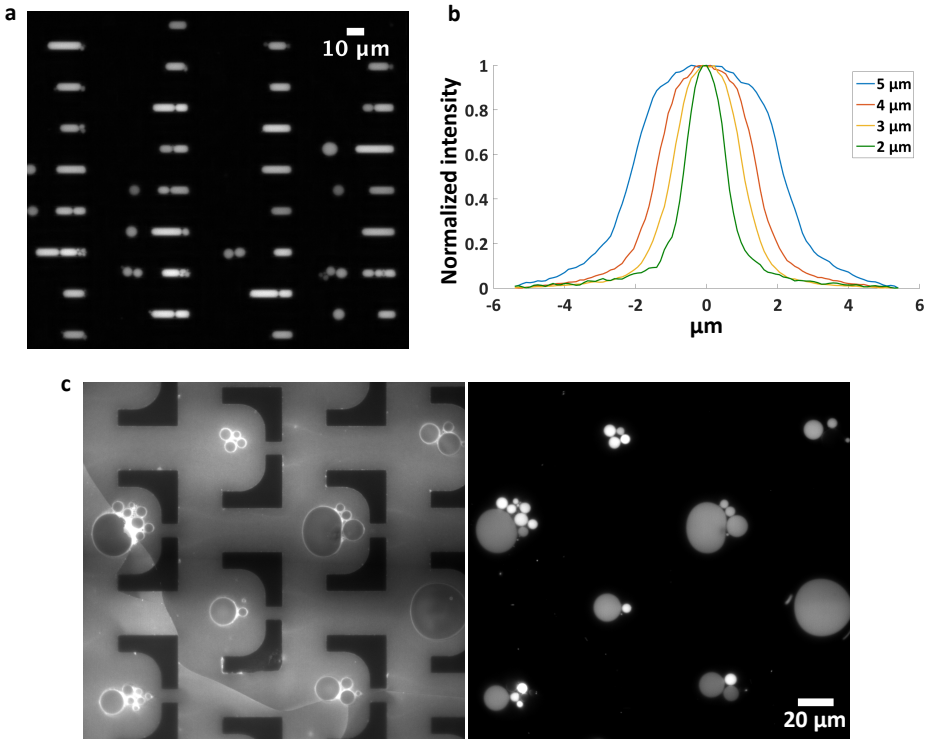

Figure S4.2: **Fluorescent images of droplets deformed into different shapes by means of a microfluidic device. (a)** Array of 5 μm-wide microfluidic traps containing water-in-oil droplets. Fluorescent signal comes from Alexa 647 fluorescent dye in the aqueous phase. **(b)** Normalized fluorescent profile of droplets in Figure 4.2b, measured at the mid-length equatorial cross section of tubular droplets over traps of different width. The plot shows the clear difference between the droplet widths. **(c)** 2 μm high disc-shaped droplets immobilized in an array of microfluidic traps. On the left image, the fluorescence signal comes from fluorescent lipids dissolved in the oil phase and partitioned at the droplet interface, while on the right image fluorescent signal comes from Alexa 647 fluorescent dye in the aqueous phase.

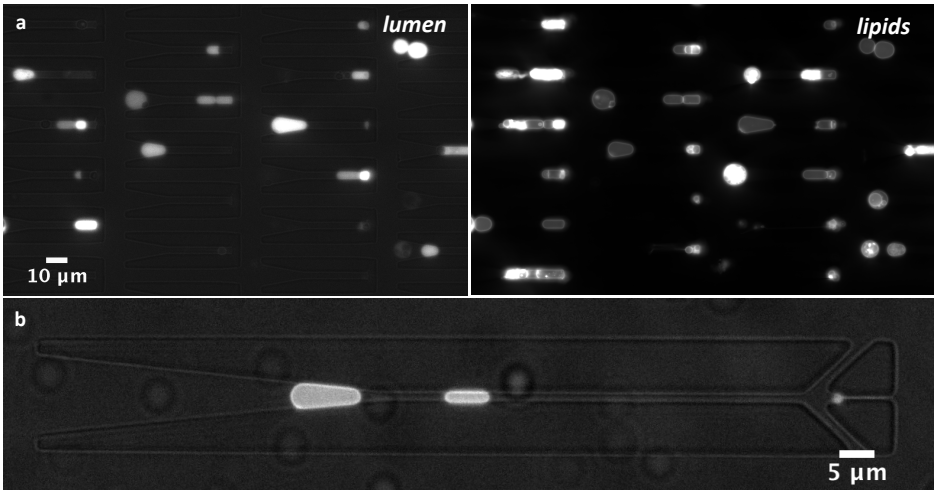

Figure S4.3: **Fluorescent images of liposomes into tubular traps. (a)** Array of tubular traps containing liposomes. Left: fluorescent signal coming from Alexa 647 inside the liposomes. Right: fluorescent signal coming from inclusion of Rhod PE embedded within the lipid membrane. Once trapped the resulting population shows some tense liposomes that did not enter into the traps, as well as liposomes that lost the fluorescent dye that was originally encapsulated at the moment of the production. We conjecture that the membrane floppiness induced by the osmotic pressure difference make the liposomes prone to split or simply to suffer temporary membrane defects during the insertion into the microfluidic chip, which would explain both the lack of membrane floppiness and loss of fluorescent dye from the lumen. **(b)** Liposome deformed into a bacteria shape and size like *E. coli* (width ~1 μm).

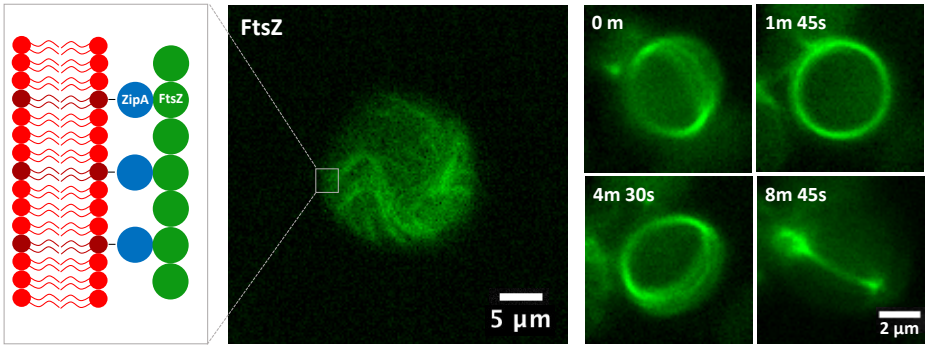

Figure S4.4: **Reconstitution of FtsZ bundles inside unilamellar liposomes.** As schematically illustrated on the left panel, FtsZ filaments bind to the lipid membrane by interacting with a soluble version of the membrane anchor protein ZipA. The arrangement of bundles on the liposome surface depends on the liposome size. In a population of liposomes ($N = 10$) with average diameter $d = 9.2 \pm 0.3$ μm (middle) multiple randomly arranged bundles ($n = 3.9 \pm 0.2$) are visible on the membrane. In contrast, a population of liposomes ($N = 10$) with a smaller diameter ($d = 3.8 \pm 0.2$ μm), closer to the natural cell size, shows FtsZ bundles that are arranged in one single ring, as observed in the time lapse on the right. Fluorescent FtsZ signal comes from Alexa488 fluorescent dye.

REFERENCES

(1) Randich, A. M.; Brun, Y. V. Molecular mechanisms for the evolution of bacterial morphologies and growth modes. *Frontiers in Microbiology* **2015**, *6*, 580.

(2) Bisson-Filho, A. W.; Zheng, J.; Garner, E. Archaeal imaging: Leading the hunt for new discoveries. *Molecular Biology of the Cell* **2018**, *29*, 1675–1681.

(3) Ivakov, A.; Persson, S. Plant cell shape: modulators and measurements. *Frontiers in Plant Science* **2013**, *4*, 439.

(4) Steinman, R. M.; Cohn, Z. A. Identification of a novel cell type in peripheral lymphoid organs of mice. *Journal of Experimental Medicine* **1973**, *137*, 1142–1162.

(5) Margolin, W. Sculpting the Bacterial Cell. *Current Biology* **2009**, *19*, R812–R822.

(6) Young, K. D. Bacterial shape. *Molecular Microbiology* **2003**, *49*, 571–580.

(7) Young, K. D. The Selective Value of Bacterial Shape. *Microbiology and Molecular Biology Reviews* **2006**, *70*, 660–703.

(8) Mulla, Y.; Aufderhorst-Roberts, A.; Koenderink, G. H. Shaping up synthetic cells. *Physical Biology* **2018**, *15*, 041001.

(9) Fletcher, D. A.; Mullins, R. D. Cell mechanics and the cytoskeleton. *Nature* **2010**, *463*, 485–492.

(10) Young, K. D. Bacterial morphology: why have different shapes? *Current Opinion in Microbiology* **2007**, *10*, 596–600.

(11) Justice, S. S.; Hunstad, D. A.; Cegelski, L.; Hultgren, S. J. Morphological plasticity as a bacterial survival strategy. *Nature Reviews Microbiology* **2008**, *6*, 162–168.

(12) Chen, C. S.; Mrksich, M.; Huang, S.; Whitesides, G. M.; Ingber, D. E. Geometric Control of Cell Life and Death. *Science* **1997**, *276*, 1425–1428.

(13) Mogilner, A.; Keren, K. The Shape of Motile Cells. *Current Biology* **2009**, *19*, R762–R771.

(14) Smith, W. P. J.; Davit, Y.; Osborne, J. M.; Kim, W.; Foster, K. R.; Pitt-Francis, J. M. Cell morphology drives spatial patterning in microbial communities. *Proceedings of the National Academy of Sciences* **2017**, *114*, E280–E286.

(15) Yang, D. C.; Blair, K. M.; Salama, N. R. Staying in Shape: the Impact of Cell Shape on Bacterial Survival in Diverse Environments. *Microbiology and Molecular Biology Reviews* **2016**, *80*, 187–203.

(16) Wu, F.; van Schie, B. G. C.; Keymer, J. E.; Dekker, C. Symmetry and scale orient Min protein patterns in shaped bacterial sculptures. *Nature Nanotechnology* **2015**, *10*, 719–726.

(17) Mannik, J.; Wu, F.; Hol, F. J. H.; Bisicchia, P.; Sherratt, D. J.; Keymer, J. E.; Dekker, C. Robustness and accuracy of cell division in Escherichia coli in diverse cell shapes. *Proceedings of the National Academy of Sciences* **2012**, *109*, 6957–6962.

(18) Frey, E.; Halatek, J.; Kretschmer, S.; Schwille, P., Protein Pattern Formation In *Physics of Biological Membranes*, Bassereau, P., Sens, P., Eds.; 3; Springer International Publishing: Cham, 2018; Vol. 113, pp 229–260.

(19) Vos, B. E.; Liebrand, L. C.; Vahabi, M.; Biebricher, A.; Wuite, G. J. L.; Peterman, E. J. G.; Kurniawan, N. A.; MacKintosh, F. C.; Koenderink, G. H. Programming the mechanics of cohesive fiber networks by compression. *Soft Matter* **2017**, *13*, 8886–8893.

(20) Dragoš, A.; Kovács, Á. T. The Peculiar Functions of the Bacterial Extracellular Matrix. *Trends in Microbiology* **2017**, *25*, 257–266.

(21) Govindan, B. S.; Spillman, W. B. Steady states of a microtubule assembly in a confined geometry. *Physical Review E* **2004**, *70*, 032901.

(22) Zelinski, B.; Müller, N.; Kierfeld, J. Dynamics and length distribution of microtubules under force and confinement. *Physical Review E* **2012**, *86*, 041918.

(23) Lagomarsino, M. C.; Tanase, C.; Vos, J. W.; Emons, A. M. C.; Mulder, B. M.; Dogterom, M. Microtubule Organization in Three-Dimensional Confined Geometries: Evaluating the Role of Elasticity Through a Combined In Vitro and Modeling Approach. *Biophysical Journal* **2007**, *92*, 1046–1057.

(24) Junier, I.; Boccard, F.; Espéli, O. Polymer modeling of the E. coli genome reveals the involvement of locus positioning and macrodomain structuring for the control of chromosome conformation and segregation. *Nucleic acids research* **2014**, *42*, 1461–1473.

(25) Marenduzzo, D.; Micheletti, C.; Orlandini, E. Biopolymer organization upon confinement. *Journal of Physics: Condensed Matter* **2010**, *22*, 283102.

(26) Jun, S.; Mulder, B. Entropy-driven spatial organization of highly confined polymers: Lessons for the bacterial chromosome. *Proceedings of the National Academy of Sciences* **2006**, *103*, 12388–12393.

(27) Olson, M. F.; Sahai, E. The actin cytoskeleton in cancer cell motility. *Clinical & Experimental Metastasis* **2009**, *26*, 273–287.

(28) McGregor, A. L.; Hsia, C.-R.; Lammerding, J. Squish and squeeze — the nucleus as a physical barrier during migration in confined environments. *Current Opinion in Cell Biology* **2016**, *40*, 32–40.

(29) Wu, F.; Swain, P.; Kuijpers, L.; Zheng, X.; Felter, K.; Guurink, M.; Solari, J.; Jun, S.; Shimizu, T. S.; Chaudhuri, D.; Mulder, B.; Dekker, C. Cell Boundary Confinement Sets the Size and Position of the E. coli Chromosome. *Current Biology* **2019**, *29*, 2131–2144.

(30) Wu, F.; Japaridze, A.; Zheng, X.; Wiktor, J.; Kerssemakers, J. W. J.; Dekker, C. Direct imaging of the circular chromosome in a live bacterium. *Nature Communications* **2019**, *10*, 2194.

(31) Schwille, P. Jump-starting life? Fundamental aspects of synthetic biology. *The Journal of Cell Biology* **2015**, *210*, 687–690.

(32) Szostak, J. W.; Bartel, D. P.; Luisi, P. L. Synthesizing life. *Nature* **2001**, *409*, 387–390.

(33) Spoelstra, W. K.; Deshpande, S.; Dekker, C. Tailoring the appearance: what will synthetic cells look like? *Current Opinion in Biotechnology* **2018**, *51*, 47–56.

(34) Buddingh', B. C.; van Hest, J. C. M. Artificial Cells: Synthetic Compartments with Life-like Functionality and Adaptivity. *Accounts of Chemical Research* **2017**, *50*, 769–777.

(35) Alvarado, J.; Mulder, B. M.; Koenderink, G. H. Alignment of nematic and bundled semiflexible polymers in cell-sized confinement. *Soft Matter* **2014**, *10*, 2354–2364.

(36) Sanchez, T.; Chen, D. T.; Decamp, S. J.; Heymann, M.; Dogic, Z. Spontaneous motion in hierarchically assembled active matter. *Nature* **2012**, *491*, 431–434.

(37) Chanasakulniyom, M.; Martino, C.; Paterson, D.; Horsfall, L.; Rosser, S.; Cooper, J. M. Expression of membrane-associated proteins within single emulsion cell facsimiles. *Analyst* **2012**, *137*, 2939–2943.

(38) Mellouli, S.; Monterroso, B.; Vutukuri, H. R.; Brinke, E. T.; Chokkalingam, V.; Rivas, G.; Huck, W. T. Self-organization of the bacterial cell-division protein FtsZ in confined environments. *Soft Matter* **2013**, *9*, 10493–10500.

(39) Miyazaki, M.; Chiba, M.; Eguchi, H.; Ohki, T.; Ishiwata, S. Cell-sized spherical confinement induces the spontaneous formation of contractile actomyosin rings in vitro. *Nature Cell Biology* **2015**, *17*, 480–489.

(40) Good, M. C.; Vahey, M. D.; Skandarajah, A.; Fletcher, D. A.; Heald, R. Cytoplasmic volume modulates spindle size during embryogenesis. *Science* **2013**, *342*, 856–860.

(41) Sokolova, E.; Spruijt, E.; Hansen, M. M. K.; Dubuc, E.; Groen, J.; Chokkalingam, V.; Piruska, A.; Heus, H. A.; Huck, W. T. S. Enhanced transcription rates in membrane-free protocells formed by coacervation of cell lysate. *Proceedings of the National Academy of Sciences* **2013**, *110*, 11692–11697.

(42) Van Nies, P.; Westerlaken, I.; Blanken, D.; Salas, M.; Mencía, M.; Danelon, C. Self-replication of DNA by its encoded proteins in liposome-based synthetic cells. *Nature Communications* **2018**, *9*, 1583.

(43) Zieske, K.; Chwastek, G.; Schwille, P. Protein Patterns and Oscillations on Lipid Monolayers and in Microdroplets. *Angewandte Chemie - International Edition* **2016**, *55*, 13455–13459.

(44) Deng, N.-N.; Vibhute, M. A.; Zheng, L.; Zhao, H.; Yelleswarapu, M.; Huck, W. T. S. Macromolecularly Crowded Protocells from Reversibly Shrinking Monodisperse Liposomes. *Journal of the American Chemical Society* **2018**, *140*, 7399–7402.

(45) Zieske, K.; Schwille, P. Reconstitution of pole-to-pole oscillations of min proteins in microengineered polydimethylsiloxane compartments. *Angewandte Chemie - International Edition* **2013**, *52*, 459–462.

(46) Holy, T. E.; Dogterom, M.; Yurke, B.; Leibler, S. Assembly and positioning of microtubule asters in microfabricated chambers. *Proceedings of the National Academy of Sciences* **1997**, *94*, 6228–6231.

(47) Deshpande, S.; Pfohl, T. Real-Time Dynamics of Emerging Actin Networks in Cell-Mimicking Compartments. *PLOS ONE* **2015**, *10*, e0116521.

(48) Huebner, A.; Bratton, D.; Whyte, G.; Yang, M.; Demello, A. J.; Abell, C.; Hollfelder, F. Static microdroplet arrays: A microfluidic device for droplet trapping, incubation and release for enzymatic and cell-based assays. *Lab on a Chip* **2009**, *9*, 692–698.

(49) Wang, W.; Yang, C.; Li, C. M. On-demand microfluidic droplet trapping and fusion for on-chip static droplet assays. *Lab on a chip* **2009**, *9*, 1504–6.

(50) Shi, W.; Qin, J.; Ye, N.; Lin, B. Droplet-based microfluidic system for individual Caenorhabditis elegans assay. *Lab on a Chip* **2008**, *8*, 1432–1435.

(51) Yu, L.; Chen, M. C.; Cheung, K. C. Droplet-based microfluidic system for multicellular tumor spheroid formation and anticancer drug testing. *Lab on a Chip* **2010**, *10*, 2424–2432.

(52) Hunt, T. P.; Issadore, D.; Westervelt, R. M. Integrated circuit/microfluidic chip to programmably trap and move cells and droplets with dielectrophoresis. *Lab Chip* **2008**, *8*, 81–87.

(53) Boukellal, H.; Selimović, Š.; Jia, Y.; Cristobal, G.; Fraden, S.; Selimović, E.; Jia, Y.; Cristobal, G.; Fraden, S. Simple, robust storage of drops and fluids in a microfluidic device. *Lab Chip* **2009**, *9*, 331–338.

(54) Christopher, G. F.; Bergstein, J.; End, N. B.; Poon, M.; Nguyen, C.; Anna, S. L. Coalescence and splitting of confined droplets at microfluidic junctions. *Lab on a Chip* **2009**, *9*, 1102.

(55) Deshpande, S.; Spoelstra, W. K.; van Doorn, M.; Kerssemakers, J.; Dekker, C. Mechanical Division of Cell-Sized Liposomes. *ACS Nano* **2018**, *12*, 2560–2568.

(56) McGrath, J.; Jimenez, M.; Bridle, H. Deterministic lateral displacement for particle separation: a review. *Lab Chip* **2014**, *14*, 4139–4158.

(57) Shim, J.-u.; Cristobal, G.; Link, D. R.; Thorsen, T.; Jia, Y.; Piattelli, K.; Fraden, S. Control and Measurement of the Phase Behavior of Aqueous Solutions Using Microfluidics. *Journal of the American Chemical Society* **2007**, *129*, 8825–8835.

(58) Shum, H. C.; Lee, D.; Yoon, I.; Kodger, T.; Weitz, D. A. Double Emulsion Templated Monodisperse Phospholipid Vesicles. *Langmuir* **2008**, *24*, 7651–7653.

(59) Shum, H. C.; Santanach-Carreras, E.; Kim, J. W.; Ehrlicher, A.; Bibette, J.; Weitz, D. A. Dewetting-induced membrane formation by adhesion of amphiphile-laden interfaces. *Journal of the American Chemical Society* **2011**, *133*, 4420–4426.

(60) Hallett, F. R.; Marsh, J.; Nickel, B. G.; Wood, J. M. Mechanical properties of vesicles. II. A model for osmotic swelling and lysis. *Biophysical Journal* **1993**, *64*, 435–442.

(61) Seifert, U.; Berndl, K.; Lipowsky, R. Shape transformations of vesicles: Phase diagram for spontaneous- curvature and bilayer-coupling models. *Physical Review A* **1991**, *44*, 1182–1202.

(62) Bi, E.; Lutkenhaus, J. FtsZ ring structure associated with division in Escherichia coli. *Nature* **1991**, *354*, 161–164.

(63) Ramachandran, G. N.; Kartha, G. Structure of collagen. *Nature* **1954**, *174*, 269–270.

(64) Den Blaauwen, T.; Hamoen, L. W.; Levin, P. A. The divisome at 25: the road ahead. *Current Opinion in Microbiology* **2017**, *36*, 85–94.

(65) Chang, F.; Martin, S. G. Shaping fission yeast with microtubules. *Cold Spring Harbor perspectives in biology* **2009**, *1*, a001347.

(66) Tønnesen, J.; Inavalli, V. K.; Nägerl, U. V. Super-Resolution Imaging of the Extracellular Space in Living Brain Tissue. *Cell* **2018**, *172*, 1108–1121.

(67) Provenzano, P. P.; Vanderby, R. Collagen fibril morphology and organization: Implications for force transmission in ligament and tendon. *Matrix Biology* **2006**, *25*, 71–84.

(68) Gutsmann, T.; Fantner, G. E.; Venturoni, M.; Ekani-Nkodo, A.; Thompson, J. B.; Kindt, J. H.; Morse, D. E.; Fygenson, D. K.; Hansma, P. K. Evidence that Collagen Fibrils in Tendons Are Inhomogeneously Structured in a Tubelike Manner. *Biophysical Journal* **2003**, *84*, 2593–2598.

(69) McMahon, H. T.; Gallop, J. L. Membrane curvature and mechanisms of dynamic cell membrane remodelling. *Nature* **2005**, *438*, 590–596.

(70) Söderström, B.; Badrutdinov, A.; Chan, H.; Skoglund, U. Cell shape-independent FtsZ dynamics in synthetically remodeled bacterial cells. *Nature Communications* **2018**, *9*, 4323.

(71) Deshpande, S.; Caspi, Y.; Meijering, A. E. C.; Dekker, C. Octanol-assisted liposome assembly on chip. *Nature Communications* **2016**, *7*, 10447.

(72) Fanalista, F.; Deshpande, S.; Lau, A.; Pawlik, G.; Dekker, C. FtsZ-Induced Shape Transformation of Coacervates. *Advanced Biosystems* **2018**, *2*, 1800136.

(73) Cunha, S.; Woldringh, C. L.; Odijk, T. Polymer-Mediated Compaction and Internal Dynamics of Isolated Escherichia Coli Nucleoids. *Journal of Structural Biology* **2001**, *136*, 53–66.

(74) Taberner, N.; Lof, A.; Roth, S.; Lamers, D.; Zeijlemaker, H.; Dogterom, M., In vitro systems for the study of microtubule-based cell polarity in fission yeast In *Methods in Cell Biology*, 2015; Vol. 128, pp 1–22.

(75) Pierucci, O. Dimensions of Escherichia coli at various growth rates: model for envelope growth. *Journal of bacteriology* **1978**, *135*, 559–574.

(76) Ahmad, M.; Nakajima, M.; Kojima, S.; Homma, M.; Fukuda, T. The Effects of Cell Sizes, Environmental Conditions, and Growth Phases on the Strength of Individual W303 Yeast Cells Inside ESEM. *IEEE Transactions on NanoBioscience* **2008**, *7*, 185–193.

(77) Marshall, W. F.; Young, K. D.; Swaffer, M.; Wood, E.; Nurse, P.; Kimura, A.; Frankel, J.; Wallingford, J.; Walbot, V.; Qu, X.; Roeder, A. H. What determines cell size? *BMC Biology* **2012**, *10*, 101.

(78) Maass, S.; Sievers, S.; Zühlke, D.; Kuzinski, J.; Sappa, P. K.; Muntel, J.; Hessling, B.; Bernhardt, J.; Sietmann, R.; Völker, U.; Hecker, M.; Becher, D. Efficient, Global-Scale Quantification of Absolute Protein Amounts by Integration of Targeted Mass Spectrometry and Two-Dimensional Gel-Based Proteomics. *Analytical Chemistry* **2011**, *83*, 2677–2684.

(79) Zhao, L.; Kroenke, C. D.; Song, J.; Piwnica-Worms, D.; Ackerman, J. J. H.; Neil, J. J. Intracellular water-specific MR of microbead-adherent cells: the HeLa cell intracellular water exchange lifetime. *NMR in Biomedicine* **2008**, *21*, 159–164.

(80) Diez-Silva, M.; Dao, M.; Han, J.; Lim, C.-T.; Suresh, S. Shape and Biomechanical Characteristics of Human Red Blood Cells in Health and Disease. *MRS Bulletin* **2010**, *35*, 382–388.

(81) Göktepe, S.; Abilez, O. J.; Parker, K. K.; Kuhl, E. A multiscale model for eccentric and concentric cardiac growth through sarcomerogenesis. *Journal of Theoretical Biology* **2010**, *265*, 433–442.

(82) Albers, S.; Eichler, J.; Aebi, M., Archaea In *Essentials of Glycobiology*; Cold Spring Harbor Laboratory Press: 2017.

(83) Suslov, D.; Verbelen, J.-P.; Vissenberg, K. Onion epidermis as a new model to study the control of growth anisotropy in higher plants. *Journal of Experimental Botany* **2009**, *60*, 4175–4187.

(84) Lederer, F. L.; Günther, T. J.; Weinert, U.; Raff, J.; Pollmann, K. Development of functionalised polyelectrolyte capsules using filamentous Escherichia coli cells. *Microbial Cell Factories* **2012**, *11*, 163.

(85) Zhao, H.; Dreses-Werringloer, U.; Davies, P.; Marambaud, P. Amyloid-beta peptide degradation in cell cultures by mycoplasma contaminants. *BMC Research Notes* **2008**, *1*, 38.

5

COMPACTION OF AN ISOLATED BACTERIAL CHROMOSOME BY YEAST CONDENSIN

DNA loops are the fundamental structural features of genome organization, as demonstrated by contact probabilities in Hi-C maps and high-resolution imaging in cells, which have shown topologically associated domains (TADs). Single-molecule *in vitro* experiments using 50 kbp DNA stretched on a surface have confirmed that Structural Maintenance of Chromosomes (SMC) complexes in various organisms are capable of extruding loops of DNA. However, it remains unclear how the formation of a single DNA loop in these *in vitro* experiments translates to the situation in a cell that contains megabases of DNA that is acted upon by large numbers of loop extruders. To shed light on this question, we isolated megabasepair-sized DNA from bacterial cells, added yeast condensin, and observed the resulting DNA compaction. Real-time compaction was observed, which was dependent on condensin concentration. Surprisingly, the loop-extruding action of condensin led to a heterogeneous chromosomal structure with persistent and dense DNA clusters, up to 150 kbp in size, as well as DNA-void regions. As the DNA extracted from the cells still contained native DNA-binding proteins and possibly residual amounts of supercoiling, it is not fully evident to what extent these structures are intrinsic, and future experiments on fully deproteinated genomes will need to verify this. Yet, these first experiments raise interesting questions on the heterogenous structure of SMC-compacted genomes.

This chapter is an adaptation of the thesis research of Roman Barth who worked on this for his master's project under supervision of Anthony Birnie and Cees Dekker.

5.1. INTRODUCTION

The organization of the genome has profound functional consequences for transcription, DNA repair, and genome segregation. There is a large variety of factors which govern genome structure and dynamics in cells, ranging from nucleosomes,[1] to supercoiling induced by transcription,[2] and epigenetic activation and repression of genes.[3] DNA looping and phase separation have come to the forefront as the organizing principles by which many observations concerning chromosomes in eukaryotic cells can be explained.[4–6]

The current hypothesis is that Structural Maintenance of Chromosomes (SMC) protein complexes are the main elements responsible for DNA looping in both interphase and metaphase stages of the cell cycle. The SMC complexes are ring-like structures, in which a 'hinge' domain and a 'heads' domain are connected by two coiled-coil arms. The heads and hinge domains both have DNA binding sites, and the head domains contain ATP binding sites. The head domains additionally feature a kleisin 'safety belt' mechanism to hold the DNA in place.[7] Overall, the structure of yeast condensin is considered to be quite flexible and dynamic as determined by high-speed AFM.[8] Single-molecule fluorescence experiments, using DNA molecules loosely stretched on a surface, have shown that condensin (yeast,[9] human,[10] and *X. laevis*[11]), cohesin (human[12,13] and *X. laevis*[11]), and also SMC5/6[14] are able to extrude loops of DNA in an ATP-dependent manner. These experiments showed that the SMCs are fast but weak motors, which means that they extrude DNA *in vitro* at rates of ~1 kbp/s but that their motor action stalls at forces below a pico-Newton. Their ATP consumption is relatively low, burning only a few ATP molecules per second. Contrary to condensin, cohesin requires assistance from loading factors to bind to the DNA, namely NIPBL-Mau2.[12,13] The molecular details of the SMC motor mechanism are an open question, although several models have recently been proposed such as the hold-and-feed model,[15] swing-and-clamp model,[16] Brownian-ratchet model,[17] DNA-segment capture model,[18,19] scrunching model,[20] and a modification of the hold-and-feed model (Oldenkamp *et al.*[21]) that allows for non-topological binding of the DNA by condensin.

The roles of cohesin and condensin are different during the cell cycle. Broadly speaking, cohesin governs the interphase, while condensin is responsible for structuring the mitotic chromosome. From contact maps generated by chromosome conformation capture-related methods (3/4/5/Hi/Micro-C)[22,23], it is known that interphase chromosomes are organized into regions of enhanced contact frequencies, also called interaction domains. Generally speaking, there are two types of domains, namely compartmental domains and Topologically Associated Domains (TAD). While the former is governed by the process of phase separation, the latter are connected to the action of cohesin. The boundaries of these TADs are often marked by convergently oriented CTCF-binding sites, which act as barriers for the loop extruding cohesin.[24–26] The packing of the interphase chromosome is rather loose and dynamic. The TADs are not only a feature in population averaged contact maps, but they also represent actual physical structures in the cell. Sub-TAD domains of a few hundred nanometers in size have been imaged with super-resolution microscopy using a multiplexed OligoPaint labeling scheme.[27,28]

The functional purpose of TADs is a subject of active debate.[29,30] In some cases, deletion of cohesin, CTCF, or alteration of the CTCF-sites led to significant changes in gene expression,[24] whereas in other cases the effect was minimal.[31] One hypothesis is that the loop domains influence promotor-enhancer interactions, and thereby gene expression. When the cell enters metaphase, the mitotic chromosome is formed, which is dependent on the loop-extruding action of condensin.[32] The resulting structure is a compact bottle-brush-like object, in which the loops are closely spaced, unlike the interphase nucleus which has more dynamic properties. Human chromosomes, in particular, are compacted by two types of condensin, namely condensin I and II, of which the former produces the larger loops of the helical mitotic chromosome structure, within which the latter adds nested smaller loops.

From the previous discussion it is clear that a significant amount of experimental knowledge exists about the organization of the chromosome by SMCs. Furthermore, computer simulations of loop extruders working on DNA seem to be able to reconstitute experimental contact maps quite accurately.[6] Nevertheless, and in the light of the many other chromosome-structuring elements in cells, the confirmation that SMCs produce loops *in vitro* on short DNA strands does not necessarily mean that that they would produce objects with similar properties to interphase or mitotic chromosomes, if they were to act on genome-sized DNA. To study this, we propose to use a genome-in-a-box approach to observe the compaction of megabase-sized DNA by SMC loop extruders (in our case: yeast condensin, with which our lab has the most experience). Genome-in-a-box is a recently developed method to study DNA organizing processes *in vitro* using megabase-sized deproteinated DNA as a substrate, and as such is suited to explore emergent effects on a large DNA length-scale, caused by locally acting DNA-binding elements.

In this chapter, we show that yeast condensin does compact megabase-sized DNA (isolated from *E. coli* but as of yet without removal of the native proteins) in an ATP-dependent manner. Condensin is found to be able to reduce the volume of the DNA object by about half. Interestingly, the compaction leads to heterogeneous structures with the emergence of dense clusters and internal DNA-void regions.

5.2. RESULTS

5.2.1. ISOLATING CHROMOSOMES FROM *E. coli* CELLS FOR EXPERIMENTS WITH CONDENSIN-MEDIATED DNA COMPACTION

For the results presented in this chapter, we used an early version of the protocol documented in chapter 3. Broadly speaking the protocols are similar, with however a few crucial differences. Briefly, *E. coli* cells were grown at 30 °C in LB broth until the culture reached OD_{600} = 0.15, after which the culture was transferred to 42 °C for 1 hour. Due to the presence of a temperature-sensitive allele of the DnaC gene, DNA replication initiation was effective halted at this higher temperature.[33,34] This led to ongoing replication of DNA to be completed, but new initiations being blocked. This resulted in a population of cells in which the majority contain a single fully replicated chromosome

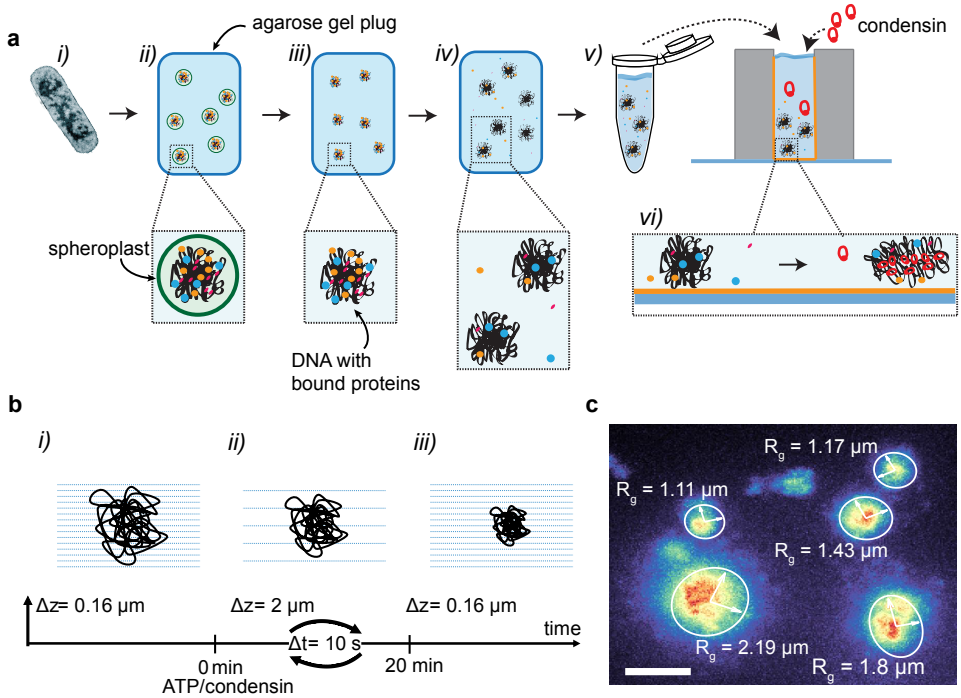

Figure 5.1: **Workflow of the experiments with megabase DNA isolated from E. coli.** **(a)** Schematic of the experimental protocol from cells to genome-in-a-box experiments. ***(i)*** *E. coli* cells were grown such that 80% of cells would contain a single chromosome (figure S5.1). Cells were then treated with lysozyme to digest the cell wall, resulting in spheroplasts. ***(ii)*** Spheroplasts were embedded in an agarose gel plug. ***(iii)*** The agarose plug was incubated in lysis buffer, leading to an osmotic shock on the spheroplasts and subsequent cell lysis. ***(iv)*** Plugs were then washed 4 times for 1 hour in a Tris-EDTA buffer. ***(v)*** The agarose gel was then digested using agarase enzyme, and the resulting solution containing the chromosomes was pipetted into an observation well. This observation well is formed by a 2.5 mm wide hole inside a PDMS block (gray) bonded to a glass coverslip (straight blue line), coated with a lipid bilayer (orange line) to prevent DNA adhesion. ***(vi)*** Genome-in-a-box experiments were performed by adding purified condensin to the observation chamber and observing the compaction process. **(b)** Imaging scheme for the genome-in-a-box experiments with condensin. ***(i)*** Z-stacks with a small z-step were taken at multiple locations in the observation well. ***(ii)*** Condensin and ATP were added, and a timelapse of z-stacks were taken at multiple locations using a larger z-step. ***(iii)*** After the compaction process, another set of z-stacks was imaged with a small z-step. **(c)** Crop of a typical field-of-view with DNA objects before compaction in a maximum-intensity projection. The objects are annotated using ellipses with axes determined by the gyration tensor, and the associated radius of gyration R_g. Scale bar 5 μm.

(figure S5.1). After the temperature treatment, about 10^9 cells were collected and treated with lysozyme to digest the cell wall, resulting in so-called spheroplasts. These spheroplasts were then resuspended in a liquid agarose solution, and left to jellify inside a plug mold, resulting in agarose gel plugs containing about 10^8 spheroplasts (figure 5.1a-*ii*). These plugs were then incubated in a low-osmolarity buffer, causing an osmotic shock that lysed the spheroplasts, thereby releasing the cellular content including the bacterial chromosome into the agarose gel matrix (figure 5.1a-*iii*). After lysis, the agarose plugs were washed 4 times for 1 hour in a Tris-EDTA buffer (figure 5.1a-*iv*). This step was origi-

nally followed to dilute away the native bacterial proteins from the agarose plug, however follow-up experiments showed that this treatment did not remove all proteins from the sample (figure S5.3). Therefore, one should consider that the DNA objects used for the experiments in this chapter still contain an unknown number of residual DNA-binding proteins. To obtain a liquid sample suitable for experiments, the agarose plugs containing extracted chromosomes were digested with beta-agarase enzyme, which converts the agarose polymers back into monomers (figure 5.1a-*v*). This liquid sample was then gently pipetted into the observation well containing ~20 μL of buffer (figure 5.1a-*vi*). The surfaces of the well were coated with a lipid bilayer to prevent DNA adhesion (figure S5.2), thereby ensuring that the DNA can freely re-organize itself during the compaction process.

To ensure that all the DNA objects were full-length circular chromosomes, we considered whether we could perform the experiments in the presence of purified ExonucleaseV (RecBCD) enzyme which degrades linear DNA under ATP hydrolysis, while leaving nicked and supercoiled circular DNA intact. We performed several preliminary tests to ensure that such a scheme would work (figure S5.6). However, for the final condensin experiments discussed in this chapter the enzyme was not used, because at the time of the experiments the enzyme was not available anymore. Furthermore, we later realized that RecBCD would probably not be able to fully digest linearized chromosomes in the sample, because the *E. coli* chromosomes contain so-called Chi-sequences that act as a stop signal to the enzyme, halting its digestion of the linear DNA.[35] For future experiments, an alternative to the RecBCD enzyme might be NEB Exonuclease VIII, which does not respond to these chi-sites, while retaining similar linear-DNA-digestion properties as RecBCD.

Before addition of the condensin/ATP, finely-spaced z-stacks spanning 30 μm were imaged across 5 fields-of-view using spinning-disk fluorescence microscopy (figure 5.1b-*i*). DNA signal came from a DNA intercalating dye Sytox Orange. An exemplary image of the DNA-objects obtained from these z-stacks is shown in figure 5.1c. After addition of ATP (5 nM) and a set amount of condensin (25, 50, or 100 nM), the imaging protocol changed to timelapse imaging with coarse z-stacks over 20 μm, in order to decrease the time between subsequent z-stacks at each field-of-view to 10 s (figure 5.1b-*ii*). After 20 min of timelapse imaging, another finely-spaced z-stack was taken of the condensed DNA objects (figure 5.1b-*iii*).

5.2.2. GLOBAL COMPACTION OF MEGABASE DNA BY CONDENSIN DEPENDS ON ATP AND CONDENSIN CONCENTRATION.

Before addition of ATP and condensin, the DNA objects displayed a strong fluorescence signal in the interior, while they were surrounded by 'fluffy' strands of DNA in the exterior. These strands of DNA could, as expected, extend over larger distances than the radius of gyration (figure 5.1c). When condensin (25, 50, or 100 nM) was added, we observed two modes of compaction, which we call 'global' and 'local' compaction. The global compaction refers to the observation that the DNA objects became smaller as a

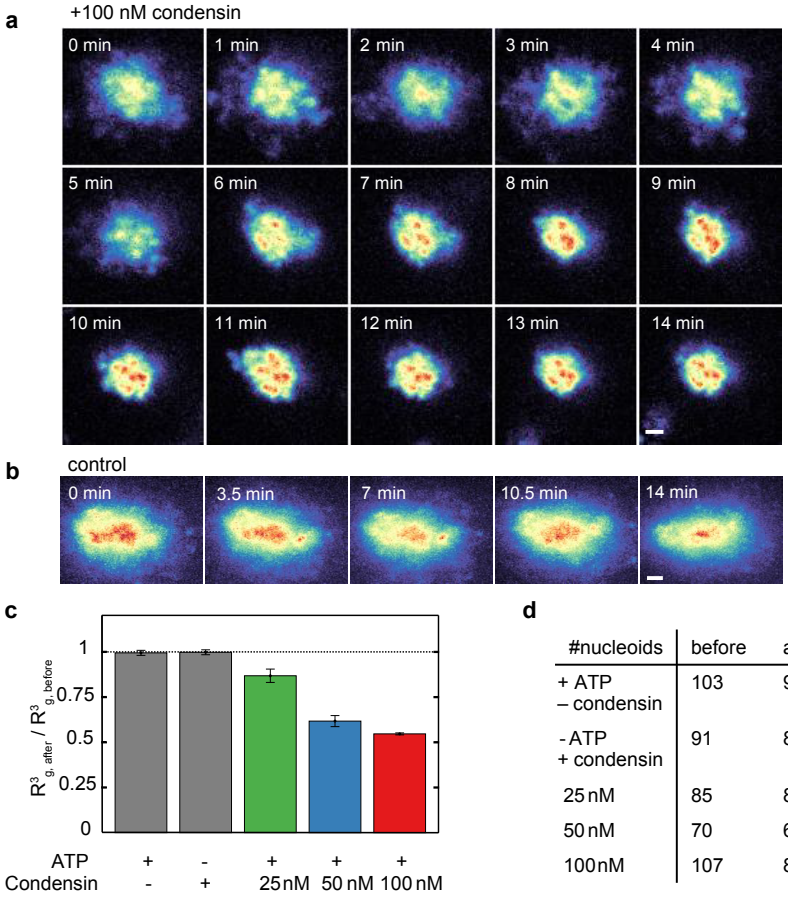

Figure 5.2: **Compaction of DNA objects by condensin. (a)** Typical example of a compacting DNA object after addition after 100 nM condensin and 5 mM ATP, imaged at 15 timepoints. Single imaging slices are displayed. Scale bar 2 μm. **(b)** Control example of a DNA object at 5 timepoints, without the addition of condensin. Scale bar 2 μm. **(c)** Radius of gyration of DNA objects, determined using detailed z-stacks before addition of ATP/condensin and 20 min thereafter. The after/before ratio of the average cubed radius of gyration is shown for 5 different conditions. **(d)** Number of DNA objects used to calculate the values shown in panel c.

whole, while the local compaction describes the appearance of local clusters of DNA within the interior of the object.

For example, figure 5.2a shows a timelapse of a compacting DNA object after addition of 100 nM condensin. In the first few minutes, the DNA object seemed unperturbed, but starting after 3-4 min, the outer strands of 'fluffy' DNA were being retracted towards the interior, causing the overall object to become smaller. This global compaction continued until about 10-11 minutes. From about 5-6 min, local higher-density regions started to appear in the interior of the DNA object (local compaction), and these increased in

number and density over the course of the following minutes. By comparison, control experiments (*e.g.*, ATP added but no condensin) did not show either the global or local compaction, with the object's size remaining constant, the interior rather homogeneous, and the boundaries fuzzy (figure 5.2b).

We quantified the compaction of the DNA objects using the radius of gyration of the object, which was computed using the finely-spaced z-stacks taken before the addition of condensin ("before") and at the end of the experiment ("after"). The cubed radius of gyration was calculated as an estimate of the volume of the DNA object, and the ratio of the average value after and before was taken as a measure of the relative volumetric compaction of the DNA objects. When either ATP or condensin was omitted, no global compaction was observed (figure 5.2b/c). These control experiments show, firstly, that addition of ATP alone does not "reactivate" any remaining native proteins, which could potentially contribute to DNA compaction, such as bacterial SMCs, topoisomerases, *etc.* Secondly, the controls show that the added condensin requires ATP to induce DNA compaction, suggesting that active loop extrusion is the major contributor to the observed compaction. Lastly, it shows that native ATP is not present at sufficient levels in order to be able to activate the added condensin. When both ATP and condensin were added, on the other hand, concentration-dependent compaction was observed. Increasing amounts of 25 nM, 50 nM or 100 nM condensin lead to a volume reduction of the DNA objects by 20%, 40%, 45% respectively. Figure 5.2d shows the numbers of DNA objects that were used to calculate the values shown in figure 5.2c.

To capture the temporal kinetics of the compaction, the data from the coarsely-spaced z-stacks was used. Although the acquisition of z-stacks at each time-point reduces the temporal resolution, it is necessary because the DNA objects are free to move within the imaging volume. By imaging in multiple planes, we increased the chances that the DNA objects were at least captured well in one of the z-slices. Figure 5.3a-d show maximum-intensity projections at different timepoints of DNA objects in four different conditions, namely control (without condensin) and three concentrations of condensin (25 nM, 50 nM, or 100 nM). Similar to what was shown in figure 5.2a, the DNA objects in the 50 and 100 nM condition are compacted in the presence of condensin and ATP, with fuzzy boundaries disappearing and internal clusters becoming more pronounced. The disappearance of the fuzzy boundaries is visualized in the intensity profiles shown in figure 5.3e, which were taken on the 100 nM object of figure 5.3d. The intensity profile across the DNA object becomes sharper over time, showing how the strands of DNA from the fuzzy boundaries are reeled in, thereby leaving a central compacted core. The degree of compaction is noticeably lower at the 25 nM condition, with the fuzzy boundaries remaining even after 15 min. The graphs on the right of Figure 5.3a-d show the relative volume reduction of the DNA objects over time. The volume of a DNA object was estimated by the cubed radius of gyration calculated from the maximum-intensity projection at each timepoint. Furthermore, the volume of each object was normalized to the average radius of gyration at $t = 0$ min. The control experiment with condensin does not show an appreciable trend, while the DNA objects with added condensin and ATP display a gradual compaction over time. For the lowest 25 nM concentration, only a slight compaction was observed, with the compaction curve become steeper with increasing

condensin concentrations. Note that although the volumetric compaction by condensin at each concentration occurs to an appreciable degree, the change in radius of gyration is obviously smaller (figure S5.4). For each condensin concentration the mean radius of gyration goes from 1.8 μm to 1.6 μm (25 nM, 10% decrease), 1.6 μm to 1.4 μm (50 nM, 17% decrease) and 2.3 μm to 1.8 μm (100 nM, 22% decrease).

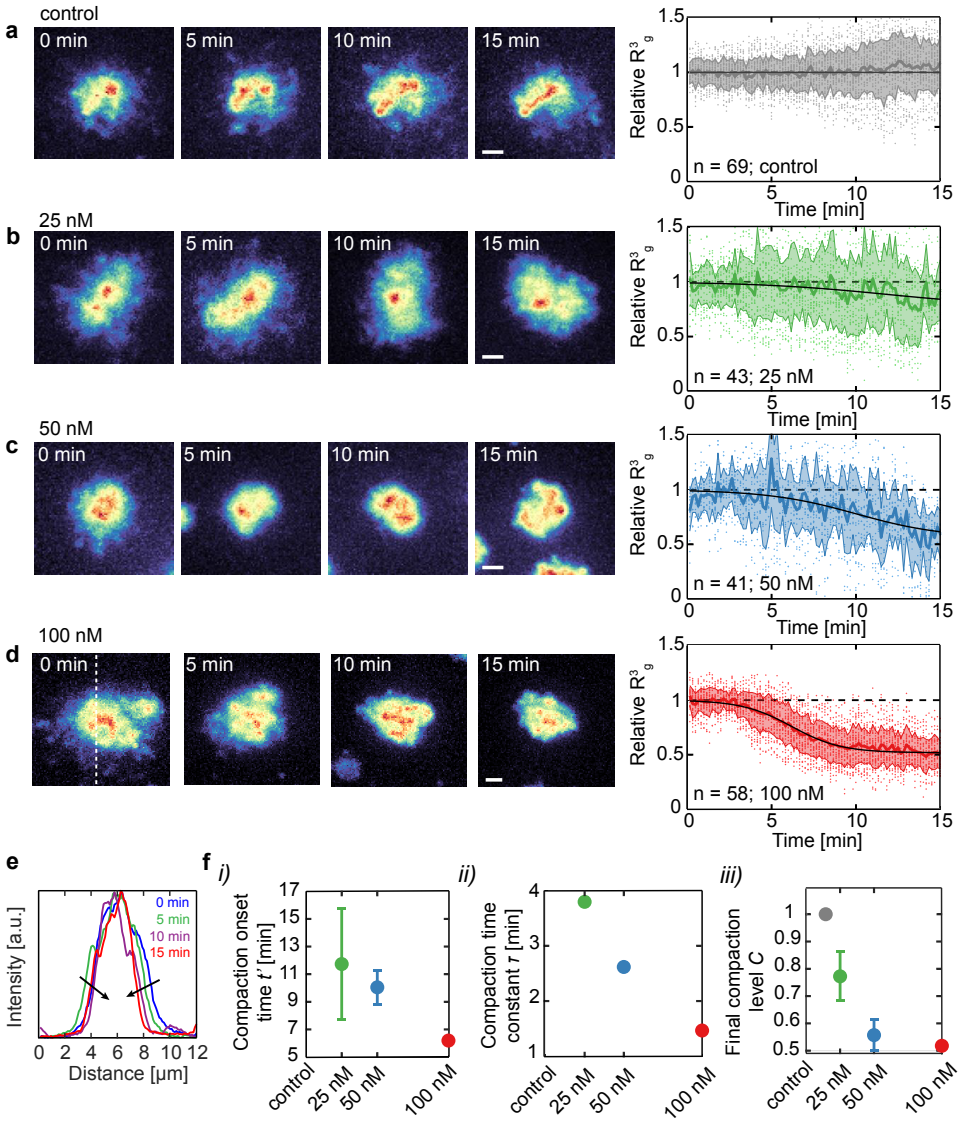

Figure 5.3: **Time dependence of the global compaction of DNA objects by condensin.** *(For caption see next page)*

Figure 5.3 *(continued from previous page)*: **Time dependence of the global compaction of DNA objects by condensin. (a)** A DNA object (control, with ATP, no condensin) shown at four timepoints after the addition of ATP. The radius of gyration R_g is calculated on the maximum-intensity projection of the z-stacks at each timepoint. On the right, the time course of the relative R_g^3 is shown, which is the ratio of the cubed R_g at each timepoint divided by the cubed R_g at t = 0 min. The thick line and shaded area in the time course are mean and standard error. Scale bar is 2 μm. **(b-d)** Same as panel a, but with increasing concentration of added condensin, namely 25 nM, 50 nM, and 100 nM. **(e)** An intensity profile taken along the dashed line (as annotated in panel d) at each of the four timepoints. The profile becomes narrower over time (inwards pointing arrows), indicating that the 'fluffy' relaxed DNA gets reeled in to the center of the DNA object. **(f)** Each time course trace in panels a-d was fitted to a sigmoidal function with three parameters. The dependence of these parameters on condensin concentration are shown: ***(i)*** the onset time t_{onset} of compaction; ***(ii)*** the compaction time constant τ; ***(iii)*** the final steady-state compaction level C. Error bars are confidence intervals and fall within the marker dots if not visible.

To further quantify the average trend of the compaction process, the mean compaction curve in each condition was fitted to a phenomenological sigmoidal function of the form:

$$\frac{R_g^3(t)}{R_g^3(t=0)} = \frac{1-C}{1+exp(\frac{t-t_{\text{onset}}}{\tau})} + C$$

In this equation, t_{onset} defines the onset of the sigmoid along the time axis, τ sets the steepness of the curve and denotes a characteristic compaction time constant, and C is the final or asymptotic level of compaction for large values of t. The resulting fit parameters are displayed in figure 5.3f. The most reliable fit is obtained for the 100 nM condition. Since the curves for the 25 nM and 50 nM conditions do not reach an asymptotic value during the experimental time frame, we are less confident about their computed fit parameters. From figure 5.3f-*i* we notice that the start of the compaction process (as quantified by the onset time t_{onset}) occurs at later timepoints for decreasing condensin concentrations, varying from ~12 min to ~6 min for 25 nM and 100 nM condition, respectively. Additionally, the compaction process is quicker for increasing condensin concentrations, as is seen from the drop in the compaction constant τ in figure 5.3f-*ii*. Lastly, the DNA objects in the 100 nM condition reach an asymptotic compaction value C of about 50%. The asymptotic compaction level of the 25 nM and 50 nM can only be inferred from regression of the data to the equation above, leading to values of 80% and 55% relative to the initial volume, respectively (figure 5.3f-*iii*). These values (obtained from maximum-intensity projection images) are in good agreement with those computed from the radius of gyration determined on the finely-spaced z-stacks (Figure 5.2c).

5.2.3. COMPACTION BY CONDENSIN LEADS TO FORMATION OF DENSE DNA CLUSTERS

Upon addition of ATP and condensin, not only the overall size of the DNA objects decreased, but also the internal structure underwent significant changes. Starting from a fairly unstructured intensity distribution within the object, with low levels of heterogeneity, local regions of increased intensity gradually formed. To quantify this spatial

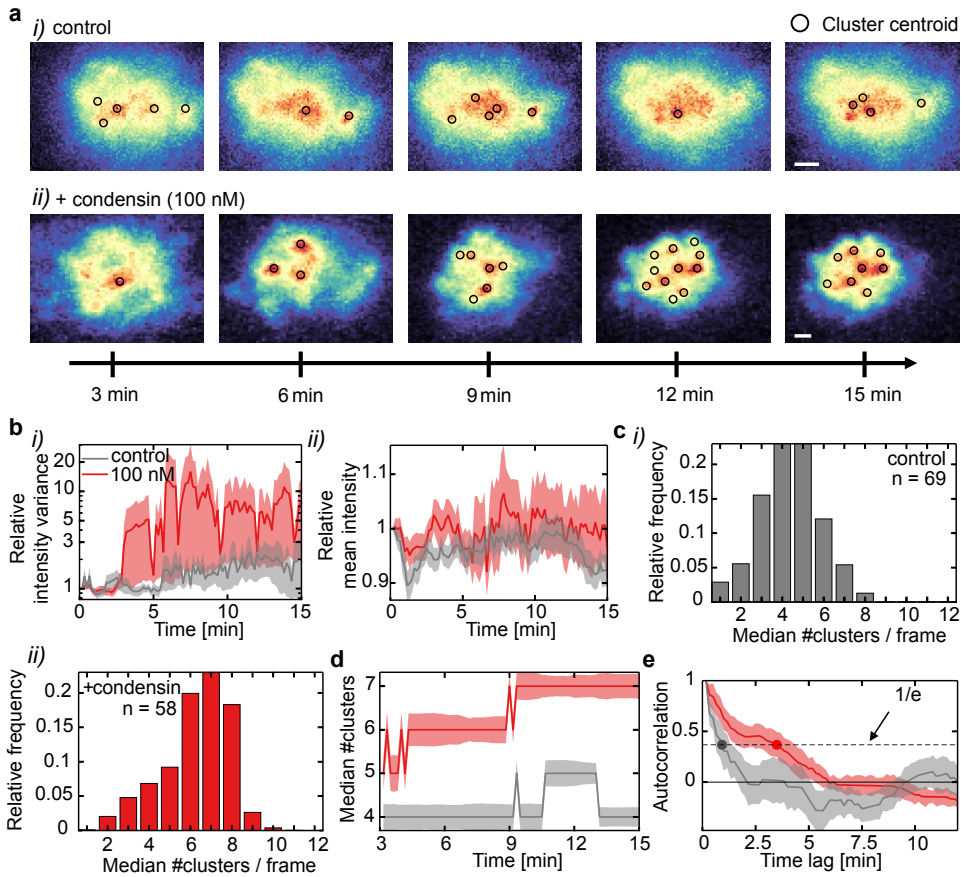

Figure 5.4: **Heterogeneous DNA distribution and local clusters due to condensin-induced compaction.** **(a)** Images of a DNA object at 5 timepoints over the 15 min time course: ***(i)*** without the addition of condensin (control); and ***(ii)*** at 100 nM condensin with ATP. The detected local clusters of increased DNA signal are annotated with blak circles. Scale bars are 1 μm. **(b)** Variance and mean of intensity values per object over time. ***(i)*** After a few minutes the relative variance of intensity values per object increases dramatically. This shows that DNA, which is initially rather homogeneously distributed, becomes clustered in spatially restricted domains. ***(ii)*** However, the mean of the intensity values stays relatively constant over time. **(c)** Median number of detected clusters per frame, evaluated for all DNA objects and all timepoints: ***(i)*** control, without condensin, shows 4-5 clusters on average; ***(ii)*** same after addition of 100 nM condensin, whereupon the average number of clusters increased to 7. **(d)** Median number of clusters per frame, which increased with time for the condensin-compacted DNA objects, while it stayed steady for the control condition. **(e)** Temporal autocorrelation calculated from the time traces of the number of clusters. The thick line and the shaded area denote mean and standard error.

heterogeneity, the intensity variance of the pixels comprising each DNA object was plotted over time and normalized to the intensity variance at $t = 0$ min (figure 5.4b-*i*). The relative intensity variance increased strongly over time, by more than order of magnitude for the in the 100 nM condensin condition. This indicates that the intensity values

of the DNA objects shifted to distribution with a sizeable variety of high and low intensity regions. Note that a maximum increase of up to factor of 2 was measured for the control condition. With condensin, the intensity variance rose sharply around the 3 min, coinciding with the timepoint at which the average compaction became different from unity (figure 5.2d-right). We tested that the action of the condensin did not alter the binding of the DNA by the intercalating dye, thereby introducing changes in the DNA staining levels, which would show up as changes in the mean intensity of the object during the compaction process. As figure 5.4b-*ii* shows, the mean intensity of a DNA object remained more or less constant (within 10% of the starting value) throughout the timelapse, for both the control and the 100 nM condensin condition, indicating that the condensin did not alter the DNA staining. Taken together, these results suggest that DNA is accumulated into local clusters by the loop-extruding action of condensin.

We sought to further quantify the formation of the clusters over time, *i.e.*, their number, size, and DNA content. As a first step, the occurrence of clusters over time was measured for every DNA object in each z-slice separately. Since there was little detectable compaction occurring in the first three minutes of the timelapse, this period was used to determine the 'baseline' intensity trace of a pixel in the DNA object. For each subsequent timepoint the probability was then computed that the pixel, based on its intensity at that time, was part of a cluster or not. Connected regions of pixels determined to be part of a cluster were then annotated in images. Figure 5.4a shows example images at various timepoints of DNA objects in the control (figure 5.4a-*i*), and the 100 nM condensin condition (figure 5.4a-*ii*), with the detected clusters annotated by black circles. From visual inspection, it is clear that the number of clusters in the control condition remained fairly constant over time, while in the 100 nM condensin condition this number rose over time. This is confirmed by counting the cluster numbers per DNA object and time frame. Taken over the whole timelapse, the cluster number was 4-5 clusters per object and frame in the control condition (figure 5.4c-*i*), while for 100 nM condensin it was higher (7 clusters per object and frame; figure 5.4c-*ii*). Over time, the number increased from 5 to 7 clusters per object in the 100 nM condition, while it remained at 4-5 clusters per object for the control condition. Since this difference in number of clusters between the two conditions seemed rather small, we tried to determine if there was a difference in cluster persistence, *i.e.*, if the clusters were transient or static. For this, we calculated the autocorrelation function of the fluctuations around the median for both conditions. The autocorrelation function of the condensin-treated DNA objects decayed much slower over increasing time lags than that for the control condition: The drop of the autocorrelation function to $1/e$ occured at 3.5 ± 0.8 min and 0.8 ± 0.5 min and for the condensin and control condition, respectively. This time indicates over what time scale the number of clusters per object remained constant, thereby confirming that the clusters in the control condition were rather transient while those in the condensin-treated DNA objects were more persistent.

To obtain more information about the cluster formation process, we next characterized the cluster size and DNA content over time. This was achieved by adding an extra layer of quantification to the cluster identification maps such as those in figure 5.4a. To this end, the intensity values within the region of each identified cluster were fitted to a spatially

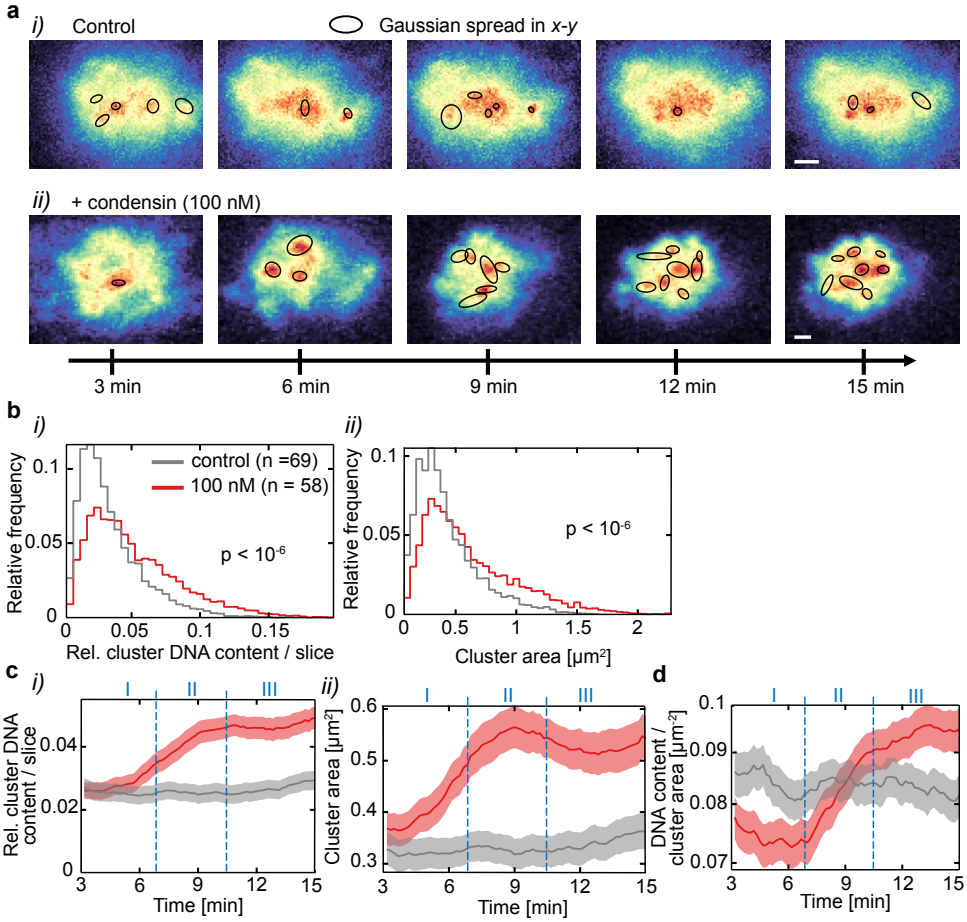

Figure 5.5: **Condensin-induced local clusters become denser over time.** **(a)** Similar to figure 5.4a, images of a DNA object at 5 timepoints over a 15 min time course: ***(i)*** without the addition of condensin (control); and ***(ii)*** 100 nM condensin and ATP. The detected local clusters of increased DNA signal are annotated with ellipses of which the axes are determined by the standard deviation of the asymmetric Gaussians that model the clusters. Scale bars are 1 μm. (b) ***(i)*** Clusters arising in the condensin-compacted DNA objects contain more DNA than the control condition, and ***(ii)*** their size is larger. Significance testing was done using a two-sample Kolmogorov-Smirnov hypothesis test. **(c)** ***(i)*** DNA contained in clusters versus time, showing a rise in the condensin sample, while staying constant in the control. ***(ii)*** Similarly, the cluster size increased over time in the compacting DNA objects, while remaining steady for the control condition. **(d)** DNA density in the clusters versus time, which also increased in the condensin sample, indicating that the cluster not only increase their size and DNA content, but also become more compact. The thick line and the shaded area denote mean and standard error. Vertical blue lines in panels c and d indicate three regimes in the compaction process, based on trend of the cluster density curve (red) in panel d.

anisotropic Gaussian function, *i.e.*, a two-dimensional Gaussian with possibly different spread in the x and y directions. From the fit parameters for each cluster, we estimated a cluster area and a 'mass', which is related to the fluorescence intensity and thereby

the amount of DNA incorporated into the cluster. Figure 5.5a shows these Gaussians displayed as ellipses, with the axes corresponding to the Gaussian spread in two dimensions. The mass of each cluster was normalized to the total intensity of the DNA object in the z-slice in which the cluster was detected, which thus corresponds to the amount of DNA present in the cluster. Taken over the complete timelapse, clusters in condensin-treated DNA objects contained slightly more DNA than those present in the control objects, namely 5% and 3% per cluster, respectively (figure 5.5b-*i*). The condensin-formed clusters were also larger than those formed in the control condition, 0.51 ± 0.43 μm^2 *vs.* 0.34 ± 0.29 μm^2 (figure 5.5b-*ii*). When plotting time courses of the relative cluster DNA content (figure 5.5c-*i*) and the cluster area (figure 5.5c-*ii*), we noticed that both the DNA content as well as the area of the condensin-formed clusters increased during the compaction process, whereas those quantities remained constant for the spontaneously formed clusters of the control condition.

Combining the information about cluster DNA content with the cluster area, we obtain a trend for the DNA density in clusters, which displays three clear regimes during the compaction process. While the cluster DNA density remained steady in the first ~7 min of the condensin condition timelapse, (regime I in figure 5.5d), then it strongly increased up to ~10 min (regime II), after which it continued to rise albeit at a lower rate (regime III). Note that the cluster DNA density continued to increase during the whole experiment, even though the global compaction had reached its asymptotic value after ~10 min (compare figure 5.3d-right). The density increase in regime II can be ascribed to the fact that during this period the rate at which DNA got added to clusters (regime I in figure 5.5c-*i*) simply outpaced the rate of area increase (regime I in figure 5.5c-*ii*). In regime III, on the other hand another explanation for the density increase is needed. Comparing the plots of cluster DNA content with the cluster area over time (figure 5.5c-*i*/*ii*), one sees that the DNA content remained constant after the global compaction halted around the 10 min mark, but that the cluster area became smaller, effectively increasing the DNA density in the clusters. As a final comment, it is interesting to note that a fully compacted DNA object contained ~7 clusters (figure 5.4c-*ii*) with each ~5% relative DNA content (figure 5.5c-*i*), meaning that up to one third of the total DNA-content became spatially aggregated in clusters.

Lastly, it can be useful to estimate the amount of DNA (in kbp) in the clusters. The clusters were on average 2.5x brighter than the intensity of the uncompacted DNA. Cluster were determined to have a final size of 0.5-0.6 μm^2, and if we assume that they are spherical, they would have a volume of 0.3 μm^3. Using the intensity profile of a compacted DNA object (figure 5.3e), the diameter at half-maximum is ~3.5 μm. Using these numbers and assuming a full-length *E. coli* chromosome of 4.6 Mbp, we estimate the average DNA content per cluster as: $\frac{\text{basepairs}}{\text{cluster}} \approx \frac{4.6\text{ Mbp}}{\frac{4\pi}{3}(3.5/2\,\mu\text{m})^3} \cdot 0.3\,\mu\text{m}^3 \cdot 2.5 \approx 155$ kbp/cluster

5.2.4. COMPACTION BY CONDENSIN LEADS TO MORE SPHERICALLY SHAPED DNA OBJECTS CONTAINING INTERNAL DNA-VOID REGIONS.

To inspect the final threedimensional structure of the compacted DNA objects, we used the finely-spaced z-stacks taken 20 min after addition of condensin. Figure 5.6a shows two DNA objects for which orthogonal slices are selected at those positions where the internal structure is best visible. Surprisingly, the compacted DNA objects are not space-filling, but contain relatively large (~1 μm diameter) voids, *i.e.*, hollow regions without DNA (indicated by the pink outlines in figure 5.6a-*i/ii*). These voids are not completely enclosed inside the DNA, but rather form pockets near the surface of the DNA object. Nearly all compacted DNA objects contained these voids. About ~50% containing of the objects contained a single void, while higher number of voids per object occurred with lower probabilities. By contrast, in control conditions, objects displayed these voids only rarely (figure 5.6c).

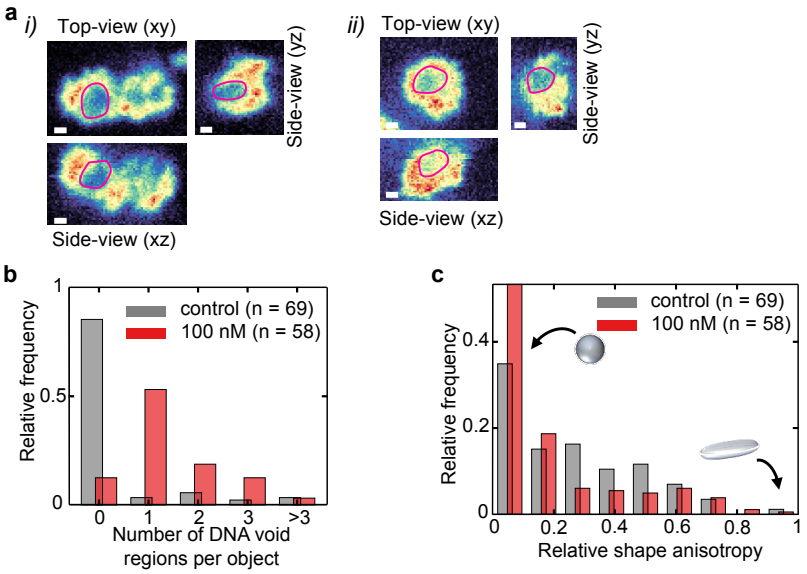

Figure 5.6: **Condensin-compacted DNA objects are mostly spherical and contain DNA-void regions.** **(a)** ***(i)*** Orthogonal slices showing the DNA-void region from three directions, outlined in pink. ***(ii)*** Same for another example. Scale bars, 1 μm. **(b)** Histogram of the number of DNA-void regions, which was manually counted for the 100 nM condensin sample, as well as the control without condensin. **(c)** Using the eigenvalues of the gyration tensor, the relative shape anisotropy was calculated for the 100 nM condensin condition and the control. After compaction, the shape anisotropy is slightly shifted towards more spherical shapes.

In addition, the shape of the DNA objects was described by calculating the relative shape anisotropy, which is a measure to described geometric shapes using the eigenvalues $\lambda^2_{x,y,z}$ of the gyration tensor. The relative shape anisotropy κ^2 can vary between 0 (a

sphere) and 1 (a tube-like object), and is calculated using the following equation[36]:

$$\kappa^2 = \frac{3}{2}\frac{\lambda_x^4 + \lambda_y^4 + \lambda_z^4}{(\lambda_x^2 + \lambda_y^2 + \lambda_z^2)^2} - \frac{1}{2}$$

The distribution of shape anisotropies in the control and 100 nM condensin condition is shown in figure 5.6d. In both cases the distribution was found to be skewed towards spherical objects. However, this skew was stronger for condensin-compacted objects, indicating that the compaction process leads to more spherically shaped objects.

5.3. DISCUSSION

In this chapter, we added yeast condensin at various concentrations to bacterial chromosomes extracted from *E. coli*, after which the resulting DNA compaction process was observed. Upon addition of 100 nM condensin, global DNA compaction was observed over the timescale of minutes. Compaction by condensin and ATP resulted in up to 50% volume reduction. Aside from global compaction, persistent clusters arose in the interior of the compacting DNA object, which grew both in size and DNA density over the course of the experiment. The resulting compacted DNA objects contained one or more DNA-void regions, which manifest themselves as non-enclosed pockets near the surface of the object. Finally, the shape of the compacted objects was more spherical compared to uncompacted DNA objects.

While these are new and interesting results, a limitation of the study presented here is the limited knowledge that we have about the initial conditions of the DNA objects, *i.e.*, about the presence of DNA-binding proteins, supercoiling state, topology (linear or circular), and object size in basepairs. There was no specific protein-removal treatment performed on the DNA extracted from the *E. coli* cells, and therefore the DNA likely still contained an unknown number of DNA-binding proteins. These DNA-binding proteins[37,38] can bend, wrap, bridge, and loop the DNA, thereby changing its properties such that it cannot be considered a free polymer. Since bacterial DNA is natively negatively supercoiled,[39,40] it is likely that the DNA objects in this study also contained an unknown number of plectonemic supercoils. Handling of the large DNA substrate may introduce several nicks into the DNA, which will relax the supercoiling, but it is not known to what extent this happens in our samples. Furthermore, the use of Sytox Orange has in retrospect been an unwise choice for DNA intercalating dye, because it is known to induce positive supercoils into constrained DNA.[41] Possibly, this action of Sytox Orange might reduce the residual amount of negative supercoiling in the DNA, however it is unknown to what extent this happens. These comments about supercoiling, combined with the knowledge that condensin's loop extrusion is inhibited on negatively supercoiled DNA,[42] makes it unclear what the interplay between supercoiling and loop extrusion is in our present study.

To avoid the use of intercalating dyes for future studies, the DNA can be covalently labeled using modified nucleotides incorporated into the genome during the cell growth

(figure S5.8). This covalent DNA labeling strategy would also be useful for experiments with multiple chromosomes encapsulated inside shape-manipulated liposomes or droplets (chapter 3 and figure S5.7). One could then observe if two chromosomes will mix or not when confined inside such a container.[43] Lastly, from chapter 2 it is clear that it is difficult to know the number of basepairs of an observed DNA object, based only on the observed fluorescence. Similarly, an observed radius of gyration can be mapped under different model assumptions to a range of size in number of basepairs.[44] All in all, the uncertainty about the initial conditions of the DNA objects unfortunately limits the impact the observed phenomena in this study. However, some useful observations can still be made.

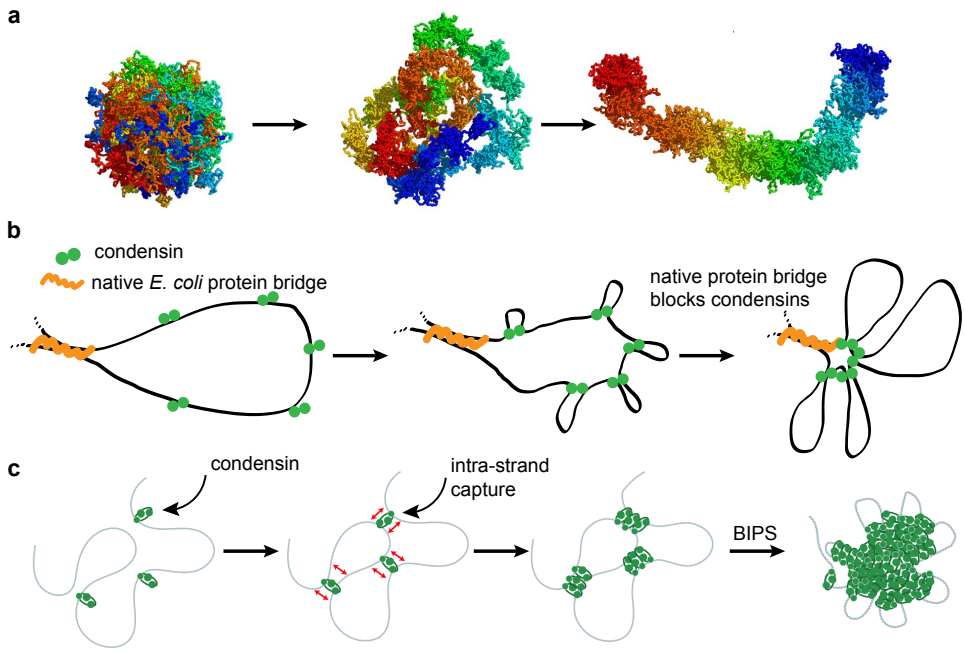

Figure 5.7: **Possible models to explain cluster formation in condensin-compacted DNA. (a)**. Simulation from Ref. [45] of megabasepair linear DNA that is compacted by loop extruders, forming a structure similar to a mitotic chromosome. **(b)** Clusters could form when loops extruded by condensin are blocked by a 'bridge' formed by native *E. coli* DNA-binding proteins, such as H-NS.[46–50] **(c)** Alternatively, clusters could form through Bridging Induced Phase Separation (BIPS). In order for this to happen, condensin must not only extrude loops in an 'intra-strand' manner, but also by capturing nearby non-contiguous DNA strands using an 'inter-strand' extrusion mechanism.[51] Thereby it forms bridges between far apart DNA loci, locally increasing the DNA concentration which induces the binding of more condensin in these locations, in the end producing a clump of DNA and condensin. Adapted from Ref. [52].

The formation of local DNA clusters and the DNA-void regions is an interesting and unexpected result of the presented experiments. Goloborodko *et al.*[45] modeled the compaction of linear chromosomes by condensins, in which the initially globular DNA object was compacted into an elongated compacted object through the action of loop extrud-

ing condensin (figure 5.7a). Their study reported neither the formation of local clusters nor DNA-void regions. The condensin in our experiments was added from the outside, whereas in the modeling study it was homogenously distributed in space. Depending on the binding kinetics of condensin to DNA, it is possible that initially only the outer parts of the DNA objects are subjected to the loop extruding action. Nevertheless, the obvious dissimilarity between our experimental results and these simulations makes it clear how important it is to specify and vary the initial conditions of a biophysical experiment.

We propose two explanations for the formation of clusters. Firstly, we should consider the presence of native DNA-binding proteins on the DNA. Although condensins have been reported to be able to pass large objects attached to DNA in *cis*,[53] it might not be possible for them to traverse a stretch of bridged DNA, leading to an accumulation of looped DNA on one side of the bridged DNA (figure 5.7b). These accumulations of loops might manifest as clusters in a fluorescence image. Bacterial H-NS might be a candidate for such a bridging protein. It oligomerizes on DNA forming bridged regions of up to 100 nm *in vitro*,[46,47,54,55] and from ChiP-seq data is was derived that *in vivo* H-NS is present in ~450 binding regions of an average length of ~1700 bp or 580 nm.[56] Additionally, these bridges have high rupture forces (>5 pN) as determined by AFM and optical tweezers,[48,49] which are certainly higher than the stalling force for condensin (<1 pN). Two additional conditions need to be met in order for a non-topologically binding condensin to be blocked by a DNA bridge. First, the coating of the DNA by H-NS needs to contiguous, *i.e.*, H-NS molecules binding back-to-back, to obstruct binding by condensin and necessitating a further "jump" towards a free stretch of DNA. Second, if the DNA-H-NS bridge is stiffer than uncoated DNA (which is the case for H-NS-DNA filaments[48]), then the condensin might be challenged in bending the bridged DNA sufficiently into the "pre-loop" needed to extrude the DNA loop. This hypothesis could be tested using a DNA stretching visualization assay in which the DNA construct contains binding sites for H-NS enabling it to form a bridged structure. Subsequently, it can be determined if condensin manages to extrude a loop while traversing this bridged stretch of DNA.

Secondly, we propose inter-strand capture of DNA by condensin and bridging-induced phase separation to explain the formation of the DNA clusters.[51,52] If condensin only acts in *cis*, *i.e.*, on the 'same' contiguous DNA strand, it would result a homogenous bottlebrush array of loops, as shown in figure 5.7a. However, if the condensin can also act in *trans*, *i.e.*, also on nearby, non-contiguous strands (inter-strand capture), the condensin can collect DNA into so-called Z-loops.[57,58] Possibly, this mode of compaction would lead to a more heterogeneous and 'clumped' DNA structure. Additionally, Atomic Force Microscopy and stretched-DNA visualization assay experiments have shown that cohesin (another member of the SMC family) can display bridging-induced phase separation (BIPS), which requires inter-strand capture.[52] When a single cohesin makes an inter-strand loop of DNA, more cohesins follow at that same location, also making loops, thereby forming a clump of cohesin molecules and DNA-loops (figure 5.7c). Although Ryu *et al.* did not show this same mechanism with condensin, we can speculate that BIPS might be responsible for the formation of the clusters in our experiments with megabasepair DNA and condensin. This hypothesis could be tested by firstly imaging

the compaction process using fluorescently labeled condensin and secondly by studying mutants that interfere with the protein's ability to exhibit BIPS while leaving the loop extrusion function intact. With these experiments, we could verify if the condensin bound the the DNA forms liquid droplets similar to those formed by cohesin, and if the cluster formation is dependent condensin's ability to do BIPS.

For some conditions, the compaction process was restricted by the experimental timeframe of 15-20 min which was limited due to difficulties in tracking the DNA objects beyond that time period. Several solutions to this issue are possible. For example, microchambers can be fabricated in order to limit the lateral motion of the DNA objects (Figure S5.5). Or alternatively, the DNA objects can be tethered to the glass surface, using a low number of biotin-streptavidin anchors, in order not to limit the free motion of the DNA too much. Lastly, linear-motion trackers, such as the Kalman algorithm in TrackMate,[59] might enable us to track large-distance motion of DNA-objects better than is possible with our current approach using optical flow (see Methods).

How physiologically relevant are condensin concentrations that were used in the experiments in this chapter, *i.e.*, 25 nM to 100 nM? *S. cerevisiae* nuclei have been estimated to have ~1150 condensins,[60] which in a 3 fL nucleus would correspond to a concentration of 640 nM. These condensins work upon the yeast genome in the nucleus with a total of 12 Mbp DNA, corresponding to a 'genome concentration' of 0.5 nM. If we want to provide the DNA objects in our experiments, which are in the megabase range (say, 4.6 Mbp) and present at ~1 pM concentrations in the observation well, with the same background concentration of condensin as in a yeast nucleus, then we should use ~0.4 nM condensin. While this seems to imply that we are using physiologically irrelevant concentrations in our experiments, with 3 orders of magnitude higher concentrations, it is unfortunately, far from trivial to translate the crowded conditions in a nucleus to concentrations used in *in vitro* experiments. Another approach is to calculate the number of condensins per unit length of DNA, which in a yeast nucleus would yield 1 condensin per ~10 kbp.[58] If the DNA objects in our experiments would have the same condensin density as in the nucleus, this would correspond to 460 condensins per 4.6 Mbp object. It is currently unknown how many condensins are bound to the DNA objects in our experiments, but the use of fluorescently labeled condensin may allow to answer this question in future experiments.

If future experiments show that the cluster formation is an innate feature of condensin-mediated compaction of long DNA, it would be interesting to know if the loci inside these clusters have similar loci contact maps to TADs in cells. *In vivo*, the formation of domains of above average contact frequency is assumed to be useful to increase the interaction probability between enhancers and promoters.[61] Possibly, by introducing spot-labels at two loci on the DNA, say 150 kbp apart (similar to the cluster size we estimated above, we could measure correlations of their motion and the distances between them. In this manner, we would directly determine if the clusters are fixed structures along the DNA, and if they lead to increased interactions between loci. Furthermore, such spot labels (chapter 3 and figure S5.10 and figure S5.9) would give an instructive readout of the local dynamics of the DNA upon compaction, and could answer the question if compaction

by condensin leads to fluidized[62] or gel-like DNA. In summary, the results presented in this chapter offer some enticing possibilities for future experiments, while also showing the potential of the genome-in-box approach to study DNA-protein interactions and chromosome organization.

5.4. METHODS

5.4.1. CELL CULTURE AND CHROMOSOME ISOLATION USING AN AGAROSE PLUG PROTOCOL

E. coli bacterial cells (HupA-mYPet frt, Ori1::lacOx240 frt, ter3::tetOx240 gmR, ΔgalK::tetR-mCerulean frt, ΔleuB::lacI-mCherry frt, DnaC::mdoB::kanR frt)[63] were incubated from glycerol stock in Lysogeny broth (LB) supplemented with 50 μg/mL Kanamycin antibiotic (K1876, Sigma-Aldrich) at 30 °C and allowed to reach OD_{600} of 0.15. The cells were then grown for 1 hour at 42 °C in order to arrest DNA-replication initiation. Next, 1 mL of cell culture was spun down at 10000 *g* for 2.5 min, the supernatant was discarded, and the procedure was repeated twice more in order to obtain a pellet at $OD_{eq} = 1$ (approx. 8 x 10^8 cells). The pellet was resuspended in 475 µL cold (4 °C) sucrose buffer (0.58 M sucrose, 10 mM Na_2HPO_4/NaH_2PO_4 buffer pH 7.2, 10 mM EDTA, 100 mM NaCl). 25 μL lysozyme (L6876 Sigma-Aldrich, 1 mg/mL in ultrapure water) was immediately added and gently vortexed into the cell/sucrose buffer suspension, followed by a 10 min incubation at room temperature and a 5 min incubation at 42 °C. The lysozyme digests the cell wall, resulting in spheroplasts. 500 µL warmed (42 °C) spheroplast/sucrose buffer suspension was added to 500 µL warm (42 °C) agarose solution (low melting point agarose, V2831 Promega, 3% w/v in ultrapure water) using a cut pipette tip. In the following steps, the Eppendorf tubes were kept at 42 °C to prevent gelation of the agarose solution. The spheroplast/agarose mixture was gently mixed using a cut pipette tip, and cast in volumes of 100 µL into a plug mold (Bio-Rad laboratories, Veenendaal, The Netherlands). To solidify the agarose plugs, the plug mold was stored at 4 °C for 1 h. Each plug at this point should contain 8 x 10^7 cells.

The solidified agarose plugs containing spheroplasts were removed from the plug mold and added to 20 mL per plug lysis buffer (10 mM Na_2HPO_4/NaH_2PO_4 pH 7.2), thereby lysing the cells and thus merely trapping the chromosomes from the spheroplasts in the agarose gel matrix. The plugs were incubated gently shaking in the lysis buffer for 1 h. Subsequently, the plugs were removed from the lysis buffer and 'washed' in 20 mL per plug TE wash buffer (20 mM Tris-HCl pH 8, 50 mM EDTA pH 8.0) for one hour while shaking. Next, the buffer was replaced and a second wash step was done. This process was repeated for a total of 4 wash steps. Initially, it was assumed that the serial dilution of the liquid surrounding the extracted chromosomes in the plug would result in proteins to be unbound from the DNA and eluted from the plug. However, the tentative result in figure S5.3 indicates that this may not be the case. At this point the plugs can either be further processed for experiments or otherwise stored for up to one week in 2 mL TE wash buffer at 4 °C. This chromosome isolation protocol was based on previous work

from the Woldringh[64,65] and Glass[66] labs.

5.4.2. FABRICATION AND SURFACE PASSIVATION OF THE OBSERVATION WELL.

The Polydimethylsiloxane (PDMS) observation well was fabricated in the following manner. PDMS and curing agent (Sylgard 184, Dow Corning) were mixed (mass ratio 10 :1), degassed and poured onto a plain silanized silicon wafer (silanization prevents adhesion of PDMS to the silicon). After baking at 80 °C for 4 h, the ~0.5 cm high PDMS slab was cut into blocks, able to fit onto small rectangular coverslips. Holes were punched into the PDMS blocks using a 2.5 mm biopsy punch (World Precision Instruments). Then, the PDMS blocks were cleaned with isopropanol, while coverslips were cleaned with ethanol, and both were dried with nitrogen flow. The PDMS blocks and coverslips were activated using oxygen plasma for 20 s using a Plasma-Preen system (Plasmatic systems), immediately bonded, and finally baked for 10 min at 80 ~C. The resulting PDMS observation well contained 15 – 20 μL.

The surfaces of the inside of the observation well were passivated in order to prevent adhesion of DNA and other biomolecules, which was achieved by means of a supported lipid bilayer (SLB). First, small unilamellar vesicles need to be produced. To this end, 100 μL DOPC lipids (10 mg/mL) were mixed in a glass vial with DOPE-Atto390 lipids. The chloroform was evaporated in vacuum over 60 min. Then, the dried lipid film was hydrated in 200 μL SUV buffer (25 mM Tris-HCl pH 7.5, 150 mM KCl) for 15 min at room temperature, resulting in a lipid concentration of 50 mg/mL. The lipid suspension was vortexed twice for 10 s and subsequently sonicated at room temperature for 30 min. The mixture was extruded 20 times through a 30 nm membrane, leading to the formation of small unilamellar vesicles (SUVs). The solution was aliquoted, snap-frozen with liquid nitrogen and stored at -80 °C until needed. For the formation of the SLB inside the observation well, SUV aliquots were thawed and sonicated for 10 min. During this time, the plasma-treatment, bonding and baking of the observation well is done (see above). The SUVs were diluted 10x using Min buffer (25 mM Tris-HCl pH 7.5, 150 mM KCl, 5 mM $MgCl_2$) to a final lipid concentration of 0.5 mg/mL. After baking, the observation wells were cooled to room temperature, the SUV solution was added to the well, and incubated at 37 °C for 45 min with the opening covered to prevent evaporation. The liquid inside the observation well was removed, but leaving the bottom surface still hydrated to keep the SLB intact. The well was washed three times with 10 mM buffer (Na_2HPO_4/NaH_2PO_4 pH 7.2), and then three times with the working buffer used for the subsequent experiment. Each washing step consisted of gently pipetting the buffer up and down inside the observation well a few times. The presence of the bilayer was verified using FRAP (figure S5.2).

5.4.3. AGAROSE PLUG DIGESTION

The agarose digestion by beta-agarase enzyme was tested in the manufacturer's buffer, condensin buffer (50 mM Tris-HCl pH 7.5, 50mM NaCl, 2.5 mM $MgCl_2$, 1 mM DTT), Exonuclease V buffer (50 mM Potassium Acetate, 20 mM Tris-acetate, 10 mM Magnesium Acetate, 1 mM DTT), and Cas9 buffer (20 mM HEPES, 100 mM NaCl, 5 mM $MgCl_2$, 0.1 mM EDTA). The digestion of the agarose was complete in all of the buffers listed above, with the exception of the Cas9 buffer, in which small chunks of undigested agarose could be noticed. In order to release the chromosomes from the agarose gel matrix, the agarose plugs were equilibrated in the necessary working buffer for 1 h. The liquid was then removed and replaced by an appropriate volume of working buffer to yield an effective agarose concentration of ~1%. The sample was heated to 65 °C to melt the agarose for 10 min, and subsequently cooled down to 42 °C. Then, two units of beta-agarase were added and allowed to incubate at 42 °C for 1 h. It is important to monitor closely the temperatures for the agarose digestion, since the success of the digestion is dependent on a completely liquid sample, and a digestion temperature between 42 and maximum 45 °C, above which the enzyme loses activity.

After agarose plug digestion, the now liquid sample was gently pipetted using a cut pipette tip into the observation well, and 250 nM Sytox Orange intercalating DNA dye was added for fluorescence imaging. For condensin experiments, the buffer was supplemented with glycerol to a final concentration of 5%, to prevent density differences between the sample and the storage buffer of the purified condensin.

5.4.4. EXONUCLEASE EXPERIMENTS FOR FIGURE S5.6.

A 4 kbp plasmid from GL019 cell line was used for the exonuclease tests. The plasmid was cut using XhoI restriction enzyme and purified using PCR clean-up kit (Promega). Circular and linearized DNA was added to exoV or condensin buffer, incubated for 30 min at 37 °C or room temperature, and loaded onto a gel. After gel electrophoresis, the gel was stained with Ethydium Bromide and imaged. For the experiments with Cas9, namely the activity assay using a DNA fragment and the experiment using extracted chromosomes, a mixture of 20 guide-RNAs (gRNAs) was used which targeted a 1 kbp region on the right arm of the *E. coli* genome. For the first experiment, the gRNA mixture was heated to 95 °C for 10 min and gradually cooled to 12 °C over several hours, ensuring proper three-dimensional folding of the gRNA. In order to form the Cas9-gRNA complex, the gRNA mixture was incubated with Cas9 at 25 °C for 30 min. Then, the Cas9-gRNA mix was added to the 3 kbp DNA fragment containing the target sequences. In the final solution the ratio of gRNA : Cas9 : DNA was ensured to be 125 : 25 : 1. After the cleavage step, protK was added to a final concentration of 1.5 mg/mL and incubated at 37 °C for 15 min, in order to degrade the Cas9 enzyme. The samples were loaded on a gel, gel electrophoresis was performed, the gel was stained with EtBr and imaged. For the second experiment, agarose plugs were digested in Cas9 buffer as described above. The gRNA-Cas9 complex was prepared as before and added to the sample in a molar ratio gRNA : Cas9 : DNA = 125 : 50 :1 and incubated at 37 °C for 30 min. Subsequently, exonuclea-

seV enzyme was added to the sample and again incubated at 37 °C for 30 minutes. The control sample underwent the same treatment except that no Cas9-gRNA step was performed. Sytox Orange was added to both samples to a final concentration of 250 nM for fluorescent imaging. Coarse z-stacks were taken over 10 planes at ~100 fields-of-view, DNA objects were counted and their radius of gyration was calculated.

5.4.5. FLUORESCENCE MICROSCOPY

DNA objects were imaged inside the observation well using an Olympus IX81 inverted microscope with a Yokogawa CSU X1 spinning disk confocal module. Imaging was done through 100x oil objective (NA = 1.4). Excitation of the DNA-intercalating Sytox Orange was provided by a 561 nm CW laser at 5 mW power, while emission was collected with a 617/73 nm filter with detection by an EM-CCD Andor iXon X3 DU897 camera (512 x 512 pixels, with 16 μm pixel size, and effective pixel size 118 nm). The images were captured with an exposure time of 10 ms and EM gain at 150. Motion was controlled by a piezo stage, and the microscope was operated using Andor iQ3 software. *Z*-stacks were taken with either 0.16 μm or 2 μm spacing, denoted by 'fine' and 'coarse' spacing, respectively. The fluorescent SLB was excited using a 390 nm CW laser at 25 mW and emission was collected through a 475/42 nm filter after an exposure of 100 ms and EM gain of 250.

The imaging of the Ori and Ter labels in bacteria was done on a Nikon Ti-E microscope with a 100x oil objective (NA = 1.45). mCerulean was excited by SpectraX LED (lumencor) at 430-450 nm in combination with a CFP filter cube (excitation / dichroic / emission = 426-446 / 455 / 460-500 nm). mCherry was excited by SpectraX LED 575/25 nm and a tripe bandpass filter 465/25 – 545/30 – 630/60 nm. Detection was provided by an Andor Zyla CMOS camera.

5.4.6. OBJECT DETECTION AND TRACKING

At each timepoint in a maximum intensity projection is made, on which the subsequent object detection, tracking and radius of gyration calculation is done. A Laplace of Gaussian filter (radius 15 pixels = 2.4 μm) was applied to the MAX-projected image.[59] Only those local maxima in the filtered image were kept whose intensity exceeded the median intensity of the unfiltered image.

DNA objects tended to display large amounts of directional flow during the experiment. A Large Displacement Optical Flow scheme was used to estimates the motion of objects or edges between subsequent frames.[67,68] Briefly, at each pixel the image gradient is calculated and the image is split into blocks of 6x6 pixels. The directions of the gradient are discretized into 9 bins, and then in each 6x6 pixel block the HOG (histogram of oriented gradients) is determined. This is done by counting how many gradient vectors fall within each bin. In this way the HOG is a local description (with in 6x6 region) of the spatial distribution of intensities. This is repeated for the whole image and also the image of the following timepoint. To get an initial guess of the optical flow between frame 1 and 2, the

HOG descriptors in each frame are matched by using a nearest-neighbour search. Then the Optical Flow is explicitly calculated by a variational approach, that is, by minimizing an energy functional under variation of estimated flow field. In this scheme there are energy penalties for mismatches in intensity values between shifted frame 1 (shifted using an estimated flow field) and frame 2. Secondly, there are requirements that the second derivatives of the field are small, *i.e.*, the flow fields are smooth. Then there is the requirement that the initial guess as described above influences the solution as the first stages of the minimization. The energy functional is minimized in steps, by processing the images at different resolution levels (obtained by various degrees of smoothing). The flow field estimated at a coarse resolution is used as an initial guess of the flow field of the subsequent finer resolution step. This is repeated until the original resolution is reached. The step in the tracking of DNA objects is correspondence linking. The means that we need to link a detected DNA object in frame 1 to a DNA object in frame 2. This is done by constructing a weights matrix, which dictate the confidence that an object in frame 1 corresponds to an object in frame 2. First of all, there is a weight associated with the prediction from optical flow, *i.e.*, what are the distances between a predicted future location of a spot in frame 1 and all the spots in frame 2. The second part of the weight matrix are the cross correlations between small regions centered around a DNA object in frame 1 and all objects in frame 2. Using these two measures, the most likely correspondence between an object in frame 1 and 2 are chosen. By performing the optical flow estimation and correspondence linking for all objects and at all timepoints, tracks of objects are reconstructed. In order to improve the yield of tracking, the optical flow-based tracking is used in combination with Single Particle Tracking algorithms (such as those in TrackMate[59]) in order to merge tracks which would have otherwise been interrupted.

5.4.7. DENOISING, OBJECT SEGMENTATION, AND RADIUS OF GYRATION CALCULATION

For each tracked DNA object, the radius of gyration needs to be calculated within a 100x100 pixel crop around the object's global maximum. A similar procedure is used as in chapter 3 with some modifications to the subtraction of the background and the object segmentation. Furthermore, the the radius of gyration in figure 5.3 is calculated on the maximum-intensity projection instead of on the full z-stack, as in figure 5.2. First, the intensity values of each pixel in the crop are normalized between -1 and 1, and are sorted from small to large. Then the lower half of the values are fit to inverse normal cumulative distribution, basically fitting the intensity values to random Gaussian noise. The fit is extrapolated to the top half of the range, and is then subtracted from the observed values, thereby removing the low intensity Gaussian noise from the image crop.[69] To filter out high-intensity Gaussian noise the following steps are taken. The image crop is median filtered and regional maxima of high intensity are found. Only those maxima with an intensity lower than half of the maximum intensity in the crop are kept. At each of the remaining local maxima a small two-dimensional Gaussian is fitted, and finally the sum of all these small Gaussian is subtracted from the image.[63] Now the image is free from both low and high-intensity Gaussian noise. The denoised image crop is binarized

using a threshold value of zero and the resulting foreground mask is cleaned and the boundary is smoothed. Then the radius of gyration can be calculated[70,71] using intensity values from the denoised image crop which fall within the foreground mask region.

5.4.8. Z-SLICE TRACKING FOR CLUSTER DETECTION

The maximum intensity projection is not suitable to analyse the formation, size and DNA content of clusters. To this end, a suitable *z*-slice at the last timepoint was manually selected, in which clusters were clearly visible. This 'in focus' *z*-slice was then backtracked through the time series by calculating the cross correlation between the current *z*-slice and all the *z*-slices at the previous timepoint, and selecting the most probable 'in focus' *z*-slice at the previous timepoint. Next translational and rotational motion (using an estimate of a rigid transformation of the object) is estimated that best aligns the image in subsequent time points.[72]

5.4.9. IDENTIFICATION OF EMERGING CLUSTERS WITH A PROBABILISTIC APPROACH

There is a probability for each pixel that it is associated with a cluster at a particular time or not. The pixel intensity in a DNA object will fluctuate for many reasons, of which noise and internal polymer dynamics are the most obvious. However, we are interested in characterizing fluctuations due to the formation of clusters as a result of DNA compaction. The first three minutes of the intensity traces of each pixel is used as baseline data, for which is assumed that no clusters exist. At every subsequent timepoint the likelihood ratio is calculated that the pixel belongs to a cluster *vs.* the null hypothesis that it does not. Then the pixel at that timepoint is assigned to the 'cluster' category by a statistical test, which determines if the obtained likelihood ratio is significant or has occurred by chance. This is done by randomized testing. The maximum likelihood ratio value of the data during the timelapse is found. Subsequently, a large number of replica data sets are generated under the null hypothesis (no clusters). For each of the replica data sets the maximum likelihood ratio value is also determined. A fraction of the total number of replica datasets will have a larger likelihood ratio than the original data, which can be used as *p*-value. If the *p*-value for a pixel at a certain time is less than 0.01, then the pixel is classified as belonging to a cluster. This procedure is done for all pixels at all timepoints beyond the baseline time period of three minutes. Regions of connected pixels classified as clusters are annotated at each time point, and in those regions local maxima of intensity are found. The number of local maxima was taken as the number of clusters in the subsequent analysis. This method was adapted from Ref[73].

MODELLING REGIONS OF EMERGING CLUSTERS WITH ANISOTROPIC GAUSSIANS

To characterize the area and DNA content of clusters, the intensity values within the cluster regions were modeled by a sum of two-dimensional Gaussians. The number of Gaussians used to fit the intensity distribution within these regions was equal to the number

of detected clusters in that region. The area of a single cluster was then defined at which the Gaussian reaches its half-maximum level. This means that the area can be described by an ellipse centered at the Gaussian's centre, and is therefore directly dependent on the Gaussian's standard deviation in the x and y direction. The DNA content of a cluster is defined as the amplitude of the Gaussian fit.

5.5. SUPPLEMENTARY INFORMATION

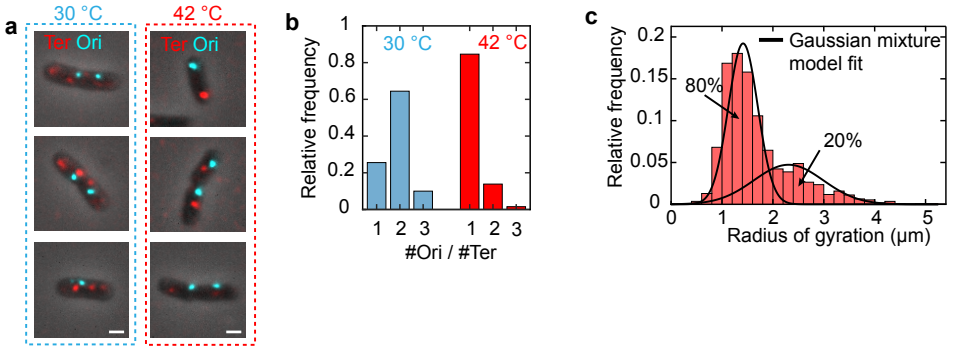

Figure S5.1: **The majority of cells contains a single chromosome after temperature-induced inhibition of replication-initiation. (a)** Cells are labeled at the origin (Ori) and terminus (Ter) of replication using FROS arrays (see methods). When grown at 30 °C (left), cells mostly show an unequal number of Ori and Ter spot labels. This indicates that replication is ongoing. The cells contain a temperature-sensitive allele of DNA-C, which is essential for replication initiation. Therefore, after shifting growth conditions to 42 °C (right), replication initiation is halted, which is demonstrated by the cells displaying equal numbers of Ori and Ter spots. Scale bar, 1 μm. **(b)** Ratio of the number of Ori and Ter spots in both growth conditions. At 30 °C only ~20% of cells contain a single chromosome, whereas this increases to 80%. after incubating at 42 °C for 1 hour. **(c)** Distribution of radius of gyrations (determined on 'fine' z-stacks) of DNA objects extracted from the temperature-treated cells, which shows two populations, as determined by fitting the distribution with two Gaussians. The two populations have a relative weight of 80% and 20%, and their means are centered at 1.4 ± 0.3 μm and 2.3 ± 0.7 μm, respectively.

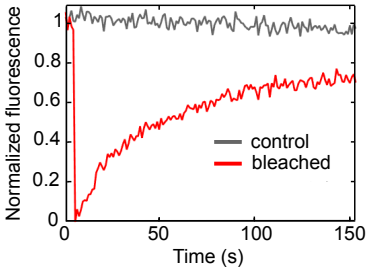

Figure S5.2: **FRAP experiment on supported lipid bilayer coating the observation well** The lipid bilayer shows recovery after photobleaching (red) compared to the control (gray) in which no photobleaching was performed, indicating that the lipids in the bilayer are mobile.

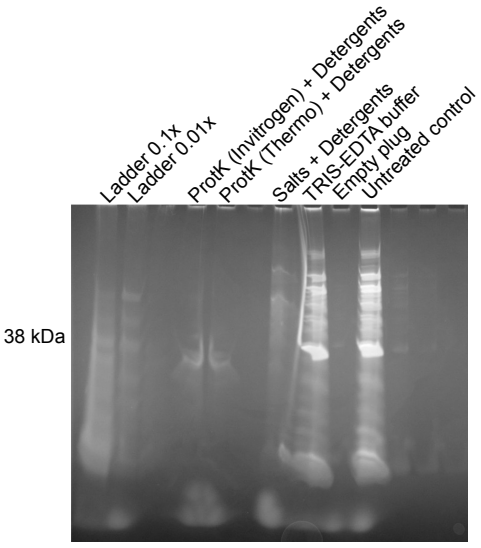

Figure S5.3: **Protein gel to indicate residual proteins in agarose plugs after various protein removal treatments.** The most relevant lanes on this gel are the 'untreated control' and the 'Tris-EDTA buffer'. It is seen that the signal in these lanes seems similar in strength. This is an indication that proteins are present in the samples to a similar degree, and therefore we conclude that that proteins were not significantly removed by washing the agarose plugs repeatedly using a high-volume Tris-EDTA buffer. This result was confirmed in a repeat of this experiment. Experiment performed by Chiel de Groot.

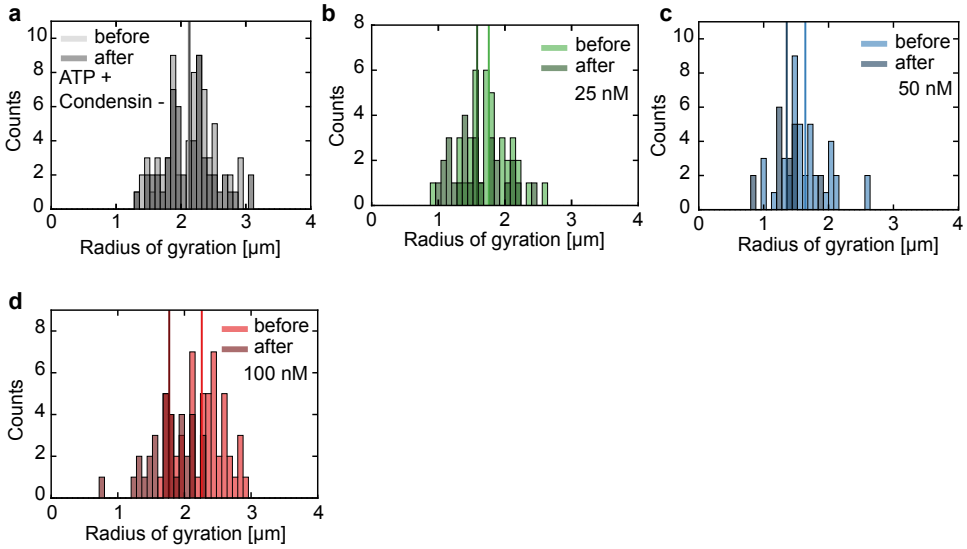

Figure S5.4: **Radius of gyration at two timepoints for control (ATP, but no condensin), and 25 nM, 50 nM and 100 nM condensin concentrations.** The distributions of the radius of gyration are shown at $t = 0$ min (before) and $t = 15$ min (after) for the data from figure 5.3. **(a)** Control condition with ATP and no condensin, with means $R_{g,\mathrm{BEFORE}} = 2.1\ \mu$m and $R_{g,\mathrm{AFTER}} = 2.1\ \mu$m. **(b)** 25 nM condensin, with means $R_{g,\mathrm{BEFORE}} = 1.8\ \mu$m and $R_{g,\mathrm{AFTER}} = 1.6\ \mu$m. **(c)** 50 nM condensin, with means $R_{g,\mathrm{BEFORE}} = 1.6\ \mu$m and $R_{g,\mathrm{AFTER}} = 1.4\ \mu$m. **(d)** 100 nM condensin, with means $R_{g,\mathrm{BEFORE}} = 2.3\ \mu$m and $R_{g,\mathrm{AFTER}} = 1.8\ \mu$m. Vertical lines in each panel denote the mean of the distribution for each timepoint.

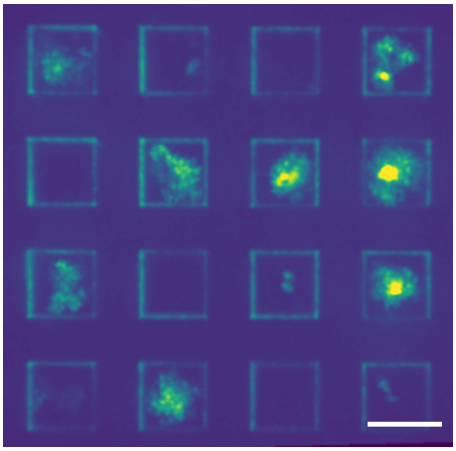

Figure S5.5: **DNA objects inside microchambers patterned in PDMS on the bottom surface of an observation well.** Normally, the bottom surface of an observation well is made by a glass coverslip (see figure 5.1a) coated with a lipid bilayer. Here, however, the glass coverslip is coated with a thin layer of PDMS and stamped onto a silicon wafer containing a pattern of small rectangular pillars of 15x15x23 μm. The resulting indentations in the PDMS coated coverslip then act as microchambers. A coverslip is bonded to the PDMS observation well, and the device is subsequently coated with a lipid bilayer. DNA objects, isolated using the bulk protocol and without protein removal treatment, are pipetted into the well and centrifuged gently to introduce them into the microchambers with up to ~50% occupancy. Without centrifugation, the occupancy of the microchambers was severely reduced. However, once the protein removal treatment is applied to the DNA objects, the centrifugation causes significant fragmentation. For this reason, this method was abandoned. Experiment performed by Martin Holub.

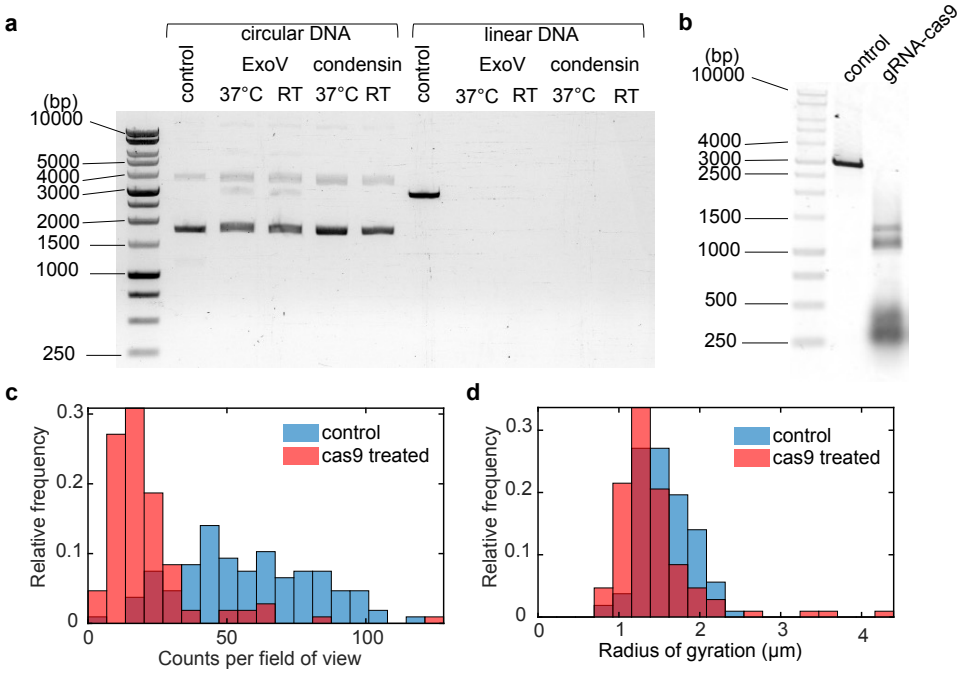

Figure S5.6: **Using Exonuclease V (RecBCD) enzyme to digest fragmented DNA objects.** Exonuclease V enzyme digests linear DNA, but leaves circular DNA intact. As it is likely that the handling of the DNA during the chromosome isolation protocol will result in fragmentation of the initially circular DNA, it was tested if Exonuclease V (ExoV) could remove these linear fragments from the sample. **(a)** ExoV is specified to be active in the buffer supplied by the manufacturer. However, we perform our experiments in condensin buffer. We therefore ascertained that ExoV could also work in the condensin buffer. To this end a ~3 kbp circular plasmid was purposefully cut using the XhoI restriction enzyme, resulting in a linear DNA. Lanes with circular control DNA produce a strong band at 1.7 kbp, corresponding to supercoiled circular DNA, and a weak band at 4 kbp from nicked (and thus relaxed) circular DNA. The linear control DNA runs at the expected 3 kbp height. Then the circular and linear DNA were incubated in the presence of ExoV enzyme in both ExoV and condensin buffer at the manufacturer-specified 37 °C and at room temperature (RT). The circular DNA was relatively unaffected by the enzyme, except that in the ExoV buffer there is weak band visible, corresponding to the size of linear DNA. The linear DNA sample, on the other hand, was completely degraded in all conditions. **(b)** To purposefully cut the genomic DNA, Cas9 enzyme was used together with a mix of 20 gRNAs targeting a 1 kbp region on the right arm of the chromosome. The activity of the mix of gRNAs was tested on a 3 kB DNA fragment containing the target region. After digestion with the cas9-gRNA complexes, the DNA fragment was cut, resulting in two bands band at $/sim1$ – 1.5 kbp, which corresponds to the DNA stretches on either side of the target region. The smear below 500 bp are from the multiple small digestion fragments. **(c)** DNA objects isolated from cells were observed in observation wells, with and without Cas9 added, and both in the presence of ExoV enzyme. The number of detected DNA objects per field-of-view in the control sample compared to the Cas9-treated sample was 57 ± 24 and 21 ± 17, respectively. **(d)** The radius of gyration (calculated on the maximum intensity projection of coarse z-stacks) of the remaining DNA objects was similar, with 1.4 ± 0.5 μm and 1.6 ± 0.3 μm, for the control and Cas9-treated sample respectively. This data show that ExoV can remove linearized DNA objects from the sample. Quoted values are mean ± standard deviation.

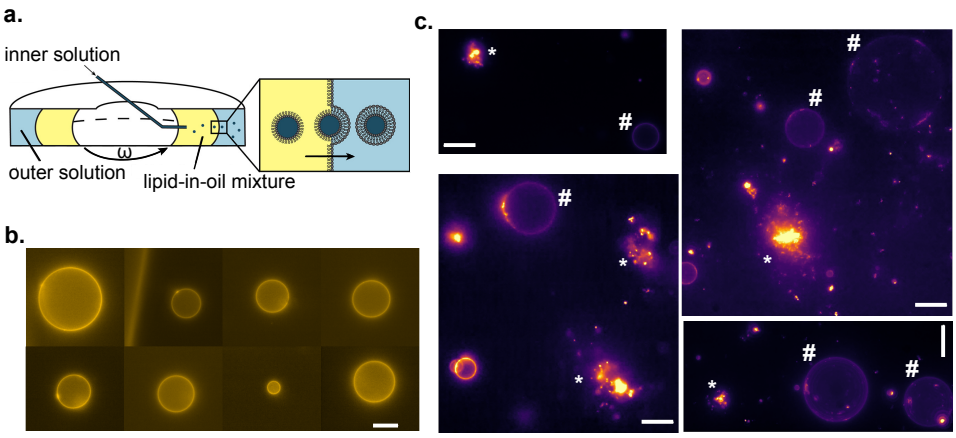

Figure S5.7: **Attempts at encapsulating isolated chromosomes inside liposomes produced with optimized cDICE method.** **(a)** The cDICE device consist of rotation chamber (an imaging dish), in which a lipid-in-oil mixture and an aqueous outer solution are present. A capillary of 200 μm diameter injects the inner solution into the chamber while it rotates at frequency ω. Droplets of inner solution pass through the lipids-in-oil-phase, and when they break through the boundary with outer solution, liposomes are formed. Adapted from ref [74]. **(b)** Examples of liposomes formed with the cDICE method. Lipids were DOPC spiked with RhodB functionalized lipids for fluorescent imaging, the inner solution was 70 mM sucrose in 10 mM Tris-HCl, and the outer solution was 100 mM glucose. Scale bar, 25 μm. **(c)** *E. coli* chromosomes isolated using the Woldringh protocol (without ProtK protein removal treatment) and stained with Sytox Orange were used as inner solution. No chromosome encapsulation was achieved: in the resulting solution there were DNA objects (denoted with *) observed outside liposomes (denoted with #). Possibly the liposomes were too small, relative to the size to the DNA object to be encapsulated, resulting in bursting liposomes. Note that Sytox Orange also stains the lipid membrane. Attempts at microfluidic encapsulation of (deproteinated) DNA inside water-in-oil droplets, double emulsion droplets, and liposomes, were not successful (apart from the example shown in figure 4.1): DNA was very obviously fragmented after encapsulation. Scale bars, 20 μm. Images in panel b taken by Rafael Jezior and in panel c by Martin Holub and Nicola De Franceschi.

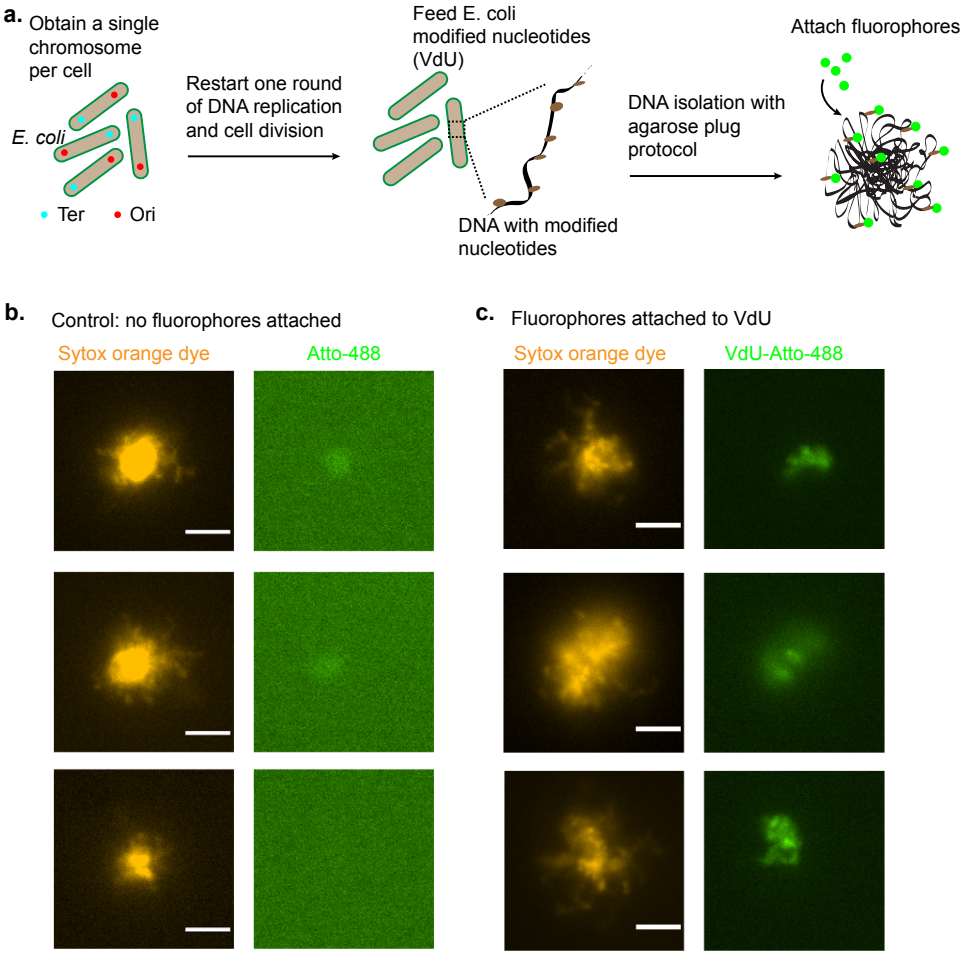

Figure S5.8: **Attempts at covalent labeling of isolated chromosome via modified nucleotides VdU. (a)** Schematic of the labeling procedure. Temperature-sensitive *E. coli* cells were grown at elevated temperature in order to obtain a single chromosome per cell (see methods of chapters 3 and 5). Modified VdU nucleotides were added to the medium and cells were briefly (~20 min) returned to a lower temperature in order to re-start DNA replication. This allowed the incorporation of the modified nucleoids into the genome. Cells were then returned to the elevated temperature, resulting in cells with a single modified chromosome per cell. DNA isolation was performed using the agarose plug protocol, after which the fluorophores Atto-488 were attached to the modified nucleotides. **(b)** Example images of DNA objects that have not undergone the last step of fluorophore attachment. Yellow signal is Sytox Orange DNA dye, and in green the signal in the Atto-488 channel. There is a little spectral overlap of the channels. Scale bars, 5 μm. **(c)** Example images of DNA objects after the last step of fluorophore attachment. Yellow signal is Sytox Orange DNA dye, and green signal is from the Atto-488 fluorophores attached to the modified VdU nucleotides. From the images it is apparent that the covalent VdU labeling did not cover the whole genome. Scale bars, 5 μm. Protocol obtained from Ref [75].

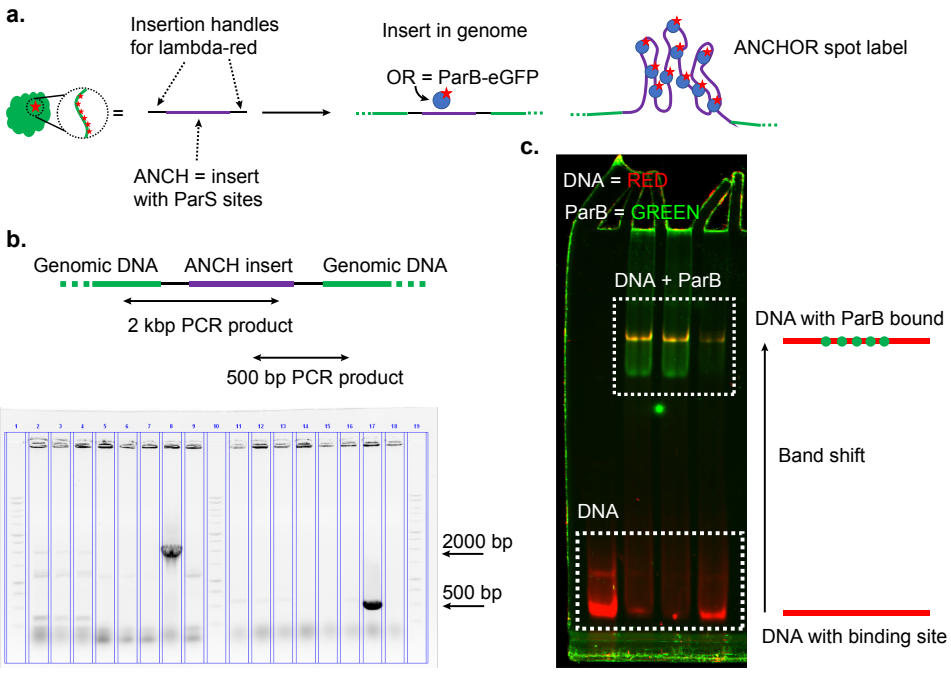

Figure S5.9: **Attempts at spot labeling isolated chromosomes using ANCHOR ParS/ParB system. (a)** Schematic of the procedure to label a genomic location using the ANCHOR system.[76] A DNA construct was made containing ParS sites (the "ANCH" in ANCHOR) which are flanked by lambda-red insertion handles, which specify the insertion location in the genome. Recombination via the lambda-red system was used to insert the ANCH into the genome of *E. coli* cells. After DNA isolation, purified ParB-eGFP (the "OR" in ANCHOR) can bind at the ParS sites and oligomerize, forming a fluorescent spot on the isolated chromosome. **(b)** To verify that the ANCH was inserted correctly, a colony PCR was performed using two primer pairs covering both ends of the ANCH insert. Bands in lane 8 and 17 indicate PCR products of the expected sizes of 500 and 2000 bp. **(c)** A band-shift assay was performed to check that the purified ParB-eGFP could bind it target DNA sequences on the ANCH insert. Lane 1 contained only the target DNA, while lanes 2/3/4 additionally contained varying concentrations of ParB-eGFP. Since the binding of the protein to the target DNA changes the electromobility of the DNA and the protein, the DNA-protein complex does not run as far into the gel as the DNA alone (band shift). Experiments in panels b and c performed by Spark Yadav and Jaco van der Torre.

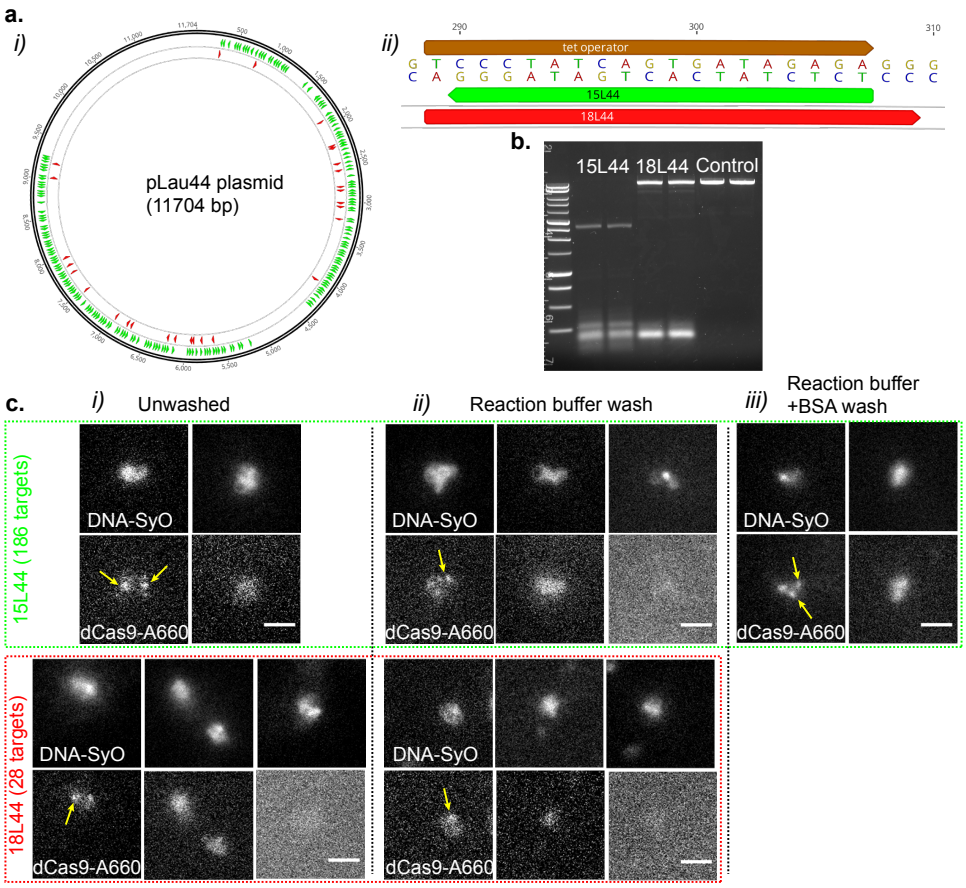

Figure S5.10: **Attempts at spot labeling isolated chromosomes using dCas9 targeting repeated sequences.** dCas9-Alexa660 was used to target repeated TetO sequences inserted near the Origin of replication in the *E.coli* genome. The procedure was performed in-plug on chromosomes isolated with the agarose plug protocol. Two truncated guide RNAs were designed resulting in either 186 targets (15L44) or 28 targets (18L44). **(a)** ***(i)*** The pLau44 plasmid contained the repeated TetO sequences as they were inserted in the bacterial genome. The green arrows are the targets of the 15L44 guide RNA, and the red arrows are the targets of the 18L44 guide RNA. ***(ii)*** The target sequences of the 15L44 and 18L44 guide RNA are shown in relation to the TetO sequence. **(b)** A cleavage assay to check for the cleavage efficiency of the designed guide RNA's. Lane 1 contains ladder. Lanes 5/6 contain the uncut pLau44 plasmid as a control. Lane 2/3 contain pLau44 plasmid incubated with dCas9 and 15L44 guide RNA. The cleavage is efficient, because only a 3 kbp band of DNA without TetO repeats and small cleavage products are visible. Lane 4/5 contain pLau44 plasmid incubated with dCas9 and 18L44 guide RNA. The cleavage is not very efficient in this case, because there is still a lot of uncleaved DNA present (bands at the same height as in the control). *(Caption continued on next page)*

Figure S5.10 *(continued from previous page)*: **(c)** Examples of DNA objects labeled with dCas9-Alexa660 using the 15L44 guide RNA (top group surround by green line) or 18L44 guide RNA (bottom group surrounded by red line). After incubation with the dCas9 and guide RNA the agarose plugs containing the DNA objects were either ***(i)*** not washed; ***(ii)*** washed with dCas9 reaction buffer; or ***(iii)*** washed with dCas9 reaction buffer supplemented with BSA and Tween-20. These washing steps were done to remove non-specifically bound dCas9. The images shown in the top row of each group are the signal from DNA stained with Sytox Orange, while the bottom row of each group is signal from dCas9-Alexa660. ***(i)*** 15L44 guide RNA (no washing): 10% of objects (N=134) show dCas9 spots (left), 90% show non-specific dCas9 signal (right). 18L44 guide RNA (no washing): 3% of objects (N=97) show dCas9 spots (left), 89% show non-specific dCas9 signal (middle) and 8% have no dCas9 signal (right). ***(ii)*** 15L44 guide RNA (reaction buffer wash): 16% of objects (N=56) show dCas9 spots (left), 66% show non-specific dCas9 signal (middle) and 18% have no dCas9 signal (right). 18L44 guide RNA (reaction buffer wash): 6% of objects (N=51) show dCas9 spots (left), 82% show non-specific dCas9 signal (middle) and 12% have no dCas9 signal (right). ***(iii)*** 15L44 guide RNA (reaction buffer with BSA and Tween-20 wash): 24% of objects (N=56) show dCas9 spots (left), 76% show non-specific dCas9 signal (right). Overall, only a minority of DNA objects showed dCas9 spots, with the majority showing non-specific dCas9 signal. This is possibly because too high dCas9 concentrations were used compared to the amount of available DNA in the agarose plug. Experiments performed by Tim Heemskerk.

REFERENCES

(1) Luger, K.; Mäder, A. W.; Richmond, R. K.; Sargent, D. F.; Richmond, T. J. Crystal structure of the nucleosome core particle at 2.8 Å resolution. *Nature* **1997**, *389*, 251–260.

(2) Wang, M. D.; Schnitzer, M. J.; Yin, H.; Landick, R.; Gelles, J.; Block, S. M. Force and Velocity Measured for Single Molecules of RNA Polymerase. *Science* **1998**, *282*, 902–907.

(3) Van Steensel, B.; Furlong, E. E. The role of transcription in shaping the spatial organization of the genome. *Nature Reviews Molecular Cell Biology* **2019**, *20*, 327–337.

(4) Mirny, L. A.; Imakaev, M.; Abdennur, N. Two major mechanisms of chromosome organization. *Current Opinion in Cell Biology* **2019**, *58*, 142–152.

(5) Rowley, M. J.; Corces, V. G. Organizational principles of 3D genome architecture. *Nature Reviews Genetics* **2018**, *19*, 789–800.

(6) Nuebler, J.; Fudenberg, G.; Imakaev, M.; Abdennur, N.; Mirny, L. A. Chromatin organization by an interplay of loop extrusion and compartmental segregation. *Proceedings of the National Academy of Sciences* **2018**, *115*, E6697–E6706.

(7) Kschonsak, M.; Merkel, F.; Bisht, S.; Metz, J.; Rybin, V.; Hassler, M.; Haering, C. H. Structural Basis for a Safety-Belt Mechanism That Anchors Condensin to Chromosomes. *Cell* **2017**, *171*, 588–600.

(8) Eeftens, J. M.; Katan, A. J.; Kschonsak, M.; Hassler, M.; de Wilde, L.; Dief, E. M.; Haering, C. H.; Dekker, C. Condensin Smc2-Smc4 Dimers Are Flexible and Dynamic. *Cell Reports* **2016**, *14*, 1813–1818.

(9) Ganji, M.; Shaltiel, I. A.; Bisht, S.; Kim, E.; Kalichava, A.; Haering, C. H.; Dekker, C. Real-time imaging of DNA loop extrusion by condensin. *Science (New York, N.Y.)* **2018**, *360*, 102–105.

(10) Kong, M.; Cutts, E. E.; Pan, D.; Beuron, F.; Kaliyappan, T.; Xue, C.; Morris, E. P.; Musacchio, A.; Vannini, A.; Greene, E. C. Human Condensin I and II Drive Extensive ATP-Dependent Compaction of Nucleosome-Bound DNA. *Molecular Cell* **2020**, *79*, 99–114.

(11) Golfier, S.; Quail, T.; Kimura, H.; Brugués, J. Cohesin and condensin extrude DNA loops in a cell-cycle dependent manner. *eLife* **2020**, *9*, e53885.

(12) Davidson, I. F.; Bauer, B.; Goetz, D.; Tang, W.; Wutz, G.; Peters, J.-M. M. DNA loop extrusion by human cohesin. *Science (New York, N.Y.)* **2019**, *366*, 1338–1345.

(13) Kim, Y.; Shi, Z.; Zhang, H.; Finkelstein, I. J.; Yu, H. Human cohesin compacts DNA by loop extrusion. *Science (New York, N.Y.)* **2019**, *366*, 1345–1349.

(14) Pradhan, B.; Kanno, T.; Umeda Igarashi, M.; Loke, M. S.; Baaske, M. D.; Wong, J. S. K.; Jeppsson, K.; Björkegren, C.; Kim, E. The Smc5/6 complex is a DNA loop-extruding motor. *Nature 2023 616:7958* **2023**, *616*, 843–848.

(15) Shaltiel, I. A.; Datta, S.; Lecomte, L.; Hassler, M.; Kschonsak, M.; Bravo, S.; Stober, C.; Ormanns, J.; Eustermann, S.; Haering, C. H. A hold-and-feed mechanism drives directional DNA loop extrusion by condensin. *Science* **2022**, *376*, 1087–1094.

(16) Bauer, B. W.; Davidson, I. F.; Canena, D.; Wutz, G.; Tang, W.; Litos, G.; Horn, S.; Hinterdorfer, P.; Peters, J. M. Cohesin mediates DNA loop extrusion by a "swing and clamp" mechanism. *Cell* **2021**, *184*, 5448–5464.

(17) Higashi, T. L.; Pobegalov, G.; Tang, M.; Molodtsov, M. I.; Uhlmann, F. A Brownian ratchet model for DNA loop extrusion by the cohesin complex. *eLife* **2021**, *10*, DOI: 10.7554/eLife.67530.

(18) Marko, J. F.; De, P.; Rios, L.; Barducci, A.; Gruber, S. DNA-segment-capture model for loop extrusion by structural maintenance of chromosome (SMC) protein complexes. *Nucleic Acids Research* **2019**, *47*, 6956–6972.

(19) Nomidis, S. K.; Carlon, E.; Gruber, S.; Marko, J. F. DNA tension-modulated translocation and loop extrusion by SMC complexes revealed by molecular dynamics simulations. *Nucleic Acids Research* **2022**, *50*, 4974–4987.

(20) Ryu, J.-K.; Katan, A. J.; van der Sluis, E. O.; Wisse, T.; de Groot, R.; Haering, C. H.; Dekker, C. The condensin holocomplex cycles dynamically between open and collapsed states. *Nature Structural & Molecular Biology* **2020**, *27*, 1134–1141.

(21) Oldenkamp, R.; Rowland, B. D. A walk through the SMC cycle: From catching DNAs to shaping the genome. *Molecular Cell* **2022**, *82*, 1616–1630.

(22) Schmitt, A. D.; Hu, M.; Ren, B. Genome-wide mapping and analysis of chromosome architecture. *Nature Reviews Molecular Cell Biology* **2016**, *17*, 743–755.

(23) Denker, A.; de Laat, W. The second decade of 3C technologies: detailed insights into nuclear organization. *Genes & development* **2016**, *30*, 1357–1382.

(24) Rao, S. S.; Huntley, M. H.; Durand, N. C.; Stamenova, E. K.; Bochkov, I. D.; Robinson, J. T.; Sanborn, A. L.; Machol, I.; Omer, A. D.; Lander, E. S.; Aiden, E. L. A 3D Map of the Human Genome at Kilobase Resolution Reveals Principles of Chromatin Looping. *Cell* **2014**, *159*, 1665–1680.

(25) Haarhuis, J. H.; van der Weide, R. H.; Blomen, V. A.; Yáñez-Cuna, J. O.; Amendola, M.; van Ruiten, M. S.; Krijger, P. H.; Teunissen, H.; Medema, R. H.; van Steensel, B.; Brummelkamp, T. R.; de Wit, E.; Rowland, B. D. The Cohesin Release Factor WAPL Restricts Chromatin Loop Extension. *Cell* **2017**, *169*, 693–707.

(26) Davidson, I. F.; Barth, R.; Zaczek, M.; van der Torre, J.; Tang, W.; Nagasaka, K.; Janissen, R.; Kerssemakers, J.; Wutz, G.; Dekker, C.; Peters, J.-M. CTCF is a DNA-tension-dependent barrier to cohesin-mediated loop extrusion. *Nature 2023 616:7958* **2023**, *616*, 822–827.

(27) Bintu, B.; Mateo, L. J.; Su, J.-H.; Sinnott-Armstrong, N. A.; Parker, M.; Kinrot, S.; Yamaya, K.; Boettiger, A. N.; Zhuang, X. Super-resolution chromatin tracing reveals domains and cooperative interactions in single cells. *Science (New York, N.Y.)* **2018**, *362*, eaau1783.

(28) Mateo, L. J.; Murphy, S. E.; Hafner, A.; Cinquini, I. S.; Walker, C. A.; Boettiger, A. N. Visualizing DNA folding and RNA in embryos at single-cell resolution. *Nature 2019 568:7750* **2019**, *568*, 49–54.

(29) Beagan, J. A.; Phillips-Cremins, J. E. On the existence and functionality of topologically associating domains. *Nature Genetics* **2020**, *52*, 8–16.

(30) Cardozo Gizzi, A. M.; Cattoni, D. I. TADs or no TADS: Lessons From Single-cell Imaging of Chromosome Architecture. *Journal of Molecular Biology* **2020**, *432*, 682–693.

(31) Rao, S. S.; Huang, S.-C.; Glenn St Hilaire, B.; Engreitz, J. M.; Perez, E. M.; Kieffer-Kwon, K.-R.; Sanborn, A. L.; Johnstone, S. E.; Bascom, G. D.; Bochkov, I. D.; Huang, X.; Shamim, M. S.; Shin, J.; Turner, D.; Ye, Z., et al. Cohesin Loss Eliminates All Loop Domains. *Cell* **2017**, *171*, 305–320.

(32) Batty, P.; Gerlich, D. W. Mitotic Chromosome Mechanics: How Cells Segregate Their Genome. *Trends in Cell Biology* **2019**, *29*, 717–726.

(33) Japaridze, A.; Gogou, C.; Kerssemakers, J. W.; Nguyen, H. M.; Dekker, C. Direct observation of independently moving replisomes in Escherichia coli. *Nature Communications 2020 11:1* **2020**, *11*, 1–10.

(34) Saifi, B.; Ferat, J. L. Replication Fork Reactivation in a dnaC2 Mutant at Non-Permissive Temperature in Escherichia coli. *PLOS ONE* **2012**, *7*, e33613.

(35) Smith, G. R. How RecBCD Enzyme and Chi Promote DNA Break Repair and Recombination: a Molecular Biologist's View. *Microbiology and Molecular Biology Reviews* **2012**, *76*, 217–228.

(36) Danilov, D.; Barner-Kowollik, C.; Wenzel, W. Modelling of reversible single chain polymer self-assembly: from the polymer towards the protein limit. *Chemical Communications* **2015**, *51*, 6002–6005.

(37) Dame, R. T.; Rashid, F.-Z. M.; Grainger, D. C. Chromosome organization in bacteria: mechanistic insights into genome structure and function. *Nature Reviews Genetics* **2020**, *21*, 227–242.

(38) Dillon, S. C.; Dorman, C. J. Bacterial nucleoid-associated proteins, nucleoid structure and gene expression. *Nature Reviews Microbiology* **2010**, *8*, 185–95.

(39) Kavenoff, R.; Bowen, B. C. Electron microscopy of membrane-free folded chromosomes from Escherichia coli. *Chromosoma* **1976**, *59*, 89–101.

(40) Lal, A.; Dhar, A.; Trostel, A.; Kouzine, F.; Seshasayee, A. S. N.; Adhya, S. Genome scale patterns of supercoiling in a bacterial chromosome. *Nature communications* **2016**, *7*, 11055.

(41) Ganji, M.; Kim, S. H.; van der Torre, J.; Abbondanzieri, E.; Dekker, C. Intercalation-Based Single-Molecule Fluorescence Assay To Study DNA Supercoil Dynamics. *Nano Letters* **2016**, *16*, 4699–4707.

(42) Kim, E.; Gonzalez, A. M.; Pradhan, B.; van der Torre, J.; Dekker, C. Condensin-driven loop extrusion on supercoiled DNA. *Nature Structural & Molecular Biology 2022 29:7* **2022**, *29*, 719–727.

(43) Jun, S.; Wright, A. Entropy as the driver of chromosome segregation. *Nature Reviews Microbiology* **2010**, *8*, 600–607.

(44) De Gennes, P. G., *Scaling Concepts in Polymer Physics*; Cornell University Press: 1979.

(45) Goloborodko, A.; Imakaev, M. V.; Marko, J. F.; Mirny, L. Compaction and segregation of sister chromatids via active loop extrusion. *eLife* **2016**, *5*, e14864.

(46) Arold, S. T.; Leonard, P. G.; Parkinson, G. N.; Ladbury, J. E. H-NS forms a superhelical protein scaffold for DNA condensation. DOI: 10 . 1073 / pnas . 1006966107/ - /DCSupplemental.

(47) Japaridze, A.; Yang, W.; Dekker, C.; Nasser, W.; Muskhelishvili, G. DNA sequence-directed cooperation between nucleoid-associated proteins. *iScience* **2021**, *24*, 102408.

(48) Liang, Y.; van der Valk, R. A.; Dame, R. T.; Roos, W. H.; Wuite, G. J. L. Probing the mechanical stability of bridged DNA-H-NS protein complexes by single-molecule AFM pulling. *Scientific Reports* **2017**, *7*, 15275.

(49) Dame, R. T.; Noom, M. C.; Wuite, G. J. L. Bacterial chromatin organization by H-NS protein unravelled using dual DNA manipulation. *Nature* **2006**, *444*, 387–390.

(50) Maurer, S.; Fritz, J.; Muskhelishvili, G. A Systematic In Vitro Study of Nucleoprotein Complexes Formed by Bacterial Nucleoid-Associated Proteins Revealing Novel Types of DNA Organization. *Journal of Molecular Biology* **2009**, *387*, 1261–1276.

(51) Bonato, A.; Michieletto, D. Three-dimensional loop extrusion. *Biophysical Journal* **2021**, *120*, 5544–5552.

(52) Ryu, J. K.; Bouchoux, C.; Liu, H. W.; Kim, E.; Minamino, M.; de Groot, R.; Katan, A. J.; Bonato, A.; Marenduzzo, D.; Michieletto, D.; Uhlmann, F.; Dekker, C. Bridging-induced phase separation induced by cohesin SMC protein complexes. *Science Advances* **2021**, *7*, 5905.

(53) Pradhan, B.; Barth, R.; Kim, E.; Davidson, I. F.; Bauer, B.; van Laar, T.; Yang, W.; Ryu, J. K.; van der Torre, J.; Peters, J. M.; Dekker, C. SMC complexes can traverse physical roadblocks bigger than their ring size. *Cell Reports* **2022**, *41*, 111491.

(54) Dame, R. T.; Wyman, C.; Goosen, N. H-NS mediated compaction of DNA visualised by atomic force microscopy. *Nucleic Acids Research* **2000**, *28*, 3504–3510.

(55) Japaridze, A.; Renevey, S.; Sobetzko, P.; Stoliar, L.; Nasser, W.; Dietler, G.; Muskhelishvili, G. Spatial organization of DNA sequences directs the assembly of bacterial chromatin by a nucleoid-associated protein. *The Journal of biological chemistry* **2017**, *292*, 7607–7618.

(56) Kahramanoglou, C.; Seshasayee, A. S.; Prieto, A. I.; Ibberson, D.; Schmidt, S.; Zimmermann, J.; Benes, V.; Fraser, G. M.; Luscombe, N. M. Direct and indirect effects of H-NS and Fis on global gene expression control in Escherichia coli. *Nucleic Acids Research* **2011**, *39*, 2073–2091.

(57) Brandão, H. B.; Ren, Z.; Karaboja, X.; Mirny, L. A.; Wang, X. DNA-loop-extruding SMC complexes can traverse one another in vivo. *Nature Structural & Molecular Biology 2021 28:8* **2021**, *28*, 642–651.

(58) Kim, E.; Kerssemakers, J.; Shaltiel, I. A.; Haering, C. H.; Dekker, C. DNA-loop extruding condensin complexes can traverse one another. *Nature* **2020**, *579*, 438–442.

(59) Tinevez, J. Y.; Perry, N.; Schindelin, J.; Hoopes, G. M.; Reynolds, G. D.; Laplantine, E.; Bednarek, S. Y.; Shorte, S. L.; Eliceiri, K. W. TrackMate: An open and extensible platform for single-particle tracking. *Methods* **2017**, *115*, 80–90.

(60) Ho, B.; Baryshnikova, A.; Brown, G. W. Unification of Protein Abundance Datasets Yields a Quantitative Saccharomyces cerevisiae Proteome. *Cell Systems* **2018**, *6*, 192–205.

(61) Dekker, J.; Mirny, L. The 3D Genome as Moderator of Chromosomal Communication. *Cell* **2016**, *164*, 1110–1121.

(62) Fosado, Y. A. G.; Howard, J.; Weir, S.; Noy, A.; Leake, M. C.; Michieletto, D. Fluidification of Entanglements by a DNA Bending Protein. *Physical review letters* **2023**, *130*, 058203.

(63) Wu, F.; Japaridze, A.; Zheng, X.; Wiktor, J.; Kerssemakers, J. W. J.; Dekker, C. Direct imaging of the circular chromosome in a live bacterium. *Nature Communications* **2019**, *10*, 2194.

(64) Cunha, S.; Woldringh, C. L.; Odijk, T. Polymer-Mediated Compaction and Internal Dynamics of Isolated Escherichia Coli Nucleoids. *Journal of Structural Biology* **2001**, *136*, 53–66.

(65) Wegner, A. S.; Alexeeva, S.; Odijk, T.; Woldringh, C. L. Characterization of Escherichia coli nucleoids released by osmotic shock. *Journal of Structural Biology* **2012**, *178*, 260–269.

(66) Lartigue, C.; Glass, J. I.; Alperovich, N.; Pieper, R.; Parmar, P. P.; Hutchison, C. A.; Smith, H. O.; Venter, J. C. Genome transplantation in bacteria: Changing one species to another. *Science (New York, N.Y.)* **2007**, *317*, 632–638.

(67) Brox, T.; Malik, J. Large displacement optical flow: Descriptor matching in variational motion estimation. *IEEE Transactions on Pattern Analysis and Machine Intelligence* **2011**, *33*, 500–513.

(68) Horn, B. K.; Schunck, B. G. Determining optical flow. *Artificial Intelligence* **1981**, *17*, 185–203.

(69) Vtyurina, N. What makes long DNA short? Modulation of DNA structure by Dps protein: cooperating & reorganizing, Ph.D. Thesis, Delft University of Technology, 2016, p 184.

(70) Fixman, M. Radius of gyration of polymer chains. *The Journal of Chemical Physics* **1962**, *36*, 306–310.

(71) Strychalski, E. A.; Geist, J.; Gaitan, M.; Locascio, L. E.; Stavis, S. M. Quantitative measurements of the size scaling of linear and circular DNA in nanofluidic slitlike confinement. *Macromolecules* **2012**, *45*, 1602–1611.

(72) Goshtasby, A., *2-D and 3-D image registration for medical, remote sensing, and industrial applications*; John Wiley & Sons: 2005, p 258.

(73) Neill, D. B.; Moore, A. W.; Sabhnani, M.; Daniel, K. Detection of Emerging Space-Time Clusters. **2005**.

(74) Van De Cauter, L.; Fanalista, F.; Van Buren, L.; De Franceschi, N.; Godino, E.; Bouw, S.; Danelon, C.; Dekker, C.; Koenderink, G. H.; Ganzinger, K. A. Optimized cDICE for Efficient Reconstitution of Biological Systems in Giant Unilamellar Vesicles. *ACS Synthetic Biology* **2021**, *10*, 1690–1702.

(75) Spahn, C. K.; Glaesmann, M.; Grimm, J. B.; Ayala, A. X.; Lavis, L. D.; Heilemann, M. A toolbox for multiplexed super-resolution imaging of the E. coli nucleoid and membrane using novel PAINT labels. *Scientific reports* **2018**, *8*, 14768.

(76) Germier, T.; Audibert, S.; Kocanova, S.; Lane, D.; Bystricky, K. Real-time imaging of specific genomic loci in eukaryotic cells using the ANCHOR DNA labelling system. *Methods* **2018**, *142*, 16–23.

ACKNOWLEDGEMENTS

Cees. Thank you for giving me the opportunity to do research on an unexplored topic in your lab. Your optimism, curiosity, and your enthusiasm for science are quite infectious. I learned from you a lot about how to communicate effectively with an audience, either in writing or in person. I enjoyed the weekly meetings with the rest of the GenBox team in which we evaluated the issues frankly and to-the-point, and tried to figure out the next step forward in the project. An aspect that I very much have come to appreciate is your direct openness in discussions, and that you prefer to look forward rather than back. Thank you for your continuing support during this PhD.

Nynke Dekker, Bela Mulder, Wilhelm Huck, Kristina Ganzinger, Remus Dame, Gijs Wuite, and Stan Brouns. I very much appreciate that you have taken the time to sit on my PhD defense committee, and to exchange ideas about the content of this thesis. During my PhD, I have read on many occasions papers written by you and your labs, and discussed these with my colleagues. In this way, elements of your research have certainly influenced my development as a scientist, for which I thank you.

Federico. We were partners on this journey of the PhD, and I cherish each moment of our work together doing "cutting edge" science, watching people pass by in Klooster, or writing poems for the Pickwick Club. We share a certain idealism about how science should be done, which was unfortunately not grounded in the reality of how things go in the department. I thank you for your friendship, the many long talks about the proper way of preparing Italian food, drinks and laughs, and your kind spirit. **Siddharth.** I can still remember your bouncing enthusiasm when I came to your office looking for a Master's Project. It was always a lot of fun to work together and chat about all kinds of things. Thank you for helping me become the scientist that I am now. **Yaron.** Master of Min, your perseverance, your principles, and your willingness to help is an inspiration to me. I remember fondly one of the first BN borrels that I attended, and you, Viki and I remained till late to discuss politics, science and philosophy. **Greg.** Padawan of Min, it did seem as if you, Fede and I were trying to battle the demons of synthetic cells together, albeit with only moderate success. I always had the feeling that you were a friendly teddy bear, but with a concealed rebellious nature. The time that we acted as Fede's paranymphs is a moment that I will not forget. **Alberto.** We bonded over Madi duty, and remained friends since then. Your knowledge of Wikipedia is legendary. It has always been fun spending time together during coffee breaks, borrels, in the lab, or at random occasions in and outside of BN. You are a good person, and I hope that you will not yield to the Cdv.

Jaco. De rots in de branding, van alle mensen in het lab heb ik waarschijnlijk het meest met jou gesproken. Je hebt het genome-in-a-box project helpen vormgeven vanaf het

begin, en je was altijd bereid om te helpen, mee te denken, en naar nieuwe richtingen te wijzen. Naast de wetenschap, hebben we veel gekletst over allerhande dingen, zoals grapjes over de 30% mensen, behalve op maandagen uiteraard. Zonder jouw hulp en vriendelijk zou dit alles niet mogelijk zijn geweest. **Sandro.** We started our journey in the lab more or less at the same time, and you were there throughout the development of genome-in-a-box. You are the prototypical cool scientist that we all strive to emulate, doing experiments, analyzing data and writing papers. Thanks for your help and advice, and I wish you all the best for the future. **Martin.** You are a courageous person for continuing the work on genome-in-a-box, although in some way I do feel guilty having played a part in convincing you that the project was in such a shape that you could start experiments straight away. I enjoyed working together, trying to get experiments to work, and writing the GenBox paper. I can probably say that without your help I would not have graduated: I am indebted to you. **Diederik, Tim, Stein, Spark, Roman, Chiel, Huygen, Rafael, Jonah.** You each were a valuable member of the GenBox-team and I enjoyed thoroughly working together with you during my PhD. I only hope that during your project I managed to teach you something about being a scientist, or helped you develop some useful skills.

Adi. We were the captains of the office, and surveyed and commented on, like proud hawks, all the lazy people walking too slow in front of the window. I will remember the many moments of strategizing, and drinking drinks, like bosses. I thank you for your friendship and the fun times that made the PhD to such a special period. **Daniel.** Always up for a coffee, a chat about stuff, science or some funny cat video. I admire your drive to do science, your positive attitude and your fascination with lasers. You were the best office mate one could imagine! **Paola.** Biophysicists in the lab talk a lot about biological relevance even though we don't have no clue what it means. You brought concrete knowledge about how things work in real cells, which was rather lacking in some parts of the lab. I also enjoyed discussing at great length how a modern career in science and academia should and could be shaped. I promise not to make any physicist's jokes about biologists in the future. Chickens are not spheres in a vacuum. For additional comments, see below.

Wayne. Or should I say Master Wayne, I truly think that you have put more things through a nanopore than anyone else. It was great fun running some gels together for the Cas9 paper. You are always attentive, a good friend and an excellent source of bribes. By the way, I found a great deal on black trash bags, in case you are interested. **Michel.** It was a lot of fun being your tax advisor, and getting paid in apple pie. You are a good friend and I enjoyed the times that I spent with you and Madi: how fast she grew up in the last five years! Also, in case this was not mentioned to you before, congrats on setting up a whole new direction in the lab during your PhD, a great achievement! **Jacob.** Naar mijn mening, is het je gelukt om twee van de mooiste bezigheden in het leven te combineren, kunst en wetenschap, op zo een manier dat ze balans met elkaar zijn. Als een gewaardeerde collega, plaatste je altijd de zaken in een nieuw licht, wanneer de experimentele resultaten somber waren, en je gaf telkens een fris perspectief op alledaagse (of wetenschappelijke) problemen. Struis hangt rustig en vreedzaam op de muur, en observeert iedere dag met verwondering en verbazing de gang van zaken. **Kevin.** You

are a funky scientist, and by now you are in control of the bugs, making them stand up straight. I remember fondly the times that you visited the Netherlands and we shared a beer. **Sergii.** King of Squash, you introduced me to many things, such as squash and condensed milk. Good luck in Twente, I hope to visit you soon. And remember: what is better than a single nanopore? A double nanopore!

Allard. Je bent een zeer indrukwekkende persoon. Bio- en quantumwetenschapper, een soort berggeit in Ierland en Portugal, en de enige persoon in het lab die niet te 'pranken' is. Ik heb je leren kennen als een vriendelijke en behulpzame collega. Dankjewel! **Oskar.** Carlsberg provided the lab with an excellent postdoc, although I am still waiting for the beer to arrive. Your enthusiasm for POC diagnostics is admirable, and your selflessness and humility in the lab are a breath of fresh air. You represent a kinder and more positive way of doing science than I had known before you arrived. **Kuba.** You are a mystery to me, plating cells, running a gel, going to the gym, having a shower, eating chicken and broccoli. But you have a gentle soul, and a true passion for science, which possibly suffered some dents during the PhD, but nevertheless stayed strong. **Xin.** It was nice to be your office mate, you were always up for a chat or a drink. I hope that you can make the DNA turbine and your reference manager to work.

Biswajit. A man of many talents, you have the ability to pick up any skill within no time and become an expert. I hope that the experiments with gold nanoparticles will lead to a new insight into the mechanism of condensin. **Yoones.** You are one of the most colorful Dutch persons I know. I apologize for my prejudice. You were actually the first person from the CD lab that I met. When playing darts in the old building, you explosively entered into the office. **JK.** Dr. Love, you might not remember, but we shared an office in the old building. You have a very happy disposition, and always seem to remain positive, which is a beautiful quality to have, even though you were sitting in the aquarium for a year. **Ana.** I can only admire and draw inspiration from the way you managed to come through that difficult time at BN, and in the end still have the strength and motivation to continue in science. Stay strong and I wish you all the best for your future endeavors. **Sabina.** It was a great experience to sing Christmas songs with you. **Laura.** It was a lot of fun working together on the Cas9 paper with Wayne. Your positive and friendly attitude are amazing. **Alessio.** We started our PhDs around the same time. Your concert performances on the guitar with Fede and the others are the stuff of legends, and you managed to mimic that NPC quite accurately! **Nils.** Sometimes I wish that I had your strength to not have WhatsApp. I still cannot quite share your love for Sharepoint, but I do applaud the effort to make the lab an easier place to navigate. I am sorry that I gifted you some plastic straws, even though I did use them to aerate the soil of the plant that Essie gifted me after hacking the barcode on a Bijenkorf gift card. **Sonja.** You introduced us to peculiarities of the Swiss and their language, hüppli hüppli. I do not think that single-molecule protein dynamics could have a better scientific ambassador than you. **Henry.** You are a fascinating person. You go underground, people do not see you for ages, except for some snatches of music and wisdom, and suddenly you emerge and announce that you sequenced a protein. **Eugene.** I wish you all the best in setting up your new lab! **Nicola.** It was fun writing a SciFi essay together. **Ashmiani and Eli.** Jullie zijn een fantastisch team. Velen realiseren zich niet dat zonder jullie werk, het hele lab stil

zou komen te liggen.

Davide. The discussions we had about DNA, polymers and what we could learn from our observations were very valuable. I wish you the best of luck setting up your own group, and foraying into the field of experimental science. **Martin Pabst and Carol de Ram.** The mass spectrometry was a crucial but tricky to obtain bit of data. I thank you both for your perseverance, patience, advice in getting the experiment to work and to interpret the resulting data. **Sung Hyun**. Mister Plectoneme, your BN Forum presentations were legendary, because they gave a perfect sense of your work as a detective-scientist, hunting for sequence-specific plectonemes. **Amanda.** Dank voor alle hulp in de afgelopen jaren met de administratieve kant van de PhD en de organisatie van allerhande zaken voor het lab en BN. Je bent altijd vriendelijk, behulpzaam en accuraat. **Parul.** Your stay in the lab was short but nevertheless very memorable. You have an interesting personality and I was sorry to see you go. **Mahipal.** You were a larger-than-life personality, especially at the Foosball table. **Sabrina, Roman, Tisma, Pinyao, Richard, Anders, Alejandro.** The CDlab PhD candidates and postdoc 'newbies', good luck with the rest of your time in the lab, make us all proud. And remember that in striving for excellence, you only compete with yourself, unlike what others might try to make you believe.

Bertus, Anne, Martin Depken and Christophe. Your lectures on evolution, biotechnology, biophysics and the origins of life provided the inspiration for me come to BN. More so than any of the "cutting edge" science, you are one of the main reasons that I decided to make BN my home for 5 years. I thank you for taking the time to be educators and make such insightful and well-crafted courses. **PI's of BN**. You are the constant factors of the department. Be careful that the department does not become a disparate collection of labs. **Juan, Anne, Elio, and Hyun.** Thank you for reminding me that to be an excellent scientist, you need not necessarily be at BN.

Safety people of TNW faculty. I thank you for your diligent work. I would recommend focusing less on lab coats and more on making sure that everyone can call the emergency services from the lab telephones and hear the fire alarm inside the labs. After four years in the new building this is still not the case. Also, I thank you for your assessment that mouth caps in combination with open flames, or ML-1 bacteria, are a larger safety risk than COVID-19 transmission. Continue the good work. **FMVG of the TNW Faculty.** You have been a worthy opponent during the past years. I thank you for the challenge, especially the situation concerning the censorship of the 'Biertje' and 'TUD loves Surveillance' posters.

Becca and Jochem. You both are very warm-hearted people. I thank you for your friendship, and the happy drinks, meals and times that we shared. I wish you all the happiness in the future! **Louis.** Your knowledge and scientific insights always amazed me, as well as your talent to bake bread and being a true explorer. **Misha.** You are a man of all seasons, an excellent scientist, musician and generous person. **Sasha.** You are a very interesting and helpful person. I enjoyed how we talked both about poetry and vacuum pumps. **Theo.** De persoon die een heel lab draaiende houdt. Ik heb veel bewondering voor jou! **Essie.** Dankjewel voor de mooie plant, ik heb geprobeerd om hem in leven

te houden. **Hirad.** We zaten beiden in de PhD Council, en we hebben met Kevin F. een gigantische hoeveelheid werk verzet om de PhD Career Day op te zetten. Ik denk dat we er trots op mogen zijn. Het was een mooie ervaring om hieraan samen te werken. Veel succes in de toekomst. **Sumit.** If not the most, probably one of the most memorable characters of BN, and always one of the classic figures at a party. You are eloquent, and observant, in a peculiar way, and you can turn a phrase like the best of them. I am not sure what you are doing now, and if you are getting paid to do it, but I am sure that you will make some waves. **Sam.** When I listen to you speak, I always have the feeling that everything is gonna be alright. You have an inspiring air of confidence and familiarity. During your time at BN, you were a fixture at every occasion, always happy to participate and be merry. Those were good times! **Helena.** You are a whirlwind; you certainly made your mark in the department in the most positive of ways. Greg still misses you, because all the bugs are dying. I am sure that you are rocking life wherever you might be. Do not forget the jazz. **Elisa.** You are a brilliant scientist, and if anyone manages to make the synthetic cell work, it will be you. In an ideal world, you, Fede and I could have done some awesome science experiments together with synthetic cells and microfluidics, however due to certain constraints, related to the politics of the department, this was not in the cards. Maybe we should have persisted more.

BN Foodies and Midweek Drinks: I would like to thank everyone who attended these regular events, leading to the sharing of food, drink, thoughts and experiences. Do not just celebrate at the end, but also along the way. **The Whiskey Club, Johannes, Patrick, Mehran, Da, Sumit.** Although we did not exist for very long, due to restrictions on happiness imposed by the Dean of the Faculty, we enjoyed many hours of distinguished company and conversation, as true gentlemen. **Squash Club, Jaco, Daniel, Sergii, Adi, Atilla and Paola.** Although I did not continue with squash, it was lots of fun to squash for an hour and then drink for two. Not very efficient from a health perspective, but definitely the way squash should be. **The Pickwick Club, Zeno, Matteo, Fede, Mehran, Paola, Johannes, Chris, Alberto.** This small collective was one of the most beautiful gatherings of the past five years. The way we combined food, poetry, art, friendship, music and an honest look into each other's souls, made the Pickwick Club to a monument and cornerstone of this time.

Dirk, Margot. Naar aanleiding van Toppers 2016 zijn we een heuse muzikale vriendschap begonnen. De vele muziekmiddagen van de afgelopen jaren zullen me bijblijven. Laten we zo doorgaan. **Christian, Raymond.** Jullie zijn mijn twee oudste vrienden. Onze vriendschap heeft als een soort constante standgehouden over de jaren, ondanks verhuizingen en andere veranderingen. Moge dit nog vele jaren zo blijven. **Papa, Mama, Aislinn.** Zonder al jullie steun en aanmoediging zou dit alles niet mogelijk zijn geweest. **Paola.** You are my Love. What we have can only accurately be described by poetry and music; simple words in the acknowledgements of a thesis are not sufficient. I look forward to spending our lives together.

CURRICULUM VITÆ

Anthony Thomas Frans BIRNIE

14-07-1986	Born in Amsterdam, The Netherlands.

EDUCATION

1998–2004	Voorbereidend Wetenschappelijk Onderwijs Vossius Gymnasium, Amsterdam
2005–2008	Undergraduate honours degree in Physics & Astronomy Universiteit van Amsterdam
2008	Erasmus Student Exchange Ludwig-Maximilians Universität, München
2008	Undergraduate research internships Max Planck Institut für Quantenoptik, München
2008–2012	Undergraduate honours degree in Music (Classical Singing) Guidhall School of Music and Drama, London
2013–2016	Postgraduate courses in Applied Physics Technische Universiteit Delft
2015–2016	Postgraduate research internships Technische Universiteit Delft & Cambridge University
2023	PhD. Biophysics Technische Universiteit Delft *Thesis:* Genome-in-a-box: Building a Chromosome from the Bottom Up *Promotor:* Prof. dr. C. Dekker

AWARDS AND SCHOLARSHIPS

2008	Erasmus Scholarship
2010	Ars Donandi Music Scholarship
2012	Prins Bernhard Cultuurfonds Scholarship
2012	Schubert Institute Scholarship
2013	Anne Wyburd Award of Guildhall School of Music
2015	Justus van Effen Research Grant, TU Delft

LIST OF PUBLICATIONS

6. **A. Birnie**,* A. Plat,* C. Korkmaz, J. P. Bothma, *Precisely timed regulation of enhancer activity defines the binary expression pattern of Fushi tarazu in the Drosophila embryo*, Current Biology, 33, 2839-2850 (2023).

5. M. Holub,* **A. Birnie**,* A. Japaridze, J. van der Torre, M. den Ridder, C. de Ram, M. Pabst, C. Dekker, *Extracting and characterizing protein-free megabasepair DNA for in vitro experiments*, Cell Reports Methods, 2, 100366 (2022).

4. **A. Birnie**, C. Dekker, *Genome-in-a-Box: Building a Chromosome from the Bottom Up*, ACS Nano, 15, 111-124 (2021).

3. F. Fanalista,* **A. Birnie**,* R. Maan, F. Burla, K. Charles, G. Pawlik, S. Deshpande, G. H. Koenderink, M. Dogterom, C. Dekker, *Shape and Size Control of Artificial Cells for Bottom-Up Biology*, ACS Nano, 13, 5439-5450 (2019).

2. W. Yang, L. Restrepo-Perez, M. Bengtson, S. J. Heerema, **A. Birnie**, J. van der Torre, C. Dekker, *Detection of CRISPR-dCas9 on DNA with Solid-State Nanopores*, Nano Letters, 18, 10, 6469–6474 (2018).

1. S. Deshpande, **A. Birnie**, C. Dekker, *On-chip density-based purification of liposomes*, Biomicrofluidics, 11, 3, 034106 (2018).

*equal contribution